Dissertation

submitted to the

Combined Faculties of the Natural Sciences and Mathematics

of the Ruperto-Carola-University of Heidelberg. Germany

for the degree of

Doctor of Natural Sciences

Put forward by

Daniel Lohner

born in: Cologne

Oral examination: 2013/10/29

Anisotropic flow of direct photons in Pb-Pb collisions at $\sqrt{s_{\mathrm{NN}}} = 2.76\,\mathrm{TeV}$

Referees: PD Klaus Reygers
Prof. Ulrich Uwer

Abstract

The measurement of direct photons is a unique tool for the study of early phases of ultra-relativistic nucleus-nucleus collisions. Since photons do not interact with the strong-coupling medium created in these collisions, they carry undistorted information about the system at their production time. During the hydrodynamic expansion of the fireball, pressure gradients turn inhomogeneities in the initial energy density distribution into azimuthal anisotropies in the produced particle spectra. Recent hydrodynamic calculations predict a substantial portion of direct photons from early phases of the collision, where the anisotropic flow has not fully developed. Thus, the direct-photon azimuthal anisotropy is generally expected to be small compared to the anisotropy of hadrons. However, measurements by the PHENIX experiment at RHIC revealed a direct-photon anisotropic flow with a magnitude similar to that for pions. This thesis presents the first measurement of the direct-photon anisotropic flow in Pb-Pb collisions at a center-of-mass energy of $\sqrt{s_{\mathrm{NN}}} = 2.76\,\mathrm{TeV}$ at the LHC. In particular, its dependence on the collision centrality and the triangular component were measured for the first time. Photons were measured by their conversion in the ALICE detector material. Background contributions of photons from hadron decays were determined in a cocktail simulation and subtracted. The results provide evidence for a hadron-like direct-photon anisotropic flow and are thus qualitatively consistent with the observations at RHIC. These findings challenge our present theoretical understanding of the time evolution of heavy-ion collisions and might indicate a significantly enhanced direct-photon emission from late stages of the system evolution.

Zusammenfassung

Die Messung von direkten Photonen eignet sich auf einzigartige Weise zur Untersuchung früher Phasen in ultrarelativistischen Kern-Kern-Kollisionen. Da Photonen nach ihrer Entstehung nicht mit dem in der Kollision erzeugten Medium wechselwirken, erlaubt ihre Messung direkte Rückschlüsse auf den Zustand des Systems zum Zeitpunkt ihrer Entstehung. Während der radialen Expansion des Mediums entstehen durch Inhomogenitäten in der anfänglichen Energiedichterverteilung anisotrope Druckgradienten, die zu einer azimutal anisotropen Teilchenproduktion führen. Theoretische Rechnungen sagen vorher, dass direkte Photonen überwiegend in einer frühen Phase der Kollision emittiert werden, in der sich der anisotrope Fluss noch nicht vollständig entwickelt hat, was impliziert, dass die azimutale Anisotropie direkter Photonen klein im Vergleich zu Hadronen ist. Messungen des PHENIX-Experimentes am RHIC haben jedoch gezeigt, dass die azimutale Anisotropie direkter Photonen vergleichbar mit der von Pionen ist. In dieser Arbeit wurde der anisotrope Fluss direkter Photonen erstmals in Kollisionen von Bleikernen bei einer Schwerpunktsenergie von $\sqrt{s_{\mathrm{NN}}} = 2.76\,\mathrm{TeV}$ am LHC untersucht. Insbesondere wurde die Abhängigkeit des Flusses von der Kollisionszentralität und zum ersten Mal neben dem elliptischen auch der triangulare Fluss bestimmt. Dabei wurden Photonen durch ihre Konversion im Material des ALICE-Detektors nachgewiesen. Untergrundbeiträge von Photonen aus Hadronzerfällen wurden mittels einer Cocktailsimulation bestimmt und abgezogen. Die Resultate dieser Arbeit deuten auf einen anisotropen Fluss direkter Photonen mit hadronähnlichen Eigenschaften hin und bestätigen somit qualitativ die Beobachtungen am RHIC. Diese experimentellen Befunde stellen unser theoretisches Verständnis der Zeitentwicklung von Schwerionenkollisionen in Frage und könnten auf höhere Beiträge späterer Phasen der Zeitentwicklung zur thermischen Photonenproduktion hindeuten.

'*Let us chase our imaginations to the heavens, or to the utmost limits of the universe;* ***we never really advance a step beyond ourselves****, nor can conceive any kind of existence, but those perceptions, which have appeared in that narrow compass.*'

'*Treatise of Human Nature*', D. Hume [1]

Contents

Introduction

> '*The ability to reduce everything to simple fundamental laws does not imply the ability to start from those laws and reconstruct the universe.*'
>
> '*More is different*', P. W. Anderson [2]

Although the initial conditions and early phases of the Universe are subject to speculation, most of today's accepted theories assume an incredibly high energy density, temperature and pressure, which led to a rapid expansion of the early Universe. Microseconds after the Big Bang, the Universe was probably filled with a quark-gluon plasma until its energy density decreased sufficiently to make the transition to ordinary hadronic matter such as protons and neutrons, the building blocks of atoms. The Large Hadron Collider at CERN is able to create similar conditions in highly relativistic collisions of lead ions, which allows us to investigate the quark-gluon plasma under laboratory conditions and to study how those conditions could evolve to the Universe we live in.

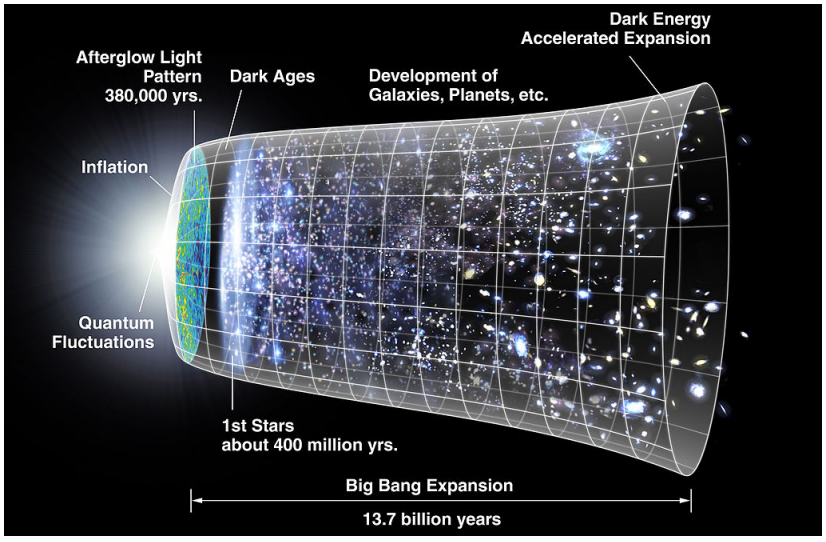

Figure 1: Time evolution of the Universe. Illustration by NASA.

Recently, the CERN experiments ATLAS and CMS have presented compelling evidence for the existence of the Higgs boson [3, 4], whose discovery completes the Standard Model (SM) of Particle Physics. Based on fundamental symmetries, the Standard Model describes the electromagnetic, weak and strong interactions of elementary particles. Despite the precise understanding of fundamental interactions in terms of its symmetries and laws, they cannot simply be extrapolated to larger and more complex many-body systems. In his article 'More is different' (1972), P.W Anderson suggested that complex physical systems may exhibit behavior that

cannot be understood only in terms of the laws governing their microscopic constituents: '*The constructionist hypothesis breaks down when confronted with the twin difficulties of scale and complexity*'. [2] The fundamental aspects of Quantum Chromodynamics, such as the spectrum of hadronic resonances and its properties, were intensively studied in hadron-hadron collisions and are well-described by the Standard Model. However, the macroscopic behavior of strongly-coupled systems at large temperatures cannot be obtained from that microscopic behavior. The main goal of ultra-relativistic heavy-ion physics is to learn more about the condensed-matter aspects of QCD and to understand its emergent macroscopic properties such as the equation of state, its viscosity and the nature of the phase transitions.

The quest for the quark-gluon plasma involves several hadronic, electromagnetic and recently also electroweak probes, which shall be discussed within this thesis. The production of hadrons is modified over the whole evolution of the strongly coupling system produced in heavy-ion collisions. The hadronic picture we observe in the particle detectors is just a snapshot of the system at the time of the last interaction. Even though the initial conditions can be studied in elementary hadron-hadron and hadron-ion collisions, the time evolution between the initial conditions and the observed final-state hadrons cannot be probed directly. Our current understanding of the intermediate phases is based on a variety of models, that start with the initial conditions and reproduce the observed final-state picture. As well as photons from hadron decays, direct photons are also emitted throughout the whole evolution of the system. Compared to hadrons, direct photons are a unique probe in the sense that photons do not interact with the strongly-coupled medium, and thus carry undistorted information about the medium at their production time.

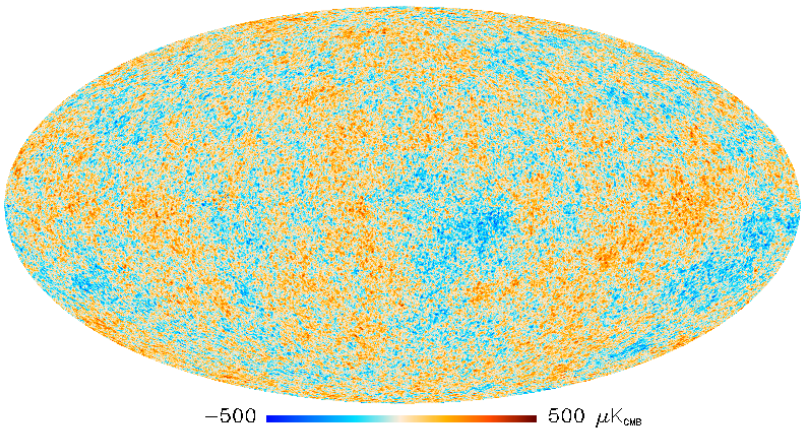

Figure 2: CMBR map measured by the PLANCK satellite [5].

There is an interesting analogy between the production of direct photons in heavy-ion collisions and the cosmic microwave background radiation (CMBR). The CMBR has a thermal black body spectrum at a temperature of about 2.73 K [6]. Within the picture of an expanding Universe, it is well explained as radiation left from an early stage about 380000 years after the Big Bang [7]. Even more interestingly, small anisotropies in the CMBR reveal quantum fluctuations in the early Universe. A recent measurement of the CMBR by the PLANCK satellite is shown in fig. 2. This measurement and also older measurements by WMAP [8] show that the CMBR is not uniform, but contains small fluctuations of the order of 0.5 mK. Qualitatively, those irregularities

are expected from small thermal variations generated by quantum fluctuations in the early Universe and give compelling evidence for the Big Bang Model. Quantitatively, those fluctuations are characterized by a multipole evolution, which is shown in fig. 3. Density perturbations in the Universe behave in part as sound waves, which give rise to the structure of anisotropies in the microwave background. The data clearly show seven acoustic peaks, which are well described by a simple six-parameter theoretical model that allow for a constraint on the parameters describing the evolution of our Universe. However, while the observations on small and intermediate angular scales agree extremely well with predictions from the Standard Model of Cosmology, the fluctuations on large angular scales (90° - 6°) are weaker than the fit of the standard model, which might suggest that some aspects of the Standard Model of Cosmology may need a rethink.

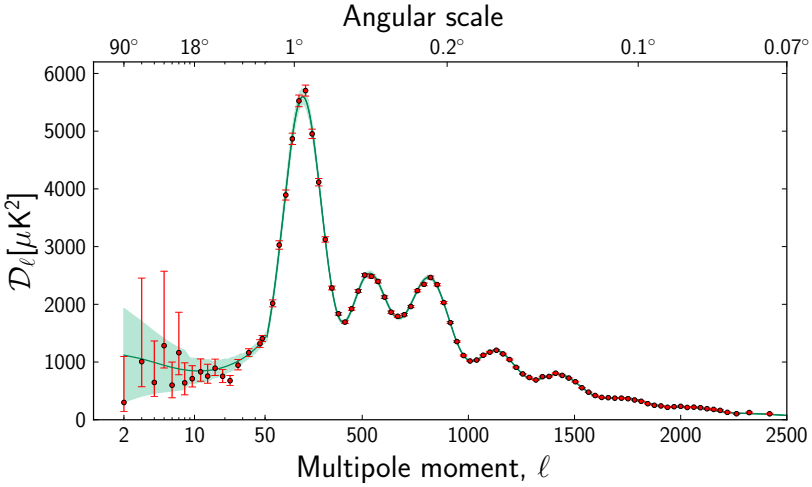

Figure 3: The temperature angular power spectrum of the primary CMBR [5].

Unlike visible matter, which is nowadays bound in planets and stars, the CMBR has not undergone any significant interactions, since it decoupled from the matter in the early Universe, and we are able to directly observe it about 13.8 billion years [5, 8] after the Big Bang. Even more remarkably, its characteristic features allow for constraints on the initial conditions of the early universe, even though those photons were produced about 380000 years after the Big Bang. Analogously, a quark-gluon plasma cannot be directly observed due to its femtoscopic lifetime, but the parameters that characterize the evolution of the fireball produced in heavy-ion collisions, such as the viscosity-to-entropy ratio, can be constrained from a Fourier expansion of angular correlations of final-state particles. During the hydrodynamic expansion of the fireball, pressure gradients turn inhomogeneities in the initial energy density distribution into azimuthal anisotropies in the produced particle spectra. The majority of the direct photons are reasonably well described by thermal radiation from the early phases of the collisions. Since azimuthal anisotropy builds up with time, the early production time of direct photons implies that their azimuthal anisotropy is expected to be significantly smaller than that of hadrons. The experimental finding at RHIC, which state that direct photons show a similar second order anisotropy compared to hadrons, is puzzling. If this result is confirmed at the LHC, it would challenge our current understanding about the time evolution of heavy-ion collisions, and might imply that most direct photons are produced in a similar phase to hadrons.

This thesis presents the first measurement of the direct-photon azimuthal anisotropy with the ALICE experiment in heavy-ion collisions in Pb-Pb collisions at a center-of-mass energy of $\sqrt{s_{\mathrm{NN}}} = 2.76\,\mathrm{TeV}$ at the LHC. For the reader, who is not familiar with heavy-ion physics, chapter 1 briefly introduces the relevant definitions of observables and their units. Chapter 2 gives a brief introduction into the condensed matter aspects of Quantum Chromodynamics with a focus on the properties of the quark-gluon plasma. Thereafter, chapter 3 sketches a standard picture for the time evolution heavy-ion collisions and introduces the idea of a thermodynamic description. Hereafter, recent experimental data is discussed and compared to theoretical models. In chapter 4, the production of direct photons in heavy-ion collisions and the puzzling discrepancy between current experimental observations and generic model expectations is discussed.
The Large Hadron Collider and the setup of the ALICE experiment are briefly described in chapter 5. The measurement of most electromagnetic observables in heavy-ion collisions requires a powerful identification of electrons from a dominant hadronic background. Chapter 6 describes the development and performance of an improved method for electron identification using the ALICE Transition Radiation Detector, which doubles the pion rejection as compared to the standard method.
In recent years, it was realized that fluctuations of the initial energy density play an important role for hydrodynamical expansion and the measurement of anisotropic flow. When most of the methods for measuring anisotropic flow were developed, fluctuations were thought to be negligible. In chapter 7, three methods for the measurement of anisotropic flow are discussed and systematic biases due to fluctuations are estimated using a Monte Carlo Glauber model. In particular, the direct-photon extraction procedure is studied with respect to the role of fluctuations. The reconstruction of photons via their conversion in the ALICE detector material is described in chapter 8. Thereafter, the measurement of the azimuthal anisotropy of neutral pions and inclusive photons is presented in chapter 9. The dominant fraction of decay photons comes from neutral pions and is subtracted from the inclusive photon measurement using a cocktail simulation based on the neutral pion measurement. The extraction of direct-photon elliptic and triangular flow is described in chapter 10. Finally, the results and their implications for our understanding of the time evolution of heavy-ion collisions are discussed in chapter 11.

1. Definitions in heavy-ion physics

Physical observables and its corresponding units are often adapted for the needs and problems in a specific field. For the reader, who is not familiar with heavy-ion physics, this chapter briefly introduces the definitions of the most relevant observables and their units.

1.1 Units

In heavy-ion physics, energy is commonly quantified by electron volts. One electron volt is the amount of energy gained by the charge of a single electron when moved across an electric potential of one volt. For practical purposes, length is expressed in femtometers, since the size of a nucleon is $\mathcal{O}(10^{-15}\,\mathrm{m})$. Femtometers are often called 'fermi' in honor of Enrico Fermi. Table 1.1 summarizes the most important observables, their dimension, their unit in heavy-ion physics and their conversions to SI units. Momentum, mass and temperature have the dimension of energy, while time has the dimension of length. An important conversion constant is given by

$$\hbar c = 197.326\,\mathrm{MeVfm}\ , \tag{1.1}$$

where c is the speed of light and $\hbar$ is the reduced Planck constant [9].

observable	dimension	unit	conversion to SI units
energy	energy	eV	$1\,\mathrm{eV} = 1.6 \times 10^{-19}\,\mathrm{kg\ m^2/s^2}$
momentum	energy	eV/c	$1\,\mathrm{eV}/c = 5.34 \times 10^{-28}\,\mathrm{kg\ m/s}$
mass	energy	eV/c^2	$1\,\mathrm{eV}/c^2 = 1.78 \times 10^{-36}\,\mathrm{kg}$
temperature	energy	eV/k_B	$38.68^{-1}\,\mathrm{eV}/k_\mathrm{B} = 300\,\mathrm{K}$
length	length	fm	$1\,\mathrm{fm} = 10^{-15}\,\mathrm{m}$
time	length	fm/c	$1\,\mathrm{fm}/c = 3.34 \times 10^{-24}\,\mathrm{s}$

Table 1.1: Observables with corresponding dimension, unit in heavy-ion physics and conversion to SI units. Values taken from [9].

1.2 Kinematics

Within this thesis, we use the common convention that $c = \hbar = k_\mathrm{B} = 1$, where k_B is the Boltzmann constant. A review of the kinematics in particle physics can be found in [9, 10]. Following the common approach, we define the z-axis along the beam direction, ϕ as the azimuthal angle in the transverse plane and θ as the inclination in beam direction, where $\theta = \pi/2$ points along the beam direction. The cartesian three momentum is then given by

$$\vec{p} = \begin{pmatrix} p_x \\ p_y \\ p_z \end{pmatrix} = \begin{pmatrix} |\vec{p}|\cos(\phi)\cos(\theta) \\ |\vec{p}|\sin(\phi)\cos(\theta) \\ |\vec{p}|\sin(\theta) \end{pmatrix}\ . \tag{1.2}$$

In relativistic kinematics, the relation between energy E, three momentum $p = |\vec{p}|$ and rest mass m is given by

$$E^2 = p^2 + m^2 \ . \tag{1.3}$$

The momentum p is defined as $p = \gamma\beta m$, with the Lorentz factor $\gamma = 1/\sqrt{1-\beta^2} = E/m$ and the velocity v divided by the speed of light, $\beta = v/c = p/E$. Rapidity is a measure of motion at relativistic velocities. In heavy-ion physics, the rapidity y is commonly defined relative to the beam axis

$$y = \frac{1}{2}\ln\left[\frac{E+p_z}{E-p_z}\right] = \tanh^{-1}\left(\frac{p_z}{E}\right) \ . \tag{1.4}$$

A rapidity of $y = 0$ implies that the particle momentum $\vec{p}$ is perpendicular to the beam axis. The transverse momentum,

$$p_{\mathrm{T}} = \sqrt{p_x^2 + p_y^2} \ , \tag{1.5}$$

is defined as the momentum component perpendicular to the beam axis. The energy and momentum of a particle can be written as as $E = m_{\mathrm{T}} \cosh y$ and $p_z = m_{\mathrm{T}} \sinh y$, where m_{T} is the transverse mass

$$m_{\mathrm{T}} = \sqrt{p_{\mathrm{T}}^2 + m^2} \ . \tag{1.6}$$

Experimentally, the pseudorapidity is often used instead of the rapidity y, which is not accessible if the particle's mass and momentum are unknown. The pseudorapidity η is defined by the angle relative to the beam axis θ,

$$\eta = \frac{1}{2}\ln\left[\frac{p+p_z}{p-p_z}\right] = -\ln\left[\tan\left(\frac{\theta}{2}\right)\right] \ . \tag{1.7}$$

For massless particles such as photons, or if masses are negligible ($p \gg m$), pseudorapidity and rapidity are identical. Finally, the conversion to cartesian momenta is given by

$$\vec{p} = \begin{pmatrix} p_x \\ p_y \\ p_z \end{pmatrix} = \begin{pmatrix} p_{\mathrm{T}}\cos\phi \\ p_{\mathrm{T}}\sin\phi \\ p_{\mathrm{T}}\sinh\eta \end{pmatrix} \qquad \text{and} \qquad |\vec{p}| = p_{\mathrm{T}}\cosh\eta \ . \tag{1.8}$$

2. Condensed matter aspects of Quantum Chromodynamics

Quantum Chromodynamics is the theory of the strong interaction between color-charged quarks and gluons. Quarks carry three different types of color charge, and antiquarks their corresponding anti-colors. Unlike the charge-neutral photon as the force carrier of the electromagnetic interaction, gluons carry color charge and thus mediate not only the strong interaction between quarks, but also between gluons themselves. As a consequence, the properties of QCD are very complex and different from those of Quantum Electrodynamics (QED). In this chapter, the concept of color confinement and asymptotic freedom shall be briefly introduced in section 2.1, followed by a brief discussion of the phase diagram of hadronic matter section 2.2.

2.1 Confinement and asymptotic freedom

The quark-antiquark potential in the strong interaction is given by

$$V_{\mathrm{s}}(r) = -\frac{4}{3}\frac{\alpha_{\mathrm{s}}}{r} + \kappa r \ , \tag{2.1}$$

where α_{s} is the strong coupling constant and κ is the ***string tension***. The second term in $V_{\mathrm{s}}(r)$ is a unique feature of QCD and implies that the strong potential increases essentially linearly as the particles are moved apart from each other. This property is linked to the concept of ***confinement*** and implies that quarks and gluons are bound in colorless hadrons in ordinary matter.

At first glance, the first term of the strong potential is similar to the Coulomb potential of QED,

$$V_{\mathrm{em}}(r) \propto -\frac{\alpha_{\mathrm{em}}}{r} \ , \tag{2.2}$$

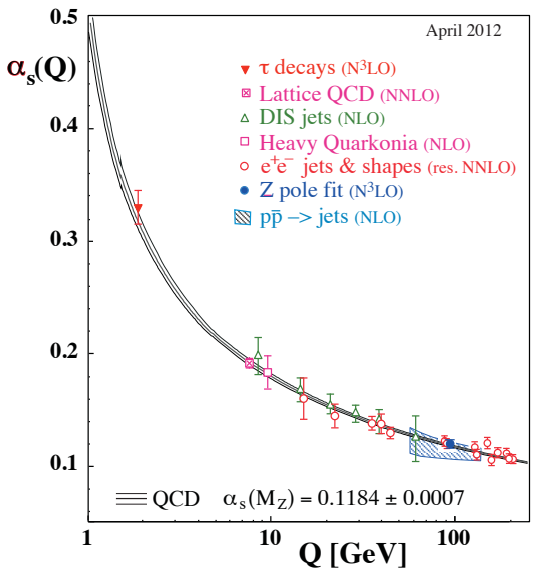

Figure 2.1: World data for α_{s} as a function of the momentum transfer Q [11].

except that the strong coupling constant α_{s} is $\mathcal{O}(10^2)$ times larger than α_{em}. The coupling constants α_{s} and α_{em} are not constants in a literal sense, but depend on the momentum transfer Q or the distance r, which are related by the de Broglie wavelength ($Q \propto 1/r$). This phenomenon is referred to as ***running coupling***. In QED, vacuum polarization leads to a slow increase of the coupling constant α_{em} with increasing momentum transfer Q (***shielding***). The fact that gluons carry two color charges involves gluon self-coupling and leads to the opposite behavior (***anti-shielding***), which implies a decrease of α_{s} with increasing momentum transfer Q. Figure 2.1 shows the latest world data for α_{s} as a function of Q. The decrease of the strong coupling constant α_{s} with increasing momentum transfer Q implies ***asymptotic freedom*** of quarks and

gluons at large Q or at small distance r. Asymptotic freedom was first formulated by J. D. Gross and F. Wilczek [12] and at the same time by H.D. Politzer [13]. They jointly received the Nobel Prize in Physics in 2004 for the discovery of asymptotic freedom in the strong interaction.
For the purpose of theoretical calculations, the feature of running coupling splits QCD into two regimes: a strongly-coupled regime at scales of the hadron masses m_{H} and a weakly-coupled sector at interactions with large momentum transfer ($Q \gg m_{\mathrm{H}}$). The latter can be treated within perturbative QCD, while the first one requires a non-perturbative treatment. A well-established approach for the non-perturbative regime is given by ***lattice QCD*** [14–17].

2.2 The phase diagram of Quantum Chromodynamics

Already in 1965, R. Hagedorn [18] argued that a universal maximum temperature for hadronic matter exists. He proposed that the number of hadronic resonances N_{H} increases exponentially with the mass m of the resonances,

$$\frac{\mathrm{d}N_{\mathrm{H}}}{\mathrm{d}m} \propto \exp\left(m/T_{\mathrm{H}}\right) , \tag{2.3}$$

where the scale of the exponential increase is given by the ***Hagedorn temperature*** T_{H}. Recent fits to data give $T_{\mathrm{H}} \approx 174\,\mathrm{MeV}/k_{\mathrm{B}}$ [19]. Ten years later, the existence of a new state of strongly interacting matter at high temperature and density was proposed by J.C. Collins and M.J. Perry [20], and by N. Cabibbo and G. Parisi [21]. In 1978, the name ***quark-gluon plasma*** was coined by E. Shuryak [22].
Figure 2.2 (left) shows the modern picture of the QCD phase diagram. The net baryon density is closely related to the baryochemical potential μ_{b}, which is the amount of energy needed to add an additional baryon to the system. The phase diagram contains three different forms of nuclear matter,

1. 'ordinary' hadronic matter at low T and low μ_{b},
2. quark-gluon plasma at high T,
3. color superconductor at low T and high μ_{b}.

The third condition might be found in neutron stars [23, 24], while the second presumably existed in the early Universe, a few microseconds after the Big Bang. Similar conditions can also be created in ultra-relativistic nucleus-nucleus collisions at hadron colliders such as the LHC. Thus, the main challenge in heavy-ion physics is to determine the properties of the different phases and the transitions that separate those states of matter. It is indicated in fig. 2.2 (left) that different experiments may explore different points at the phase boundary. The net baryon density decreases with increasing collision energies, which is linked to the phenomena of nuclear stopping and transparency [25]. At LHC and RHIC energies, the net baryon density is rather small and the quark-gluon plasma and hadronic phase are believed to be separated by a crossover transition. It is a subject of intense discussions, whether the phase transition turns into a first order chiral transition above some critical point [15, 17]. During the RHIC beam energy scan, the collision energy was lowered in multiple steps down to 7.7 GeV in order to learn more about the onset of deconfinement [26]. The future FAIR accelerator will be operated at similar center-of-mass energies and aims at studying the possible chiral transition and searching

for the critical point [27].

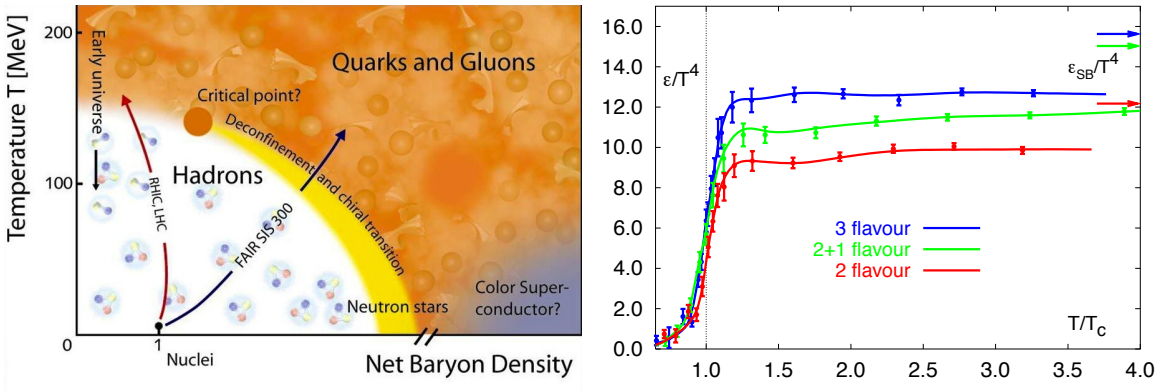

Figure 2.2: (left) Modern phase diagram of QCD (Figure by CBM collaboration). (right) Lattice QCD calculation for the scaled energy density ϵ/T^4 [16].

Figure 2.2 (right) shows a lattice QCD calculation at zero baryochemical potential for the scaled energy density ϵ/T^4. For a relativistic Bose or Fermi gas, the energy density in thermal equilibrium scales with the fourth power of temperature $\epsilon = gT^4$, where g is related to the number of degrees of freedom, for instance the spin degeneracy and the number of color states. The normalized energy density ϵ/T^4 is thus proportional to the number of degrees of freedom. The calculation was done for different quark flavor compositions (two or three quark flavors of equal mass ('2','3') or two light quarks plus one 'heavy' strange quark ('2+1') [28]) and reveals a sharp transition at the ***critical temperature*** T_c. The steep increase at $T = T_c$ can then be interpreted as the opening from hadron to quark and gluon degrees of freedom [29, 30]. The increase is more pronounced as the number of degrees of freedom in the calculation is increased from two to three quark flavors. Estimates for the critical temperature T_c at zero baryochemical potential range from 150 - 170 MeV/k_B [16, 31–33], which interestingly is close to the Hagedorn temperature T_H.

It should be noted that at temperatures close to T_c, the quark-gluon plasma is not at all in the asymptotically free regime of QCD. Estimates for the initial temperature created in heavy-ion collisions in Pb-Pb collisions at $\sqrt{s_{NN}} = 2.76$ TeV range from 500 - 600 MeV/k_B [34,35], such that the strong coupling constant is still $\alpha_s \approx 0.2$ - 0.3 [30]. Thus, a quark-gluon plasma close to the phase boundary must be considered as a strongly-coupled medium, which is often denoted by the abbreviation sQGP. This has two implications: first, the sQGP cannot be considered as an ideal gas with no interaction of particles, but rather as a nearly perfect liquid [36]. Second, its properties can only be studied in non-perturbative approaches such as lattice QCD.

3. Time evolution of ultra-relativistic nucleus-nucleus collisions

The goal of ultra-relativistic heavy-ion physics is to study the condensed matter aspects of Quantum Chromodynamics, in particular to create and to study a quark-gluon plasma under laboratory conditions. The existence of the quark-gluon plasma as a deconfined phase of hadronic matter has been predicted as an emerging property of Quantum Chromodynamics.
After a first characterization of heavy-ion collisions, section 3.1 describes the initial geometry and energy density and their relation with the experimentally observed charged particle multiplicity. In this context, the basic concepts of the Glauber model are introduced. In section 3.2, it is sketched how the radial expansion of the fireball can be described in hydrodynamics. In particular, it is shown that pressure gradients translate inhomogeneities in the initial energy density distribution into azimuthal anisotropies in the final state particle spectra. In section 3.3, recent experimental data for the hadron spectra and yields are compared to thermal and hydrodynamic models. Thereafter, the properties of the anisotropic flow of hadrons are discussed in detail in section 3.4.

3.1 Characterization of heavy-ion collisions

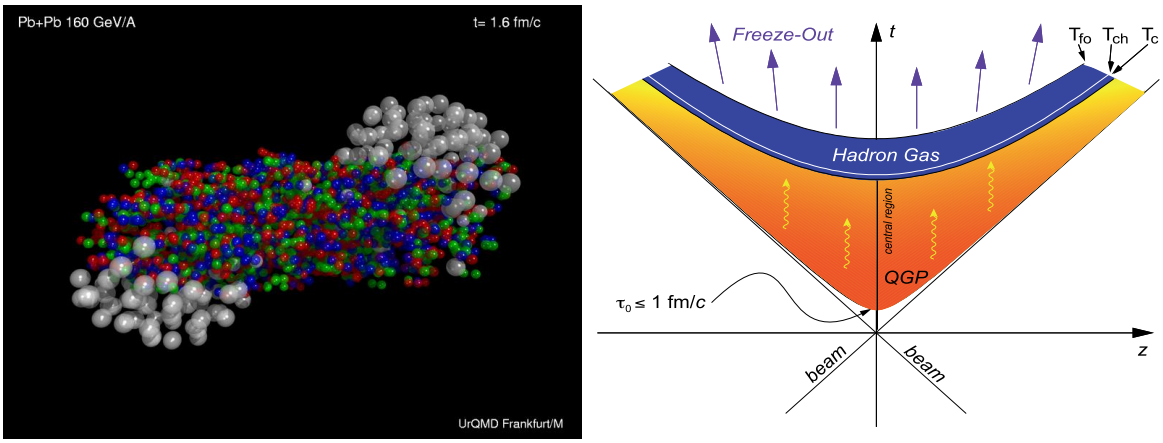

Figure 3.1: (left) Snapshot of a Pb-Pb collision in the UrQMD model. Figure taken from [37]. (right) Light cone of an ultra-relativistic nucleus-nucleus collision. For simplicity, only the longitudinal dimension is shown. Figure taken from [38].

Figure 3.1 (left) shows a snapshot of a collision of two lead nuclei in the UrQMD model [39, 40] 1.6 fm/c after the collision. Hadrons are shown in white and quarks in green, red and blue, corresponding to their color charge.
The two nuclei are collided at velocities close to the speed of light. Due to Lorentz contraction, the two nuclei appear as flat discs in the centre-of-mass system and pass through each other in a collision time of $t_{\mathrm{coll}} = \frac{2R}{\gamma} < 5 \cdot 10^{-3}\,\mathrm{fm}/c$, with $\gamma \approx 3000$ at $\sqrt{s_{\mathrm{NN}}} = 2.76\,\mathrm{TeV}$ and

$R_{\mathrm{Pb}} \approx 7.5\,\mathrm{fm}$[1] [42]. Quarks and gluons are liberated on a time scale of $0.1\,\mathrm{fm}/c$ and start to equilibrate. After a thermalization time of about $\tau_0 = 1\,\mathrm{fm}/c$ [30,43,44], quarks and gluons form a strongly correlated quark-gluon plasma. Over the whole time evolution, pressure gradients push the medium towards regions of lower energy density such that the medium expands and cools down. The quark-gluon plasma lasts only for a few fm/c and freezes out in a crossover transition to a hadron gas.
Figure 3.1 (right) shows the light cone of such a collision, which gives a more schematic representation of the evolution. It illustrates the transition from the quark-gluon plasma to a hadron gas as the temperature drops below the critical temperature T_{c}. The hadrons still undergo inelastic collisions until the system reaches the ***chemical freeze-out*** at $T_{\mathrm{ch}} \leq T_{\mathrm{c}}$, where the hadron composition of the medium is 'frozen'. After the chemical freeze-out elastic collisions between the recombined hadrons are maintained. As the density drops and interactions cease, the mean free path of the hadrons becomes larger than the system size and the system reaches the ***kinetic freeze-out*** at $T = T_{\mathrm{fo}}$. The lifetime of the system and the freeze-out temperature depend on the system size and collision energy [45–49]. At LHC energies, the lifetime is about $10\,\mathrm{fm}/c$ [50] with $T_{\mathrm{fo}} \approx 100\,\mathrm{MeV}/k_{\mathrm{B}}$ [51].

3.1.1 Initial geometry

Figure 3.2 sketches the initial geometry of a heavy-ion collision along the beam axis and in the azimuthal plane. The ***centrality*** of a collision is characterized by the ***impact parameter*** b, which is defined by the distance between the centers of the two nuclei. The directions of the impact parameter $\vec{b}$ and of the beam axis define the ***reaction plane***, while its azimuthal orientation in the laboratory system Ψ_{RP} is given by the impact parameter direction $\vec{b}$. The impact parameter b also determines the size of the nuclear overlap, where the nucleons undergo interactions, and particle production takes place. Those nucleons are called ***participants***, while the nucleons, which continue unaffected, are called ***spectators***.

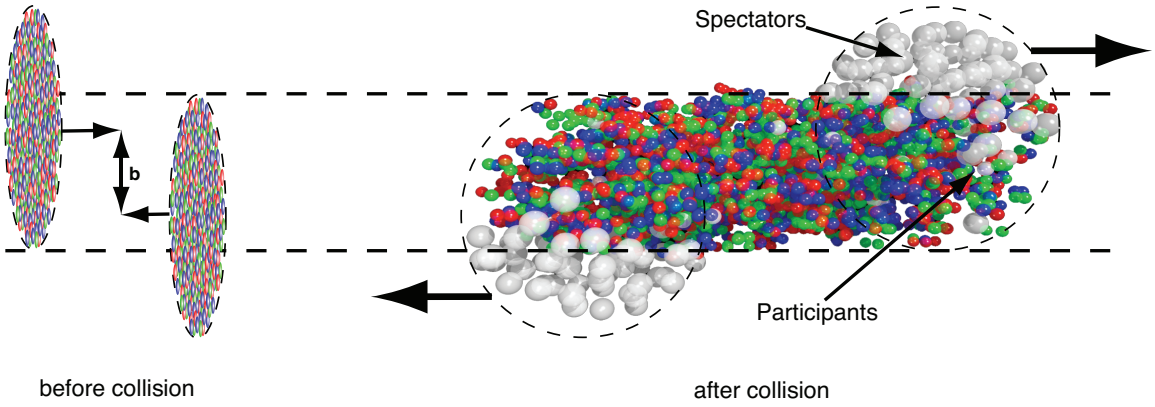

Figure 3.2: (left) The two heavy ions before collision with impact parameter b. (right) The spectators pass by unaffected, while in the participant zone particle production takes place. Both figures taken from [52].

[1] The charge radius of a lead nucleus is about 7.5 fm ($R = r_0 A^{\frac{1}{3}}, r_0 = 1.25\,\mathrm{fm}, A_{Pb} = 208$) [41].

As nuclei are made up of nucleons – that are, protons and neutrons – it is a natural approach to compare heavy-ion collisions with pp collisions. In a simplified picture, collisions of composed nuclei can be understood as a trivial superposition of individual collisions of nucleons. In this picture nucleus-nucleus collisions can be characterized by the number of participating nucleons N_{part} and the number of binary nucleon-nucleon collisions N_{coll}. Experimentally those quantities are intractable due to the femtoscopic length scales of the collision, precluding any direct observation. Theoretical techniques that estimate these quantities are generally referred to as ***Glauber models***, after Roy Glauber [53]. These quantities are an important baseline for comparisons of the particle production in elementary hadron-hadron, hadron-nucleus and nucleus-nucleus collisions. More complex models, such as saturation models, also take modifications of the initial state into account.

3.1.1.1 The Monte Carlo Glauber model

The Monte Carlo Glauber model is a static geometric model, which is motivated by the fact that the collision time t_{coll} is about a factor of 1000 smaller than the transverse size of the nucleus. Figure 3.3 shows the schematic view of a Pb-Pb collision as obtained from a Glauber model. Nucleons appear as black discs with a geometrical radius

$$r = \frac{1}{2}\sqrt{\frac{\sigma_{\mathrm{pp,inel}}}{\pi}} \tag{3.1}$$

with the inelastic pp cross section $\sigma_{\mathrm{pp,inel}}$. The nucleons are distributed according to a Woods-Saxon distribution as a parameterization of the nuclear thickness function. The collision is modeled overlaying the nucleon distributions of both nuclei with a given impact parameter b. If the distance of two nucleons from different nuclei is smaller than $2r$, their geometrical overlap is considered as a binary collision. The participant nucleons are marked with filled circles, with open circles representing the spectator nucleons. The x' and y' coordinates are the symmetry axes of the participant distribution referred to as ***participant plane***. Due to fluctuations in the nucleon distribution, the orientation of the participant plane Ψ_{PP} is usually different from the reaction plane angle Ψ_{RP}, which is defined by the impact parameter orientation.

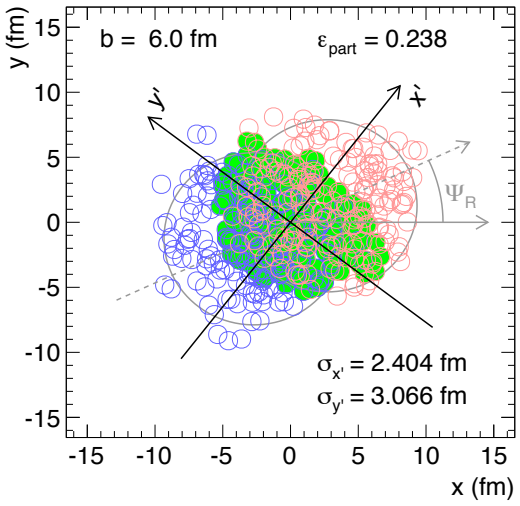

Figure 3.3: A schematic view of a Pb-Pb collision with an impact parameter $b = 6$ fm as obtained from the Glauber model [54].

3.1.1.2 Saturation models

At very high momentum transfers Q^2 and low Bjorken-x, the particle production in QCD is gluon-dominated and the parton density function for gluons increases like a power-law. Saturation models assume that the gluon density saturates at a certain saturation scale Q_{s}, which is manifested in the geometrical scaling in DIS data [55]. Above the saturation scale, non-linear coherence phenomena take over. Saturation models assume – unlike Glauber models – that the

parton density functions inside nuclei are not just an incoherent superposition of free protons and neutrons. Within the ***Color Glass Condensate*** formalism, the nuclear wave-functions are treated as classical correlated multi-parton states [56, 57]. More complex saturation models also take an impact parameter dependence into account ('IPSat') [58].

3.1.2 Initial energy density

Estimates for the critical energy density ϵ_c can be obtained from lattice QCD [30, 59]:

$$\epsilon_c \approx 0.6 \pm 0.3\,\mathrm{GeV/fm^3} \tag{3.2}$$

Interestingly, the critical energy density is only about a factor of four larger than the energy density inside ordinary nuclear matter. The energy density inside a nucleus consisting of A nucleons can be estimated by

$$\epsilon_0 \approx \frac{M_A}{\frac{4}{3}\pi R_A^3} \approx \frac{m_p}{\frac{4}{3}\pi r_p^3} \approx 0.14\,\mathrm{GeV/fm^3}\ , \tag{3.3}$$

with $R_A \approx A^{\frac{1}{3}} r_p$, $M_A \approx A m_p$, $m_p \approx 1\,\mathrm{GeV}$ and $r_p \approx 1.21\,\mathrm{fm}$ [41].

3.1.2.1 The Bjorken estimate

Experimentally, the initial energy density ϵ_0 can be estimated within the Bjorken model [60] from the transverse energy rapidity density $\mathrm{d}E_T/\mathrm{d}y$:

$$\epsilon_0 = \frac{1}{A_T \tau_0} \frac{\mathrm{d}E_T}{\mathrm{d}y} \tag{3.4}$$

with the nuclear overlap area A_T and the formation time τ_0 as a measure of the longitudinal dimension of the cylinder. While A_T is constrained by the transverse size $R = r_p A^{\frac{1}{3}}$ and can be estimated from a Glauber calculation, the thermalization time τ_0 is strongly model dependent: While at SPS it was assumed that $\tau_0 \approx 1\,\mathrm{fm}/c$ different models indicate that the thermalization time is much shorter at RHIC and LHC energies [61].
Measurements in 0 - 5% central Pb-Pb collisions at the LHC yield a value of $\epsilon_0 \tau_0 \approx 16\,\mathrm{GeV/(fm^2}\,c)$ [62] for the initial energy density. Even with moderate estimates for the thermalization time $\tau_0 = 1\,\mathrm{fm}/c$, the initial energy density is one order of magnitude above the critical energy density ϵ_c. Assuming almost equal thermalization times at RHIC and the LHC, the energy density at the LHC is about a factor of three larger than the energy density at RHIC [63].

3.1.2.2 Shape of the energy density profile

A measure of the deformation with respect to azimuthally symmetric conditions in the transverse plane is given by the ***eccentricity*** ϵ. It must be distinguished between two sources of eccentricity, the asymmetry of the nuclear overlap and the one arising from fluctuations.
Elliptic eccentricity mainly arises due to the asymmetry of the nuclear overlap in the transverse plane in non-central collisions. Two definitions for the elliptic eccentricity can be found

in literature [53, 64–67], the reaction plane eccentricity,

$$\epsilon_2^{\text{std}} = \frac{\sigma_x^2 - \sigma_y^2}{\sigma_x^2 + \sigma_y^2} \,, \tag{3.5}$$

and the participant eccentricity,

$$\epsilon_2^{\text{part}} = \frac{(\sigma_x^2 - \sigma_y^2)^2 + 4\sigma_{xy}^2}{\sigma_x^2 + \sigma_y^2} \,, \tag{3.6}$$

where σ_x^2 and σ_y^2 are the variances, and σ_{xy} is the covariance of the participant weighted nucleon distribution in the transverse plane. The x is axis defined along to the reaction plane direction Ψ_{RP}. Consequently, ϵ_2^{std} is the eccentricity in the reaction-plane frame and ϵ_2^{part} in the participant-plane frame.
More generally, the deformation can be expressed as a Fourier series in polar coordinates with coefficients ϵ_n [57, 68, 69]:

$$\epsilon_n^{\text{part}} = \frac{\sqrt{\langle r^n \sin(n\phi)\rangle^2 + \langle r^n \cos(n\phi)\rangle^2}}{\langle r^n \rangle} \tag{3.7}$$

For the second harmonic, eq. (3.7) is identical with eq. (3.6), which can be shown by using that $\sigma_x^2 - \sigma_y^2 = \langle r^2 \cos(2\phi)\rangle$, $\sigma_x^2 + \sigma_y^2 = \langle r^2 \rangle$ and $4\sigma_{xy}^2 = \langle r^2 \sin(2\phi)\rangle$. Higher-order eccentricity and also elliptic eccentricity in the most central collisions is dominantly driven by fluctuations in the initial energy density distribution. Long range correlations such as anisotropic flow can only be produced at early times. Therefore, estimates for the initial energy density distribution are the starting point of any hydrodynamic calculation. Figure 3.4 shows the initial energy density profile as determined from a Glauber model and an IP glasma model. Various prescriptions for the relation between the initial energy density and the density of participants and binary collisions can be found in the literature [70–73]. It can be seen in fig. 3.4 that fluctuations are much more pronounced in the IP glasma model. It is shown in [58] that saturation models generally tend to give larger eccentricities than Glauber models.

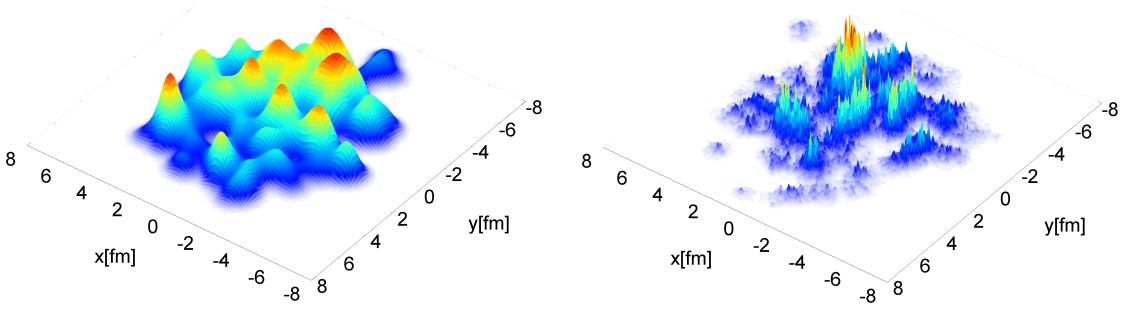

Figure 3.4: Initial energy density profile from a Glauber model (left) and an IP glasma model (right) [58].

3.1.3 Charged particle multiplicity

The most fundamental experimental observable in heavy-ion experiments is the multiplicity of final state charged particles. It is essential for the study of heavy-ion collisions to relate final state observables with quantities that characterize the initial conditions such as the collision centrality. With regard to the multiplicity production, it is often distinguished between 'soft' and 'hard' production processes:

Soft production means the fragmentation of color flux tubes that hold the constituents of the nucleons together. One can also interpret this as the excitation and decay of wounded nucleons. Consequently, the contribution of soft processes is expected to scale with the number of wounded nucleon participants N_{part}.

Hard production, on the other hand, means the fragmentation of color strings produced in hard parton-parton interactions. Those processes are expected to scale with the number of binary collisions N_{coll}.

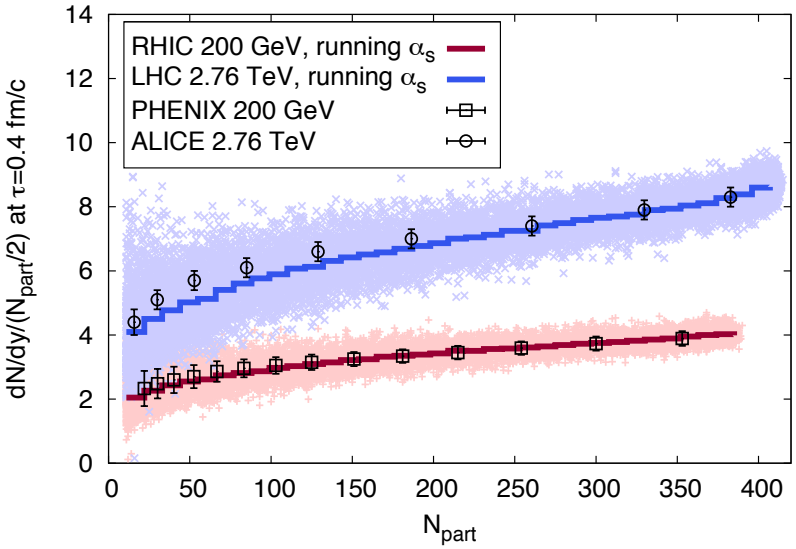

Figure 3.5: Charged particle multiplicity density at mid rapidity normalized by N_{part} [63, 74] compared to gluon multiplicity from an IP saturation model [75].

It was first found in hadron-nucleus collisions with 50 - 200 MeV/c pion, kaon and proton beams [76] at Fermilab that the charged particle multiplicity density $\mathrm{d}N_{\mathrm{ch}}/\mathrm{d}\eta$ is proportional to the number of participants N_{part}. It was concluded that the multiplicity production is dominated by soft processes. Figure 3.5 shows the N_{part}-scaled charged particle multiplicity density as a function of N_{part} measured at mid rapidity in Pb-Pb collisions at $\sqrt{s_{\mathrm{NN}}} = 2.76\,\mathrm{TeV}$ [74] and Au-Au collisions at $\sqrt{s_{\mathrm{NN}}} = 200\,\mathrm{GeV}$ [63]. The data points from LHC and RHIC have the same shape, but the N_{part} scaled multiplicity density increases by a factor of two from RHIC to the LHC. The increase in charged particle multiplicity density per participant indicates a clear deviation from N_{part} scaling. Consequently, one has introduced the concept of ***ancestors*** as the number of independently emitting sources of particles. It is shown in [77] that a two component model $N_{\mathrm{ancestors}} = fN_{\mathrm{part}} + (1-f)N_{\mathrm{coll}}$ with $f \approx 0.8$ describes the data points, which indicates a significant contribution of hard processes to the multiplicity production. It is shown in [78] that

this discrepancy is partially overcome by the use of constituent quark participants instead of nucleon participants. In the IP saturation model, the multiplicity production is related with the gluon multiplicity [75]. Figure 3.5 also shows the mean gluon multiplicity $\mathrm{d}N_\mathrm{g}/\mathrm{d}y$ normalized by $N_\mathrm{part}/2$ in comparison to the data. The pale bands denote results from individual events and illustrate the range of fluctuations. Except for some discrepancy to the LHC data for small N_part, the IP saturation model gives a reasonable description of the multiplicity production.

The IP saturation model is an extremely sophisticated model compared to the Glauber model, which can give a reasonable description of the multiplicity production using the concept of ancestors. Due to its simplicity, the Glauber model is commonly used by experimentalist to relate the multiplicity to the collision centrality and thus the impact parameter. Figure 3.6 illustrates the relation between the experimentally observed final-state multiplicity N_ch, the average impact parameter $\langle b \rangle$ and the average number of participants $\langle N_\mathrm{part} \rangle$ determined from a Glauber calculation. The distribution of $N_\mathrm{ancestors}$ describes the experimentally observed multiplicity distribution and thus quantiles of the measured multiplicity distribution called ***centrality classes*** can be related to quantiles of the impact parameter distribution [77]. Consequently, the collision centrality can be experimentally accessed via the measured multiplicity and can be related to an average impact parameter $\langle b \rangle$, number of participants $\langle N_\mathrm{part} \rangle$ and number of binary collisions $\langle N_\mathrm{coll} \rangle$.

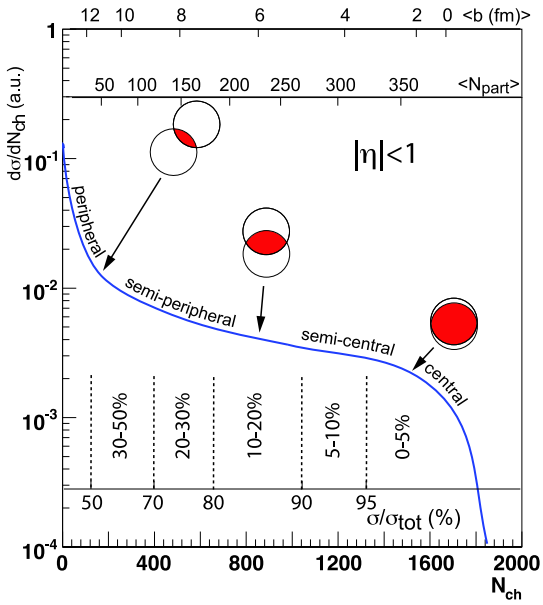

Figure 3.6: Illustration of the correlation between experimental charged particle multiplicity N_ch and Glauber calculated quantities $\langle b \rangle$ and $\langle N_\mathrm{part} \rangle$ [53].

3.1.4 Hanbury Brown-Twiss interferometry

The dimensions of the fireball can be determined from Bose-Einstein correlations (BEC) between identical bosons, which are related to the coherent superposition of wave amplitudes. Hanbury Brown-Twiss interferometry (HBT) was developed in the 1950's as a method to determine the dimensions of distant astronomical objects from interference effects [79,80] and was first applied to Bose-Einstein correlations by Goldhaber et. al [81]. Nowadays, HBT is a standard tool to determine the dimensions of the fireball created in nucleus-nucleus collisions [50]. A detailed theoretical review can be found in [82]. The correlation function is given by

$$C_2(p_1, p_2) = \frac{P(p_1, p_2)}{P(p_1)P(p_2)} \tag{3.8}$$

Classically, one would expect $C_2 = 1$, since the rate of pair coincidences is just given by the product of the two individual probabilities $P(\vec{p}_1, \vec{p}_2) = P(\vec{p}_1)P(\vec{p}_2)$. Without going into the details of the quantum mechanical calculation, the probability to find two particles in the same phase

space volume ($\vec{p}_1 - \vec{p}_2 \approx 0$) is enhanced for bosons and reduced for fermions due to positive and negative interference of the wave functions, respectively. The 'closeness in phase space' is expressed in terms of the relative three momentum $\vec{q} = \vec{p}_2 - \vec{p}_1$. In the ***Bertsch-Pratt notation***, the relative momentum $\vec{q} = (q_{\text{out}}, q_{\text{side}}, q_{\text{long}})$ is decomposed into its components in the longitudinal comoving system (LCMS), which correspond to the axes parallel ('out') and perpendicular ('side') to the pair momentum and along the beam axis ('long'). The correlation function $C_2(\vec{q})$ is then related to the size of the source $\vec{R} = (R_{\text{out}}, R_{\text{side}}, R_{\text{long}})$ via the correlation strength λ as:

$$C_2(\vec{q}) = 1 + \lambda \exp\left(-\left(q_{\text{out}}^2 R_{\text{out}}^2 + q_{\text{side}}^2 R_{\text{side}}^2 + q_{\text{long}}^2 R_{\text{long}}^2\right)\right) \quad [83\text{–}86] \tag{3.9}$$

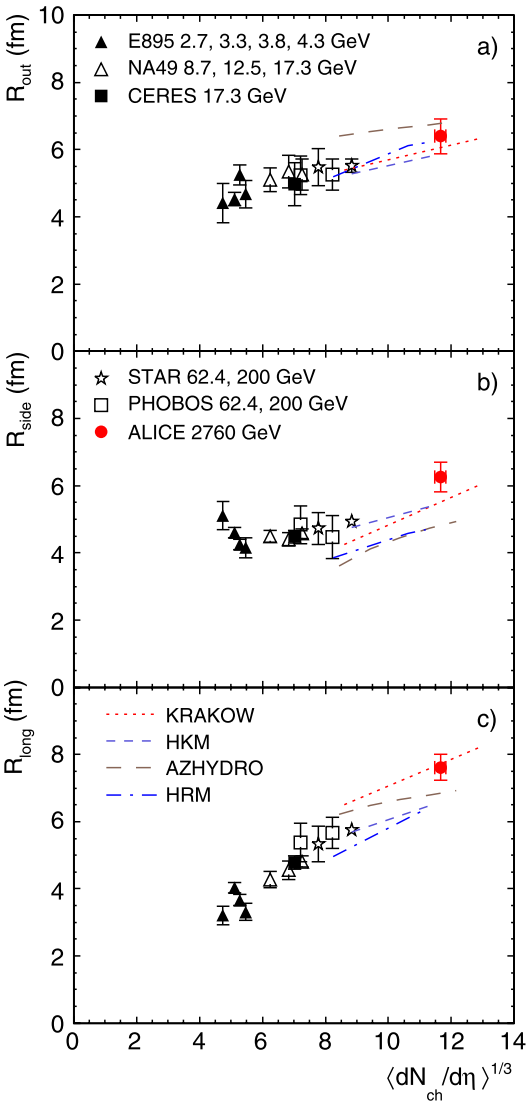

Figure 3.7: Pion HBT radii measured in 0 - 5% central Pb-Pb collisions compared to earlier measurements for other systems [50].

More complex versions of the correlation function also include cross terms between q_{long} and q_{out} and terms for the Coulomb interaction between charged bosons [50]. The correlation function peaks at vanishing momentum difference at a value of $C_2(\vec{q}) = 2$ for for spin-less and $C_2(\vec{q}) = 3/2$ for spin one bosons. BEC correlations at the femtoscopic scale are expected to appear at relative momentum of about $q \ll \hbar/\text{fm} \approx 200\,\text{MeV}/c$. The uncorrelated denominator of the correlation function can be estimated from the mixing of uncorrelated events.

Figure 3.7 shows the HBT radii in the 0 - 5% most central collisions as a function of the cube-root of the charged multiplicity $(\mathrm{d}N_{\text{ch}}/\mathrm{d}\eta)^{1/3}$ as determined in different collisions systems. The charged multiplicity density $\mathrm{d}N_{\text{ch}}/\mathrm{d}\eta$ is a measure of the number of nucleon participants and thus the transverse size and energy density of the system at the collision time. R_{side} and R_{out} are comparable in size due to the almost symmetric reaction plane in central collisions. It should be noted that the HBT radii are not directly related to the spatial dimensions of the system, but rather describe the homogeneity length, i.e. the size of the region that contributes to the pion spectrum. The magnitude of the longitudinal component R_{long} is proportional to the kinetic freeze-out time τ_{fo}, which is essentially the lifetime of the fireball. It can be seen that R_{long} and thus the lifetime increases with the cube-root [87] of the charged particle multiplicity density $\mathrm{d}N_{\text{ch}}/\mathrm{d}\eta$. At the LHC, τ_{fo} is about 10 - 11 fm/c with a kinetic freeze-out temperature of $T_{\text{fo}} = 100\,\text{MeV}/k_{\text{B}}$ [51]. The increase in the lifetime and the transverse size directly implies an increase of the fireball volume [50].

3.2 Hydrodynamic evolution

3.2.1 Applicability of hydrodynamics

The use of hydrodynamic concepts such as temperature, pressure and fluid velocity cannot be strictly justified for matter formed in a heavy-ion collision. Although the number of particles is sufficiently large to be considered as a macroscopic system, standard thermodynamics is about systems in global thermodynamic equilibrium, which implies that all intensive parameters are constant throughout the whole volume and the system is at rest. Even though none of these conditions is essentially strictly fulfilled, one can still argue for partial equilibration in small fluid cells and collective behavior, if the mean free path is smaller than the characteristic dimensions of the system. The Knudsen number $Kn = \lambda/R$ is defined as the ratio of the mean free path λ and the characteristic size of the system R. Fluid dynamics only applies, if $Kn \ll 1$ implying that frequent collisions occur and momentum is transferred from denser regions toward less dense regions. At initial particle densities of the order of $5\text{ - }10\,\mathrm{fm}^{-3}$ and even with modest estimates of cross sections of the order of 1 - 2 mb, we obtain values for the mean free path smaller than 1 fm and thus much below the nuclear size $2R_A \geq 10\,\mathrm{fm}$, which gives $Kn \approx 0.1$ and justifies the application of hydrodynamics [88, 89].

3.2.2 Radial expansion

A detailed description of the hydrodynamic picture can be found in [88]. In the following, it shall be briefly sketched how the main properties of the hydrodynamic expansion can derived from the basic conservation laws of thermodynamics. The conservation equations of energy and momentum ($\partial_\mu T^{\mu\nu} = 0$) are given by:

$$\frac{\partial \epsilon}{\partial t} + \vec{\nabla} \cdot ((\epsilon + P)\vec{v}) = 0 \qquad \frac{\partial}{\partial t}((\epsilon + P)\vec{v}) + \vec{\nabla} P = \vec{0} \tag{3.10}$$

In order to study the propagation of small disturbances in the fluid, the energy density ϵ and pressure P are expressed as

$$\epsilon(t,x,y,z) = \epsilon_0 + \delta\epsilon(t,x,y,z) \qquad P(t,x,y,z) = \epsilon_0 + \delta P(t,x,y,z)\ , \tag{3.11}$$

where ϵ_0 and P_0 correspond to the uniform fluid and $\delta\epsilon$ and δP to the disturbance. Inserting eq. (3.11) into eq. (3.10) and linearizing gives:

$$\frac{\partial \delta\epsilon}{\partial t} + (\epsilon_0 + P_0)\vec{\nabla} \cdot \vec{v} = 0 \qquad (\epsilon_0 + P_0)\frac{\partial \vec{v}}{\partial t} + \vec{\nabla}\delta P = \vec{0} \tag{3.12}$$

The first equation describes energy conservation: It states that the energy density decreases, if the velocity field diverges ($\vec{\nabla} \cdot \vec{v} > 0$), i.e. the volume of the system increases. The second equation is Newton's second law: The inertia of the fluid multiplied by its acceleration equals the force. It follows that the force per unit volume is $-\vec{\nabla}\delta P$, i.e. the fluid is pushed towards regions of lower pressure. From that we can already see that a system with a given energy density that is surrounded by vacuum will increase in volume. The collective radial expansion of the medium is referred to as ***radial flow***. The radial component of eq. (3.12) is given by

$$\frac{\partial v_r}{\partial t} = -\frac{1}{\epsilon + P}\frac{\partial P}{\partial r}\ . \tag{3.13}$$

We consider the system evolution as an isentropic process and substitute $\mathrm{d}\epsilon/(\epsilon+P)=\mathrm{d}\ln s$. We define the velocity of sound $c_\mathrm{s}=\sqrt{\partial P/\partial\epsilon}$ and obtain

$$\frac{\partial v_r}{\partial t}=-c_\mathrm{s}^2\frac{\partial \ln s}{\partial r}\ . \tag{3.14}$$

For simplicity, we assume a Gaussian entropy density profile at the thermalization time $\tau=\tau_0$:

$$s(r)=s_0\exp\left(-\frac{r^2}{2\rho^2}\right) \tag{3.15}$$

ρ is the transverse size at the thermalization time. Integrating over t, we obtain for small times

$$\beta_r=\frac{v_r}{c}=\frac{c_\mathrm{s}^2 r}{\rho^2}t\ . \tag{3.16}$$

It can be seen that the radial flow velocity increases essentially linearly in time for small times after the thermalization time τ_0.

3.2.3 Freeze-out

Within the ***Cooper-Frye freeze-out picture*** [90], the momentum distribution of the outgoing free particles measured by the particle detectors is essentially the momentum distribution of particles within the fluid after the hydrodynamic expansion. The transition from the fluid to individual particles cannot be described by fluid dynamics, so it is assumed that the late stages of the expansion do not alter the essential features of the momentum distributions [88].
A detailed description of the thermal properties of the hadron spectra can be found in [91]. The invariant momentum spectrum of particles radiated by a thermal source with temperature T is given by

$$E\frac{\mathrm{d}^3N}{\mathrm{d}^3p}=\frac{\mathrm{d}N}{\mathrm{d}y m_\mathrm{T}\mathrm{d}m_\mathrm{T}\mathrm{d}\phi}=\frac{gV}{(2\pi)^3}E\exp\left(-\frac{E-\mu}{T}\right)\ , \tag{3.17}$$

where g is the spin/isospin degeneracy factor, μ the grand canonical potential

$$\mu=B\mu_\mathrm{B}+S\mu_\mathrm{S}+Q\mu_\mathrm{Q} \tag{3.18}$$

as originating from its baryon number B, strangeness number S and electric charge Q. The ***transverse mass*** was defined in eq. (1.6) and equals the energy of a particle in the transverse plane ($p_z=0$). For simplicity, quantum statistics is neglected and instead a Boltzmann distribution is used. Integrating over the surface of the source, we obtain the invariant momentum distribution

$$\frac{\mathrm{d}N}{m_\mathrm{T}\mathrm{d}m_\mathrm{T}}=\frac{gV}{(2\pi)^2}m_\mathrm{T}K_1\left(\frac{m_\mathrm{T}}{T}\right)\underset{m_\mathrm{T}\gg T}{\rightarrow}\sqrt{m_\mathrm{T}}\exp\left(-\frac{m_\mathrm{T}}{T}\right)\ , \tag{3.19}$$

with the modified Bessel function K_1 that behaves asymptotically like

$$K_\alpha(z)\approx\sqrt{\frac{\pi}{2z}}\exp(-z)\,(1+\mathcal{O}(\frac{\alpha^2}{z}))\qquad\text{for } z\gg 1\ \ [92]\ . \tag{3.20}$$

For a static thermodynamic source, the m_{T}-spectra for various particle types are expected to have an exponential spectrum with almost uniform common slope $1/T$. This behavior known as ***transverse mass scaling*** is broken, if the fluid moves. It can be shown that eq. (3.19) transforms under a Lorentz boost with ***transverse rapidity*** ρ to:

$$\frac{\mathrm{d}N}{m_{\mathrm{T}}\mathrm{d}m_{\mathrm{T}}} \propto \int_0^R r\mathrm{d}r m_{\mathrm{T}} K_1\left(\frac{m_{\mathrm{T}}\cosh(\rho)}{T}\right) I_0\left(\frac{p_{\mathrm{T}}\sinh(\rho)}{T}\right) \tag{3.21}$$

The transverse rapidity is given by $\rho = \tanh^{-1}(\beta_r(r))$, where the transverse velocity distribution inside the fireball β_r is parametrized by $\beta_{\mathrm{r}}(r) = \beta_{\mathrm{s}}\left(\frac{r}{R}\right)^n$ with the surface velocity β_{s}. It can be immediately seen that for a static source ($\rho = 0$), eq. (3.21) is identical[2] to the unboosted distribution eq. (3.19). In general it can be distinguished between ***comoving particles*** ($p_{\mathrm{T}} \approx m\beta\gamma$) and ***fast particles*** ($p_{\mathrm{T}} > m\beta\gamma$), implying different limits for the Bessel functions. For fast particles, we use that $I_0(z) \approx \exp(z)/\sqrt{2\pi z}$ [92] and eq. (3.21) becomes an exponential function:

$$\frac{\mathrm{d}N}{m_{\mathrm{T}}\mathrm{d}m_{\mathrm{T}}} \propto \int_0^R r\mathrm{d}r \sqrt{\frac{m_{\mathrm{T}}}{p_{\mathrm{T}}}} \exp\left(-\frac{m_{\mathrm{T}}\cosh(\rho) - p_{\mathrm{T}}\sinh(\rho)}{T}\right) \tag{3.22}$$

In the limit of negligible mass ($m_{\mathrm{T}} \approx p_{\mathrm{T}}$ for $p_{\mathrm{T}} \to \infty$) this relation simplifies to:

$$\lim_{m_{\mathrm{T}} \to p_{\mathrm{T}}} \frac{\mathrm{d}N}{m_{\mathrm{T}}\mathrm{d}m_{\mathrm{T}}} \propto \int_0^R r\mathrm{d}r \exp\left(-\frac{m_{\mathrm{T}}(\cosh(\rho) - \sinh(\rho))}{T}\right) \tag{3.23}$$

A better understanding of the slope can be achieved by taking the log of eq. (3.23) and differentiating with respect to m_{T}. As explicitly shown in [91], using that $\cosh(x) - \sinh(x) = \exp(x)$ and $\tanh^{-1}(x) = 1/2 \ln((1+x)/(1-x))$ we obtain:

$$\lim_{m_{\mathrm{T}} \to \infty} \frac{\mathrm{d}}{\mathrm{d}m_{\mathrm{T}}} \ln\left(\frac{\mathrm{d}N}{m_{\mathrm{T}}\mathrm{d}m_{\mathrm{T}}}\right) = -\frac{\cosh(\rho) - \sinh(\rho)}{T} = -\frac{1}{T}\sqrt{\frac{1-\beta_r}{1+\beta_r}} \tag{3.24}$$

Thus, the inverse slope parameter or ***apparent temperature*** T_{eff} can be understood as the blue-shifted original temperature of the source T:

$$T_{\mathrm{eff}} = T\sqrt{\frac{1+\beta_r}{1-\beta_r}} \tag{3.25}$$

At small values of m_{T} ($p_{\mathrm{T}} \approx m$), the situation is much less clear because at low m_{T} the Bessel functions tend to steepen the spectra, while large hadron masses tend to flatten the spectra [91].

3.2.4 Azimuthal anisotropy

In the following, it shall be demonstrated that deformations of the initial energy density distribution translate into azimuthally anisotropic pressure gradients. The deformation of the Gaussian entropy profile eq. (3.15) is described by the Fourier decomposition with the eccentricity

[2] $\beta_r(r) = 0 \to \rho = 0$ implies that $\sinh(0) = 0 \to I_0(0) = 1$ and $\cosh(0) = 1$.

coefficients ϵ_n defined in eq. (3.7):

$$s(r,\phi) = s_0 \exp\left(-\frac{r^2\left(1+\sum_n \epsilon_n \cos\left(n\left(\phi-\Psi_n\right)\right)\right)}{2\rho^2}\right) \quad [93] \tag{3.26}$$

The fluid velocity is then given by

$$\beta_r\left(\phi\right) = \frac{v_r}{c} = \beta_0\left(1+\sum_n \epsilon_n \cos\left(n\left(\phi-\Psi_n\right)\right)\right) \ , \tag{3.27}$$

with $\beta_0 = c_s^2 rt/\rho^2$. It can be explicitly seen that the pressure gradients transform the deformation of the initial entropy density distribution into larger radial flow velocities along Ψ_n, which is the reference angle of the n-th order eccentricity ϵ_n. The expansion of the medium results into a blue-shift of the particle spectra, which depends on the azimuthal emission angle. In other words, the pressure gradients turn the initial asymmetry in the coordinate space into an anisotropy in momentum space. The azimuthal distribution $\mathrm{d}N/\mathrm{d}\phi$ of particles produced in an individual heavy-ion collision can be expressed as a Fourier series,

$$\frac{\mathrm{d}N}{\mathrm{d}\phi} = \frac{N_0}{2\pi}\left(1+2\sum_{n\geq 1} v_n \cos\left(n\left(\phi-\Psi_n\right)\right)\right) \ , \tag{3.28}$$

where N_0 is the average particle yield, v_n is the magnitude and Ψ_n is the corresponding angle of the maximum n-th order anisotropy. The coefficient v_n is defined as

$$v_n = \frac{\int_0^{2\pi} \mathrm{d}\phi \frac{\mathrm{d}N}{\mathrm{d}\phi} \cos\left(n\left(\phi-\Psi_n\right)\right)}{\int_0^{2\pi} \mathrm{d}\phi \frac{\mathrm{d}N}{\mathrm{d}\phi}} \ . \tag{3.29}$$

In the following, it shall be explicitly shown how v_n is related with the eccentricity and the radial flow velocity. We introduce the fluid 4-velocity with $u = \sinh(\rho)$ and $u^0 = \cosh(\rho)$. For simplicity, the r dependence of the fluid velocity shall be neglected in the following. From the identity $\cosh^2(x) - \sinh^2(x) = 1$, it follows that $u^0 = \sqrt{1+u^2}$. First order Taylor expansions at $\beta = \beta_0$ yield

$$u = \sinh\left(\tanh^{-1}\left(\beta\right)\right) \approx \beta \tag{3.30}$$

and

$$u^0 = \sqrt{1+\beta^2}|_{\beta_0} \approx \sqrt{1+\beta_0^2} + \frac{\beta_0}{\sqrt{1+\beta_0^2}}(\beta-\beta_0) \ . \tag{3.31}$$

Using that $\gamma = 1/\sqrt{1+\beta_0^2}$ and considering only the n-th order eccentricity ϵ_n, we can write:

$$u\left(\phi\right) = \beta_0(1+2\epsilon_n \cos\left(n\left(\phi-\Psi_n\right)\right) \tag{3.32}$$

$$u^0(\phi) = \frac{1}{\gamma} + 2\gamma\beta_0^2\epsilon_n \cos\left(n\left(\phi-\Psi_n\right)\right) \tag{3.33}$$

We insert eq. (3.32) and eq. (3.33) in eq. (3.23) and obtain

$$\frac{\mathrm{d}N}{m_\mathrm{T}\mathrm{d}m_\mathrm{T}} \propto \sqrt{m_\mathrm{T}}p_\mathrm{T}\exp\left(-\frac{m_\mathrm{T}u^0(\phi)-p_\mathrm{T}u(\phi)}{T}\right) \tag{3.34}$$

$$= \sqrt{m_\mathrm{T}}p_\mathrm{T}\exp\left(-\frac{(m_\mathrm{T}\gamma-p_\mathrm{T}\beta_0)}{T}\right) \times \exp\left(-\frac{(m_\mathrm{T}\gamma\beta_0-p_\mathrm{T})}{T}2\beta_0\epsilon_n\cos\left(n\left(\phi-\Psi_n\right)\right)\right) . \tag{3.35}$$

Using a Taylor expansion of the exponential function ($\exp = 1 + x$) we obtain

$$\frac{\mathrm{d}N}{m_\mathrm{T}\mathrm{d}m_\mathrm{T}} \propto N_0\left(1+2\beta_0\epsilon_n\frac{(p_\mathrm{T}-m_\mathrm{T}\gamma\beta_0)}{T}\cos\left(n\left(\phi-\Psi_n\right)\right)\right) . \tag{3.36}$$

Comparing eq. (3.36) with eq. (3.28), the n-th-order azimuthal anisotropy v_n is given by

$$v_n = \frac{\epsilon_n\beta_0}{T}(p_\mathrm{T}-\gamma\beta_0 m_\mathrm{T}) . \tag{3.37}$$

In ideal hydrodynamics, the azimuthal anisotropy increases essentially linearly with p_T. At a fixed p_T, the transverse mass m_T is larger for heavier particles, which implies that light particles have a larger azimuthal anisotropy than heavy particles. This feature known as ***mass ordering*** is a clear fingerprint of hydrodynamic behavior. Finally, it shall be noticed that eq. (3.37) is not valid for low energetic (comoving) particles. It is shown in [94, 95] that v_n vanishes at low transverse momentum as p_T^n, if the momentum distribution is regular at $p_\mathrm{T} = 0$.

3.3 Hadron spectra and yields

It shall be briefly discussed, how the measured hadron spectra and yields compare with the hydrodynamic description and which conclusions about the time evolution can be drawn.

3.3.1 Isotropic radial flow

Figure 3.8 shows the transverse momentum spectra for pions, kaons and protons in Pb-Pb collisions at $\sqrt{s_\mathrm{NN}} = 2.76\,\mathrm{TeV}$ and Au-Au collisions at $\sqrt{s_\mathrm{NN}} = 200\,\mathrm{GeV}$. It can be seen that the spectra at the LHC are flatter than those at RHIC, which indicates a stronger radial flow at the LHC. The radial flow velocity β and the corresponding temperature T can be extracted with a combined Blast-Wave fit based on eq. (3.21) of all spectra. The data in 0 - 5% central Pb-Pb collisions is well described by a Blast-Wave fit with an average radial flow velocity of $\langle\beta\rangle_\mathrm{bw} = 0.65 \pm 0.02$ and $T_\mathrm{bw} = 95 \pm 10\,\mathrm{MeV}/k_\mathrm{B}$ [51]. As compared with similar fits to 0 - 5% central Au-Au collisions at $\sqrt{s_\mathrm{NN}} =$

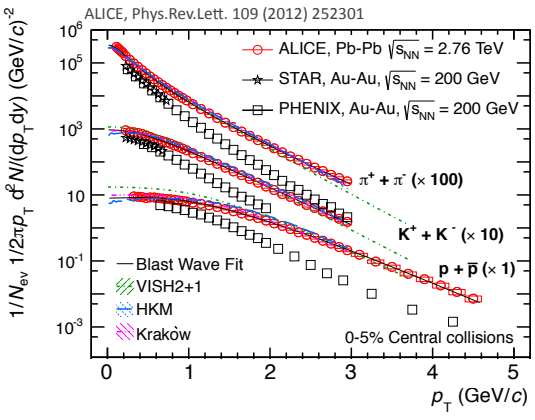

Figure 3.8: Identified hadron spectra in Pb-Pb collisions at $\sqrt{s_\mathrm{NN}} = 2.76\,\mathrm{TeV}$ with a Blast-Wave fit and compared to RHIC data [51].

200 GeV [96], β is about 10% higher at the LHC, while the extracted temperatures are comparable within errors.

3.3.2 Thermal model

It was already observed in e^+e^-collisions at the CERN LEP [97] that the hadron production rates seem to be proportional to $m^{3/2}\exp(-m/T)$, which follows just from the assumption that the phase space is filled thermally at the hadronization. Higher temperatures enhance the thermal production of heavy hadrons.
The thermal model is a quantum statistical description of the Cooper-Frye freeze-out picture. It describes the thermal composition of particle yields in heavy-ion collisions using the partition function of a grand canonical ensemble,

$$\ln Z_i(T,V,\mu) = \frac{V g_i}{2\pi^2}\int_0^\infty \pm p^2 \mathrm{d}p \ln\left(1 \pm \exp\left(-\frac{E_i-\mu_i}{T}\right)\right) \ , \tag{3.38}$$

with + for fermions and − for bosons. The partition function describes all thermodynamic properties of the fireball composed of hadrons. The average number of particles $\langle N_i\rangle = V n_i$ of a given species can be calculated from the number density n_i and the volume V. For the final particle composition, also contributions from decays of higher hadronic resonances have to be taken into account [30].

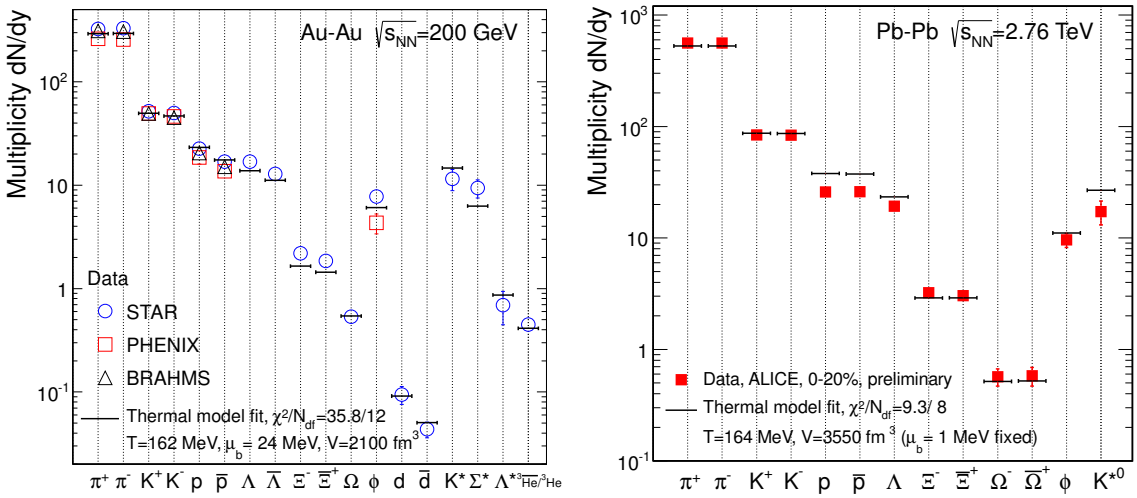

Figure 3.9: Thermal model fits to hadron production in (left) Au-Au collisions at $\sqrt{s_{\mathrm{NN}}} =$ 200 GeV at RHIC and (right) central Pb-Pb collisions at $\sqrt{s_{\mathrm{NN}}} = 2.76$ TeV at the LHC [98].

Figure 3.9 shows a compilation of RHIC and LHC data for hadron production in heavy-ion collisions. In the RHIC data, protons are slightly above antiprotons indicating that the net baryon density is still above zero. A non-zero net baryon density results from the fact that particles are collided with particles and not particles with its antiparticles. It can be seen that the particle multiplicities at the LHC are larger than those at RHIC, due to the increased collision energy. As a consequence, protons and antiprotons are at the same level, since the initial baryon composition of the colliding nuclei becomes negligible. The thermal fit to the LHC data yields a temperature of $T_{\mathrm{th}} = 164\,\mathrm{MeV}/k_{\mathrm{B}}$ being close to the critical temperature T_{c}.

It can be observed that the proton and anti-proton production is unexpectedly low at the LHC (about 50%) compared the thermal model fit. Protons and anti-protons have been excluded from the fit, since their inclusion would drive the temperature to rather low values. However, the apparent proton anomaly is puzzling and the physical origin needs to be clarified. The authors of [98] argue that the anomaly is already indicated by the RHIC data and might be due to proton-antiproton annihilation in the hadronic phase.

3.3.3 Transverse mass scaling

Transverse mass scaling states that hadron differential cross sections plotted as a function of the transverse mass m_{T} have all the same shape $f(m_{\mathrm{T}})$ with an absolute normalization factor C_{h} for each species:

$$E\frac{\mathrm{d}^3N}{\mathrm{d}p^3} = C_{\mathrm{h}} f(m_{\mathrm{T}}) \tag{3.39}$$

Hagedorn proposed the following empirical formula to describe hadron p_{T} differential invariant cross sections [99]:

$$E\frac{\mathrm{d}^3N}{\mathrm{d}p^3} = \frac{A}{(1+\frac{p_{\mathrm{T}}}{p_0})^n} \approx \begin{cases} A\exp\left(\frac{-np_{\mathrm{T}}}{p_0}\right) & \text{for } p_{\mathrm{T}} \to 0 \\ A\left(\frac{p_0}{p_{\mathrm{T}}}\right)^n & \text{for } p_{\mathrm{T}} \to \infty \end{cases} \tag{3.40}$$

It assumes exponential behavior at small transverse momentum p_{T} and becomes a power law at large transverse momentum. The power law behavior is inspired by the quark-interchange model, which states that the hadron invariant spectra should behave like $(m^2+p_{\mathrm{T}}^2)^{-4} = m_{\mathrm{T}}^{-8}$ [100]. Other parametrisations, in particular for the hadron spectra in nucleus-nucleus collisions, can been found in the literature [101].

Figure 3.10 shows a compilation of various meson production cross sections in pp and Au-Au collisions at $\sqrt{s_{\mathrm{NN}}} = 200\,\mathrm{GeV}$. The data are compared to a parameterization based on m_{T} scaling [102]. It can be seen that all measured spectra in pp collisions can be described by m_{T} scaling. In particular, η's and kaons follow the same m_{T} scaling prediction, since they have similar masses[3]. In Au-Au collisions, the spectra are flatter due to the presence of radial flow. While m_{T} scaling still describes the η spectrum, kaons are now clearly enhanced compared to the m_{T} scaling expectation, which is known as ***strangeness enhancement***.

Historically, m_{T} scaling was rather an empirical and phenomenological finding [103–106] and not related with any theory about the hadron production. As shown in section 3.2.3 (eq. (3.19)), the scaling in the transverse mass directly follows from the freeze-out of thermal distributions. However, it is not obvious why thermal models give a satisfactory description of particle spectra and abundances in pp and even e^+e^-collisions, where thermal equilibrium is not expected at all [88]. It is argued that the m_{T} scaling behavior could arise from the hadronization (i.e. fragmentation): Within the phenomenological Lund scheme [107, 108] the probability for string breaking during the fragmentation is given by $\exp(-\pi m_{\mathrm{T}}^2/\kappa)$, where κ is the string tension. The PYTHIA event generator is based on the Lund scheme and it can be seen in [109] that PYTHIA gives similar results compared to m_{T} scaling.

[3] $m_\eta = 547.85\,\mathrm{MeV}/c^2, m_{K^\pm} = 493.67\,\mathrm{MeV}/c^2$ [9]

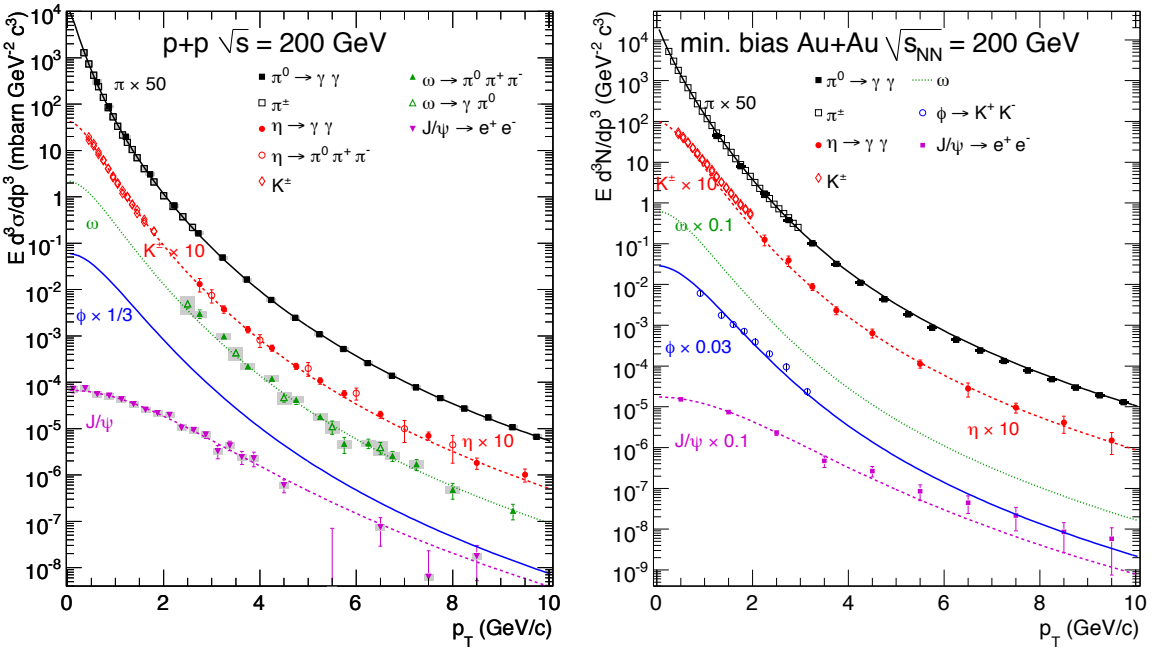

Figure 3.10: Compilation of meson production cross sections in (left) pp and (right) Au-Au collisions at $\sqrt{s_{\mathrm{NN}}} = 200\,\mathrm{GeV}$. The data are compared to a parameterization based on m_{T} scaling [102].

3.3.4 Implications for the chemical and kinetic freeze-out temperature

The temperature extracted from thermal model fit to the particle yields (cf. section 3.3.2) can be interpreted as the chemical freeze-out temperature T_{ch}. While the chemical freeze-out temperature explains both, the particle spectra and ratios, in pp collisions, the presence of hydrodynamic flow in heavy-ion collisions results in flatter spectra. As a consequence, the temperatures from the spectra using the Blast-Wave fit T_{bw} (cf. section 3.3.1) are smaller than the temperature from the particle ratios T_{th}. This finding can be interpreted by a lower temperature at the kinetic freeze-out $T_{\mathrm{fo}} \approx T_{\mathrm{bw}}$. The fact that $T_{\mathrm{ch}} > T_{\mathrm{fo}}$ is interpreted in the following way: inelastic collisions maintain the chemical equilibrium and stop after the temperature drops below the chemical freeze-out temperature, but there are still elastic collisions that maintain the kinetic equilibrium until the kinetic freeze-out. Thus, particles abundances are already frozen at the chemical freeze-out, while the kinematic properties and thus the shape of the spectra is determined at the kinetic freeze-out at a later stage of the time evolution.

3.3.5 Jet quenching

Jets are collimated sprays of particles originating from the fragmentation of hard scattered partons. The hard production of partons can be described by perturbative QCD, while the process of fragmentation is theoretically hard to access, since the coupling α_{s} becomes stronger during the fragmentation. The vacuum fragmentation of partons into hadrons can be experimentally accessed and is parametrized in fragmentation functions. In the absence of any initial and final state modification, such as the modification of the nuclear structure function and jet-medium interaction, respectively, one would just expect that the high-p_{T} particle production in nucleus-nucleus collisions scales with the number of binary collisions N_{coll} compared to

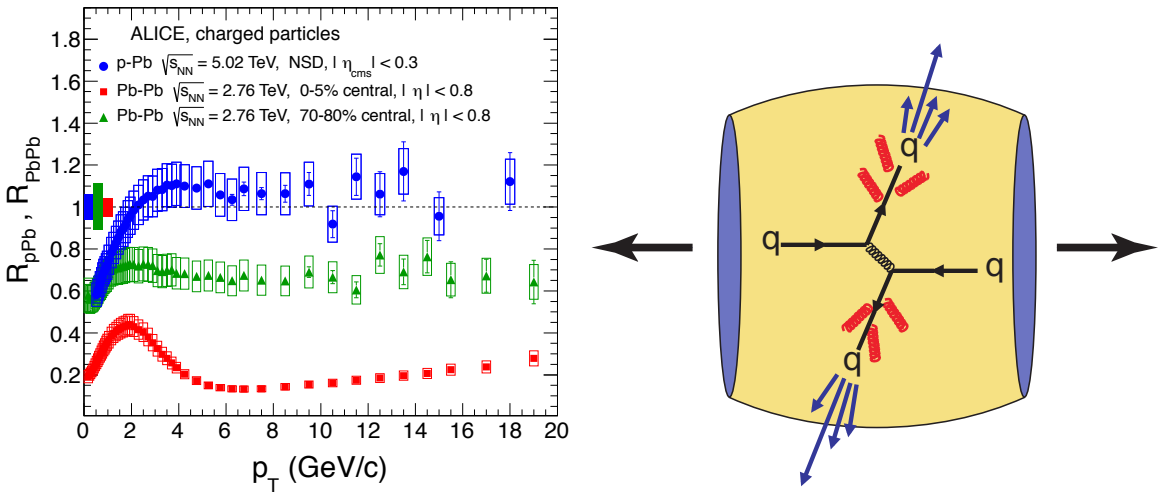

Figure 3.11: (left) Nuclear modification factor R_{AA} in central and peripheral Pb-Pb collisions and p-Pb collisions [110]. (right) Schematic illustration of jet-quenching. Figure by K. Reygers [111].

elementary hadron collisions. Thus, a useful measure of any in-medium modification is given by the ***nuclear modification factor***:

$$R_{\mathrm{AA}} = \frac{\mathrm{d}N_{\text{Pb-Pb}}/\mathrm{d}p_{\mathrm{T}}}{N_{\mathrm{coll}} \cdot \mathrm{d}N_{\mathrm{pp}}/\mathrm{d}p_{\mathrm{T}}} \tag{3.41}$$

Experimental methods for jet analysis are either based on a full reconstruction of the jet fragmentation [112, 113] or study the particle production at large transverse momentum. Figure 3.11 (right) illustrates the production of two partons, the interaction with the medium with radiative energy loss (gluons), and the fragmentation. The study of the parton energy loss allows us to learn more about QCD in the regime of deconfinement. The sensitivity of the parton energy loss to the parton flavor and color content is studied in measurements of the nuclear modification factor for identified particles with different quark content (cf. [114–122]). Since particles emitted along the the impact parameter have a shorter path length through the medium compared to those emitted perpendicular to the reaction plane, measurements of the elliptic azimuthal anisotropy v_2 at large momenta might help to unveil the path length dependence of the energy loss (cf. [123–126]).

Figure 3.11 (left) shows the nuclear modification factor for charged particles measured in p-Pb and Pb-Pb collisions. In peripheral and even more in the 0 - 5% most central Pb-Pb collisions, particle production is significantly suppressed (R_{AA}<1), which is attributed to the in-medium parton energy loss and referred to as ***jet quenching***. Due to the absence of medium effects, nucleon-nucleus collisions are an important test for any initial state modification such as ***nuclear shadowing*** [127], gluon saturation [128], or the ***Cronin effect*** [129]. The Cronin effect describes the enhancement of the hadron production at intermediate p_{T} in R_{pA}, which is generally attributed to multiple scattering of projectile partons propagating through the target nucleus [130]. Nuclear shadowing and saturation effects lead to a nuclear modification factor smaller than unity, while the Cronin effect is expected to increase the production at intermediate p_{T}. While significant Cronin enhancement was observed in d-Au collisions at RHIC [131, 132],

the LHC R_{pA} data are consistent with unity above 2 GeV/c, which indicates that the strong suppression of the hadron production at high p_{T} in Pb-Pb collisions is not due to any initial-state effect, but the fingerprint of jet quenching in hot QCD matter [110].

3.4 Anisotropic flow

It was demonstrated in section 3.2.4 that azimuthally anisotropic flow results in azimuthal anisotropic particle spectra. A historical review of collective flow can be found in [133, 134]. Since the microscopic particle production processes are azimuthally isotropic, the observation of azimuthal anisotropy is a clear experimental signature of macroscopic hydrodynamic behavior. At large transverse momenta, the particle production is dominated by the fragmentation of jets. In that regime, azimuthal anisotropy dominantly originates from the path length dependence of jet quenching discussed in section 3.3.5. In the present section, we will focus on the aspects of the hydrodynamic flow at small transverse momenta.
Experimentally, it is not always possible to measure the event-by-event particle distribution and to extract the azimuthal anisotropy as defined in eq. (3.29). A common experimental definition is given by

$$v_n = \langle \cos\left(n\left(\phi - \Psi_n\right)\right)\rangle \ , \tag{3.42}$$

where the brackets indicate an average over all particles of interest in all events [52, 135–137]. Details of different experimental methods are discussed in chapter 7.

3.4.1 Centrality dependence of the p_{T}-integrated anisotropic flow

Flow is the response of the system to deformations of the initial energy density distribution. It was found in section 3.2.4 that the azimuthal anisotropy v_n is essentially proportional to the corresponding eccentricity ϵ_n of the initial energy density profile for small values of ϵ_n. Non-linearities are stronger for higher harmonics, which might be due to shock waves that hinder the development of anisotropies [93]. Due to momentum conservation, the p_{T}-integrated ***directed flow*** v_1 is small at mid rapidity or integrated over a symmetric rapidity window [138, 139]. Thus, we will focus on higher-order anisotropic flow in the following.

Figure 3.12 shows the first four higher order harmonics of the p_{T}-integrated anisotropic flow for charged particles as a function of the centrality.
Elliptic flow v_2 is mainly induced by the almond shape of the reaction plane. This can be seen by the strong centrality dependence: v_2 is maximal for mid-central collisions and decreases for more central collisions until it reaches a limit, where the reaction plane is almost symmetric and ϵ_2 is dominated by fluctuations.
Triangular flow v_3 is mainly induced by fluctuations, which is indicated by the weak centrality dependence. Measurements of the correlation between the second and third order event plane yield no significant correlation and thus support the initial state fluctuation origin of triangular flow [140]. Figure 3.12 shows also a v_3 measurement with respect to $\Psi_2 \approx \Psi_{\mathrm{RP}}$ (green points), which is consistent with zero. Thus, triangular flow is not correlated with the reaction plane.

The linear relation between v_n and ϵ_n does not hold for higher harmonics. In [68] it is shown that ϵ_4 alone is not a sufficient estimator of ***quadrangular flow*** v_4, but interestingly a combination of ϵ_4 and ϵ_2^2. In other words, v_4 is induced by v_2. Similarly, for ***pentagonal flow*** v_5 a combination of ϵ_5 and non-linear terms of $\epsilon_2\epsilon_3$ are necessary to describe v_5 [68].
Figure 3.12 also shows the ratio of v_n/ϵ_n. The eccentricity was estimated from a Monte-Carlo Glauber calculation [53] and a Color-Glass-Condensate (CGC) model [142]. Saturation models such as the CGC generally tend to give larger eccentricities than Glauber models [58], which results into smaller values for v_n/ϵ_n. However, in both models the anisotropy over eccentricity ratio is not constant, but decreases as a function of the centrality, which might be due to different viscous corrections for central and mid-central collisions. For the CGC model v_2/ϵ_2 and v_3/ϵ_3 are almost equal in central collisions, which is expected for an almost perfect liquid with $v_n \propto \epsilon_n$ [93]. For mid-central and peripheral collisions, v_3/ϵ_3 is slightly smaller than v_2/ϵ_2, which might indicate larger viscous corrections for v_3 [141].

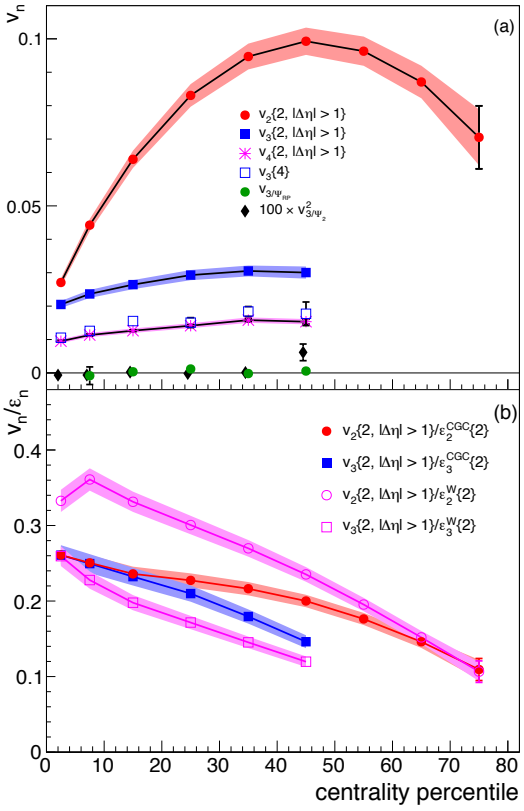

Figure 3.12: (top) v_2, v_3 and v_4 ($0.2 < p_T < 5.0\,\mathrm{GeV}/c$) as a function of the event centrality. (bottom) v_2 and v_3 divided by the corresponding eccentricity ϵ_n as determined from a Glauber Model (W) and a Color-Glass-Condensate (CGC) [141].

3.4.2 Event-by-event fluctuations

Within a given centrality class, the eccentricity fluctuates from one event to the other due to fluctuations of the impact parameter and the position of the participant nucleons. Therefore, fluctuations make the elliptic flow larger in the participant plane Ψ_{PP} than in the reaction plane Ψ_{RP}. since the direction of maximum anisotropy Ψ_2 fluctuates around Ψ_{RP} and is stronger correlated with Ψ_{PP} [137]. At the LHC, particle multiplicities are large enough to measure the v_n event-by-event probability distributions, which are shown in fig. 3.13. For v_3 and v_4, the probability distributions are well described by Gaussian distributions, which fails for v_2 except for the most central collisions, since ϵ_2 in non-central collisions is dominantly induced by the asymmetry of the reaction plane and not purely driven by fluctuations as ϵ_3.

3.4.3 Quark coalescence

In vacuum, the hadronization of a single parton is described in terms of string-breaking scenarios or parametrized in fragmentation functions. The hadronization is strongly affected by the presence of other partons close in phase space: In a dense phase-space scenario, colored partons essentially 'coalesce' into colorless bound states, similar to the formation of light nuclei. Even more remarkably, the objects that coalescence appear to be valence quarks. This finding is

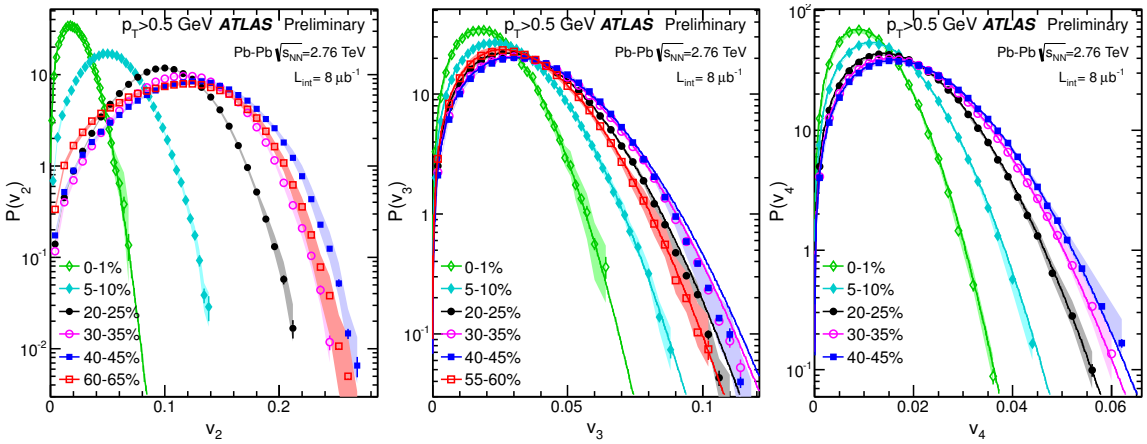

Figure 3.13: Event-by-event probability distribution of v_n for (left) elliptic, (mid) triangular, and (right) quadrangular flow of charged particles with $p_{\mathrm{T}} > 0.5\,\mathrm{GeV}/c$ [143].

surprising, since partons are overwhelmingly gluons and non-valence quarks at small Bjorken-x [144]. In a coalescence picture, the hadron momentum is just the sum of the momenta of its n_{q} valence quarks with $n_{\mathrm{q}} = 2$ for mesons and $n_{\mathrm{q}} = 3$ for baryons:

$$\vec{p}_{\mathrm{h}} = \sum_{i=0}^{n_{\mathrm{q}}} \vec{p}_{\mathrm{q},i} \tag{3.43}$$

The magnitude of the anisotropic flow v_n of a bulk system of quarks and the hadrons into which they coalesce is given by

$$v_n^{\mathrm{h}}(p_{\mathrm{T}}) = \sum_{i=0}^{n_{\mathrm{q}}} v_n^{\mathrm{q},i}\,(x_i p_{\mathrm{T}}) \ , \tag{3.44}$$

with the momentum fraction x_i and $\sum_{i=0}^{n_{\mathrm{q}}} x_i = 1$. In the event that the constituent quarks have similar elliptic flow – which requires that the coalescing quarks are close in phase space – this gives the ***number-of-constituent-quark scaling*** (NCQ scaling):

$$v_n^{\mathrm{h}}(p_{\mathrm{T}}^{\mathrm{h}}) = n_{\mathrm{q}} v_n^{\mathrm{q}}(p_{\mathrm{T}}^{\mathrm{q}}) \Rightarrow \frac{v_n^{\mathrm{b}}(p_{\mathrm{T}}^{\mathrm{b}}/3)}{3} = \frac{v_n^{\mathrm{m}}(p_{\mathrm{T}}^{\mathrm{m}}/2)}{2} \tag{3.45}$$

NCQ scaling was first observed at RHIC and will be further discussed in section 3.4.4. The observation of quark coalescence provides clear evidence for a thermalized state of partonic matter. Coalescence also provides a natural explanation for the observation of baryon enhancement at intermediate p_{T} and for the separation of meson and baryon nuclear modification factors [144].

3.4.4 p_{T} dependence

It was demonstrated in section 3.2.4 (eq. (3.37)) that v_n is expected to increase linearly with p_{T} in ideal hydrodynamics, which can be observed at low transverse momentum ($p_{\mathrm{T}} < 1\,\mathrm{GeV}/c$) in the data shown in fig. 3.14. The presence of fluctuations leads to a different structure of gradients, which reduce or increase v_n at a given p_{T}. Those gradients increase radial flow at higher p_{T}, which reduces v_n at higher p_{T} [146, 147]. In addition, v_n is significantly reduced

by non-zero viscosity ($\eta/s > 0$) and thus the measurement of v_n constrains the viscosity of the quark-gluon plasma (cf. section 3.4.6). At high momentum, v_n decreases due to the increasing dominance of particle production from jet fragmentation. Figure 3.14 shows the elliptic flow v_2 of identified charged hadrons measured at the LHC and at RHIC. The data clearly shows the expected mass ordering:

$$v_n^{\pi^\pm}(p_\mathrm{T}) > v_n^{\mathrm{K}^\pm}(p_\mathrm{T}) > v_n^{\mathrm{p}^\pm}(p_\mathrm{T}) \tag{3.46}$$

at $p_\mathrm{T} \lesssim 2\,\mathrm{GeV}/c$, which is a fingerprint of the hydrodynamic evolution. Similar mass ordering can also be observed for other harmonics [145]. The hierarchy is even more pronounced in the LHC data, which might be attributed to the stronger radial flow at the LHC that gives more weight to the m_T part in eq. (3.37) and thus enhances the mass splitting. If this behavior is driven by a hydrodynamic pressure, v_n for each particle species should scale with the ***transverse kinetic energy*** $KE_\mathrm{T} = m_\mathrm{T} - m$ [148]. In other words, the pressure gradient is directly linked to the collective kinetic energy of the emitted hadrons.

At intermediate $p_\mathrm{T} \approx 2\text{-}4\,\mathrm{GeV}/c$, mass ordering is broken. The observation that the baryon azimuthal anisotropy is by a factor of $3/2 = n_{\mathrm{q,b}}/n_{\mathrm{q,m}}$ larger than the anisotropy of mesons is expected from the coalescence picture and implies that v_n is more sensitive on the quark composition of the particles than on their mass. This has been attributed to the dominance of the quark coalescence mechanism at mid p_T [149]. The breakdown of this scaling as the beam energy is reduced might indicate that the initial energy of the system is below the threshold for a quark-gluon plasma creation and thus shed light on the onset of deconfinement [144]. Recently, the PHENIX collaboration proposed a generalized scaling behavior of $v_n/n_\mathrm{q}^{n_\mathrm{q}/2}(KE_\mathrm{T}/n_\mathrm{q})$ that holds for different harmonics [150].

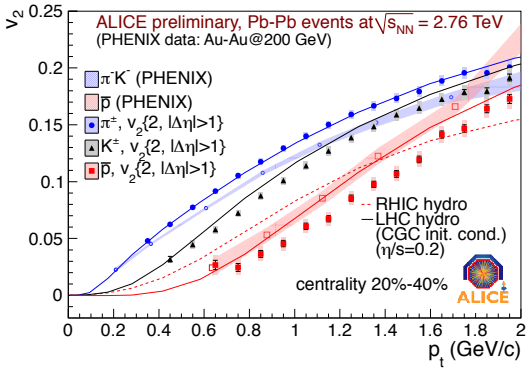

Figure 3.14: p_T dependence of v_2 for identified hadrons [145].

3.4.5 Breakdown of number-of-constituent-quark scaling

The STAR collaboration has measured the difference in the p_T integrated v_2 between particles and their corresponding anti-particles $v_2(X) - v_2(\bar{X})$ as a function of the center-of-mass energy. The results shown in fig. 3.15 (left) demonstrate that NCQ scaling between particles and their corresponding anti-particles is broken at small beam energies [26, 151], which might indicate a contribution from the hadronic phase. Interestingly, pions show opposite behavior compared to the baryons, while kaons are almost symmetric. The broken degeneracy of positive and negative particles might also be explained by electric quadrupole moments induced by chiral magnetic waves in the bulk, known as the ***chiral magnetic effect*** [153]. Furthermore, the results for ϕ mesons provide evidence for a smaller v_2 compared to other particles in the frame of the number-of-constituent quark scaling [154]. Figure 3.15 (right) shows the NCQ-scaled identified particle v_2 as a function of KE_T normalized to pions. It can be seen that pions and kaons agree

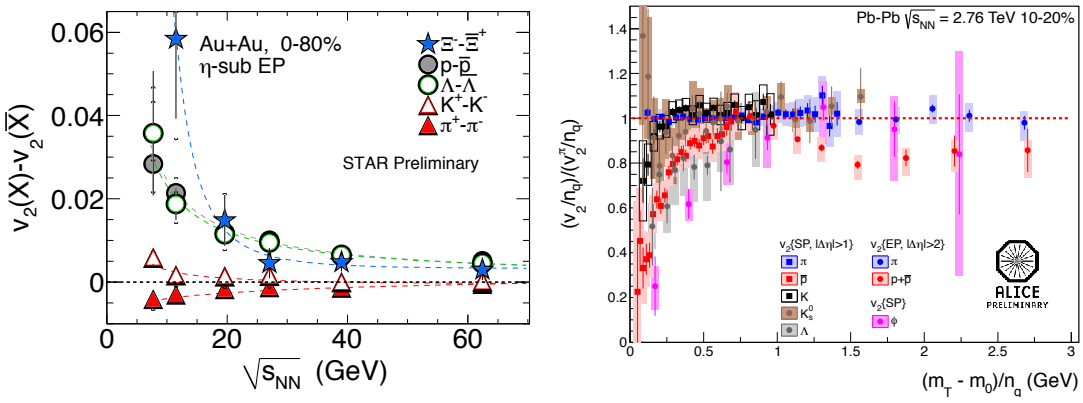

Figure 3.15: (left) Difference in v_2 between particles and their corresponding anti-particles as a function of the center-of-mass energy in 0 - 80% central Au-Au collisions [151]. (right) NCQ-scaled identified particle v_2 as a function of KE_T normalized to pions [152].

within uncertainties above 0.25 GeV/c, but deviates at low p_T. The azimuthal anisotropy of baryons such as protons and Λ baryons are overestimated by the NCQ-scaled pion measurement at intermediate and particularly at low p_T.

However, even though NCQ scaling still gives a satisfactory description of the intermediate p_T region at higher collision energies a detailed quantitative understanding of the intermediate p_T region is still missing. It seems impossible to separate an intermediate p_T region from a the low-p_T domain dominated by hydrodynamics and mass scaling and a high-p_T domain dominated by the path length dependence of jet energy loss [155, 156].

3.4.6 Viscous corrections

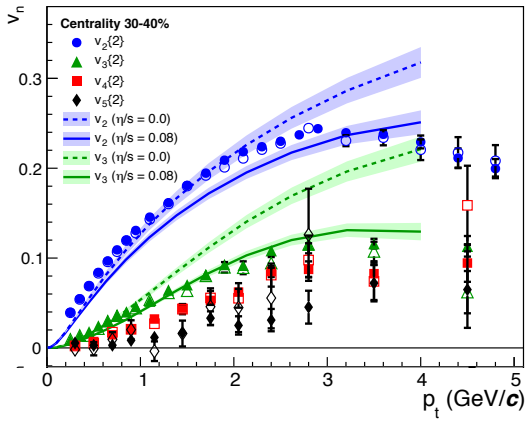

Figure 3.16: v_2,v_3,v_4, and v_5 as a function of transverse momentum p_T in mid-central collisions (30 - 40%) in comparison to hydrodynamic model calculations [141, 157].

It is obvious that the perfect fluid picture ($Kn \to 0$) is just an approximation. A more accurate description of the system evolution requires to take the leading corrections to the ideal-fluid picture into account. Those corrections are linear to the first order in Kn and involve several transport coefficients, namely the diffusion, shear, and bulk viscosity. In general, viscosity describes the energy exchange between different regions of the fluid. It is related to its ability to return to local thermal equilibrium after being driven away from equilibrium by gradients of the macroscopic flow. The magnitude of viscosity is related to the relaxation time and viscous effects disappear as the relaxation time approaches zero. In the microscopic language of particles physics, a low viscosity translates into a small mean free path or large rescattering cross sections between the particles. The ***bulk vis-***

cosity reduces the radial acceleration and thus inhibits the buildup of radial flow. The ***shear viscosity*** reduces flow anisotropies, i.e. it hinders the medium to translate deformations in the initial energy density profile into azimuthal anisotropies in the particle production. Thus, bulk velocity leads to steeper p_{T} spectra, while shear viscosity renders them flatter and reduces azimuthal anisotropies [88, 158, 159].

fluid	P [Pa]	T [K]	η $[Pa \cdot s]$	η/s $[\hbar/k_{\mathrm{B}}]$
H_2O	$0.1 \cdot 10^6$	370	$2.9 \cdot 10^{-4}$	8.2
^{4}He	$0.22 \cdot 10^6$	5.1	$1.7 \cdot 10^{-6}$	0.7
QGP	$88 \cdot 10^{33}$	$2 \cdot 10^{12}$	$\leq 5 \cdot 10^{11}$	0.4

Table 3.1: Pressure P, temperature T, viscosity η, and viscosity-to-entropy-density ratio η/s for various fluids. Data taken from [160].

In a simple picture, the shear viscosity of a liquid scales like

$$\eta \approx n \exp\left(\frac{E}{T}\right) , \tag{3.47}$$

where n is the density, T the temperature, and E an activation energy. It can be seen that the viscosity grows as the temperature is lowered. The viscosity of a typical fluid has a minimum as a function of temperature in the vicinity of the liquid-gas phase transition. A simple estimate for the viscosity of a dilute gas is $\eta = \frac{1}{3}\frac{\langle p \rangle}{\sigma}$, where $\langle p \rangle$ is the average momentum and σ the transport cross section. This implies that the viscosity of a dilute gas grows with temperature ($pT^{1/2}$), while the viscosity of a liquid decreases, which gives a minimum viscosity in the vicinity of the liquid-gas phase transition [161]. Experimental results show that the minimum value of the viscosity of good fluids – such as water and liquid helium – and a quark-gluon plasma differs by many orders of magnitude (see table 3.1). Thus it is desirable to normalize the viscosity to a suitable thermodynamic quantity in order to make more useful comparisons. For non-relativistic gases a suitable normalization is provided by the viscosity-over-mass density $\rho = mn$ known as the kinematic viscosity. In relativistic hydrodynamics the Reynolds number is defined in terms of the ratio $\eta/(sT)$, which indicates that the viscosity-to-entropy-density ratio η/s could serve for comparisons. Good fluids are characterized by $\eta/s \approx \hbar/k_{\mathrm{B}}$. Estimates for the shear viscosity of the quark-gluon plasma can be obtained from lattice QCD [14, 162], but the actual value is still under discussion. It can be seen that η/s of the quark-gluon plasma is even smaller than that of liquid helium, which makes it the most perfect liquid. A universal lower bound on the viscosity to entropy ratio in strongly interacting quantum field theories,

$$\frac{\eta}{s} > \frac{1}{4\pi} \approx 0.08 , \tag{3.48}$$

has been proposed on the basis of a correspondence with black-hole physics (AdS/CFT) [163]. Experimentally, values for the viscosity can be constrained by comparison of hydrodynamic calculations with different viscosity to the data. Figure 3.16 compares the data to hydrodynamic model calculations using Glauber initial conditions with $\eta/s = 0$ and $\eta/s = 0.08$. It can be seen that the p_{T} dependence is described by both calculations, but the magnitude is better fitted by

$\eta/s = 0$ for v_2, while v_3 is better described by $\eta/s = 0.08$. This effect may be due to the Glauber initial conditions [141].
It is argued that the shear viscosity η/s can be best estimated from p_{T}-integrated v_n measurements in the most central collisions [164]. Fits to ATLAS data [165] constrain the shear viscosity to $0.07 \leq \eta/s \leq 0.43$ [164]. Another calculations [166] yields a similar result of $\eta/s \approx 0.2$ with a systematic uncertainty of about 50%. The systematic uncertainty arises from the initial conditions and is usually estimated by comparing calculations with different initial conditions from Glauber and saturation models.

3.4.7 Non-flow effects

Non-flow effects include any correlations of particles that are not due to the collective hydrodynamic expansion of the medium, e.g. jets, particle decays, or Bose-Einstein correlations. The correlation of particles from jets appear only in a small cone around the leading particle. Consequently, non-flow effects can be suppressed by requiring a certain pseudorapidity gap $|\eta_i - \eta_j| > \Delta\eta_{\mathrm{min}}$ between the particles. Assuming no hydrodynamic flow in pp collisions, non-flow contributions can be estimated by comparing azimuthal correlations in pp collisions to those measured in heavy-ion systems [167].

3.5 Summary

The present chapter discussed our present understanding of the time evolution in heavy-ion collisions. In particular, it was shown in that the initial energy densities created in these collisions are large enough to form a quark-gluon plasma. It was further shown that experimentally observed hadron spectra and yields can be described by hydrodynamic and thermal models, which is a clear evidence for thermodynamic behavior. In particular, the measurement of hadron spectra and yields allow us to constrain the chemical and kinetic freeze-out temperature. Hydrodynamic models describe the general features of the spectra and the azimuthal anisotropy at low p_{T}. The transverse expansion velocity of the medium is about 2/3 of the speed of light. Measurements of higher-order harmonics of the Fourier decomposition of the azimuthal anisotropy constrain the shear viscosity-to-entropy-density ratio to $\eta/s \approx 0.2$, which implies that a quark-gluon plasma behaves much like a perfect fluid [36].

4. Direct photon production in heavy-ion collisions

Photons originate from a variety of production mechanisms that are relevant at different stages of the collision evolution, which is illustrated in fig. 4.1. First, it shall be distinguished between photons from hadron decays that occur on typical time scales[1] of $10^7\,\mathrm{fm}/c$ and photons that are produced on time scales of the fireball evolution $t \leq t_{\mathrm{fo}} \approx 10\,\mathrm{fm}/c$. We define the latter component as ***direct photons***.

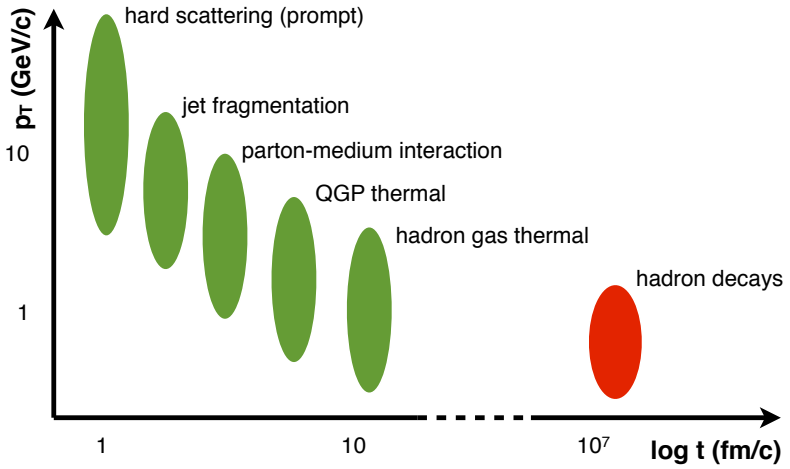

Figure 4.1: Time scales and momentum ranges of different photon production mechanisms in heavy-ion collisions.

Direct photons are a unique tool for the study of the collision evolution in nucleus-nucleus collisions. Since electromagnetic interactions are much weaker compared to strong interactions, a strongly-coupled medium of femtoscopic size can be considered to be transparent to photons. The mean free path of a $1\,\mathrm{GeV}/c$ photon in a quark-gluon plasma at a temperature of $T = 200\,\mathrm{MeV}/k_{\mathrm{B}}$ is about $\lambda = 430$ - $480\,\mathrm{fm}$ [168, 169] and thus much larger than the characteristic size of the system, which are of order 10 fm at freeze-out time (cf. section 3.1.4). Thus, direct photons can escape without interaction from the strongly-coupled medium once they are created.

Experimentally, it is not possible to distinguish between direct photons and decay photons on an event-by-event basis even though the time scales for the production are separated by orders of magnitude. The decay length of strongly and electromagnetically decaying hadrons cannot be resolved experimentally and thus the production vertex of decay photons cannot be distinguished from the primary vertex. A typical secondary vertex resolution is of the order of 100 µm [170] and thus four orders of magnitude larger than the neutral pion decay length. The most common technique to access the direct-photon spectrum is the ***statistical subtraction***

[1] The decay length of $\pi^0 \to \gamma\gamma$ is $c\tau = 25.5\,\mathrm{nm}$ [9].

technique, which is described in section 4.1.

Direct photons can be further distinguished with respect to their production mechanisms (cf. [29, 171–177]):

Prompt photons are produced at the short time scale of the collision and can be traced directly to incoming partons. Prompt photons are produced in next-to-leading-order perturbative QCD processes in the hard scattering of incoming partons and the fragmentation of outgoing partons. In heavy-ion collisions, the fragmentation is modified by in-medium effects and additional photons arise from the interaction of high-p_{T} partons with the medium.

Thermal photons are emitted by the scattering of thermalized particles in the quark-gluon plasma and the hadron gas.

The production of prompt and thermal photons is discussed in sections 4.2 and 4.3, thereafter the direct-photon azimuthal anisotropy in section 4.4 and Hanbury Brown-Twiss interferometry for direct photons in section 4.5.

4.1 Statistical direct-photon extraction

The experimentally observed sum of direct photons $N_{\gamma,\mathrm{dir}}$ and hadronic decay photons $N_{\gamma,\mathrm{bg}}$, mainly $\pi^0 \to \gamma\gamma^{(*)}$, is commonly referred to as ***inclusive photons***

$$N_{\gamma,\mathrm{inc}} = N_{\gamma,\mathrm{bg}} + N_{\gamma,\mathrm{dir}} \ . \tag{4.1}$$

The contribution of photons from hadron decays is usually estimated from the measured hadron spectra using a ***cocktail simulation*** and subtracted from the inclusive photon measurement, which implies that direct-photons can only be identified statistically averaged over many events.

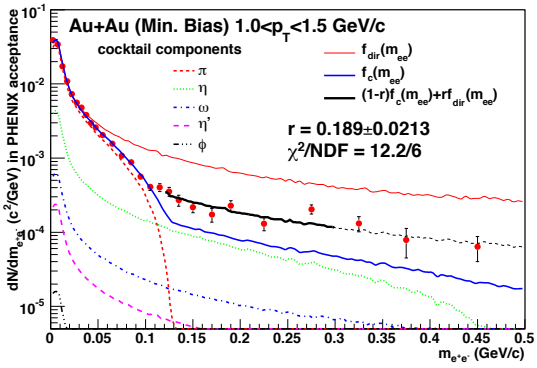

Figure 4.2: Electron pair invariant mass distribution [102].

It can be distinguished between virtual and real photons. While virtual photons already convert into dilepton pairs (e.g. $\gamma^* \to e^+e^-$) inside the medium (***internal conversion***), real photons can escape the interaction zone and then either be measured in an electromagnetic calorimeter or be reconstructed from the externally converted dilepton pair, which can be tracked as charged particles. The latter approach is called ***external conversion method*** and described in detail in section 8.2. Virtual photons can be extracted in a similar way from the dilepton spectra, which is referred to as ***internal conversion method***. Figure 4.2 shows the dielectron invariant mass distribution for small $M_{\mathrm{e^+e^-}} < 500\,\mathrm{MeV}/c^2$. The background from hadron decays is estimated from a cocktail simulation including the decays of the scalar mesons π^0, η and η' and the vector mesons ω and ϕ. It can be seen that for small $M_{\mathrm{e^+e^-}}$ the spectrum is dominated by the neutral pion ***Dalitz decay*** $\pi^0 \to \gamma\gamma^*$, while at $M_{\mathrm{e^+e^-}} > 120\,\mathrm{MeV}/c^2$ the direct

photon signal-to-background ratio improves. The number of dilepton pairs per photon is given by the Kroll-Wada formula [178],

$$\frac{1}{N_\gamma}\frac{\mathrm{d}N_{\mathrm{ee}}}{\mathrm{d}M_{\mathrm{e^+e^-}}} = \frac{2\alpha}{3\pi}\sqrt{1-\frac{4m_{\mathrm{e}}^2}{M_{\mathrm{e^+e^-}}^2}}\left(1+\frac{2m_{\mathrm{e}}^2}{M_{\mathrm{e^+e^-}}^2}\right)\frac{1}{M_{\mathrm{e^+e^-}}}S\ , \tag{4.2}$$

with

$$S = \begin{cases} \left|F\left(M_{\mathrm{e^+e^-}}^2\right)\right|^2\left(1-\frac{M_{\mathrm{e^+e^-}}^2}{M^2}\right)^3 & \text{for hadron decays} \\ 1 & \text{for point like processes with } p_{\mathrm{T}} \gg M_{\mathrm{e^+e^-}} \end{cases} \tag{4.3}$$

where $M_{\mathrm{e^+e^-}}$ is the dilepton invariant mass, m_{e} is the electron mass, M is the hadron mass and $F\left(M_{\mathrm{e^+e^-}}^2\right)$ is a form factor. The Kroll-Wada formula is fitted at small $M_{\mathrm{e^+e^-}} < 30\,\mathrm{MeV}/c^2$ for direct photons $f_{\mathrm{dir}}(M_{\mathrm{e^+e^-}})$ (orange line) and background $f_{\mathrm{c}}(M_{\mathrm{e^+e^-}})$ (blue line). The direct-photon excess $R^{\gamma,dir} = N^{\gamma^*,\mathrm{dir}}/N^{\gamma^*,\mathrm{inc}}$ ($M_{\mathrm{e^+e^-}} < 30\,\mathrm{MeV}/c^2$) can be extracted by a two component fit of $f_{\mathrm{dir}}(M_{\mathrm{e^+e^-}})$ and $f_{\mathrm{c}}(M_{\mathrm{e^+e^-}})$ to the data in the range 120 - 300 MeV/c^2 (black line).

4.2 Prompt photons (pQCD)

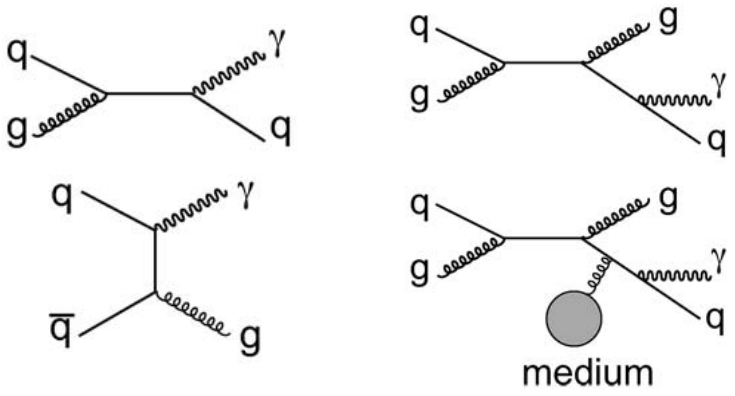

Figure 4.3: Feynman diagrams for next-to-leading-order pQCD prompt photon production [29].

Figure 4.3 shows the next-to-leading-order perturbative QCD diagrams for prompt photon production. The first kind of process includes quark-gluon Compton scattering $q+g \to q+\gamma$ (upper left) and quark-antiquark-annihilation $q+\bar{q} \to g+\gamma$ (lower left). A Feynman diagram for the vacuum fragmentation ($q+g \to g+q+\gamma$) is shown in the upper right panel. The rates of such processes for elementary hadron-hadron collisions can be calculated in next-to-leading-order (NLO) perturbative QCD.

It is expected that the prompt photon production in heavy-ion collisions scales with the number of binary collisions N_{coll}. Thus, prompt photons are an important tool to study the nuclear modification of the initial state parton distributions. Furthermore, prompt photons are sensitive to the modification of jets in the medium. As illustrated in the lower left panel in fig. 4.3, the jet fragmentation is modified by the in-medium energy loss of partons and additional photons

are produced by ***jet-bremsstrahlung*** and ***jet-plasma conversions***[2].

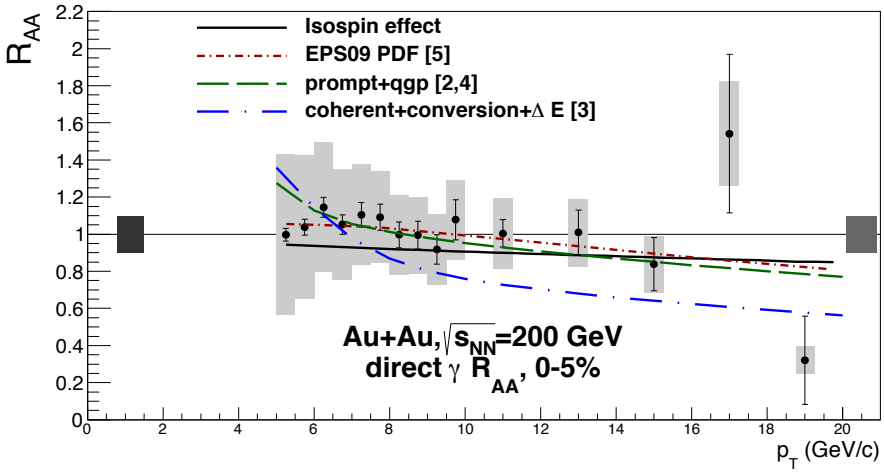

Figure 4.4: Direct-photon nuclear modification factor R_{AA} for 0 - 5% central events compared with theoretical calculations for different modification scenarios (see text) [180].

Figure 4.4 shows a measurement of the direct-photon nuclear modification factor R_{AA} in the transverse momentum range 4 - 22 GeV/c for Au-Au collisions at RHIC. We have seen in section 3.3.5, that the production of hadrons is significantly suppressed in nucleus-nucleus collisions, which is interpreted as the fingerprint of jet quenching in hot QCD matter. Photons do not show a similar suppression as hadrons in nucleus-nucleus collisions, which is consistent with the picture of transparency. The data are compared to theoretical calculation for possible modifications of the photon production including initial and final-state effects. The nuclear structure functions might be modified compared to an incoherent superposition of free protons [127, 128]. In addition, the prompt photon production might be modified by the ***isospin effect***, which accounts for the different isospin components of the nucleus[3]. Those effects are included in the 'EPS09 PDF' [182] calculation and also in 'prompt+QGP' [174, 175]. The latter calculation takes also into account that the parton energy loss can reduce the contribution of fragmentation photons. Yet another calculation ('coherent+conversion+ΔE' [183]) also includes final-state effects such as jet-Bremsstrahlung, the ***LPM effect***[4] and jet-plasma conversions. While both first scenarios are consistent with the data, the third one predicts the strongest deviation from unity and disagrees with the data [180]. In summary, the data are consistent with unmodified binary scaled prompt photon production in pp collisions. Small modifications might arise from slight modifications of the initial state compared to pp and in-medium instead of vacuum fragmentation, whereas final-state effects are unlikely.

A similar probe than prompt photons are the electroweak W and Z boson, which are also produced in NLO pQCD processes and not expected to interact with the medium. In measurements at the LHC the production of W and Z bosons was found to be consistent with binary

[2] Production of a high-p_{T} photon by the scattering of a hard parton on a thermal parton [179].

[3] The cross sections for $p+p$, $p+n$ and $n+n$ are different due to the different quark charge content of protons compared to neutrons [181].

[4] The Landau-Pomeranchuk-Migdal (LPM) effect describes a reduction of the Bremsstrahlung and pair production cross sections at high energies or matter densities [184]

scaled NLO pQCD calculations [185, 186], which together with the finding for prompt photons confirms the binary scaling of the particle production in pQCD processes.

Prompt photons produced in quark-gluon Compton scattering or quark-antiquark annihilation processes are associated with an outgoing parton that fragments into a jet in the opposite direction. Such processes can also be tagged experimentally by identifying ***isolated photons*** and their correlation with associated hadrons in the opposite azimuthal direction. Isolated photons are photons that have no accompanying particles or energy within some angular range. They can be reasonably assumed to be direct photons at high transverse momentum, because any parent hadron would be nearby at a close angle. It should be noted that the definition of isolated photons explicitly excludes fragmentation photons. However, in heavy-ion collisions it very challenging to search for isolated photons due to the large multiplicity densities [29, 187, 188]. The ATLAS and CMS collaboration have recently presented an isolated photon spectrum in Pb-Pb collisions at $\sqrt{s_{\mathrm{NN}}} = 2.76\,\mathrm{TeV}$ [189, 190]. The isolated photon spectrum in pp and Pb-Pb is reasonably well described by (binary scaled) next-to-leading-order pQCD calculations and the isolated photon nuclear modification factor is consistent with unity.

4.3 Thermal photons

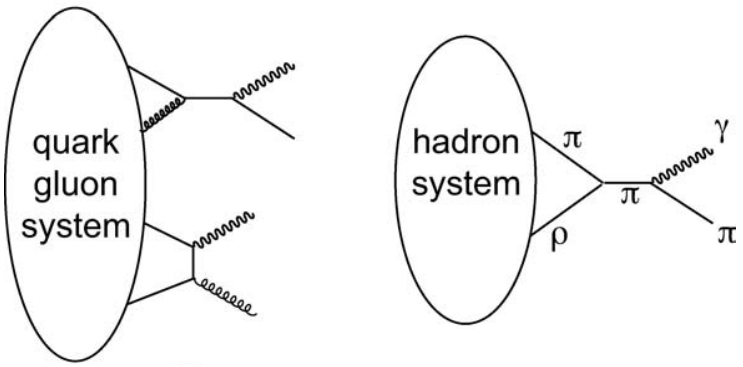

Figure 4.5: Illustration of thermal photon production [29].

It was suggested long ago [22,191] that rescattering of quarks in local thermal equilibrium would lead to emission of real and virtual photons. Due to the transparency of the medium, those photons could reveal the undistorted information about the system at their production time. However, from the transparency of the medium it also immediately follows that photons can never be in thermal equilibrium with the QCD medium. Thus, the thermal photon production cannot be described by black body radiation, where the photon rate R is given by the Planck formula,

$$E\frac{\mathrm{d}R}{\mathrm{d}^3p} \propto \frac{E}{\exp\frac{E}{T}-1} \underset{E\gg T}{\rightarrow} \exp\left(-\frac{E}{T}\right), \tag{4.4}$$

and the total radiated power increases with the fourth power of the temperature. Instead, the

thermal photon production involves individual processes, where the lowest order diagrams give

$$E\frac{\mathrm{d}R}{\mathrm{d}^3p} \propto \alpha_{\mathrm{em}}\alpha_{\mathrm{s}}T^2 \exp\left(-\frac{E}{T}\right) \log\left(\frac{ET}{k_{\mathrm{c}}^2}\right) \underset{E\gg T}{\rightarrow} \exp\left(-\frac{E}{T}\right) \ , \tag{4.5}$$

where k_{c} is an infrared cutoff that regulates the infrared divergence. As illustrated in fig. 4.5, thermal photons are produced either through the scattering of partons (e.g. $q+\bar{q}\rightarrow g+\gamma$ or $q+g\rightarrow q+\gamma$) during the quark-gluon plasma phase or by hadronic interactions (e.g. $\pi^{\pm}+\rho\rightarrow \pi^{\pm}+\gamma$) in the hot hadron gas phase.

It should be noted that any photon production process requires electrically charged particles, which puts further constraints on the thermal photon production: Since the quark-producing cross sections are smaller in perturbative QCD than those for gluon production [192], it is expected that the medium is gluon dominated at early times [193] and it is not clear at which stage of the system evolution electric charge is produced. Earlier, it was even argued that a quark-gluon plasma would produce more photons at the same temperature than a hadron gas, since quarks become massless due to chiral symmetry restoration in the quark-gluon plasma (cf. [102,194–196]) and thus highly abundant. It is also under discussion, whether pre-equilibrium radiation – e.g. from a stage, where the medium is kinetically equilibrated, but not chemically – contributes to the direct-photon spectrum [29].

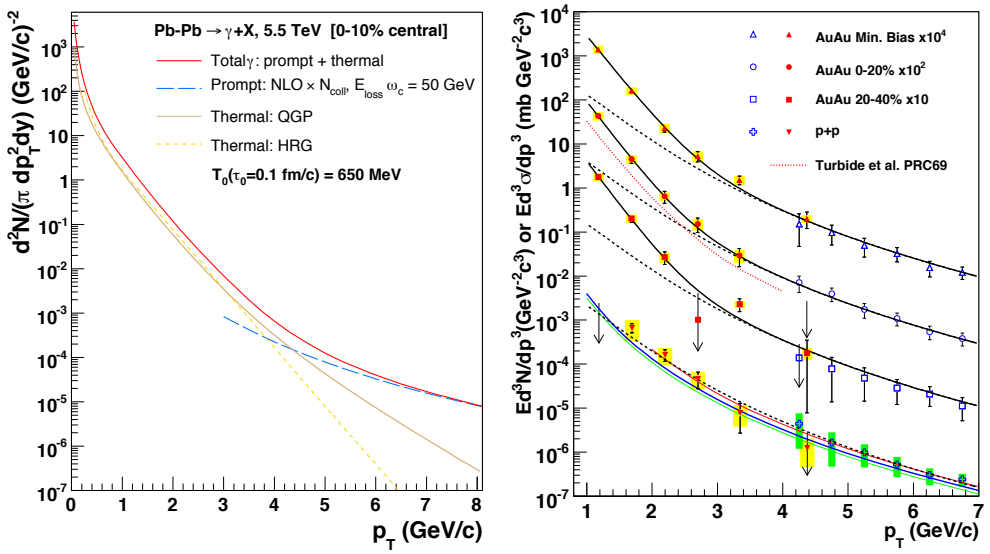

Figure 4.6: (left) Prediction for the direct photon production in Pb-Pb collisions at $\sqrt{s_{\mathrm{NN}}}=$ 5.5 TeV [197]. (right) Direct-photon spectrum in Au-Au and pp collisions at $\sqrt{s}=200$ GeV. The black dashed lines represent a fit to the pp measurement scaled by N_{coll} [123].

Figure 4.6 (left) shows a prediction for the direct photon production at the full LHC energy. It can be seen that thermal photons have an exponentially decreasing spectrum, while prompt photons follow a power law. Figure 4.6 (right) shows the direct-photon spectra in Au-Au and the cross section in pp collisions at RHIC. The low-p_{T} data points are determined by the internal conversion method [187], while the high-p_{T} data points are obtained from real photons [198,199]. The pp measurement is reasonably well described by a binary scaled pQCD calculation for prompt and fragmentation photons [172]. The black dashed lines represents a fit to the

pp measurement scaled by the number of binary collisions N_{coll}. The binary scaled pp yield describes the Au-Au data for transverse momenta p_{T} above $4\,\mathrm{GeV}/c$, which is expected from the dominance of pQCD photons at high-p_{T}. At smaller transverse momenta, the spectra in fig. 4.6 (right) show a clear excess above the binary scaled pp fit and pQCD calculations for prompt photons. The low-p_{T} data points in the spectrum are fitted with $A\exp\left(-E/T_{\mathrm{eff}}\right)$, which is the expected thermal photon rate from eq. (4.5) in the limit of $p_{\mathrm{T}} \gg T_{\mathrm{eff}}$, where T_{eff} is the apparent temperature introduced in eq. (3.25) and A an arbitrary normalization. The PHENIX collaboration reports an inverse slope parameter of $T_{\mathrm{eff}}^{\mathrm{RHIC}} = (220 \pm 19^{stat} \pm 19^{sys})\,\mathrm{MeV}/k_{\mathrm{B}}$ in 0 - 20% Au-Au collisions at $\sqrt{s_{\mathrm{NN}}} = 200\,\mathrm{GeV}$ [200]. First measurements of the LHC in 0 - 40% central Pb-Pb collisions by the ALICE collaboration yield an apparent temperature of $T_{\mathrm{eff}}^{\mathrm{LHC}} = (304 \pm 51^{stat+sys})\,\mathrm{MeV}/k_{\mathrm{B}}$ [201]. Since the functional form for thermal production is the same for a hadron gas and a QGP, the shape of the spectrum alone cannot specify the nature of the emitting medium. As a consequence of the higher temperature the photons originating from the quark-gluon plasma have a slightly flatter spectrum compared to those from the hadron gas. Recent calculations such as fig. 4.6 (left) include a substantial portion of thermal photons from the quark-gluon plasma, which is expected from the photon production rates being proportional to the second power of the temperature (eq. (4.5)). Estimates for the initial temperature range from 300 - 600 $\mathrm{MeV}/k_{\mathrm{B}}$ [200] at RHIC and 500 - 600 $\mathrm{MeV}/k_{\mathrm{B}}$ at the LHC [34, 35].

4.4 Azimuthal anisotropy of direct photons

Since the azimuthal anisotropy of direct photons depends strongly on their production mechanism, a measurement of $v_n^{\gamma,\mathrm{dir}}$ allows to put additional constraints on their production time.
Prompt photons from the initial hard scattering are expected to be produced isotropically, if they do not interact with the medium ($v_n^{\gamma,\mathrm{pQCD}} = 0$) [202]. Due to the path-length dependence of the in-medium energy loss, jets are more quenched along the long symmetry axis perpendicular to Ψ_n. Thus, photons from jet-fragmentations are also more suppressed in the out-of-plane direction ($v_n > 0$), while the photons produced in jet-medium interactions are enhanced out-of-plane ($v_n < 0$). Consequently, it is expected, that these contributions almost cancel out and the prompt photon production is considered as almost isotropic [202].
Thermal photon production is affected by the hydrodynamic anisotropic flow, so that photons emitted along Ψ_n get a stronger boost and blue shift. This results in a positive anisotropic flow for thermal photons, while the magnitude depends on the magnitude of the anisotropic flow of the system at the photon production time. Consequently, thermal photons from the quark-gluon plasma phase are expected to have a small positive anisotropic flow, while photons from the hadron gas are produced just before the chemical freeze-out and thus have an anisotropic flow similar to hadrons. Current hydrodynamic calculations include a substantial portion of thermal photons from the quark-gluon plasma, so that a rather small thermal-photon anisotropic flow $v_n^{\gamma,\mathrm{therm}}$ is expected [203].
It can be seen in figs. 4.6 (left) and 4.6 (right), that prompt photon production is dominant at large transverse momenta and thermal photon production at small transverse momenta below 3 - 4 GeV/c. Consequently, the general expectation is that $v_n^{\gamma,\mathrm{dir}}$ is is positive and small at low momentum and vanishes at high momenta above $4\,\mathrm{GeV}/c$.

Figure 4.7 shows a measurement for the neutral pion, inclusive and direct-photon v_2 at RHIC.

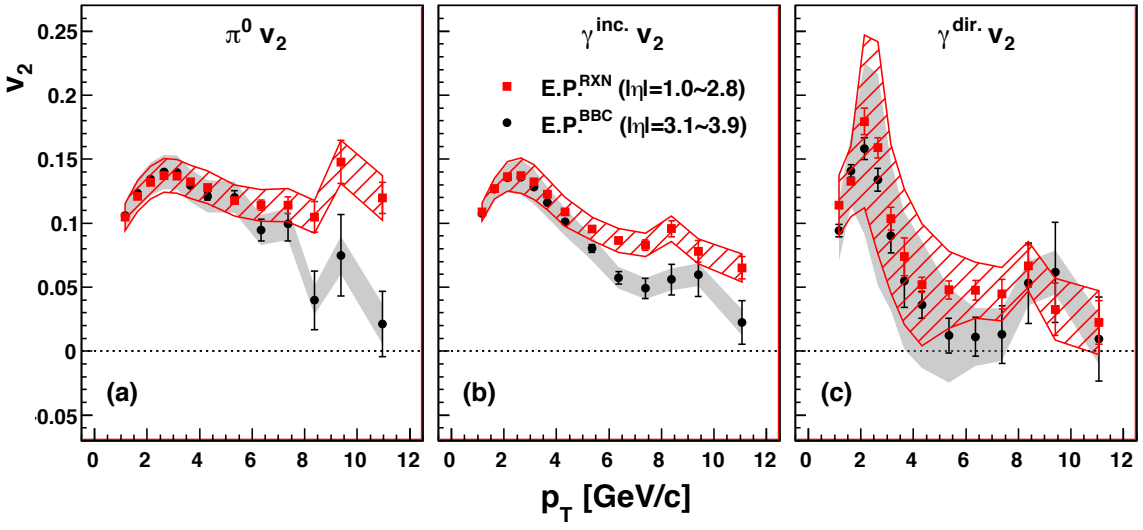

Figure 4.7: v_2 in minimum bias Au-Au collisions at $\sqrt{s_{\mathrm{NN}}} = 200\,\mathrm{GeV}$, using two different reaction plane detectors for (left) neutral pions (right) inclusive photons and (c) direct photons [204].

The two data sets correspond to different techniques for the neutral pion and inclusive photon elliptic flow measurement. The direct-photon azimuthal anisotropy $v_2^{\gamma,\mathrm{dir}}$ can be calculated from the inclusive-photon anisotropy $v_2^{\gamma,\mathrm{inc}}$ as

$$v_2^{\gamma,\mathrm{dir}} = \frac{R v_2^{\gamma,\mathrm{inc}} - v_2^{\gamma,\mathrm{bg}}}{R-1}\,, \tag{4.6}$$

with $R^{\gamma,dir} = N_{\gamma,\mathrm{inc}}/N_{\gamma,\mathrm{bg}}$ [204]. The azimuthal anisotropy of decay photons $v_2^{\gamma,\mathrm{bg}}$ can be estimated from $v_2^{\pi^0}$ in a cocktail simulation.
At large transverse momentum, the direct-photon $v_2^{\gamma,\mathrm{dir}}$ is consistent with zero within its uncertainties, which is expected from the dominance of prompt photons. At small transverse momentum, the elliptic flow of direct photons is comparable in magnitude to the elliptic flow of inclusive photons and neutral pions, which is not expected from hydrodynamic calculations and the considerations made above. A large thermal photon v_2 might indicate a dominant contribution of thermal photons from the late stages of the evolution, where the bulk flow has fully developed. It was even argued by Basar et al. [205] that the large azimuthal anisotropy anisotropy might result from a novel photon production mechanism stemming from the conformal anomaly of QCD × QED and the existence of strong spectator magnetic fields. This hypothesis can be tested by measuring the triangular direct-photon flow, since the direction of triangular flow is uncorrelated with the reaction plane and thus the spectator magnetic fields.

4.5 Photon Hanbury Brown-Twiss interferometry

The production time of direct photons could be constrained by Hanbury Brown-Twiss interferometry, which measures the size of the region that contributes to the direct-photon spectrum. Since photons are produced either directly from the medium or by the decay of hadrons, the interferometry of photons includes two length scales: the femtoscopic scale of the medium and the nanometer scale of decays. However, the large scale correlations will appear at a momentum

difference of $q \ll \hbar/nm \approx 200\,\mathrm{eV/c}$ [29], which much smaller than typical momentum resolutions in heavy-ion detectors[5]. The first measurement of direct-photon HBT was performed by the WA98 experiment at the CERN SPS [207]. The correlation was studied as a function of the invariant relative momentum q_{inv}, which equals the invariant mass $M_{\gamma\gamma}$ for two massless particles. The measurement yielded HBT radii for direct photons being only slightly smaller than those for pions, which suggests that the direct photons are emitted in the late hadron gas stage of the collision. It will be interesting to see further measurements from RHIC and the LHC. The STAR experiment has published preliminary data for photon correlations and observes a significant peak at small q_{inv}, but it is not understood yet to what content this correlation is due to Bose-Einstein correlations and apparatus effects [208].

For a fully chaotic source, the correlation strength λ is directly related to the fraction of direct photons $N_{\gamma,\mathrm{dir}} = \sqrt{2\lambda} N_{\gamma,\mathrm{inc}}$ [209], which allows one to measure the direct-photon yield at very small transverse momenta. The direct-photon spectrum in $\sqrt{s_{\mathrm{NN}}} = 158\,\mathrm{GeV}$ Pb-Pb collisions at the CERN SPS are shown in fig. 4.8. The first two low-p_{T} data points were determined from HBT correlations (closed circles), whereas the other data points were measured by the statistical subtraction method (open circles, or arrows indicating upper limits). While the data points that were determined by the statistical subtraction method [210] are described by the theoretical calculation, the limits and data points measured via Hanbury Brown-Twiss interferometry at low transverse momentum clearly exceed the theoretical expectation.

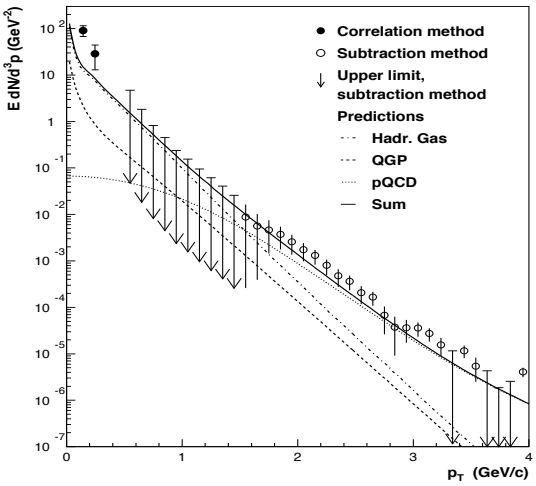

Figure 4.8: Direct-photon invariant yield in $\sqrt{s_{\mathrm{NN}}} = 158\,\mathrm{GeV}$ Pb-Pb collisions [207].

4.6 Summary and motivation for this thesis

Direct photons are produced over the whole time evolution of heavy-ion collisions. Since photons do not interact with the strongly-coupled medium, they carry the undistorted information about the medium at their production time. At high p_{T}, direct-photon production can be described by binary scaled next-to-leading-order pQCD calculations. At low p_{T}, experiments at SPS, RHIC and the LHC have revealed a significant excess above the pQCD expectation, which is interpreted as a contribution from thermal photons. Current hydrodynamical calculations include a substantial portion of thermal photons from the hot quark-gluon plasma phase and thus early times are expected to dominate the thermal photon production. Since the anisotropic flow builds up with time, the thermal photon anisotropic flow is expected to be small compared to the one of hadrons. However, measurements of the azimuthal anisotropy $v_2^{\gamma,\mathrm{dir}}$ at RHIC

[5] The momentum resolution of the ALICE TPC is about is about 0.7% at $p_{\mathrm{T}} = 1\,\mathrm{GeV/}c$ and the detector cannot cannot track well below $100\,\mathrm{MeV/}c$ due to the large curvature of charged tracks in the magnetic field [206].

indicate that the direct-photon elliptic flow has a similar magnitude compared to the elliptic flow of hadrons. Furthermore, results from direct-photon Hanbury Brown-Twiss interferometry at the SPS suggest that the size of the direct-photon source is comparable to the source of hadrons. These results might indicate that photons are produced at a later stage of the evolution than expected by hydrodynamic calculations. Within this thesis, the direct-photon azimuthal anisotropy is studied in Pb-Pb collisions at $\sqrt{s_{\mathrm{NN}}} = 2.76\,\mathrm{TeV}$, which will shed more light on the production time of direct photons. In particular, the first measurement of the triangular direct-photon flow will allow us to test, to which content the direct-photon azimuthal anisotropy could be explained by mechanisms related with spectator magnetic fields.

5. The LHC and ALICE

The Large Hadron Collider (LHC) at the European Organization for Nuclear Research (CERN) near Geneva is the world's largest, most complex, and highest-energy particle collider ever constructed. It collides hadrons at almost the speed of light, and such allows physicists to test the predictions and theories of particle and high-energy physics. In collisions of lead nuclei, the LHC is able to recreate conditions similar to those just after the Big Bang.
In the following, the LHC design and operation shall be briefly discussed. The LHC is equipped with four large experiments with different physical aim. ALICE is the dedicated heavy-ion experiment designed for the quest after the quark-gluon plasma.

5.1 The Large Hadron Collider

The LHC is a 26.6 km long accelerator ring situated about 100 m underneath the surface between Switzerland and France. The two adjacent parallel beam pipes of the LHC are placed in a tunnel with a circumference of 26.6 km. The LHC reuses the tunnel that was built for the previous big accelerator at CERN, the Large Electron Positron collider (LEP). Each of the two beam pipes contains a proton or heavy-ion beam traveling in opposite directions. 1232 dipole magnets keep the beams on their circular path, additionally 392 quadrupole magnets are used to keep the beam focussed. At the nominal magnetic dipole field of 8.33 T, the LHC is capable to collide either protons or fully stripped lead $^{208}Pb^{82+}$ ions at a centre-of-mass energy of $\sqrt{s} = 14\,\text{TeV}$ and $\sqrt{s_{\text{NN}}} = 5.5\,\text{TeV}$ per nucleon, respectively [211, 212].
The LHC has been finished in 2008, with total material costs of about 4.6 billion CHF [212]. The first collisions at a centre-of-mass energy of 900 GeV were expected to take place in September 2008. On September 19$^{\text{th}}$, 2008, during powering tests a fault occurred in the electrical bus connection in the region between a dipole and a quadrupole, resulting in mechanical damage, causing a loss of approximately six tonnes of liquid helium [213, 214]. A total of 53 magnets were damaged in the incident and had to be repaired or replaced [215]. First particle collisions took place on November 23, 2009, at 450 GeV beam energy. In February 2013, the LHC finished its first period of operation [216]. Due to the accident in 2008, the LHC was operated at a decreased centre-of-mass energy during its first period of operation. After a technical stop of about 2 years, the LHC will resume its operation at the nominal energy in 2015.

While protons can be directly extracted from a bottle of hydrogen, lead ions are created from isotopically pure solid ^{208}Pb, which is vaporized in an ohmic heated micro-oven at a temperature of about 500 °C. The lead vapor or the hydrogen are ionized in an electron cyclotron resonance (ECR) ion source [218], bunched, and accelerated by a radio frequency quadruple. The accelerator complex at CERN sketched on fig. 5.1 is a succession of machines that accelerate particles to increasingly higher energies. $^{208}Pb^{23+}$ ions are further accelerated in the linear accelerator LINAC3, LEIR, PS, SPS and finally injected into the LHC. During these acceleration steps, the remaining electrons are subsequently stripped of by carbon foils, which finally gives $^{208}Pb^{82+}$. For protons, the acceleration procedure is different. Protons are first accelerated in the LINAC2, then in the PS booster, PS, SPS and finally injected into the LHC.

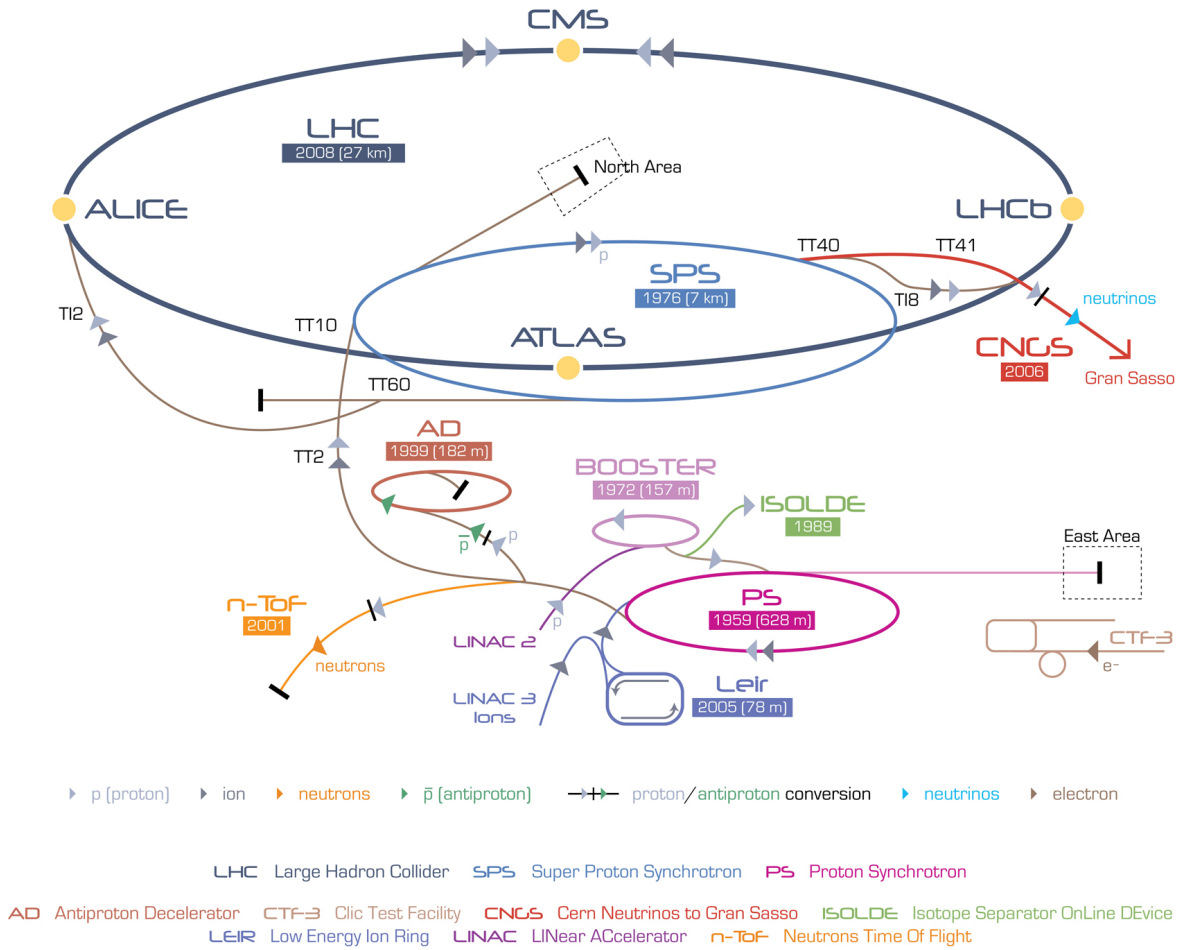

Figure 5.1: Schematic sketch of the CERN accelerator complex and the LHC with its four experiments ATLAS, CMS, LHCb and ALICE [217].

The two LHC beams can be collided at four intersection points, where besides smaller experiments [219, 220] the four large experiments are placed, ***ATLAS***, ***CMS***, ***LHCb*** and ***ALICE***. The main purpose of ATLAS [221] and CMS [222] is the search for the Higgs boson [3, 4], and for new elementary particles predicted by supersymmetric extensions of the Standard Model [223, 224]. Both experiments have similar physical purpose with complementary design. LHCb [225] investigates the asymmetry between matter and antimatter by measuring the CP violation in the decay of b-hadrons [226]. ALICE [227] is the dedicated experiment for heavy-ion collisions, designed to study the properties of the quark-gluon plasma.

The luminosity at these intersection points is defined by

$$\mathcal{L} = \frac{nN_1N_2f}{A} \,, \tag{5.1}$$

where n is the number of bunches, N_1 and N_2 are the number of particles per bunch, $f = v/l$ is the circulation frequency, and A is the cross sectional area of the beam at the intersection point. For a Gaussian profile with root mean square beam size σ, the cross sectional area can be estimated by $A = 4\pi\sigma_x\sigma_y$, where σ_x and σ_y are the standard deviations of the distribu-

tion of particles in x and y direction, respectively [41]. In the nominal pp operation, the LHC will be filled with about 2800 bunches with 10^{11} protons each. Both beams with a width of $\sigma = 16\,\mu$m cross each other at a frequency of $f = 11\,$kHz, which yields a nominal peak luminosity of $\mathcal{L}_{\text{pp}} \approx 10^{34}\,\text{cm}^{-2}\text{s}^{-1}$. In the Pb-Pb mode, the LHC will be operated with beams consisting of 592 ion bunches with 7×10^7 lead ions per bunch yielding a nominal peak luminosity of $\mathcal{L}_{\text{Pb-Pb}} \approx 10^{27}\,\text{cm}^{-2}\text{s}^{-1}$. The total cross section for removal of an ion from the beam is 514 b ($1\,\text{b} = 10^{-28}\,\text{m}^2$), which yields an interaction rate of about 0.5 MHz [228].
During the first run period the LHC was operated at 50% of the nominal energy. In the first heavy-ion run in 2010, the peak luminosity was about a factor 10 smaller compared to the nominal luminosity, $\mathcal{L}_{\text{Pb-Pb}} \approx 0.1 \times 10^{27}\,\text{cm}^{-2}\text{s}^{-1}$ [229] yielding an integrated luminosity of $\int \mathcal{L}dt \approx 10\,\mu\text{b}^{-1}$. The inelastic hadronic cross section is about $\sigma^{\text{H}}_{\text{inel}} \approx 8\,\text{b}$ [77, 230], which yields about 80 million inelastic Pb-Pb collisions at $\sqrt{s_{\text{NN}}} = 2.76\,$TeV.

5.2 The ALICE experiment

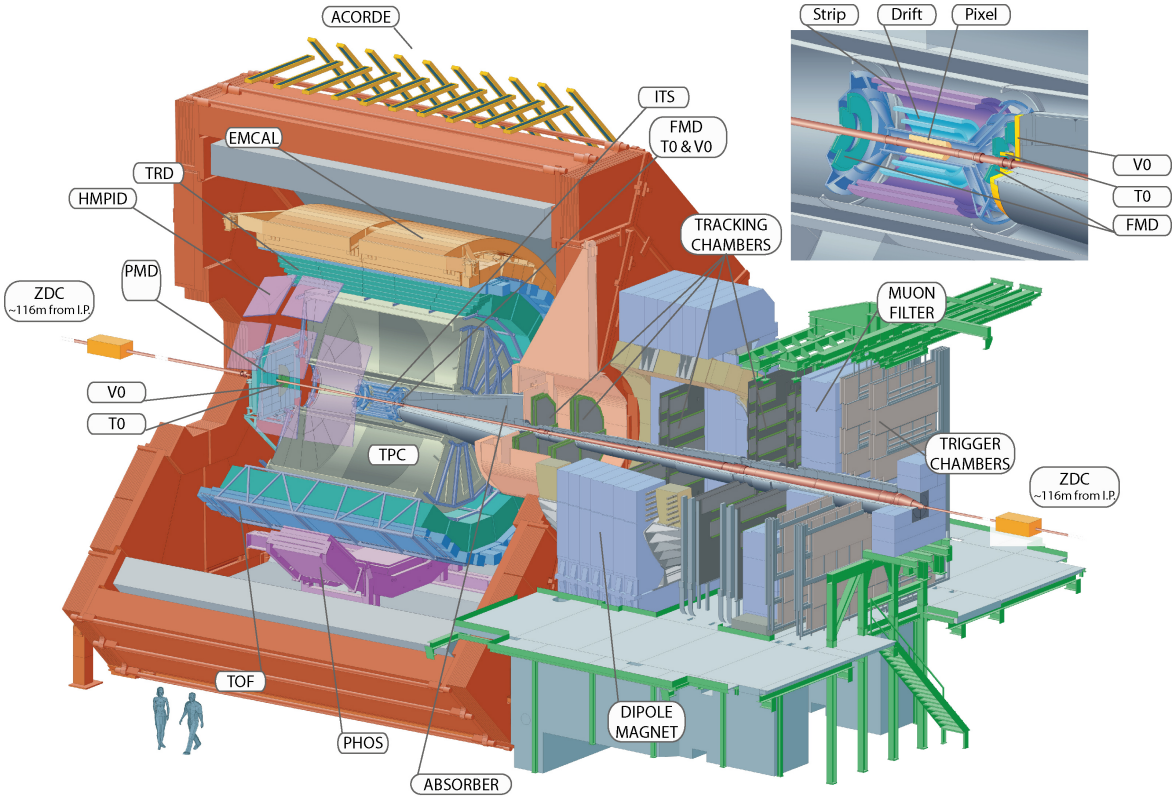

Figure 5.2: Layout of the ALICE detector [227].

ALICE (***A Large Ion Collider Experiment***) is one of the four large particle detectors at the LHC. Figure 5.2 illustrates the design of ALICE. With a length of around 26 m and a diameter of around 16 m, ALICE has a weight of around 10000 t. ALICE is composed of 18 subdetector systems for tracking and particle identification. The central barrel detector components at mid rapidity ($|\eta| \leq 0.9$) are symmetrically arranged around the intersection point and placed in the red L3 magnet, a solenoid that generates a uniform (within $\pm 2\%$) magnetic field of up to 0.5 T. In addition, ALICE has one ***muon arm*** at forward rapidity.

In the following, the detector components relevant for this thesis and their performance are briefly discussed [227, 231]:

(ITS) The Inner Tracking System consists of 6 cylindrical layers of high-resolution silicon detectors and is designed for vertex detection. It provides charged particle tracking with a spatial resolution better than 100 µm in the transverse plane, combined tracking together with the TPC, primary vertex reconstruction with a resolution better than 20 µm in central Pb-Pb collisions, and reconstruction of secondary decay vertices of charmed mesons and hyperons. The two innermost bands are made of silicon pixel detectors (SPD), the two intermediate of silicon drift detectors (SDD) and the two outermost of double-sided silicon strip detectors (SSD). The two innermost layers are fundamental for the determination of the position of the primary vertex and the impact parameter of secondary tracks from weak decays of strange, charm and beauty particles. The two outer layers of the ITS are crucial for the connection of tracks from the ITS to the TPC. They also provide $\mathrm{d}E/\mathrm{d}x$ information to assist particle identification for low-momentum particles [170, 232].

(TPC) The Time Projection Chamber is the main device for particle reconstruction and identification. Particles traversing the gas volume of the TPC ionize the gas along their path and can be tracked and identified by their specific energy loss. The TPC is placed between an inner radius of 85 cm and an outer radius of 250 cm. With a length of 500 cm the TPC has a total active volume of 88 m^2 filled with a $\mathrm{Ne/CO_2/N_2}$ (85.7/9.5/4.8%) gas mixture, which makes it the largest TPC ever built. The two end caps are instrumented by two rings with 18 multi-wire proportional chambers (MWPC) with segmented readout pads, which gives 557.568 individual readout channels in total. The TPC provides tracking of charged particles in a p_{T}-range of 0.2 - 100 GeV/c with a spatial resolution in the transverse plane of 800 µm for the inner readout chambers (IROC) and 1100 µm for the outer readout chambers (OROC). The resolution along the beam axis is 1250 µm. After a truncation, the distribution of the characteristic energy loss at a given momentum is almost normal distributed with a width of about $\sigma_{\mathrm{TPC}} \approx 5\%$ [233–235]. For analysis purposes, the TPC signal $\mathrm{d}E/\mathrm{d}x_{\mathrm{meas}}$ is usually expressed as the deviation to the expected energy loss $\mathrm{d}E/\mathrm{d}x_{\mathrm{exp}}$ in units of σ_{TPC},

$$N_{\sigma,\mathrm{TPC}} = \frac{\mathrm{d}E/\mathrm{d}x_{\mathrm{meas}} - \mathrm{d}E/\mathrm{d}x_{\mathrm{exp}}}{\sigma_{\mathrm{TPC}}} \ . \tag{5.2}$$

(TRD) The Transition Radiation Detector is placed at a radial position between the TPC and TOF. Since only electrons produce transition radiation at momenta below 100 GeV/c, the TRD provides additional separation between electrons and other particles even at higher momenta above 1 GeV/c [236]. More details can be found in section 6.2.1.

(TOF) The Time-Of-Flight detector is a multi gap resistive plate chamber (MRPC) placed at a radius of 370 cm from the interaction region. It consists of 1638 double gap MRPC strips with an intrinsic time resolution better than 40 ps, which gives a time resolution of $\sigma_{\mathrm{TOF}} \approx 85$ ps, including the resolution of the start time measurement by the T0 detector ($\sigma_{\mathrm{T0}} = 50$ ps). In conjunction with the momentum and track length measured by the tracking detectors, the time of flight between the intersection point and the TOF detector is used to separate particles by their mass in a momentum range of 0.5 - 5 GeV/c [237]. Analogously to the energy loss

measurement in the TPC, the time-of-flight information t_{meas} is expressed as the deviation to the expected time of flight t_{exp} in units of σ_{TOF},

$$N_{\sigma,\text{TOF}} = \frac{t_{\text{meas}} - t_{\text{exp}}}{\sigma_{\text{TOF}}} \ . \tag{5.3}$$

(V0) The V0 detector is composed of two arrays of scintillator tiles covering the full azimuth at forward rapidity. The C-side component (V0-C) is placed 90 cm away from the interaction point, the A-side component (V0-A) 340 cm, which results in a pseudorapidity coverage of $-3.7 < \eta < -1.7$ (V0-C) and $2.8 < \eta < 5.1$ (V0-A), respectively. The V0 detectors are mainly used for multiplicity measurements, centrality determination and as a reference detector for anisotropic flow measurements [238].

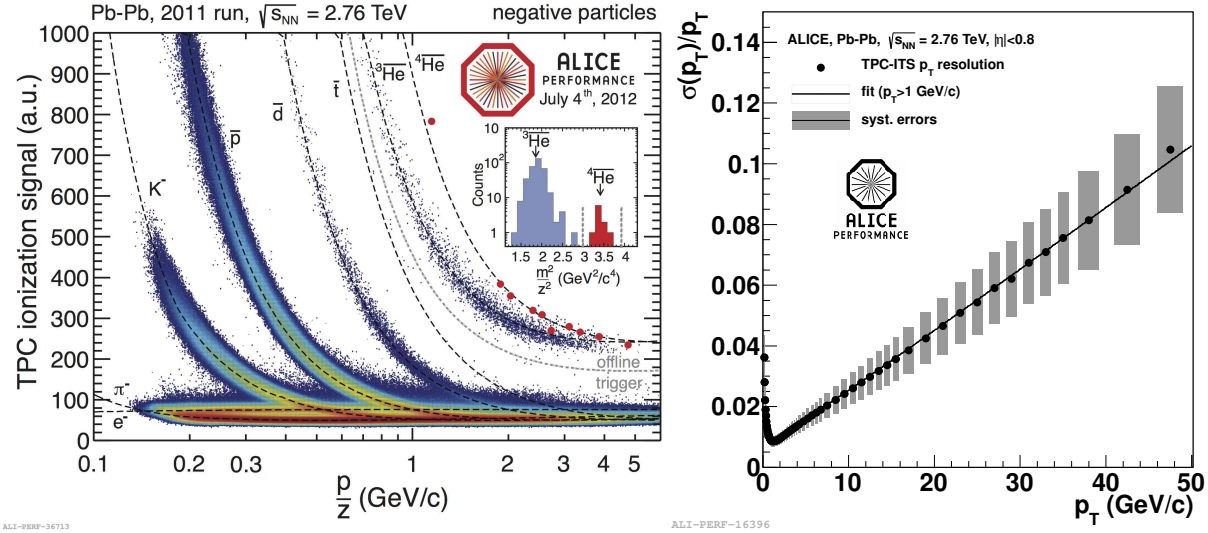

Figure 5.3: (left) TPC signal as a function of the momentum over charge ratio p/Z [234]. (right) Relative p_{T} resolution for TPC-ITS combined tracks as a function of p_{T} [239].

The event reconstruction with ALICE is described in [206]. Figure 5.3 (right) shows the relative p_{T} resolution for the combined track reconstruction using ITS and TPC. Both detectors are aligned with respect to each other to the level of a few hundred millimeters using cosmic-ray and proton-proton collision data [240]. The p_{T} resolution is better than 4% for tracks with a transverse momentum below 10 GeV/c. The best resolution is reached at about 1.5 GeV/c with about 1%. Towards smaller momenta, the resolution deteriorates due to multiple scattering in the detector material, towards larger momenta, the tracks become straight and the uncertainty on the measurement of the radius of curvature increases. For comparison, the best momentum resolution of the ATLAS experiment of about 4% is reached at 20 GeV/c and deteriorates rapidly towards smaller momenta to about 10% at 5 GeV/c. On the other hand, the ATLAS momentum resolution is smaller than 5% up to momenta of 200 GeV/c [241].
ALICE is the dedicated heavy-ion experiment at the LHC, designed to study identified particles at small momenta, where thermal and hydrodynamic behavior is visible. Figure 5.3 (left) illustrates the particle identification capabilities of the ALICE TPC. The characteristic energy loss bands for electrons, pions, kaons and protons, but even for bound systems like deuterium, tritium, ^{3}He and ^{4}He are clearly separated over a broad momentum range.

6. A bidimensional approach for electron identification with the ALICE Transition Radiation Detector

The ALICE Transition Radiation Detector (TRD) provides reconstruction of charged particle trajectories and electron identification via their specific energy loss due to ionization and transition radiation at momenta above 1 GeV/c [236]. In combination with the tracking and particle identification capabilities of the Inner Tracking System (ITS) and the Time Projection Chamber (TPC), it gives access to the dilepton continuum and the production of light and heavy vector-mesons such as the J/ψ meson, which is a key observable for deconfinement (cf. [242–250]). In addition, the ALICE TRD is able to provide trigger information on single electrons, electron-positron pairs or jets [251].
Transition radiation detectors make use of the threshold like onset of transition radiation production for charged particles traversing a stratified material. For momenta below 100 GeV/c, only electrons produce detectable transition radiation, which allows to separate them efficiently from the hadronic background produced in hadron collisions. Besides heavy-ion physics with ALICE, transition radiation detectors are also used in various other fields of high energy physics [252, 253], for example by the ATLAS experiment [254, 255] and by the AMS experiment installed at the International Space Station (ISS) [256, 257].
The first approach for electron identification with the ALICE TRD was a likelihood method based on the accumulated energy loss [258]. Compared to the TPC ionization energy loss measurement, this method benefits from an improved separation of the electron and the hadron characteristic energy loss due to the additional transition radiation for electrons. By its design, the TRD provides a position sensitive measurement of the energy loss: while ionization is deposited along the whole pass of the particle, the energy deposition of TR photons is most likely happen in a small area in the close vicinity of the radiator. Thus, a significantly improved performance is expected from multivariate PID taking into account the position sensitive energy loss measurement.
This chapter presents a detailed study of a bidimensional likelihood approach, which divides the trajectory in two parts: one in regions, where transition radiation photons are expected to contribute and one, where only ionization energy loss is important. The performance of the bidimensional approach is studied in pp collisions as well as in Pb-Pb collisions and compared to other approaches.

6.1 Transition radiation production by charged particles

Charged particles can be identified via their characteristic energy loss due to electromagnetic interaction with a medium. The relevant processes are ionization, Bremsstrahlung, Cherenkov radiation and transition radiation in case of inhomogeneous media.
Transition radiation (TR) is produced by charged particles crossing the boundary between two

media of different dielectric constants. It had been predicted by Ginzburg and Frank [259] in 1946 and was first observed by Goldsmith and Jelley [260] in 1959. Its relevance for particle identification was realized in the late 70th [261, 262].

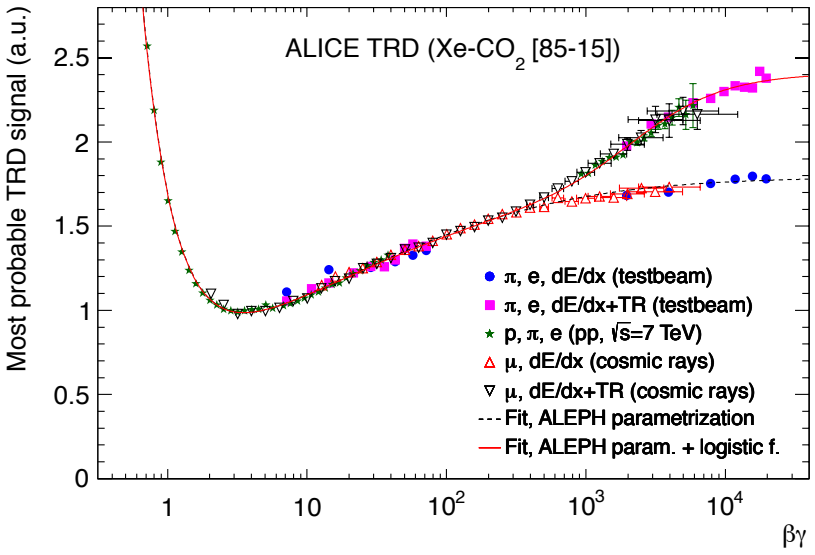

Figure 6.1: Most probable TRD signal as a function of $\beta\gamma$ measured in pp collisions at $\sqrt{s} = 7\,\text{TeV}$, testbeam and from cosmic rays [239, 263].

The probability for TR photon emission and its energy depend on the Lorentz factor γ of the incident charged particle and show a threshold-like onset at around $\gamma \approx 1000$ [253]. Figure 6.1 shows the most probable signal measured by the ALICE TRD as a function of $\beta\gamma = p/m$ of the incident particle. Data points from test beam data and cosmic ray (muons) measurements for exclusive ionization energy loss ($\mathrm{d}E_{\text{ion}}/\mathrm{d}x$) and in combination with TR ($\mathrm{d}E_{\text{ion}}/\mathrm{d}x$ +TR) are shown. Both measurements overlap at small $\beta\gamma$ and split up after the onset of TR at $\beta\gamma \approx 400$. From this measurement it is evident that in a wide momentum range from 1 - 100 GeV/c exclusively electrons and positrons can generate detectable TR[1].

The most probable energy of TR photons emitted by electrons at 1 GeV/c is of the order of 10 keV (cf. [264]) and TR photons are emitted almost collinear in the direction of flight of the particle [265]. Due to its small emission angle the TR signal overlaps with the particles' ionization energy loss, which is about 5 - 12 keV for electrons at 2 GeV/c in Xe/CO_2 [266, 267]. The emission probability for a TR photon increases with the number of crossed boundaries. A typical radiator consists of periodically arranged materials of different dielectric constants. In the ALICE TRD radiator electrons at 2 GeV/c produce 1.29 TR photons per transit on average, while 25% of the electrons do not produce TR [266]. Thus, the efficiency of the electron identification can be significantly increased by multiple independent measurements in a stack of radiators and readout detectors.

[1] At momenta above 100 GeV/c also pions have a sufficiently large $\beta\gamma$ to generate detectable TR: $m_{\pi^\pm} = 139.57\,\text{MeV}/c^2 \Rightarrow \beta\gamma = p/m > 700$ [9]

6.2 Design of the ALICE Transition Radiation Detector

6.2.1 Technical design

The ALICE Transition Radiation Detector is installed in the L3 magnet space frame at radial position ($2.9 \leq r \leq 3.7$ m) between the Time Projection Chamber and the Time Of Flight detector. The TRD layout is shown in fig. 6.2. It consists of 18 super modules with five stacks with six layers of readout chambers each. One super module and one chamber are displaced for clarity in fig. 6.2. The TRD has a length of 7 m along the beam axis, which corresponds to a pseudorapidity coverage of $|\eta| < 0.9$. It has an active area of roughly 675 m^2 with an average size of $135 \times 103 \times 12$ cm per readout chamber [236].

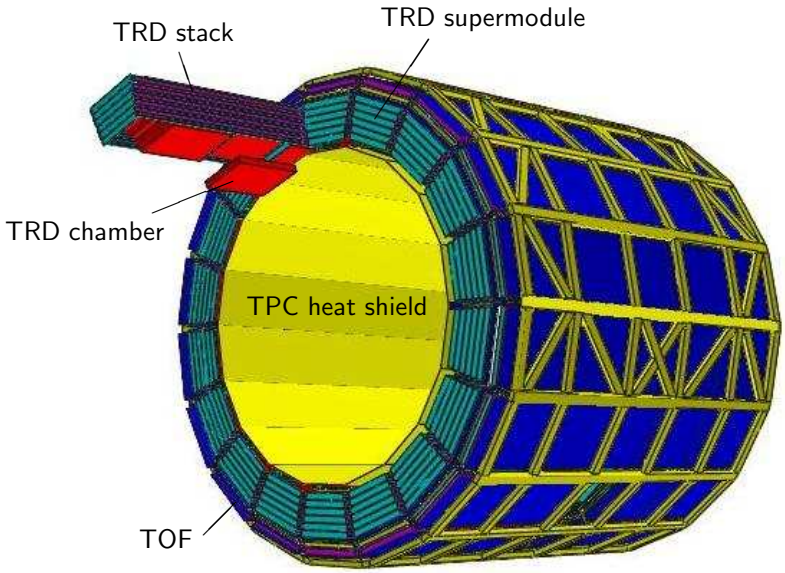

Figure 6.2: Schematic drawing of the TRD layout in the ALICE space frame. Figure taken from [227].

Figure 6.3 shows the cross section of a TRD chamber. Each readout chamber consists of a carbon fiber sandwich radiator of 48 mm thickness, a drift region of 30 mm thickness and a multi-wire-proportional-chamber of 7 mm thickness with individual pad readout. The radiator is a sandwich of polypropylene fibers and Rohacell foam. The drift volume is filled with a gas mixture of Xe/CO_2 (85%/15%). Xe has been chosen for the main gas, since its high charge number $Z = 54$ provides a high probability to absorb the produced TR photons. CO_2 is used as a quencher gas and has been chosen due to its inflammability. Further details about the design can be found in [236].

6.2.2 Principle of operation

Figure 6.3 also illustrates the principle of operation. A charged particle crosses a TRD readout chamber and ionizes the gas atoms along its path. In addition, electrons produce TR photons in the radiator. The absorption length for TR photons is about 4 mm for a 5 keV photon [269] and thus the absorption of TR photons is confined to a small region of the drift volume close to the entrance window. The electrons produced by TR and ionization drift in a field of about 700 keV/cm towards the amplification region, which is located between the cathode wires and

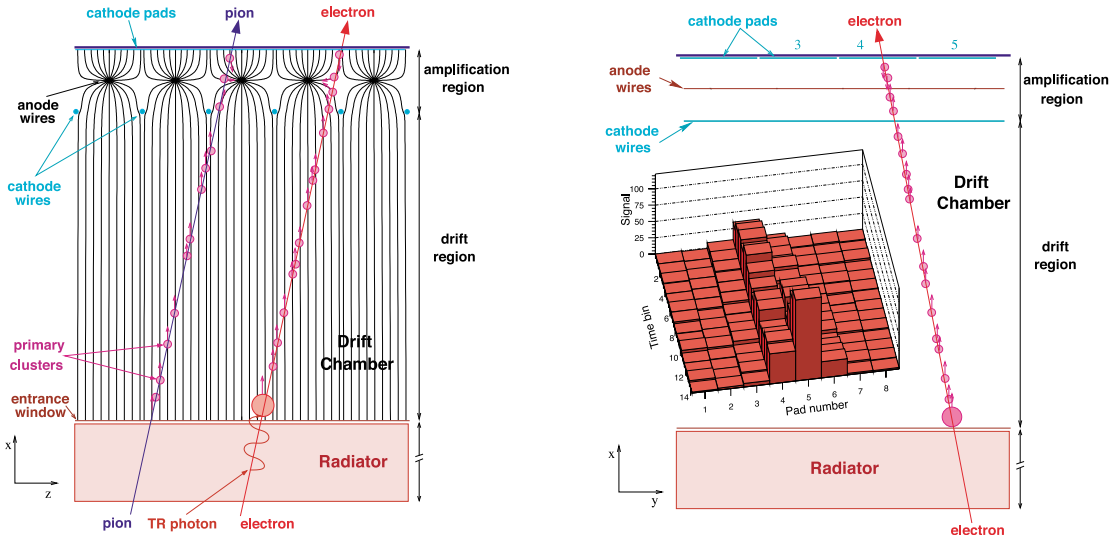

Figure 6.3: Cross section of a TRD readout chamber and schematic illustration of the principle of operation. (left) Projection in xz plane. Schematic signals produced by the energy loss of a pion and an electron. (right) Projection in the xy plane. The insert shows the distribution of the pulse height (signal) over pads and time bins [268].

the readout pad plane. The gas gain of the TRD is about 4000 [270]. The electrons create an avalanche that induces a detectable signal on the cathode plane, which is segmented in pads of a typical size of 0.7×8.8 cm [236]. The drift time of about 2 µs is sampled in 20 time bins of 100 ns. In each time bin the signal is distributed over typically two or three adjacent pads. During the reconstruction signals in adjacent pads are grouped to ***clusters***. The y position of the cluster is calculated from the charge distribution on the readout pads, while the z position is given by the center of the pad and the radial position in the drift volume is derived from the drift time. The signal induced on the read out pads is dominated by the signal of the ions. Since the mobility of ions is about 1000 times lower than that of electrons [265], the signal is spread over a longer time range than the duration of one time bin. As a consequence, the ion tail of the signal would overlap with the signal in subsequent time bins or even be interpreted as an additional cluster. These effects are significantly suppressed by a tail cancellation [271]. Finally, the particle trajectory can be reconstructed from the measured clusters along the particle path. The reconstruction process is described in detail in [272].

Since the amplification is almost linear, the pulse height of the clusters is proportional to the primary deposited charge Q and thus the energy loss ΔE. Figure 6.4 (left) shows the average pulse height as a function of the drift time for incident particles with 2 GeV/c momentum. The peak at short drift times is due to the charge deposit in the amplification region, since at early times the charge drifts from both sides to the anode wire, which is placed in the middle between the cathode wires and the cathode pad plane. The plateau for pions and electrons without TR production (dashed line) at intermediate drift times originates from the almost constant energy loss in the drift region. According to the Bethe-Bloch formula electrons have on average a higher ionization energy loss than pions [41, 265]. Due to their short mean free path in the Xe/CO_2

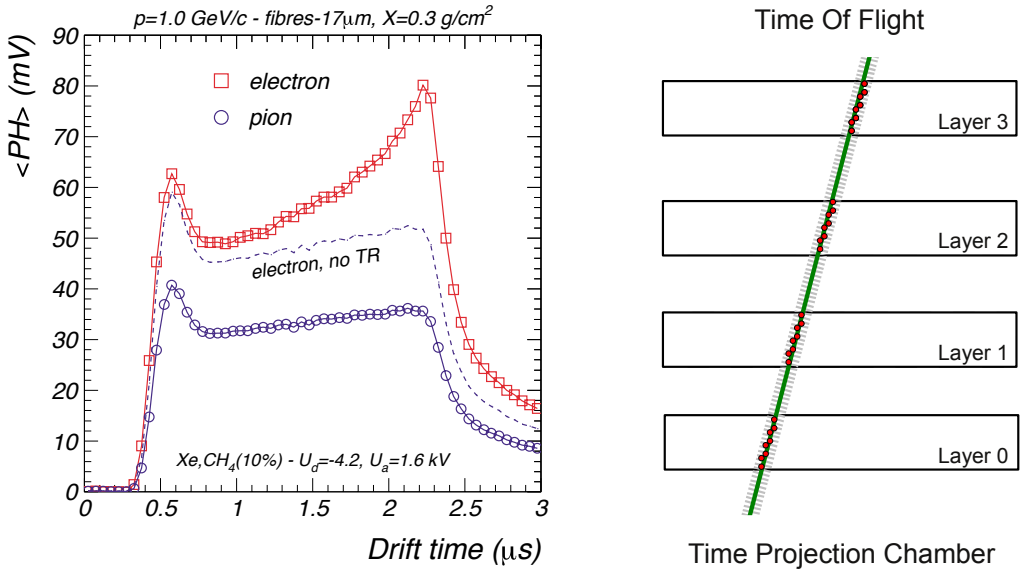

Figure 6.4: (left) Average pulse height as function of the drift time for pions and electrons with a momentum of 1 GeV/c [268]. (right) Illustration of the TRD track reconstruction.

gas mixture, TR photons are absorbed close to the radiator resulting in a characteristic peak in the average pulse height distribution for electrons at large drift times.

6.2.3 Track reconstruction and energy loss calculation

The track reconstruction in the central barrel starts with a pattern recognition procedure that combines TPC clusters at the outer wall of the TPC in such a way that they could form a track that points towards the primary vertex. Those track seeds are then further propagated towards the primary vertex and all clusters that might belong to the track are added. This procedure is followed by the primary vertex reconstruction using hits in the ITS and several Kalman filtering steps of the tracks [206, 273]. If tracks have been successfully reconstructed in ITS and TPC, the reconstructed track is extrapolated towards the TRD. The situation is sketched in fig. 6.4 (right). For simplicity, only four chambers with eight clusters each are shown. The red points denote the reconstructed TRD clusters. The TPC track extrapolation defines a search corridor (light grey dashed area) for TRD clusters that are likely to belong to the extrapolated track. The width of the search corridor is given by the expected error of the TPC track extrapolation plus a systematic error accounting for misalignment and miscalibration of the TRD readout chambers. In each layer, a local linear approximation of the track, a ***tracklet***, is calculated from the attached clusters and a filtering is applied in order to remove outliers. Finally, the track is refitted with the attached TRD tracklets and the track is extrapolated further outwards to TOF. Alternatively, TRD tracks can be reconstructed with a stand-alone tracking algorithm, which is described in [274].

The performance of the track reconstruction and cluster collection depends on the quality of the calibration and alignment of the TRD readout chambers. The conversion of drift times into radial positions requires a calibration of the start and end point of the signal (t_0 calibration) and of the drift velocity [275]. A Krypton calibration for each individual readout pad ensures

a uniform amplification within the readout chambers [276]. All chambers were aligned with respect to the TPC [276, 277].

The charge deposit along the trajectory is sampled in eight/seven slices. After the 2010 pp data taking, the drift voltage was increased and the number of sampled time bins reduced. In addition, the implementation was changed for technical reasons to seven slices (Pb-Pb data in this work), but the change was not applied to older reconstructions (pp data in this work). The charge deposit $\mathrm{d}q_i/\mathrm{d}l$ per unit length in slice i is given by

$$\frac{\mathrm{d}q_i}{\mathrm{d}l} = \frac{\int_{x^i_{\mathrm{min}}}^{x^i_{\mathrm{max}}} q(x)\mathrm{d}x}{\sin(\phi)\cos(\theta)\mathrm{d}x} \ , \tag{6.1}$$

where $q(x)$ is the charge deposit as a function of the radial coordinate x with

$$x^i_{\mathrm{min}} = x_{\mathrm{start}} + i\frac{x_{\mathrm{end}} - x_{\mathrm{start}}}{N_{\mathrm{slices}}} \tag{6.2}$$

defining the starting point in radial direction of the slice i and

$$x^i_{\mathrm{max}} = x_{\mathrm{start}} + (i+1)\,\frac{x_{\mathrm{anode}} - x_{\mathrm{start}}}{N_{\mathrm{slices}}} \tag{6.3}$$

defining the corresponding end point. x_{start} is the radial coordinate of the bottom of the drift volume and x_{anode} the radial position of the anode wire. ϕ and θ are the inclinations in y and z direction of the linear approximation of the particle trajectory (tracklet). A number of eight/-seven slices has been found as a performant tradeoff that provides a sufficient granularity on the one hand and on the other hand a sufficient suppression of statistical fluctuations arising from the measurement and the statistical nature of the energy loss.

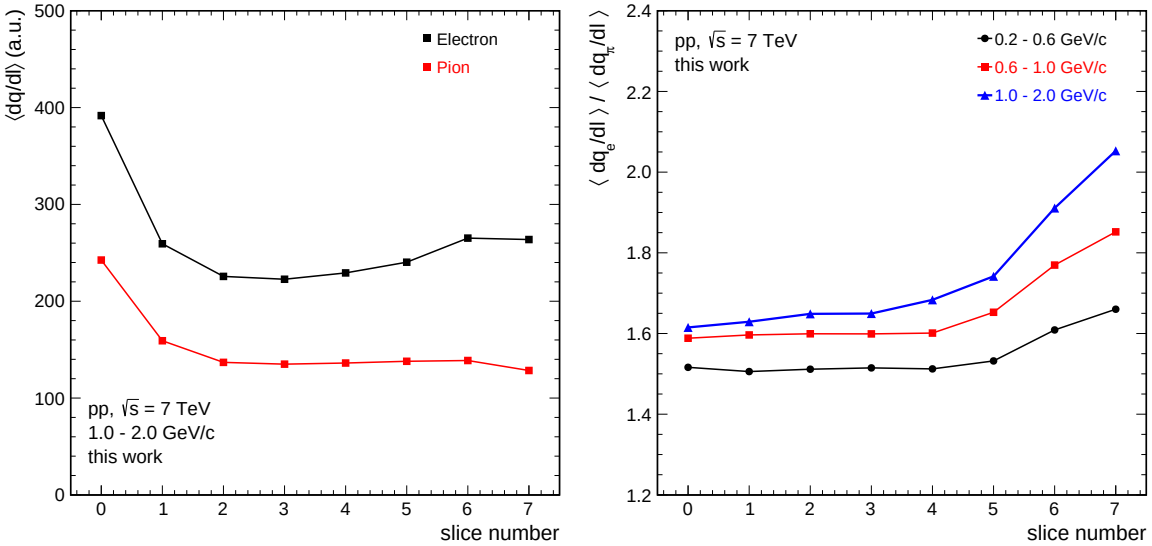

Figure 6.5: (left) Average charge deposit per unit track length $\langle \mathrm{d}q/\mathrm{d}l \rangle$ for electrons and pions in eight slices. (right) Ratio of electron to pion charge deposit for various momentum bins.

Figure 6.5 (left) shows the average charge deposit $\langle \mathrm{d}q/\mathrm{d}l \rangle$ for electrons and pions as a function of the slice number. It reproduces the characteristics of the time dependence of the average pulse height shown in fig. 6.4 (left), namely the amplification peak in the first slices and the TR peak for electrons in the last slices. Figure 6.5 (right) shows the ratio of mean electron $\langle \mathrm{d}q_\mathrm{e}/\mathrm{d}l \rangle$ and pion $\langle \mathrm{d}q_\pi/\mathrm{d}l \rangle$ charge deposit in different momentum ranges. It can be clearly seen that the electron energy loss is by about a factor of 1.5 - 1.6 larger than for pions in the first slices corresponding to early drift times. With incrementing slice number the ratio increases, while the relative change depends on the momentum. The increase is most pronounced for 1 - 2 GeV/c with an about 25% larger value in the last slice than in the first slices. For 0.6 - 1 GeV/c the ratio increases by about 15%, which can be attributed to the onset of TR production. However, even at smaller momenta the ratio is about 5% larger than in the first slice, which cannot be attributed to TR. A possible explanation are artifacts of the $\mathrm{d}q/\mathrm{d}l$ calculation in slices, e.g. a slight miscalibration of radial coordinates.

6.3 Approaches for electron identification with the ALICE TRD

6.3.1 Classical methods for particle identification

The simplest approach for particle identification neglects the drift time dependence of the charge deposit and deals with the total accumulated charge $\mathrm{d}Q/\mathrm{d}l$ per layer,

$$\frac{\mathrm{d}Q}{\mathrm{d}l} = \frac{1}{N_\mathrm{slices}} \sum_{i=0}^{N_\mathrm{slices}} \frac{\mathrm{d}q_i}{\mathrm{d}l} \ . \tag{6.4}$$

Figure 6.6 (left) shows the distribution of $\mathrm{d}Q/\mathrm{d}l$ for electrons and pions with a momentum of 1 - 2 GeV/c. The distribution for electrons peaks at an almost twice as high value than pions. Both distributions follow a Landau probability distribution [278] with an overlap towards higher $\mathrm{d}Q/\mathrm{d}l$ values. The simplest approach for electron identification follows the common strategy used in time projection chambers such as the ALICE TPC. Using a truncation, the Landau tails disappear and the distribution of $\mathrm{d}Q/\mathrm{d}l$ in the TPC becomes almost Gaussian with a width of about 5% [234]. As defined in eq. (5.2), the measured energy loss $\mathrm{d}E/\mathrm{d}x$ is usually expressed as the deviation from the expected value $\langle \mathrm{d}E/\mathrm{d}x \rangle$ expressed in units of the standard deviation of the distribution, $N_{\sigma,\mathrm{TPC}}$. Electrons can be identified with a certain efficiency and purity by selecting all particles with a band around the expected energy loss, for example a selection cut on $\left| N^\mathrm{e}_{\sigma,\mathrm{TPC}} < 3 \right|$ should contain 99.7% of all electrons.

Another approach is based on cluster counting. Figure 6.6 (right) shows the number of reconstructed TRD clusters per track. Due to the higher charge deposit, electrons produce more clusters than pions and thus electrons can be separated from pions by requiring a minimum number of clusters. A more sophisticated approach for cluster counting makes use of the fact that the deposited charge of TR clusters is larger than for ionization clusters. Thus, ionization clusters can be suppressed by choosing an appropriate cluster charge threshold. A discussion of several approaches can be found in literature [267, 279, 280]. It has been demonstrated that the ALICE TRD shows a better performance using the deposited charge approach than cluster counting [281].

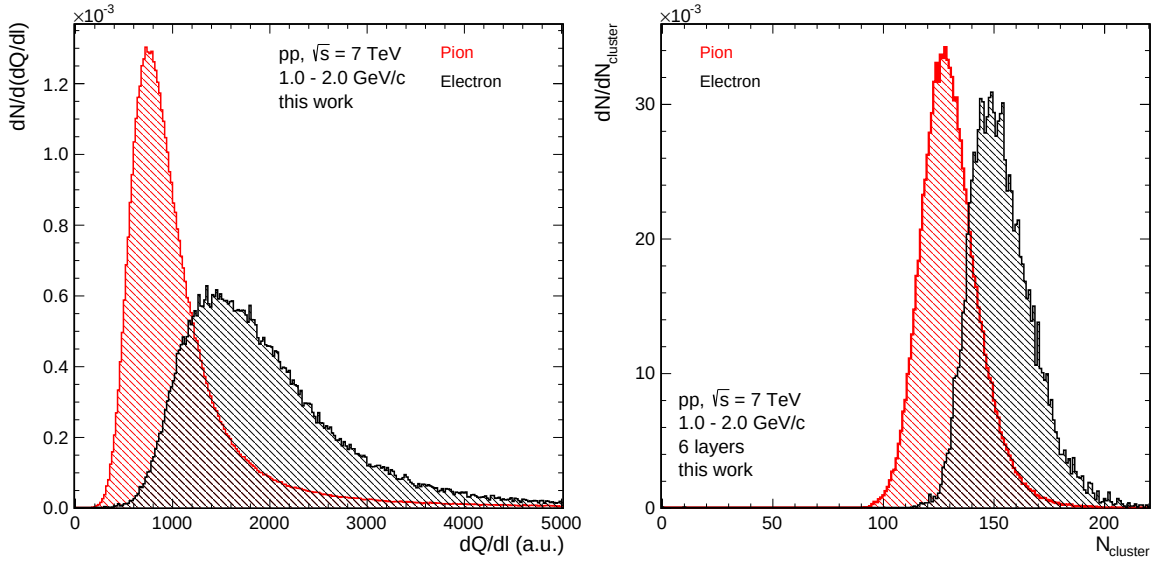

Figure 6.6: Distribution of electrons and pions for (left) the accumulated charge deposit per unit track length $\mathrm{d}Q/\mathrm{d}l$ per layer and (right) the number of clusters per track with six contributing layers.

In case of multiple, independent measurements, the most powerful approach to combine the measurements is based on a likelihood calculation. Since the TRD consists of six stacked layers of readout chambers, it provides up to six independent measurements and thus the standard approach is based on a likelihood on the total deposited charge, which is described in the following.

6.3.2 Likelihood on the total deposited charge (LQ1D)

6.3.2.1 Electron likelihood

After normalization, both distributions in fig. 6.6 (left) are considered to describe the conditional probability function $P(Q|k)$, which is the conditional probability to measure a total charge deposit $Q = \mathrm{d}Q/\mathrm{d}l$ for a particle of species k in one TRD readout chamber. The relation between $P(\mathrm{e}|Q)$ and $P(Q|\mathrm{e})$ is given by Bayes' theorem [282],

$$P(\mathrm{e}|Q) = P(Q|\mathrm{e})\frac{P(Q)}{P(\mathrm{e})} \approx P(Q|\mathrm{e})\frac{P(\mathrm{e}) + P(\pi)}{P(\mathrm{e})} \ , \tag{6.5}$$

where $P(k)$ is the prior probability to find a particle of species k. For practical reasons only electrons and pions are considered, since pions are the main source of background in hadron collisions. The prior probability is determined by the experimental conditions and does not depend on the measurement of the energy loss Q. In pp, as well as in Pb-Pb collisions, much more pions than electrons are produced such that pions have a higher prior probability than electrons ($P(\pi) \gg P(\mathrm{e})$). Taking those prior probabilities into account, P(e —Q) would always favor the pion hypothesis due to the dominant pion prior probability:

$$P(\pi) \gg P(\mathrm{e}) \Rightarrow P(\mathrm{e}|Q) \to 0 \tag{6.6}$$

Instead, the electron likelihood $L(\mathrm{e}|Q)$ shall be defined as

$$L(\mathrm{e}|Q) = \frac{P(Q|\mathrm{e})}{\sum_k P(Q|k)} = \frac{P(Q|\mathrm{e})}{P(Q|\mathrm{e}) + P(Q|\pi)} \ , \tag{6.7}$$

which does not consider the prior probabilities. The distribution for $L(\mathrm{e}|Q)$ is shown for various momentum ranges on fig. 6.7 (left). For low Q values up to 1000 $L(\mathrm{e}|Q)$ is dominated by $P(Q|\pi)$ and thus the pion hypothesis is favored. Particles with $Q \approx 1200$ have a 50% likelihood to be either an electron or pion, which corresponds to the intersection of the electron and pion distribution in fig. 6.6 (left). At larger values the electron hypothesis becomes dominant until the likelihood saturates and even slightly decreases due to the shape of the Landau tails of $P(\mathrm{e}|Q)$ and $P(\pi|Q)$. It can be seen that the electron likelihood $L(\mathrm{e}|Q)$ is not a monotonous increasing function of the deposited charge Q, which explains why a cut on a minimum likelihood can provide a better separation than a cut on $\mathrm{d}Q/\mathrm{d}l$.

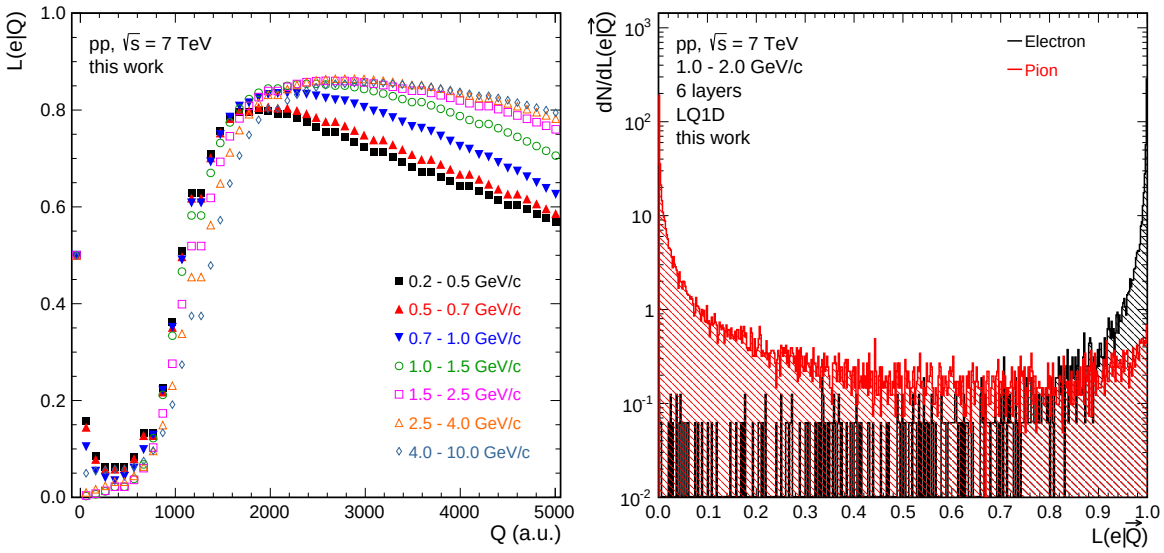

Figure 6.7: (left) Electron likelihood $L(\mathrm{e}|Q)$ as a function of the accumulated charge Q in one readout chamber. (right) Distribution of the electron likelihood $L(\mathrm{e}|\vec{Q})$ for electron and pion tracks with six contributing layers with a momentum of 1 - 2 GeV/c.

It should be noticed that the electron likelihood $L(\mathrm{e}|Q)$ defined in eq. (6.7) is not the conditional probability $P(\mathrm{e}|Q)$. In fig. 6.6 (left) the integrals of both distributions are normalized to unity, which gives the conditional probability $P(Q|\mathrm{e})$.

6.3.2.2 Combined electron likelihood

The ALICE TRD consists of six stacked individual readout chambers (cf. section 6.2.1) and thus TRD provides up to six independent measurements of the energy loss $\mathrm{d}Q/\mathrm{d}l$ per track. The combined TRD electron likelihood for a set of measurements $\vec{Q} = \{Q^0, Q^1, \ldots, Q^5\}$ with

$Q^i = \mathrm{d}Q^i \mathrm{d}l$ is defined as

$$L(\mathrm{e}|\vec{Q}) = \frac{P(\vec{Q}|\mathrm{e})}{\sum_k P(\vec{Q}|k)} \ , \tag{6.8}$$

while the combined probability for a certain particle species $P(\vec{Q}|k)$ is given by

$$P(\vec{Q}|k) = \prod_i P^i(Q^i|k) \underset{P^i=P}{=} \prod_i P(Q^i|k). \tag{6.9}$$

It is explicitly assumed that all TRD readout chambers are technically equivalent and well calibrated ($P^i = P$). Under this assumption, the probability distributions $P(Q|k)$ can be considered to be universal for all readout chambers. Figure 6.7 (right) shows the electron likelihood distribution $\mathrm{d}N/\mathrm{d}L(\vec{Q}|\mathrm{e})$ for electron and pion tracks with six contributing layers at 1 - 2 GeV/c. Electrons peak at $L(\mathrm{e}|Q) = 1$ and pions at $L(\mathrm{e}|Q) = 0$. For pions, a second peak can be observed at $L(\mathrm{e}|Q) = 1$, which is about three orders of magnitude smaller compared to the peak at $L(\mathrm{e}|Q) = 0$. The peak might be due to a small electron contamination of $\mathcal{O}(10^{-3})$ in the pion sample, which is discussed in detail in section 6.5.

6.3.2.3 Technical implementation

Details on the implementation and performance of the LQ1D method can be found in [258]. For the LQ1D approach, reference distributions for electrons and pions were obtained from tests with a prototype stack of the ALICE TRD using a test beam at the CERN Proton Synchrotron (PS) [283]. Electrons and pions were identified using a combination of a Cherenkov detector and lead glass calorimeter. The energy of the beam consisting of electrons and pions was increases in integer momentum steps from 1 to 10 GeV/c. The distributions for electrons and pions in integer were fitted with a modified Landau function. Sine the width and most probable value depend on the calibration of the detector, both parameters were adjusted such that the distributions describe the LHC data. Within this thesis, exclusively electron and pion reference samples from reconstructed V0s as described in section 6.5 are used.

6.3.3 Bidimensional likelihood on the deposited charge (LQ2D)

Within the bidimensional approach (LQ2D) the drift time dependence of the charge deposit $\mathrm{d}q/\mathrm{d}l$ shown in fig. 6.5 (left) is sampled in two input variables Q_0 and Q_1, which are defined as the accumulated charges in the first four and last four/three slices, respectively:

$$Q_0 = \sum_0^3 \frac{\mathrm{d}q_i}{\mathrm{d}l l} \qquad\qquad Q_1 = \sum_4^{N_{\mathrm{slices}}} \frac{\mathrm{d}q_i}{\mathrm{d}l} \tag{6.10}$$

Figure 6.8 shows the distribution of the input variables Q_0 and Q_1 for electrons and pions with a momentum of 1 - 1.5 GeV/c. The distributions for electrons and pions have a different shape. The pion distribution indicates two almost uncorrelated Landau tails, one towards large Q_1 values at $Q_0 \approx 500$ and another one at $Q_1 \approx 300$ towards large Q_0 values, respectively. This behavior can be understood in terms of independent fluctuations of the energy loss in the first and last slices. For electrons, Q_0 and Q_0 seem to be stronger correlated and no such tails can be observed. Due the production of transition radiation, the energy loss Q_1 is generally larger

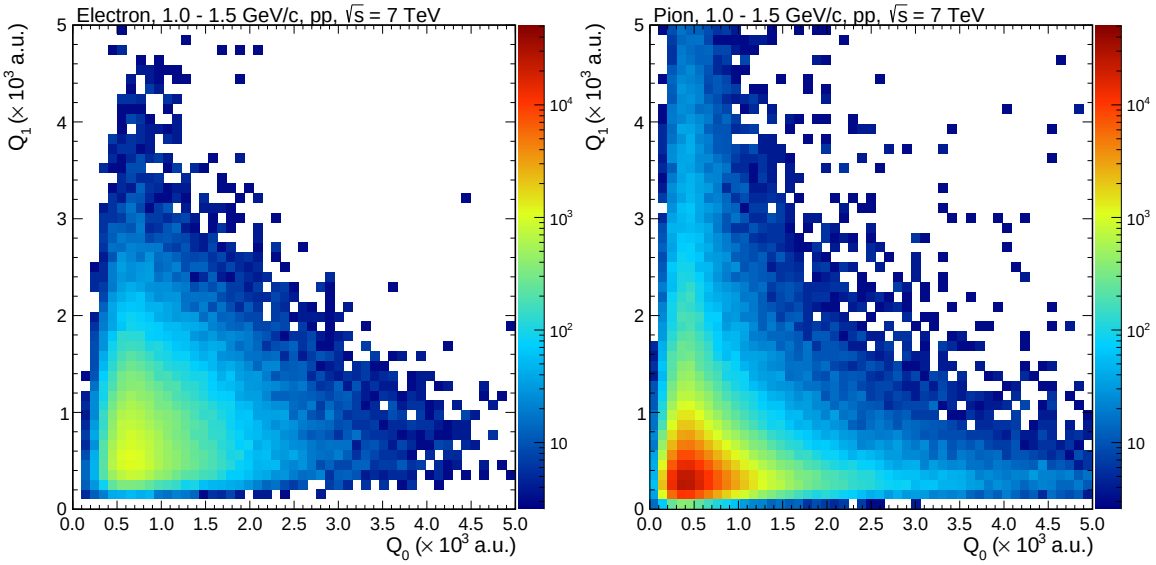

Figure 6.8: Distribution of the input variables Q_0 and Q_1 for electrons and pions.

than for pions and less sensitive to fluctuations of the ionization energy loss, which results into the observed shape.

6.3.3.1 Electron likelihood in the bidimensional approach

Analogously to the LQ1D approach, the combined probability in all TRD stacks for a for a particle of species k for a measured charge deposit $(\vec{Q_0}, \vec{Q_1})$ is given by

$$P(\vec{Q_0}, \vec{Q_1}|k) = \prod_i P(Q_0^i, Q_1^i|k) \tag{6.11}$$

and the electron likelihood is analogously defined as

$$L(\mathrm{e}|\vec{Q_0}, \vec{Q_1}) = \frac{P(\vec{Q_0}, \vec{Q_1}|\mathrm{e})}{\sum_k P(\vec{Q_0}, \vec{Q_1}|k)} \ . \tag{6.12}$$

Following the approach of the LQ1D method, the conditional probability function $P(Q_0^i, Q_1^i|k)$ can be obtained from the V0 identified reference samples for electrons and pions (cf. section 6.5). In the LQ1D method, the conditional probability distributions $P(Q|k)$ are parametrized by modified Landau distributions providing a stable description of the peaks and the tails (cf. [258]). The shape and particularly the correlation of the two dimensional distribution is more complex, thus a function that describes the data reasonably could not be found. Instead, a design based on multidimensional binary search trees [284] was developed, which is described in the following.

6.3.3.2 Multidimensional binary search trees

A multidimensional binary search tree is a data structure for storage of information to be retrieved by associative searches. They are commonly called k d-trees, where k is the dimensionality of the search space. The data is stored in a binary space-partitioning tree in which each node corresponds to a k-dimensional point. Every non-leaf node divides the space into two sub-

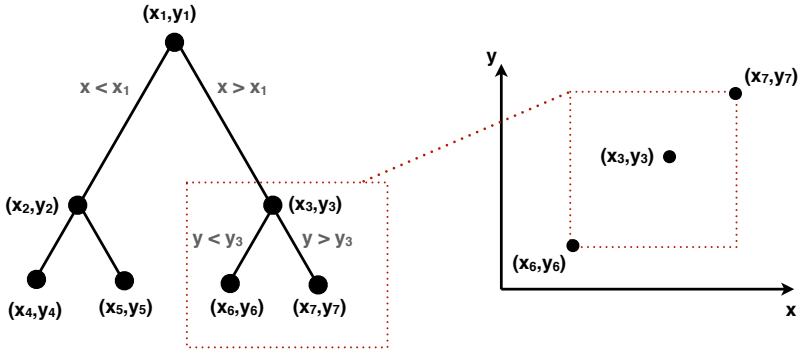

Figure 6.9: Illustration of the k d-tree data structure.

trees. Figure 6.9 shows a schematic illustration of a 2 dimensional tree. The first node (x_1, y_1) splits the tree into the left subtree with $x < x_1$ and the right subtree with $x > x_1$. The non-leaf node (x_3, y_3) defines a subspace $[x_6 \leq x \leq x_7,\ y_6 \leq y \leq y_7\ ]$ spanned between node (x_6, y_6) and (x_7, y_7). A node can be thought of as an implicitly generated hyperplane that divides the space into two parts, whereas points to the left of this hyperplane represent the left subtree of that node and points right of the hyperplane are represented by the right subtree. The hyperplane direction is chosen perpendicular to the axis with the largest spread. Roughly speaking, the k-d tree splits the data space into subtrees, while nodes at the same depth hold subtrees, which define subspaces of equal number of nodes [284].

6.3.3.3 Probability density estimation using nearest neighbor search

As every tree structure, k d-trees provide a fast search algorithm for nearest neighbors. The probability density function can estimated from the number of nearest neighbors $N_{\text{Neighbors}}$ within a maximum distance $r = \sqrt{Q_0^2 + Q_1^2}$:

$$P(Q_0, Q_1) = \frac{N_{\text{Neighbors}}}{2\pi r^2} \tag{6.13}$$

However, the nearest neighbor search algorithm requires the availability of the full data during computation, which is not favorable due to its high memory consumption. The memory consumption can be drastically reduced using an interpolator approach described in the following.

6.3.3.4 Probability density interpolation

Even though the shape of $P(Q_0, Q_1|k)$ cannot be described by a trivial function it can be approximated by a hyperplane interpolation in the vicinity of sampling points. The sampling points need to be chosen such that areas with alternating gradients are more frequently populated by sampling points than areas of approximately constant gradients. A sophisticated choice of sampling points is given by the subspaces defined by the non-leaf nodes of the k d-tree, which are small in the region of high probability $P(Q_0, Q_1|k)$ and large in the tails. The sampling points are chosen as the center of gravity of the subspaces. The following hyperplane equation is used for the interpolation:

$$P(Q_0, Q_1) = a_0 + a_1 Q_0 + a_2 Q_1 + a_3 Q_0 Q_1 + a_4 Q_0^2 + a_5 Q_1^2 \tag{6.14}$$

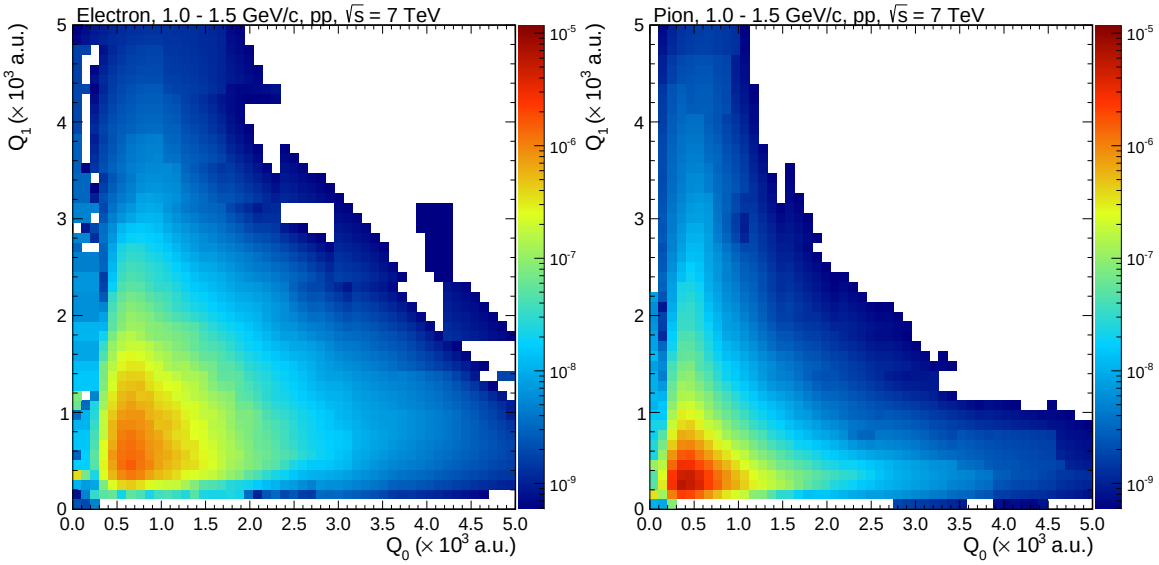

Figure 6.10: Conditional probability density function $P(Q_0, Q_1|k)$ for electrons and pions calculated with the k-d tree interpolation.

The hyperplane interpolation is calculated at each sampling point and the interpolation parameters are stored. The conditional probability $P(Q_0, Q_1|k)$ for a variable pair (Q_0, Q_1) can be estimated as follows: A nearest neighbor algorithm searches for the closest sampling point and the hyperplane interpolation using the parameters at the sampling point is evaluated at (Q_0, Q_1). The results of the k d-tree interpolation for the probability density of electron and pions is shown in fig. 6.10. The likelihood profile describes the reference data reasonably well and reproduces all features of the distribution. Small deviations can occur at the tails of the distribution close to the Q_0 and Q_1 axis, where the hyperplane fit cannot describe the asymptotic behavior $L(\mathrm{e}|\vec{Q_0}, \vec{Q_1}) \to 0$ for $Q_0 \to 0$ or $Q_1 \to 0$. In the default implementation, the value at the closest sampling point is used if the uncertainty of the interpolation is larger than the uncertainty of the node value.

6.3.4 Multivariate approaches for electron identification

The PID approaches discussed so far are referred to as linear approaches, since the decision process can be reduced to linear equations of the measured charged deposit. Non-linear approaches include decision making tools such as neural networks, random forests or boosted decision trees, just to label some of them. It has been demonstrated in various applications that non-linear statistical data modeling is a very powerful tool for complex relationships between input and output variables. The performance of those decision making tools is a potent argument compared to linear approaches, while those have substantial advantages in terms of their understandability. An approach using artificial neural networks (NN) is discussed in [285–287]. However, those approaches have fundamental drawbacks compared to linear approaches in terms of their robustness and maintenance requirements.

6.4 Electron and pion efficiency

Electrons and pions can be separated with a given efficiency by requiring that electron candidates exceed a minimum electron likelihood. Electron and pion efficiency are defined as

$$\epsilon_{\mathrm{e}} = \frac{\text{'electrons after TRD PID'}}{\text{'electrons before TRD PID'}} \qquad \text{and} \qquad \epsilon_{\pi} = \frac{\text{'pions after TRD PID'}}{\text{'pions before TRD PID'}} \ . \tag{6.15}$$

The pion efficiency can be understood in terms of the probability of misidentifying a pion as electron. The separation power is also often expressed by the pion rejection, which is the inverse of the pion efficiency $1/\epsilon_{\pi}$. A pion rejection factor of 100 means that 1% of the pion sample is misidentified as electrons.

6.4.1 Efficiency estimation

The usual approach to estimate selection efficiencies is to treat the number of selected candidates m out of a sample of N candidates as a binomially distributed variable. If ϵ_{true} is the true selection efficiency, the probability to select m candidates is given by

$$P(m, \epsilon, N) = \frac{N!}{m!(N-m)!}\epsilon^{m}(1-\epsilon)^{N-m} \quad [288, 289] \ . \tag{6.16}$$

The best estimator for the efficiency is given by

$$\hat{\epsilon} = \frac{m}{N} \ , \tag{6.17}$$

which is the value that maximizes the log-likelihood function $\ln L(\epsilon)$.
Consequently, the electron and pion efficiency for a given threshold value $L(\mathrm{e}|\vec{Q})_{\epsilon_{\mathrm{e}}}$ can be calculated from the likelihood distribution $\mathrm{d}N/\mathrm{d}L(\vec{Q}|\mathrm{e})$ as

$$\epsilon_{\mathrm{e},\pi} = \frac{\int_{L(\mathrm{e}|\vec{Q})_{\epsilon_{\mathrm{e}}}}^{1} \mathrm{d}N_{\mathrm{e},\pi}/\mathrm{d}L(\mathrm{e}|\vec{Q})}{\int_{0}^{1} \mathrm{d}N_{\mathrm{e},\pi}/\mathrm{d}L(\mathrm{e}|\vec{Q})} \ . \tag{6.18}$$

6.4.2 Uncertainty of the efficiency estimate

In the most common approach for binomial confidence intervals, the distribution of estimators $\hat{\epsilon}$ is approximated by a normal distribution, which is usually justified by the central limit theorem. Assuming that N is constant and applying Gaussian error propagation with the uncorrelated random variables m and $N-m$, we obtain

$$\sigma_{\hat{\epsilon}}^{2} = \left(\frac{\partial\hat{\epsilon}}{\partial m}\sigma_{m}\right)^{2} + \left(\frac{\partial\hat{\epsilon}}{\partial(N-m)}\sigma_{N-m}\right)^{2} \tag{6.19}$$

$$= \left(\frac{N-m}{N^{2}}\sqrt{m}\right)^{2} + \left(\frac{m}{N^{2}}\sqrt{N-m}\right)^{2} \tag{6.20}$$

$$= \frac{m(N-m)}{N^{3}} \ . \tag{6.21}$$

The estimator for the standard deviation $\sigma_{\hat{\epsilon}}$ is then given by

$$\sigma_{\hat{\epsilon}} = \sqrt{\frac{\hat{\epsilon}(1-\hat{\epsilon})}{N}} = \sqrt{\frac{m(1-m/N)}{N^2}} \; . \tag{6.22}$$

It follows that

$$\hat{\epsilon} + \sigma_{\hat{\epsilon}} \leq 1 \qquad \text{and} \qquad \hat{\epsilon} - \sigma_{\hat{\epsilon}} \leq 0 \; , \tag{6.23}$$

which implies that the standard deviation vanishes, if the efficiency becomes zero ($m=0$) or one ($m=N$). It is important to notice that $\hat{\epsilon}=1$ and $\sigma_{\hat{\epsilon}}=0$ do not necessarily mean that the true efficiency ϵ_{true} is one and that the true standard deviation of the estimator is zero, but rather that both quantities are the most probable values for the given sample. It follows that the estimate for $\sigma_{\hat{\epsilon}}$ given by Equation (6.22) is rather useless for small or large efficiencies [290].

Usually, efficiencies are estimated from Monte Carlo simulations or from independent data samples, such that one is more interested in confidence intervals for the distribution of efficiency estimators from different data samples. In particular, the accuracy of the estimated efficiency depends on the size of the data sample N. Consequently, we consider $P(\epsilon|m,N)$ as the conditional probability to find m candidates for a data sample with N candidates and selection efficiency ϵ. In the Bayesian approach, the posterior probability density for ϵ is given by

$$P(\epsilon|m,N) = \frac{P(m|\epsilon,N)P(\epsilon)}{P(m|N)} \tag{6.24}$$

with

$$P(m|N) = \int_0^1 P(m|\epsilon,N)\mathrm{d}\epsilon \; . \tag{6.25}$$

Assuming that we have no prior knowledge about the prior probability of the efficiency, $P(\epsilon)$ can be chosen uniform between zero and one, and we obtain

$$P(\epsilon|m,N) = \frac{\Gamma(N+2)}{\Gamma(m+1)\,\Gamma(N-m+1)}\epsilon^m\epsilon^{N-m} \; [289,290] \; . \tag{6.26}$$

Figure 6.11 (left) shows the conditional probability density function $P(\epsilon|m,N)$ for different values for N and m. The distribution for $m=N$ has a tail towards $\epsilon \leq 1$, which implies a non-zero probability that the true efficiency is smaller than one. For $m<N$, the distributions are asymmetric with stronger tails towards smaller efficiencies. As the N increases, the distributions become sharper, which implies that the estimates for the efficiencies become more accurate. Instead of using binomial errors, the uncertainty of the efficiency estimator $\hat{\epsilon}$ can be expressed by the upper and lower limits of the 68.3% confidence interval of the conditional probability density function eq. (6.26). This functionality is provided by the ROOT class *TEfficiency* [291]. Figure 6.11 (right) shows the upper and lower uncertainty divided by the binomial errors defined in eq. (6.22) for different values for N. It can be seen that the Bayesian uncertainties are symmetric at $\epsilon=0.5$. For $\epsilon<0.5$, the upper uncertainties are generally larger and the lower uncertainties smaller than binomial errors. Deviations to binomial errors diverge as $\epsilon \to 0$. At small efficiencies, the lower uncertainty is much smaller than the upper uncertainty, since the

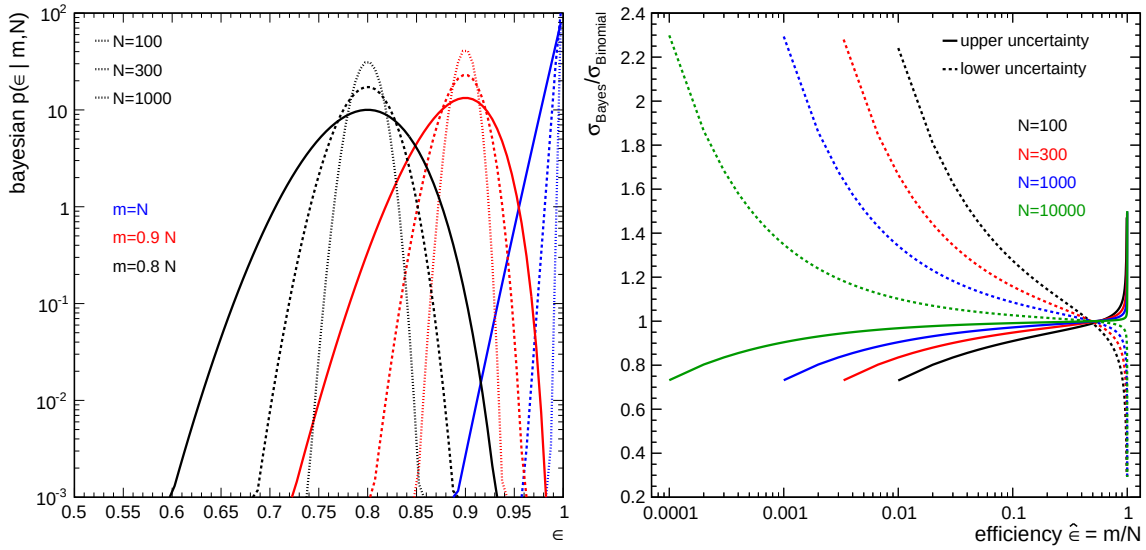

Figure 6.11: (left) Bayesian conditional probability distribution $P(\epsilon|m,N)$ for different values for N and m. (right) Comparison of Bayesian uncertainties with binomial uncertainties for different values of N and $\hat{\epsilon}=m/N$.

efficiency is confined by zero. If $m=1$, which gives $\epsilon=1/N$, binomial errors are about 50% smaller than Bayesian errors.

The ALICE TRD is designed for a pion efficiency of 1% at 90% electron efficiency. From the considerations made above it is evident that deviations between binomial and Bayesian confidence intervals can only be neglected for efficiencies around 50%. For expected pion efficiencies on the order of 1% those effects cannot be neglected and thus Bayesian confidence intervals are used within this thesis.

6.5 Reference track selection

This performance analysis is based on Pb-Pb and pp collisions recorded in 2010. Figure 6.12 shows a schematic cross section of the ALICE experiment during the 2010 data taking with seven TRD super modules (yellow) installed. In 2011 and 2012, three more super modules were installed each. The detector will be completed during the first long shut down, which started in February 2013.
Reference samples for electrons and pions can be obtained from photon conversions in the detector material to e^+e^- and K^0_s decays into $\pi^+\pi^-$. The reconstruction of secondary neutral vertices allows to identify neutral particles and their decay daughters just by topological cuts, which yields rather clean samples of electrons and pions without any particle identification. The purity of the samples can be checked and further enhanced using the dE/dx information of the TPC or the TOF measurement. This section discusses the selection of reference samples, with particular emphasis on the impact of the purity in the samples on the measured TRD PID performance.

period	collision type	$N_{\text{electrons}}$	N_{pions}
LHC10e	pp, $\sqrt{s} = 7\,\text{TeV}$	7×10^5	2×10^6
LHC10h	Pb-Pb, $\sqrt{s_{\text{NN}}} = 2.76\,\text{TeV}$	1×10^5	1×10^6

Table 6.1: Data sets and corresponding number of electron and pion reference tracks with a momentum of 0.2 - 10 GeV/c.

6.5.1 Topological cuts

The reconstruction of secondary decay vertices is described in detail in [293, 294] (for photons cf. section 8.2). While the K^0_{s} has a decay length of 2.68 cm [9], photons are stable particles that can convert far away from the primary vertex. Dielectron tracks of those converted photons can have a slightly different angles of incidence in the TRD compared to primary tracks. In order to select tracks with similar properties compared to primary tracks, it is required that the distance of closest approach (dca) to the primary vertex in xy direction (bending plane) is smaller than 5 cm and along the beam axis (direction of magnetic field) smaller than 10 cm. It was checked that a further tightening of the dca cut has no significant impact on the results. Reference tracks are required to have a TRD prolongation with at least four tracklets. Table 6.1 shows the number of electron and pion reference tracks with a momentum of 0.2 - 10 GeV/c in Pb-Pb and pp collisions after topological cuts.

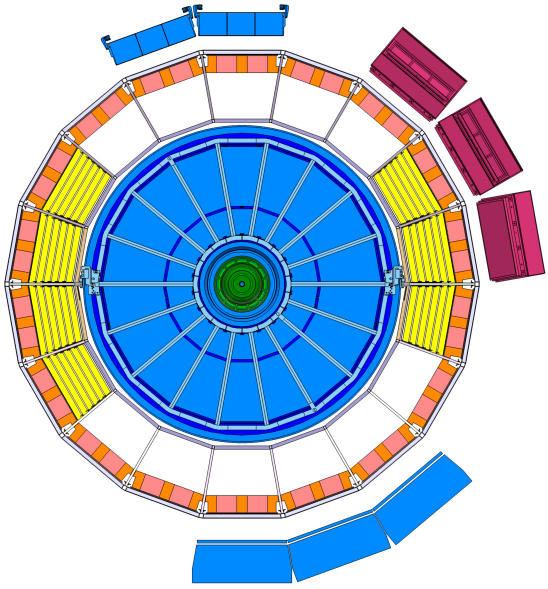

Figure 6.12: Schematic cross section of the ALICE experiment showing the TRD (yellow) installation status during the 2010 data taking [292].

6.5.2 Energy loss measurement in the TPC

Figure 6.13 (left) shows the distribution of $N_{\sigma,\text{TPC}} = (\text{d}E/\text{d}x_{\text{meas}} - \text{d}E/\text{d}x_{\text{exp}})/\sigma_{\text{TPC}}$ for V0 identified electrons and pions, where $\text{d}E/\text{d}x_{\text{meas}}$ is the measured energy loss, $\text{d}E/\text{d}x_{\text{exp}}$ is the expected energy loss and σ_{TPC} is the standard deviation of the $\text{d}E/\text{d}x$ distribution. Electrons are expected to be follow a Gaussian distribution around zero, while the energy loss of pions is expected to be much smaller, since the Bethe-Bloch curves for both species are well separated in the momentum range of 1 - 2 GeV/c. The V0 tagged electron sample shows a double peak structure with a large peak at zero and an about one order of magnitude smaller second peak at -6σ. The pion distribution peaks at about -6σ. Comparing the distribution for V0 tagged electrons to the distribution for pions, the smaller peak of the electron distribution can be identified as a significant contamination of pions in the electron sample. In addition, pions have a strong, asymmetric tail towards the electron distribution.

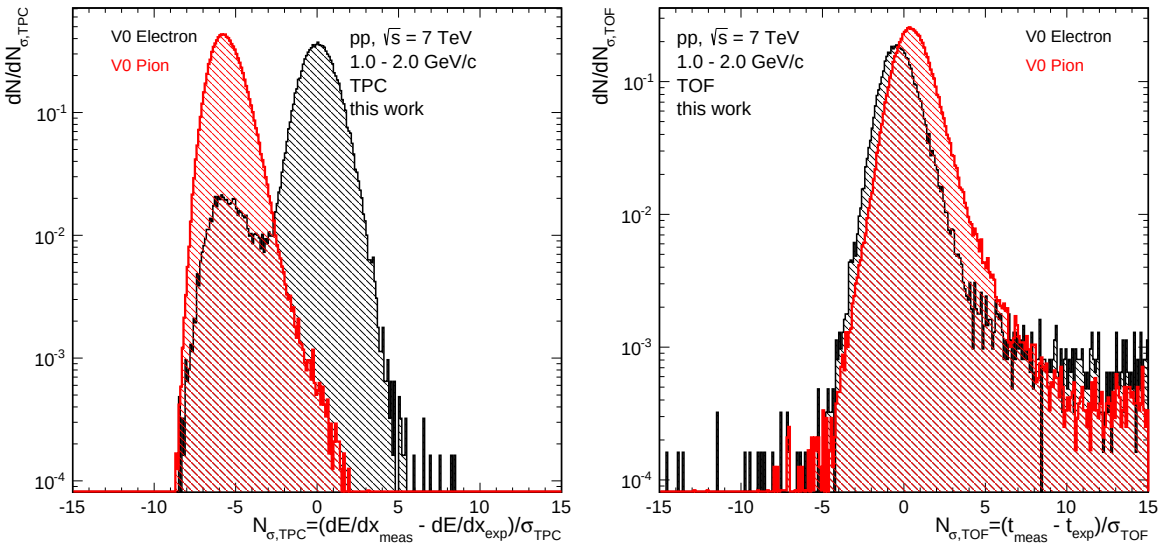

Figure 6.13: (left) $N^{\mathrm{e}}_{\sigma,\mathrm{TPC}}$ and (right) $N^{\mathrm{e}}_{\sigma,\mathrm{TOF}}$ for V0 identified electrons and pions at 1 - 2 GeV/c.

6.5.3 Time of flight measurement with TOF

Figure 6.13 (right) shows the distribution of $N_{\sigma,\mathrm{TOF}} = (t_{\mathrm{meas}} - t_{\mathrm{exp}})/\sigma_{\mathrm{TOF}}$ for electrons and pions, where t_{meas} is the measured time of flight, t_{meas} is the expected time of flight for electrons and σ_{TOF} is the standard deviation. The time of flight depends on the velocity $\beta = p/E$, which implies that electrons are faster than pions at the same given momentum due to their smaller mass. It can be seen that both distributions overlap, since the time of flight becomes similar as the momentum increases, since the rest energy becomes negligible. Consequently, unlike in the $\mathrm{d}E/\mathrm{d}x$ distribution measured with the TPC, the pion contamination in the electron sample cannot be seen as a separate peak. In addition, both distributions show a large tail towards positive values. Interestingly, the distribution of V0 tagged electrons is shifted from zero toward negative values. The reason is that those electrons do not come from the primary vertex, but from photon conversions, which can happen far away from the primary vertex. Those electrons have a shorter time of flight, since photons travel on straight trajectories at the speed of light.

6.5.4 Impact of contamination on the pion and electron efficiency

A pion contamination in the electron sample gives a contribution at small values in the electron likelihood distribution for electrons, which results in a smaller electron efficiency compared to the true electron efficiency. In addition, an electron contamination in the pion sample contributes at large values in the electron likelihood distribution for pions and results into a higher pion efficiency compared to the true efficiency.
Quantitative estimates for the purity of the sample can be determined within a Monte Carlo simulation. Without particle identification using the TPC or TOF the electron sample has a contamination of about 5% and the pion sample contains an electron contamination of about 0.1 - 0.3%. The impact of that contamination shall be clarified with a simple calculation. It is assumed that the true pion efficiency is 1% at 90% electron efficiency. The application of TRD electron identification removes 10% of the electrons and 99% of the pion contamination in the

electron sample, which yields

$$\epsilon_{\mathrm{e}}^{\mathrm{obs}} = \frac{90\% + 5\% \cdot (1 - 99\%)}{100\% + 5\%} \approx 85.8\% \tag{6.27}$$

instead of $\epsilon_{\mathrm{e}}^{\mathrm{true}} = 90\%$. Analogously, the pion efficiency comes out to

$$\epsilon_{\pi}^{\mathrm{obs}} = \frac{1\% + 90\% \cdot 0.3\%}{100\% + 0.3\%} \approx 1.3\% \tag{6.28}$$

instead of $\epsilon_{\pi}^{\mathrm{true}} = 1\%$. Thus, an electron contamination of 0.3% in the pion sample leads to a relative bias of almost 30% in the pion efficiency. In addition, the measured electron efficiency is much smaller and evaluating the pion efficiency at $\epsilon_{\mathrm{e}}^{\mathrm{obs}} = 90\%$ would even give a much larger pion efficiency.

6.5.5 Application of TOF and TPC particle identification

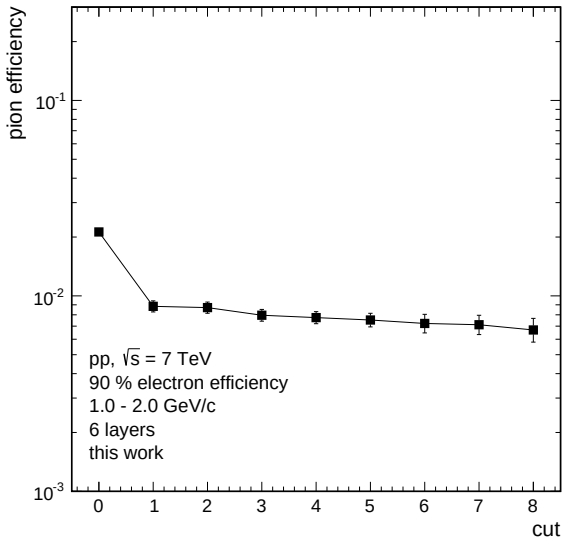

	Electrons		Pions	
cut	$N^{\mathrm{e}}_{\sigma,\mathrm{TPC}}$	$N^{\mathrm{e}}_{\sigma,\mathrm{TOF}}$	$N^{\pi^\pm}_{\sigma,\mathrm{TPC}}$	$N^{\pi^\pm}_{\sigma,\mathrm{TOF}}$
0	-	-	-	-
1	[-5,5]	-	[-5,5]	-
2	[-5,5]	[-5,5]	[-5,5]	[-5,5]
3	[-4,4]	[-4,4]	[-4,4]	[-4,4]
4	[-3,3]	[-3,3]	[-3,3]	[-3,3]
5	[-1,3]	[-3,3]	[-3,1]	[-3,3]
6	[0,2]	[-3,3]	[-2,0]	[-3,3]
7	[0,2]	[-2,2]	[-2,0]	[-2,2]
8	[0,2]	[-1,1]	[-2,0]	[-1,1]

Figure 6.14: Pion efficiency at 90% electron efficiency for various cuts on TPC and TOF PID. Cut 5 was chosen as standard cut.

The purity of the V0 tagged electron sample can be further increased by applying TPC and TOF particle identification. In this momentum range already for electron candidates with $\mathrm{d}E/\mathrm{d}x$ value smaller than 5 σ the contamination is rather small. If the contamination would be exactly known the measured electron and pion efficiencies could be corrected for contamination. However, the agreement between the experimentally observed $\mathrm{d}E/\mathrm{d}x$ distributions and the distributions in Monte Carlo is not perfect and deviations will be most pronounced if the contaminations is small, in particular if the applied cuts are tight. In the following, the impact of contamination on the pion efficiency of the LQ2D method shall be investigated by a variation of the $\mathrm{d}E/\mathrm{d}x$ and tof cut from open cuts to tight cuts.

Figure 6.14 shows the pion efficiency for different cuts on the TPC $\mathrm{d}E/\mathrm{d}x$ and TOF time measurement. The cut values are listed in the table right of fig. 6.14. The PID cuts are applied

in addition to the topological V0 cuts. Cut 0 are the default topological cuts without any additional particle identification using TPC or TOF. Cut 1 to cut 8 are selection cuts, which are expected to increase the purity of the selected electron and pion samples subsequently. Asymmetric cuts for $N_{\sigma,\mathrm{TPC}}$ are applied, since the electron and pion distribution overlap at negative values.
It can be seen that the pion efficiency changes significantly if a TPC PID cut of $\pm 5\,\sigma$ is applied. According to fig. 6.13 (left) it removes the dominant fraction of the pion contamination in the electron sample and vice versa. Additional cuts on the TOF PID and a further tightening of the TPC slightly decreases the pion efficiency until it saturates at cut 5. Hereafter, only the statistical uncertainties increase such that cut 5 was chosen as the standard cuts for the following performance studies.

6.6 Impact of TRD track properties on the PID performance

The quality of the TPC track prolongation within the TRD is described by the reduced χ^2_{red} of the fitted TRD tracklets, which shall be defined as

$$\chi^2_{\mathrm{red}} = \frac{1}{N_{\mathrm{layer}}} \sum_{i}^{N_{\mathrm{layer}}} \frac{(y^i_{\mathrm{track}} - y^i_{\mathrm{tracklet}})^2}{{\sigma^i_y}^2} \,, \tag{6.29}$$

where y^i_{track} is the position of the tracklet and y^i_{track} is the position of the prolongated track at the radial position of the tracklet x^i_{tracklet} with the corresponding error σ^i_y. The estimated error is derived from the propagated covariance of the TPC track and includes a systematic error in order to account for misalignment and miscalibration of the TRD. Since the track is only prolongated and the TRD is not changing the track the number of degrees of freedom is equal to the number of tracklets.

As described in section 6.2.3 the cluster collection for a given track prolongation depends on the estimated tracklet position and its covariance defining a search corridor for the cluster attachment. Consequently, the cluster attachment and thus also the $\mathrm{d}E/\mathrm{d}x$ calculation depend on the quality of the reconstructed track.

6.6.1 χ^2_{red} dependence in 2010 pp data

Figure 6.15 (left) shows the χ^2_{red} distribution for electrons and pions in pp collisions recorded in 2010. It can be seen that the χ^2_{red} distribution for electrons has larger tails than for pions, which is an artifact of the cluster attachment in the TRD track reconstruction. After the first reconstruction passes, the cluster attachment was changed and first applied for the reconstruction of 2010 Pb-Pb data (cf. section 6.6.3).

Figure 6.15 (right) shows the most probable $\mathrm{d}Q/\mathrm{d}l_{\mathrm{mpv}}$ and mean $\langle \mathrm{d}Q/\mathrm{d}l \rangle$ charge deposit as a function of χ^2_{red}. While the most probable value is almost independent of χ^2_{red}, $\langle \mathrm{d}Q/\mathrm{d}l \rangle$ shows a significant increase at large values for χ^2_{red}. The $\mathrm{d}Q/\mathrm{d}l$ distributions for both particle species are shown in figs. 6.16 (left) and 6.16 (right) for $\chi^2_{\mathrm{red}} < 5$ and $\chi^2_{\mathrm{red}} > 5$. The distributions for $\chi^2_{\mathrm{red}} > 5$ have less entries at the most probable value and much more entries in the tails compared to small χ^2_{red} values, which explains the observed increase of the mean value. Since χ^2_{red} is a

measure for deviations between track extrapolation and TRD clusters i.e. tracklets it is strongly connected with the width of the search corridor during the cluster attachment. In particular, a larger χ^2_{red} value corresponds to a larger search corridor and vice versa. Thus, a large χ^2_{red} value coincidences on average with a larger amount of collected charge in case of high detector occupancy. This artifact of the track reconstruction leads to a broadening and smearing of the $\mathrm{d}Q/\mathrm{d}l$ measurement and result into a deterioration of the pion rejection.

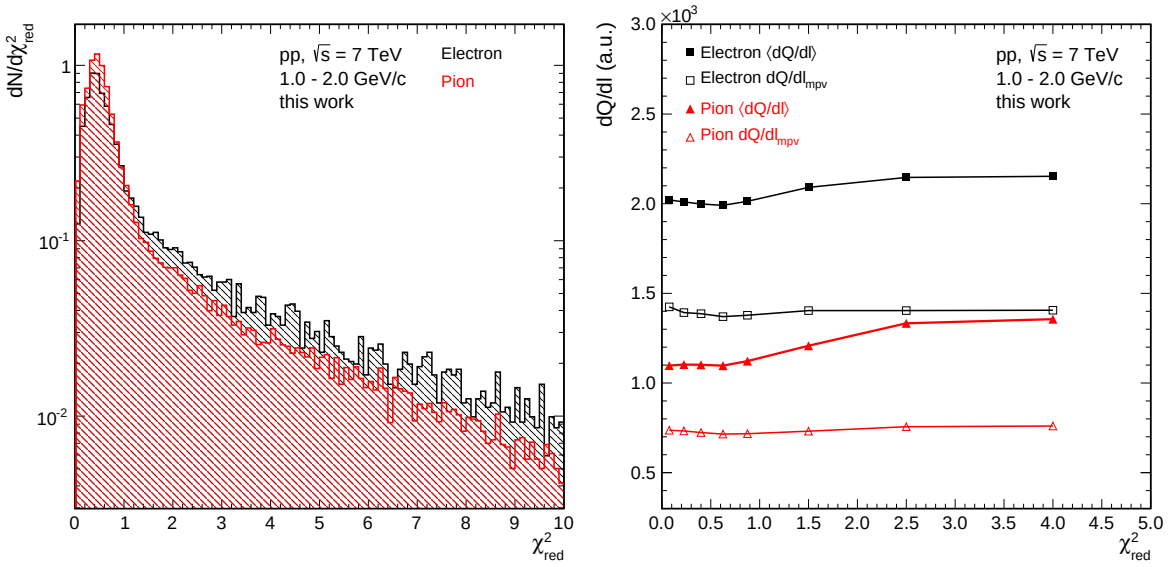

Figure 6.15: (left) χ^2_{red} distribution for pions and electrons. (right) Mean value $\langle \mathrm{d}Q/\mathrm{d}l \rangle$ and most probable value $\mathrm{d}Q/\mathrm{d}l_{\mathrm{mpv}}$ for electrons and pions as a function of χ^2_{red}.

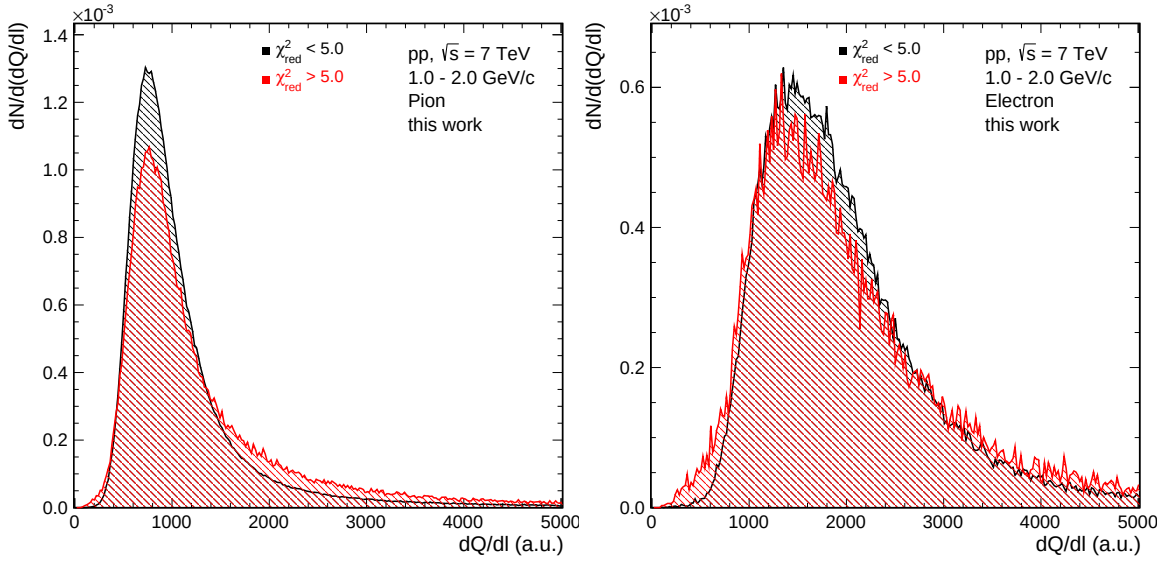

Figure 6.16: $\mathrm{d}Q/\mathrm{d}l$ distribution for pions (left) and electrons (right) for tracks above and below a χ^2_{red}-cut at $\chi^2_{\mathrm{red}} = 5$.

Figure 6.17 shows the pion efficiency at 90% electron efficiency as a function of χ^2_{red} for all tracks and separately for positively and negatively charged tracks. The pion rejection improves

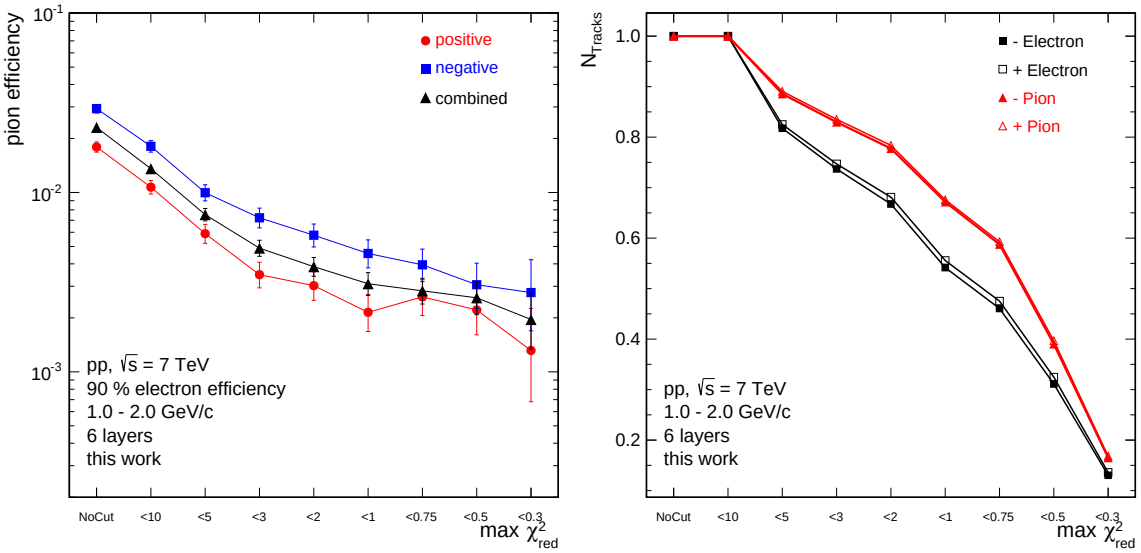

Figure 6.17: (left) Pion Efficiency as a function of a cut on χ^2_{red}. (right) Corresponding number of tracks surviving the χ^2_{red}-cut.

significantly from about 1% without any χ^2_{red}-cut to less than 0.3% for tracks with a $\chi^2_{\text{red}} <$ 0.5. However, the improvement in the pion efficiency coincides with a significant loss in the number of tracks fulfilling the χ^2_{red}-cut. For practical purposes a standard value of $\chi^2_{\text{red}} < 5$ has been chosen for the performance studies in pp collisions. The standard cut removes about 10% of the pion tracks and 20% of the electron tracks in the tails of the χ^2_{red} distribution. In addition, comparing the curves for positively and negatively charged particles in fig. 6.17 a significant charge dependence of the pion efficiency and the number of tracks fulfilling the cut conditions can be observed. Positively charged tracks have a 0.3% smaller pion efficiency ($\chi^2_{\text{red}} < 5$) than negative charged tracks. In addition about 2 - 3% more positive electron tracks survive the χ^2_{red}-cut, while the discrepancy is negligible for pions. This might point to the conclusion that electrons and positrons have slightly different χ^2_{red} distributions, while positive and negative pions have similar distributions. Since the track references are obtained from V0 decays, the number of positively and negatively charged tracks is approximately equal and thus the combined result is simply given by the mean of both charges. The charge dependence is further discussed in section 6.6.4.

6.6.2 Modification of the cluster attachment procedure

After the first reconstruction passes in pp collisions with the artifacts described in section 6.6.1, the concept of cluster attachment was modified in order to deal with the increased detector occupancy in Pb-Pb collisions. Instead of adding individual clusters within a search corridor, in the new implementation tracklet segments are attached based on a likelihood approach taking into account the distance of the tracklet to the track, the inclination of the tracklet, the quality of the tracklet fit and the number of clusters per tracklet [295]. In the following, the impact of these modifications is studied in data from Pb-Pb collisions.

6.6.3 χ^2_{red} dependence in 2010 Pb-Pb data

Figure 6.18 (left) shows the χ^2_{red} distribution for pions and electrons in Pb-Pb collisions. In section 6.6.1 a huge tail above $\chi^2_{\mathrm{red}} \approx 5$ was found and in addition significant differences for electrons and pions. Both observations disappear in Pb-Pb data. The dependence of the pion rejection on χ^2_{red} of the TRD track prolongation is shown in fig. 6.18 (right). In all centrality classes the pion efficiency decreases as the χ^2_{red}-cut is tightened. This finding supports the earlier statement that the cluster attachment depends on the detector occupancy and the matching of the prolongation with the TRD measurement. For the performance analysis in the Pb-Pb data a standard cut of $\chi^2_{\mathrm{red}} < 2$ is used.

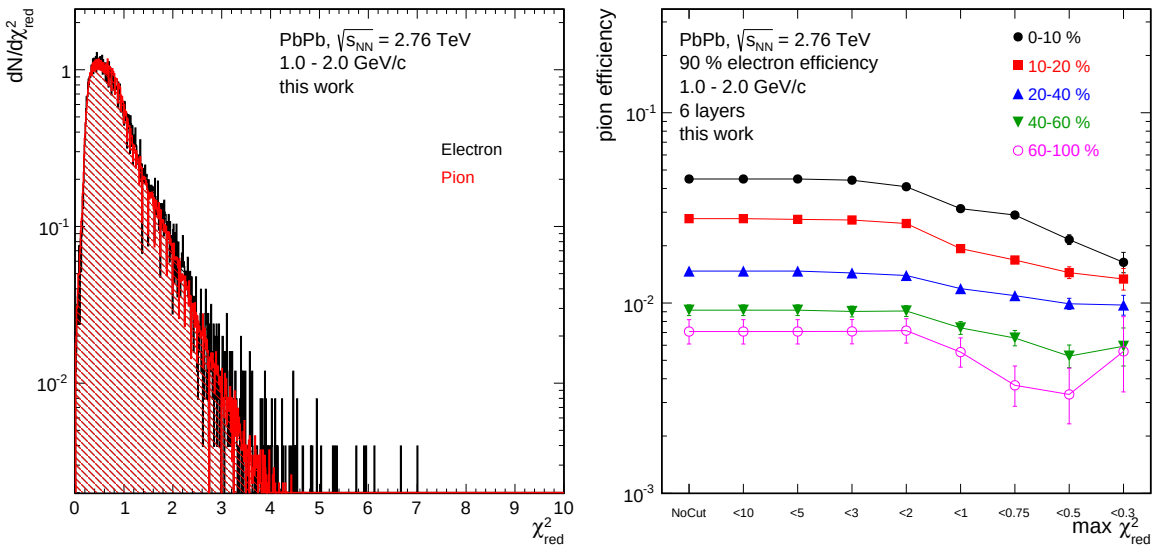

Figure 6.18: (left) χ^2_{red} distribution for pions and electrons. (right) Pion Efficiency as a function of a cut on χ^2_{red} for various centralities.

6.6.4 Charge dependence

Figure 6.19 shows the pion efficiency in minimum bias Pb-Pb collisions as a a function of the χ^2_{red}-cut for positively and negatively charged tracks and combined. While a similar charge dependence of the pion efficiency compared to fig. 6.17 is observed, the number of tracks surviving the χ^2_{red}-cut seems to depend neither on the charge nor on the particle species. It can be concluded that the observed charge dependence is rather an artifact of the detector performance than of the track reconstruction. The charge dependence might be understood as a result of the charge collection on the pad plane. Due to the presence of a magnetic field, the drift direction has a small inclination with respect to the direction of the electric field, which is known as the Lorentz angle. Tracks with a local inclination parallel to the Lorentz angle deposit their charge on a small area on the readout pad plane, while oppositely charged tracks will spread their charge over a larger area. Tail cancellation will affect positive and negative tracks in a different way. This effect could be tested in runs with different polarizations for the magnetic field.

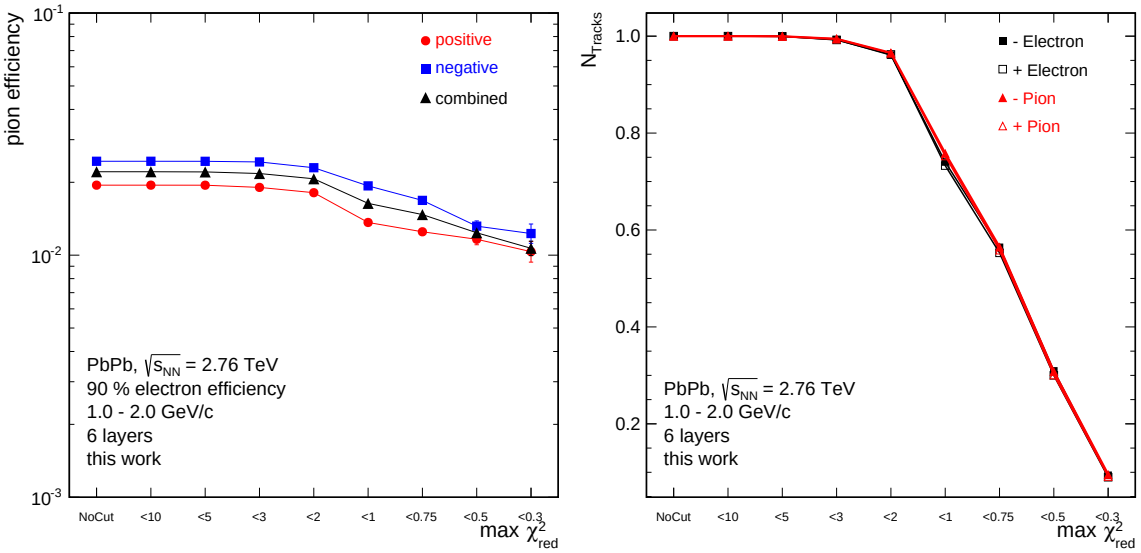

Figure 6.19: (left) Pion efficiency as a function of the χ^2_{red}-cut for positively and negatively charged tracks and combined. (right) Corresponding number of tracks surviving the χ^2_{red}-cut.

6.7 Performance of the bidimensional likelihood approach

Since the performance of the TRD PID is not accessible in Monte Carlo simulations yet, it is important for analysis purposes to control the electron efficiency. Thresholds defined according to eq. (6.18) are provided for six nominal electron efficiencies (70%, 75%, 80%, 85%, 90%, 95%). In the following, the performance of the electron identification is studied in terms of the pion efficiency, which is the probability to identify pions as electrons and thus a benchmark for the significance of any electron analysis using TRD electron identification. In the following, the pion efficiency is studied as a function of the selected electron efficiency, the momentum and the on the number of contributing TRD layers. The performance studies are shown for pp collisions at $\sqrt{s} = 7\,\mathrm{TeV}$ and for Pb-Pb collisions at $\sqrt{s_{\mathrm{NN}}} = 2.76\,\mathrm{TeV}$.

For pp collisions, the results are compared to the results obtained with a neural network (NN) [287] and a truncated mean method [296]. The truncation method calculates the truncated energy loss in all six layers, which results into almost Gaussian distributions. Analogously to the TPC PID discussed in section 6.5.2, electrons can be separated from pions by setting a threshold on the deviation of the measured energy loss from the expected energy loss. The method is very robust and can be applied for difference particle species. All other methods are based on a electron likelihood approach. The neutral network uses the signal in all 8 (7) slices and was trained with the V0 identified electron and pion samples with similar cuts than for the LQ2D and LQ1D method [287] .

6.7.1 Performance in pp collisions at $\sqrt{s} = 7\,\mathrm{TeV}$

6.7.1.1 Pion efficiency vs electron efficiency

Figure 6.20 shows the pion efficiency as a function of the electron efficiency as obtained with the LQ1D and LQ2D method in comparison to the neural network (NN) and the truncated mean

method. The pion efficiency can be reduced by requiring a higher threshold value for the electron likelihood threshold value, which on the same time reduces the number of electrons above the threshold and thus the electron efficiency. The smallest pion efficiency is reached with the NN method, while the pion efficiency with the LQ2D method is only slightly higher and at high electron efficiency even consistent with the NN method performance. At 90% electron efficiency the LQ1D method provides a pion rejection factor of 75 ($\epsilon_\pi = 1.35\%$), while the LQ2D method provides a pion rejection factor of 134 ($\epsilon_\pi = 0.75\%$) for tracks with 6 contributing layers. Thus, the pion efficiency reached with the LQ1D method is about a factor of 2 larger than for the LQ2D method. However, for practical purposes the LQ1D method is much more robust against calibration and detector performance effects, since it is based on the total charge deposition in individual TRD readout chamber. The calculation $\mathrm{d}q/\mathrm{d}l$ in small slices depends strongly on the calibration of the detector and thus the LQ2D and even more the NN method are confronted with a higher workload for maintenance issues.

6.7.1.2 Dependence on the number of contributing TRD layers

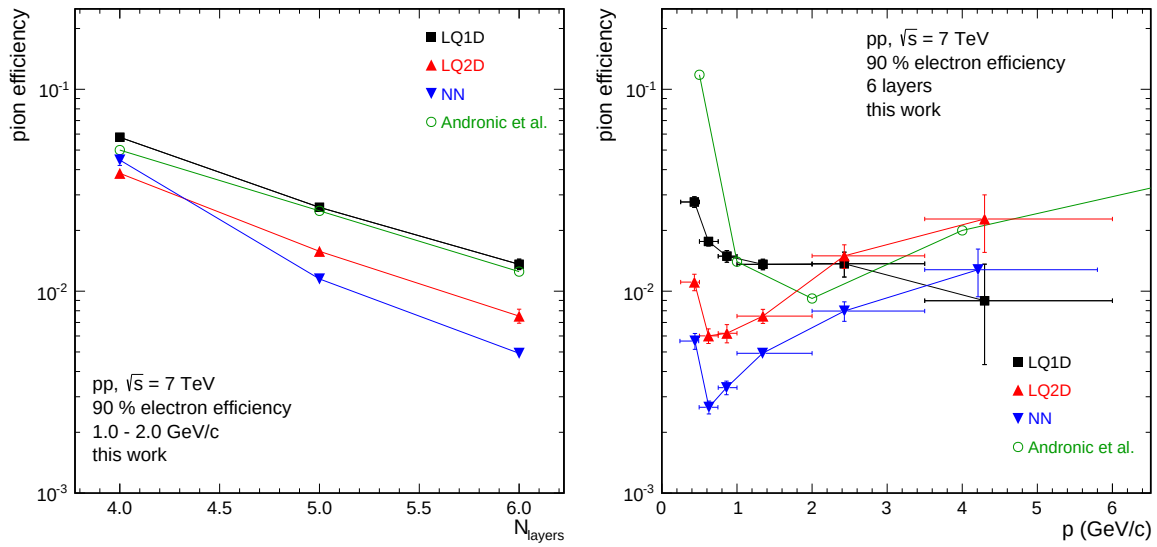

Figure 6.21: Pion rejection obtained with LQ1D, LQ2D and NN method at 90% electron efficiency as a function of the number of contributing layers (left) and the momentum (right). For comparison a simulation for the LQ1D method [253] is shown.

Due to the overlap of the probability density functions $P(\pi, Q)$ and $P(\mathrm{e}, Q)$, electrons can have a high probability for the pion particle hypothesis and vice versa due to fluctuations of the energy loss in a single measurement of the charge deposit $\mathrm{d}q/\mathrm{d}l$. Multiple independent measurements $\vec{Q}$ reduce the impact of those fluctuations on the electron likelihood $L(\mathrm{e}|\vec{Q}_0, \vec{Q}_1)$.
Figure 6.21 (left) shows the pion efficiency as a function of the number of contributing layers as obtained with the LQ1D, LQ2D and NN method. For comparison, a simulation for the LQ1D method by Andronic et al. [253] is shown, where the pion rejection scales linearly with the number of contributing layers, while any additional measurement improves the pion efficiency by a factor of 2. The simulation focusses only on the performance of the electron identification and neglects the tracking performance. The ALICE TRD consists of six layers per stack, but

due to tracking inefficiencies, limited acceptance and inactive readout chambers a considerable fraction of tracks has less than six TRD tracklets. During the 2010 data taking the TRD was operated with 7 supermodules and about 10% of the chambers are not available for analysis. In order to get a sufficient description of the TRD track, at least four consecutive tracklets are required in order to provide particle identification. The pion efficiency in data shows the expected improvement with the number contributing layers. For the LQ1D method the results for 4,5 and 6 layers are in reasonable agreement with the simulation. The pion rejection for the LQ2D (LQ1D) is 3.8% (5.7%) for 4 layers, 1.6% (2.6%) for 5 layers and 0.75% (1.3%) for 6 layers. As expected, the improvement for each additional layer is approximately a factor of 2, for 4 to 5 layers it is somewhat higher, which can be explained by differences in the track quality, i.e. the χ^2_{red} distributions for 4 layers is slightly different than for 5 and 6 layers. The smallest pion rejection (0.5%) is reached with the NN method for the case of six contributing layers. However, the pion efficiency obtained from the NN method does not follow the expected linear scaling such that the result for four tracklets is even higher than that of the LQ2D method. This observation might be attributed to the non-linear behavior of the neutral network approach and its lack of robustness compared to the linear likelihood approaches.

6.7.1.3 Momentum dependence of the pion rejection

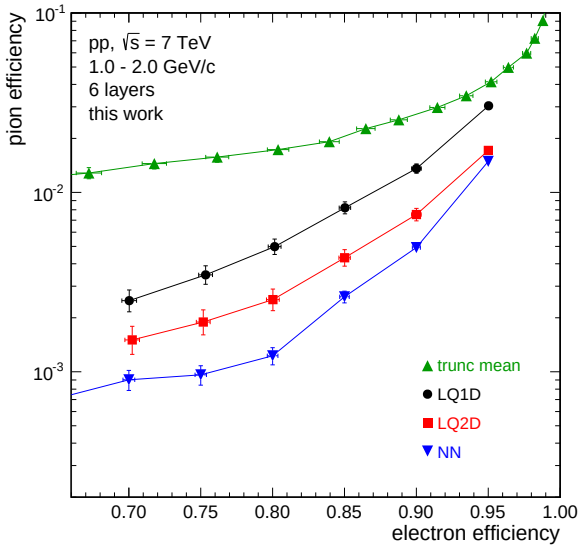

Figure 6.20: Pion efficiency as a function of the electron efficiency for LQ1D and LQ2D method, a neural network (NN) and a truncated mean method.

The momentum dependence of the pion efficiency in pp collisions is shown in fig. 6.21 (right). At a first glance, the momentum dependence has a similar shape compared to the simulation: the pion rejection power improves significantly between 0.5 GeV/c and 1 GeV/c as a result of the onset of TR production. The LQ1D methods reaches the smallest pion efficiency at about 1 - 2 GeV/c, while the LQ2D and NN method yield a minimum pion efficiency at about 0.6 GeV/c, which is the momentum, where TR production for electrons sets in (cf. fig. 6.5 (right)).

At about 0.45 GeV/c pions are minimum ionizing particles, while electrons are almost in the relativistic rise and still below energies, where TR becomes significant, but the LQ2D and NN method still provide a smaller pion efficiency than the LQ1D method. The LQ2D method treats the energy loss in the lower and upper half of the drift volume independently even though there is some small correlation between adjacent clusters. Obviously, the LQ2D method also provides a much better performance than the LQ1D method at lower momenta, where TR does not contribute. A possible explanation might be that the pulse height – even in absence of TR – still depends on the drift time. Thus, further improvement in that momentum range can be reached with the NN method, which make use of the $\mathrm{d}q/\mathrm{d}l$ measurement in smaller slices. At higher momenta the TR production saturates and the pion efficiency increases as a

consequence of the relativistic rise of the ionization energy loss of pions. Since the simulation for the LQ1D method [253] was done for eight contributing layer it was scaled by 4, as expected from the linear scaling with the number of contributing layers (cf. section 6.7.1.2). Compared to the data the simulation shows a similar momentum dependence, but reaches its smallest pion efficiency at a somewhat higher value than observed in the data, which might indicate a bias due to detector effects in the data.

6.7.2 Performance in Pb-Pb collisions at $\sqrt{s_{\mathrm{NN}}} = 2.76\,\mathrm{TeV}$

6.7.2.1 Centrality dependence

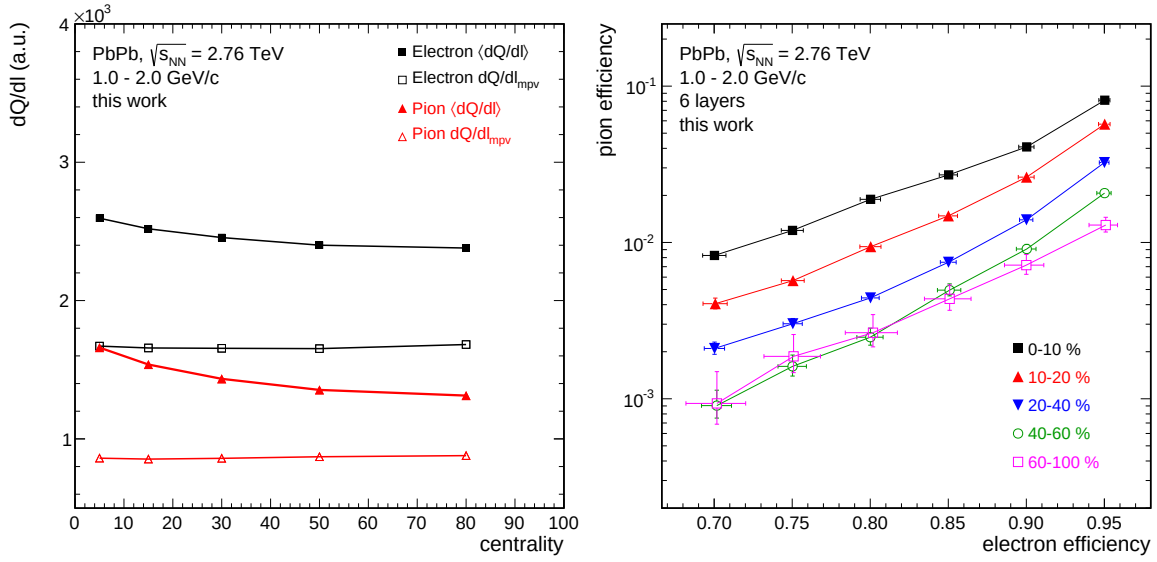

Figure 6.22: (left) Centrality dependence of mean $\langle \mathrm{d}Q/\mathrm{d}l \rangle$ and most probable $\mathrm{d}Q/\mathrm{d}l_{\mathrm{mpv}}$ charge deposit. (right) Pion efficiency as a function of the electron efficiency in different centrality bins.

Figure 6.22 (left) shows the centrality dependence of the mean $\langle \mathrm{d}Q/\mathrm{d}l \rangle$ and most probable $\mathrm{d}Q/\mathrm{d}l_{\mathrm{mpv}}$ charge deposit for electrons and pions. While the most probable value is rather constant, the mean value increases with centrality, which can be attributed to additional cluster attachment with increasing charged particle densities and detector occupancy. In central collisions it is more likely that additional clusters are falsely attached to a track due to the higher detector occupancy. Those additional clusters are visible in the tails of the $\mathrm{d}Q/\mathrm{d}l$ distributions and shift the mean value $\langle \mathrm{d}Q/\mathrm{d}l \rangle$ towards higher values. The large tails in the $\mathrm{d}Q/\mathrm{d}l$ distributions increase the overlap of both probability density distributions $P(Q|k)$ and thus reduce the separation power.

Figure 6.22 (right) illustrates the centrality dependence of the pion efficiency. The best performance is reached in peripheral collisions were track multiplicities are similar compared to pp collisions. The pion rejection at 90% electron efficiency in 60 - 100% peripheral collisions is about 140 (0.71%), while a rejection of 134 (0.75%) was determined in pp collisions. In 0 - 10% central collisions the pion rejection is about 25 (4%).

6.7.2.2 Momentum dependence of the pion rejection

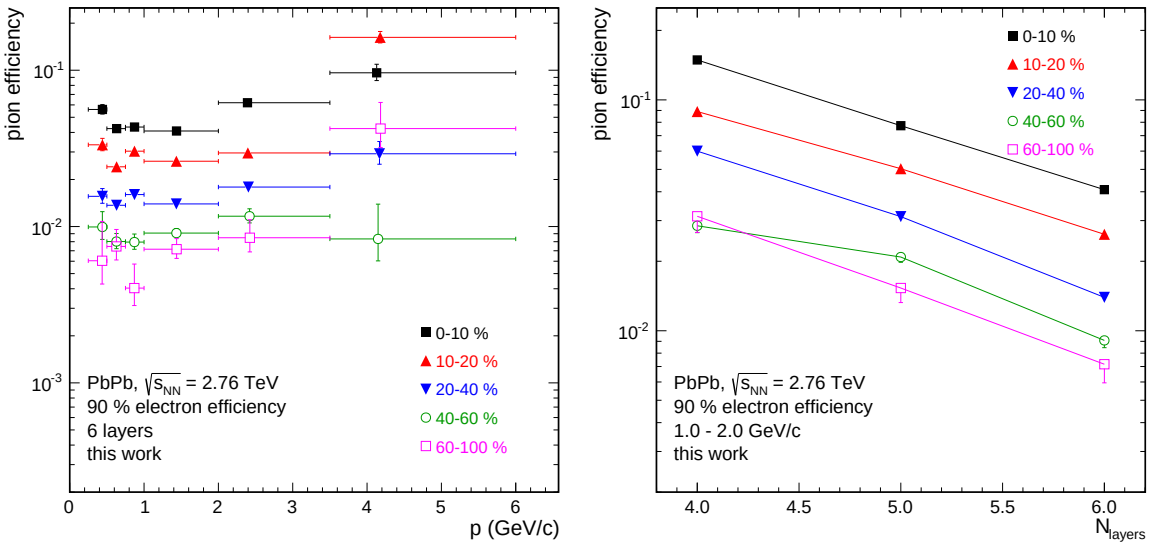

Figure 6.23: Pion efficiency for various centrality classes as a function of the track momentum (left) and as a function of the number of contributing layers (right).

Figure 6.23 (left) show the momentum dependence of the pion efficiency in Pb-Pb collisions. The centrality dependence is visible at all momenta. The results in peripheral and midcentral Pb-Pb collisions indicate the same momentum dependence of the pion efficiency as in pp collisions discussed in section 6.7.1.3. An optimal performance is found at a momentum of 0.6 GeV/c, where the production of TR for electrons sets in (cf. fig. 6.5 (right)), while more central collisions do not show a distinct minimum at low momenta. Non-continuity in the momentum dependence can be explained by the fact that the likelihood is computed from reference distributions in fixed momentum ranges.

6.7.2.3 Dependence on the number of contributing TRD layers

Figure 6.23 (right) show pion efficiency as a function of the number of contributing layers. Qualitatively the results are in agreement with the observations in pp (cf. section 6.7.1.2) and the pion efficiency improves roughly by a factor of 2 for each additional layer. Slight deviations from the expected linear scaling can be observed for mid-central and peripheral collisions, which might be explained by artifacts of the track reconstruction.

6.8 Summary and outlook

In this chapter the technical implementation and performance of a bidimensional likelihood approach (LQ2D) for electron identification with the TRD was described and discussed in detail. Reference samples for electrons and pions were obtained from topological cuts on photon conversions and K^0_s decays. It was demonstrated that further particle identification cuts using the TPC and TOF were necessary to clean the samples from impurities. It was further shown in section 6.5.4 that already small contaminations can introduce a rather large bias of the extracted electron and pion efficiencies and thus restrictive cuts were chosen.

Within this thesis it was found that the pion rejection depends on the χ^2_{red} of the track prolongation from the TPC into the TRD. For the study of pp collisions rather restrictive cuts were applied during the track selection (cf. section 6.6.1). In particular, systematic differences for electrons and pions were observed and about 20% electron and 10% pion tracks were removed by a χ^2_{red}-cut. It could be argued by the large χ^2_{red} value that the track prolongation from the TPC to the TRD failed for those tracks and thus the TRD PID cannot be applied to those tracks.
For the reconstruction of the Pb-Pb data an improved cluster attachment algorithm was introduced in order to deal with the increased detector occupancy, which solved the discrepancy between electrons and pions. Furthermore, a significant charge dependence of the pion rejection was observed, which seems to be an artifact of the interplay between the drift field and the magnetic field of the L3 magnet. This hypothesis could be tested by comparing runs with different polarizations of the magnetic field.

Data Sample		pion efficiency	pion rejection
pp, $\sqrt{s} = 7\,\text{TeV}$		$(0.75 \pm 0.06)\%$	134
Pb-Pb, $\sqrt{s_{\text{NN}}} = 2.76\,\text{TeV}$	60 - 100%	$(0.71 \pm 0.04)\%$	140
Pb-Pb, $\sqrt{s_{\text{NN}}} = 2.76\,\text{TeV}$	40 - 60%	$(0.91 \pm 0.05)\%$	110
Pb-Pb, $\sqrt{s_{\text{NN}}} = 2.76\,\text{TeV}$	20 - 40%	$(1.39 \pm 0.05)\%$	72
Pb-Pb, $\sqrt{s_{\text{NN}}} = 2.76\,\text{TeV}$	10 - 20%	$(2.62 \pm 0.08)\%$	38
Pb-Pb, $\sqrt{s_{\text{NN}}} = 2.76\,\text{TeV}$	0 - 10%	$(4.08 \pm 0.09)\%$	25

Table 6.2: Pion efficiency at 90% electron efficiency in pp and Pb-Pb data for various centrality bins for tracks with 1 - 2 GeV/c momentum.

Finally, the performance in terms of its pion rejection was determined for the bidimensional approach in pp and Pb-Pb collisions. The results are summarized in table 6.2. According to the technical design report [236], the TRD was designed for a pion efficiency of 1% at 90% electron efficiency for tracks with six contributing layers with a momentum between 1 - 2 GeV/c. The performance in pp and Pb-Pb collisions is summarized in table 6.2. In pp data as well as in peripheral and mid-central Pb-Pb collisions the bidimensional method is able to provide electron identification at the design performance or even better. In central Pb-Pb collisions the performance suffers from additional charged attachment due to the high detector occupancy. However, even in the 0 - 10% most central collisions still a pion rejection factor of 25 at 90% electron efficiency is reached.

It will be interesting to see the TRD PID applied to physical analyses such as the J/ψ or heavy flavor electron analysis (cf. [297]). For the purpose of photon reconstruction, which is part of this work, the TRD electron identification was not used for two reasons. First, it is shown in section 8.2.4 that the contamination of photon conversion after TPC and TOF PID is even in central Pb-Pb collisions small enough and dominated by electron combinatorics. Second, during the first period of LHC operation the TRD was not fully installed. The common approach is to use TRD information if it is available. However, this reduces azimuthally nonuniform systematic effects, which is undesirable for the purpose of anisotropic flow analyses.

7. Analyzing direct-photon anisotropic flow from fluctuating initial conditions

The physical aspects of transverse flow and its implications for our understanding of the time evolution of heavy-ion collisions was discussed in section 3.4. This chapter focusses on the technical aspects of the anisotropic flow measurement.
If the number of particles of interest is large enough, the Fourier coefficients of the azimuthal anisotropy can be extracted directly from the laboratory azimuthal distribution in each individual event. While this approach is used to measure the event-by-event probability distribution of the bulk flow, this method is inappropriate for identified particles or differential flow measurements, since statistical fluctuations in the particle yields would dominate the measurement. Instead, the azimuthal anisotropy is measured averaged over many events, either from multi-particle correlations (***cumulants***) or the azimuthal distribution is measured with respect to an ***event plane***, which is an event-by-event estimate of the direction of the n-th order transverse flow Ψ_n. A slightly modified version of the event-plane method is the ***scalar-product method***. When those methods were developed, it was assumed that event-by-event fluctuations of v_n were negligible [298]. Nowadays, it is known that v_n fluctuates significantly within a class of events (cf. section 3.4.2), which has different implications for the outcome of the three methods mentioned above [65, 298]. As described in section 4.1, direct photons cannot be separated from decay photons on a event-by-event basis. The most common approach is to measure inclusive photons and hadrons, and to subtract the spectrum and anisotropy of decay photons, which is estimated from a cocktail simulation based on the measured hadron spectra and azimuthal anisotropy. However, unlike hadrons and decay photons, direct photons are produced over the whole time evolution of the system and it is not obvious what the correlation of particles emitted from different stages of the fireball evolution measures. Therefore, it will be important to understand the direct-photon flow extraction in detail and to ensure that a large direct-photon anisotropy cannot arise due to artifacts of the experimental method.
In this chapter, the effects of fluctuations expected for Pb-Pb collisions at $\sqrt{s_{\mathrm{NN}}} = 2.76\,\mathrm{TeV}$ are estimated within a Glauber Monte Carlo simulation. The extraction of the direct-photon anisotropic flow is tested for different scenarios for the direct photon production.

7.1 Flow fluctuations from Glauber initial conditions

In section 3.4.1, it was shown that v_2 and v_3 are proportional to the second and third order eccentricity ϵ_2 and ϵ_3, respectively. As a consequence, relative flow fluctuations $\sigma_{v_n} / \langle v_n \rangle$ should be described by $\sigma_{\epsilon_n} / \langle \epsilon_n \rangle$, which can be determined from initial state models such as the Glauber model. The eccentricity used in this work is the participant eccentricity defined in eq. (3.7). In addition to the standard Glauber calculation, the eccentricity is also estimated from a quark constituent Glauber calculation with three constituent quarks with $\sigma_{\mathrm{qq}} = 1/9 \sigma_{\mathrm{nn}}$ with $\sigma_{\mathrm{nn}} = 64\,\mathrm{mb}$ instead of nucleons. This approach is inspired by the ***Additive Quark Model*** [299–301].
Figure 7.1 (left) shows the mean eccentricity $\langle \epsilon_n \rangle$ as a function of N_{part} as determined from

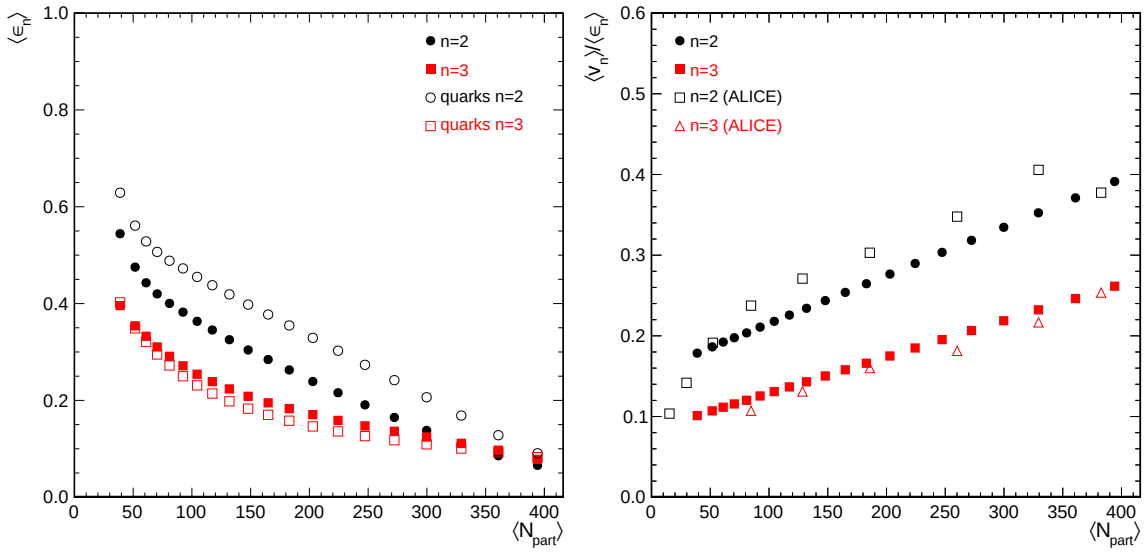

Figure 7.1: (left) Mean eccentricity $\langle\epsilon_n\rangle$ as determined from nucleon and quark participants. (right) p_{T}-integrated elliptic and triangular flow measured by ALICE [141] divided by the mean nucleon eccentricity as a function of N_{part}.

nucleon and quark participants. In central collisions, the elliptic and triangular eccentricity are of similar magnitude. As the impact parameter goes to zero, the system becomes radially symmetric and thus also the elliptic eccentricity is exclusively induced by fluctuations. At non-zero impact parameters, ϵ_2 is always larger than ϵ_3 due to the asymmetry of the nuclear overlap. At large impact parameters, fluctuations due to small numbers of participants drive $\epsilon_n \to 1$.
Figure 7.1 (right) shows the p_{T}-integrated elliptic and triangular flow measured by ALICE [141] divided by the mean nucleon eccentricity as a function of N_{part}. It was already discussed in section 3.4.1 that proportionality of the anisotropic flow v_n and the eccentricity ϵ_n change with the centrality, which might be explained by different viscous corrections for central and mid-central collisions. In order to parametrize this effect, it is assumed that $v_n = (a + bN_{\mathrm{part}})\,\epsilon_n$ with parameters a and b extracted from ALICE data [141]. The resulting v_n/ϵ_n ratios in the simulation are also shown in fig. 7.1 (right).

The event-by-event probability distribution for v_2 and v_3 is shown in fig. 7.2 for different values of $\langle N_{\mathrm{part}}\rangle$. Looking at the probability density function for elliptic flow, it can be seen that the most probable value is shifted towards higher values as the collisions become less central and N_{part} decreases. This effect is driven by the asymmetry of the nuclear overlap in non-central collisions. In addition, the probability density functions show large asymmetric tails towards smaller values in non-central collisions and towards towards larger values in the most central collisions. The most probable value of the triangular flow shows only a weak increase with decreasing centrality compared to the elliptic flow, since triangular flow is only driven by fluctuations and independent from the asymmetry of the nuclear overlap.

Finally, fig. 7.3 shows the ratio $\sigma_{\epsilon_n}/\langle\epsilon_n\rangle$ as obtained from Glauber initial conditions and $\sigma_{v_n}/\langle v_n\rangle$ measured by ATLAS [143] as a function of $\langle N_{\mathrm{part}}\rangle$. For triangular flow, the data points are in agreement with pure Gaussian fluctuations ($\sigma_{\epsilon_n}/\langle\epsilon_n\rangle = \sqrt{4/\pi - 1}$ [302, 303]). Both, the

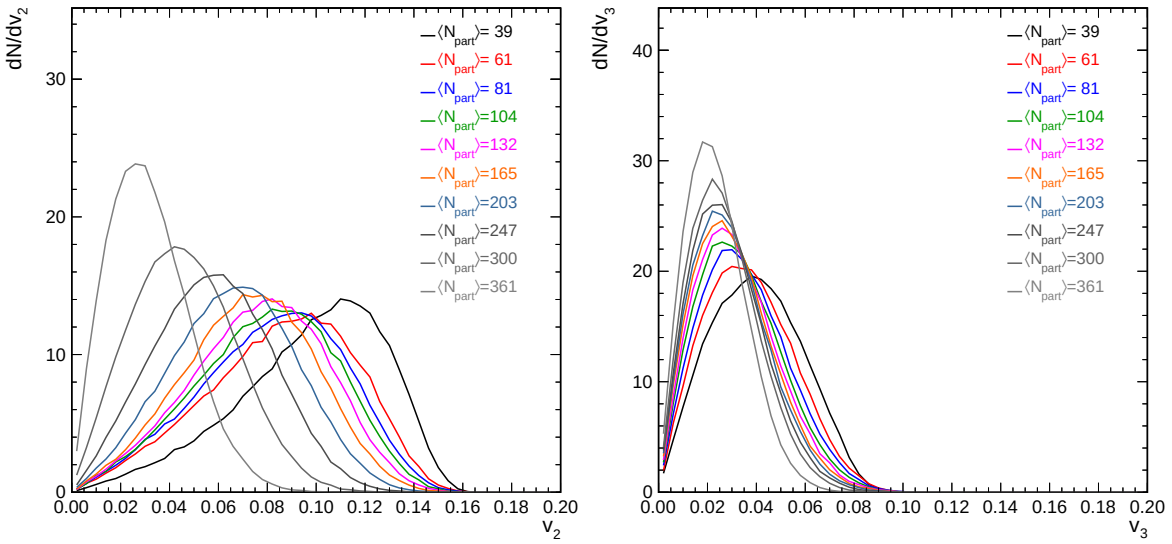

Figure 7.2: Event-by-event probability density function for v_2 (left) and v_3 (right) for different values of $\langle N_{\mathrm{part}} \rangle$.

standard nucleon and quark participant Glauber calculation, describe the data points in central and mid-central collisions. In peripheral collisions, the Glauber model deviates from pure Gaussian fluctuations and underestimates the data, which can be understood from the fact that $\epsilon_n \to 1$ at large impact parameters.

For elliptic flow, data points and Glauber calculation are below the limit of pure Gaussian fluctuations, except for the most central collisions. Quark participants yield a much smaller relative width of fluctuations compared to nucleon participants, which can be interpreted by the smoothening of eccentricity fluctuations in the quark participant model. In central and mid-central collisions the data points lie between the values obtained by the quark and nucleon participant model, which implies that adjustments in the cross-section σ_{qq} could give a better agreement between data and the Glauber Monte Carlo simulation. Similar to the triangular eccentricity, the relative magnitude of fluctuations decrease in peripheral collisions as a consequence of $\epsilon_n \to 1$.

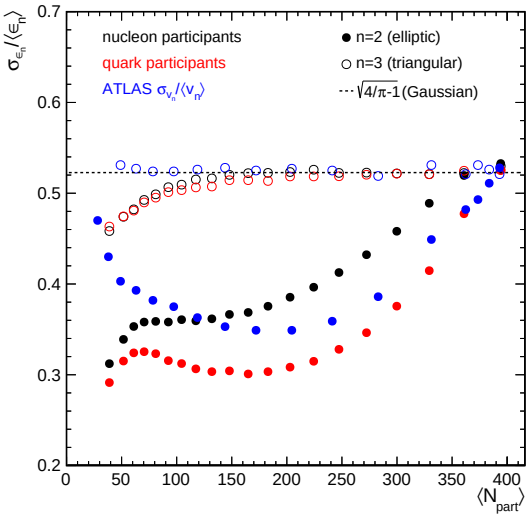

Figure 7.3: Relative eccentricity fluctuations $\sigma_{\epsilon_n} / \langle \epsilon_n \rangle$ for nucleon and quark participants in comparison to $\sigma_{v_n} / \langle v_n \rangle$ for charged particles ($0.5 < p_{\mathrm{T}} < 1\,\mathrm{GeV}/c$) [143] vs. N_{part}.

In summary, v_3 and in central collisions also v_2 can be understood as induced by pure Gaussian fluctuations in the energy density profile. In mid-central and peripheral collisions, the second order eccentricity is dominantly driven by the asymmetry of the nuclear overlap in the transverse plane and thus flow fluctuations are significantly reduced.

7.2 Multi-Particle cumulant method

A method for measuring anisotropic flow based on genuine multi-particle correlations was proposed by Borghini, Dinh and Ollitrault in 2001 [304–306]. Compared to the scalar-product and event-plane method, this approach allows to subtract non-flow effects from flow measurements.

7.2.1 Two- and four-particle cumulant

The cumulant method correlates each particle with every other particle in the same event. The two-particle cumulant c_2 is defined as [52, 136, 137]

$$c_2 = \langle \cos\left(n\left(\phi_1 - \phi_2\right)\right)\rangle \ , \tag{7.1}$$

where ϕ_1 and ϕ_2 denote the azimuthal angles of two different particles and the brackets $\langle ... \rangle$ an average over all particles of interest in all events. The two-particle cumulant estimate for the n-th order anisotropy $v_n\{2\}$ is given by

$$v_n\{2\} = \sqrt{c_2} \ . \tag{7.2}$$

Analogously, the four-particle cumulant c_4 and the corresponding estimate $v_n\{4\}$ are defined as [52, 136, 137]:

$$c_4 = \langle \cos\left(n\left(\phi_1 + \phi_2 - \phi_3 - \phi_4\right)\right)\rangle \tag{7.3}$$

$$v_n\{4\} = \left(2c_2^2 - c_4\right)^{\frac{1}{4}} \tag{7.4}$$

7.2.2 What does the cumulant method measure?

Assuming that the correlation between the particles is only due to the collective expansion and using the definition of v_n given in eq. (3.29), one obtains

$$v_n\{2\} = \sqrt{\langle \cos\left(n\left(\phi_1 - \Psi_n\right)\right)\rangle \langle \cos\left(n\left(\Psi_n - \phi_2\right)\right)\rangle} = \sqrt{\langle v_n^2 \rangle} \ . \tag{7.5}$$

It can be immediately seen that the two particle cumulant method $v_n\{2\}$ measures the root mean square of v_n. The magnitude of flow fluctuations is given by

$$\sigma_{v_n}^2 = \left\langle v_n^2 \right\rangle - \langle v_n \rangle^2 \ , \tag{7.6}$$

which implies that

$$v_n^2\{2\} = \left\langle v_n^2 \right\rangle = \langle v_n \rangle^2 + \sigma_{v_n}^2 \ . \tag{7.7}$$

Analogously, we obtain for the four-particle cumulant estimate

$$v_n^2\{4\} = \sqrt{2\left\langle v_n^2 \right\rangle^2 - \left\langle v_n^4 \right\rangle} \approx \langle v_n \rangle^2 - \sigma_{v_n}^2 \ . \tag{7.8}$$

The anisotropic flow measurement from two-particle correlations $v_n\{2\}$ is sensitive to non-flow correlations δ_{nf}, while $v_n\{4\}$ is almost insensitive to non-flow effects [137]. Assuming that both

non-flow and fluctuations are present, we obtain

$$v_n^2\{2\} - v_n^2\{4\} = \delta_{\mathrm{nf}} + 2\sigma_{v_n}^2 \ , \tag{7.9}$$

which implies that non-flow effects can be estimated from the comparison of two- and four-particle cumulants.

7.3 The event-plane method

The event-plane method was introduced by Voloshin and Zhang in 1994 [307]. Historically, the event plane was though as an estimate of the reaction-plane orientation. However, by definition, the event-plane angle points towards the direction of maximum p_{T}-integrated flow, which – taking the role of fluctuations into account – can be identified with the participant-plane orientation rather than the reaction-plane orientation.

7.3.1 Flow vector

The flow vector $\vec{Q}_n$ for the n-th order harmonic is defined by [135, 308]:

$$\vec{Q}_n = \begin{pmatrix} X_n \\ Y_n \end{pmatrix} = \begin{pmatrix} \sum_i^{N_{\mathrm{ref}}} w_i \cos\left(n\phi_i\right) \\ \sum_i^{N_{\mathrm{ref}}} w_i \sin\left(n\phi_i\right) \end{pmatrix} \tag{7.10}$$

The sum goes over all N_{ref} reference particles in an individual event. Optimal weights w_i in eq. (7.10) in terms of small statistical errors and high angular resolution of the event-plane angle are given by $v_n\left(p_{\mathrm{T}}\right)$ itself [304], a simple parametrization of the p_{T} dependence of v_n (cf. section 3.4.4) is given by:

$$w_i = \begin{cases} p_{\mathrm{T}}[\mathrm{GeV}/c] & \text{for} \quad p_{\mathrm{T}} < 2\,\mathrm{GeV}/c \\ 2 & \text{for} \quad p_{\mathrm{T}} \geq 2\,\mathrm{GeV}/c \end{cases} \tag{7.11}$$

The flow vector measures the magnitude and direction of the p_{T}-integrated reference flow $\bar{v}_n$. If the weights w_i are neglected ($w_i = 1$), the normalized flow vector $\vec{Q}_{n,\mathrm{red}}$ is related with the two-particle cumulant c_2 as follows [136]:

$$\vec{Q}_{n,\mathrm{red}} = \frac{\left|\vec{Q}_n\right|}{N_{\mathrm{ref}}} = \sqrt{\frac{1}{N_{\mathrm{ref}}} + \frac{N_{\mathrm{ref}} - 1}{N_{\mathrm{ref}}} c_2} \underset{1/N_{\mathrm{ref}} \to 0}{\to} \bar{v}_n \tag{7.12}$$

Thus, the flow vector measures the strength of the reference flow $\bar{v}_n$ for sufficiently large numbers of reference particles N_{ref}. Accordingly, the two-particle cumulant can be estimated from the flow vector as

$$c_2 = \frac{\vec{Q}_{n,\mathrm{red}}^2 - \frac{1}{N_{\mathrm{ref}}}}{1 - \frac{1}{N_{\mathrm{ref}}}} \tag{7.13}$$

This approach reduces computational costs to $\mathcal{O}(N_{\mathrm{ref}})$ instead of $\mathcal{O}(N_{\mathrm{ref}}^2)$. Similarly, also four-particle cumulants can be estimated from the flow vector [136]. Figure 7.5 (left) shows the normalized flow vector $\vec{Q}_{2,\mathrm{red}}$ as a function of the reference flow strength $\bar{v}_2$ as obtained from

different number of reference particles $\langle N_{\mathrm{ref}} \rangle$. Since $\vec{Q}_{2,\mathrm{red}}$ is shown as a function of $\bar{v}_2$, fluctuations are explicitly excluded and $\vec{Q}_{2,\mathrm{red}}$ coincidences with $\bar{v}_2$ for large $\bar{v}_2$ and $\langle N_{\mathrm{ref}} \rangle$. For small values of $\bar{v}_2$, the reduced flow vector $\vec{Q}_{n,\mathrm{red}}$ is dominated by multiplicity fluctuations, which gives the lower bound $\vec{Q}_{2,\mathrm{red}} \geq 1/\sqrt{N_{\mathrm{ref}}}$.

7.3.2 Event-plane angle

The direction of maximum n-th order anisotropy Ψ_n can be estimated from the flow vector. The estimate is referred to as event plane and defined as [308]

$$\Psi_n^{\mathrm{EP}} = \frac{1}{n}\left(\tan^{-1}\frac{Y_n}{X_n}\right) . \tag{7.14}$$

The event-plane angle Ψ_n^{EP} points towards the direction of maximum n-th order transverse flow Ψ_n, which is ambiguous in the laboratory system for $n \geq 2$. Figure 7.4 shows a schematic diagram illustrating the orientation of the elliptic Ψ_2 and triangular Ψ_3 flow direction in relation to the initial distribution of participant nucleons from a Glauber Monte Carlo simulation. By definition, eq. (7.14) yields an angle in the range $[0, \pi/n]$, which is equivalent to any $\Psi_n^{\mathrm{EP}} + i\pi/n$ for $i \in \mathbb{R}$ due to the periodicity of the cosine.

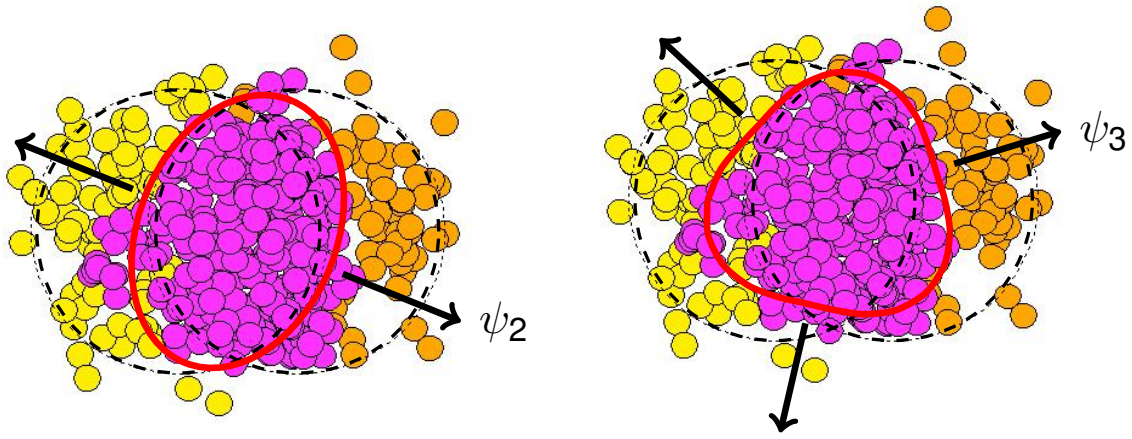

Figure 7.4: Schematic diagram illustrating the orientation of the elliptic and triangular flow direction in relation to the initial distribution of participant nucleons from a Glauber Monte Carlo simulation [309].

7.3.3 Transverse flow measurement with respect to the event plane

The event-plane estimate of the n-th order anisotropic flow $v_n\{\mathrm{EP}\}$ is given [134, 135, 308] by

$$v_n\{\mathrm{EP}\} = \frac{\left\langle \cos\left(n\left(\phi - \Psi_n^{\mathrm{EP}}\right)\right)\right\rangle}{R} . \tag{7.15}$$

The respective particle of interest is always subtracted from the flow vector $\vec{Q}_n$ in order to avoid autocorrelations. The measured anisotropy is smeared out by the dispersion χ of the event-plane

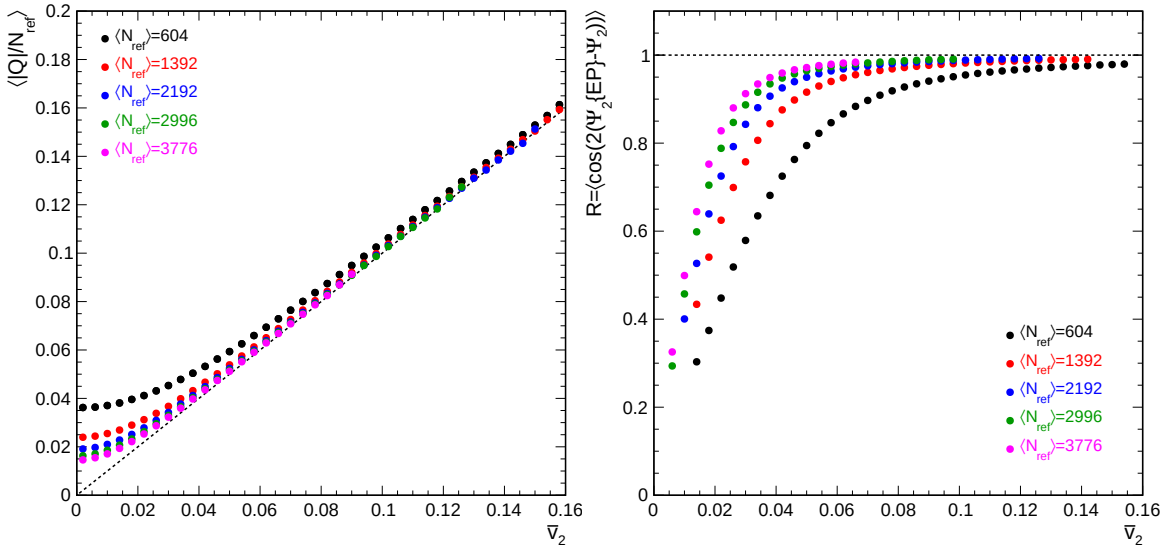

Figure 7.5: (left) $\left\langle \vec{Q}_{2,\mathrm{red}} \right\rangle$ and (right) $R = \left\langle \cos\left(2\left(\Psi_n^{\mathrm{EP}} - \Psi_2\right)\right)\right\rangle$ as a function of reference flow strength $\bar{v}_2$. The black dashed lines represent the limit of perfect correlation between the flow vector and reference flow.

estimate Ψ_n^{EP}. In appendix A, it is shown that resolution correction R is given by

$$R = \left\langle \cos\left(n\left(\Psi_n^{\mathrm{EP}} - \Psi_n\right)\right)\right\rangle \ . \tag{7.16}$$

The relation between the resolution correction $R(\chi)$ and the dispersion χ is given [134, 137] by

$$R(\chi) = \frac{\sqrt{\pi}}{2} e^{-\chi^2/2} \chi \left(I_0\left(\frac{\chi^2}{2}\right) + I_1\left(\frac{\chi^2}{2}\right)\right) \ , \tag{7.17}$$

where I_0 and I_1 are modified Bessel functions.
In general, the dispersion χ is related to the p_{T}-integrated reference flow strength $\bar{v}_n$ and the number of particles N_{ref} used for the event-plane estimate as [134, 137]:

$$\chi \propto \bar{v}_n \sqrt{N_{\mathrm{ref}}} \tag{7.18}$$

Figure 7.5 (right) shows the resolution correction R as a function of the reference flow strength $\bar{v}_2$ for different values for the reference particle multiplicity $\langle N_{\mathrm{ref}} \rangle$. In the limit of perfect resolution, the correction factor R approaches unity. It can be seen that the estimate of the event plane gets more precise as $\bar{v}_2$ and N_{ref} increase.

7.3.4 Estimation of the event-plane resolution

The resolution correction factor $R(\chi)$ can be estimated from the correlation between the reference detector and at least one additional detector. Three cases can be distinguished:

1. There are two identical detectors A and B, which are symmetric around mid rapidity and

separated by a pseudorapidity gap. Then the resolution correction factor is given by:

$$R = \sqrt{\langle \cos\left(n\left(\Psi_n^{\mathrm{A}} - \Psi_n^{\mathrm{B}}\right)\right)\rangle} \tag{7.19}$$

2. If there is no such symmetry, a third reference detector C is required. The resolution correction for detector A is then given by:

$$R = \sqrt{\frac{\langle \cos\left(n\left(\Psi_n^{\mathrm{A}} - \Psi_n^{\mathrm{B}}\right)\right)\rangle \langle \cos\left(n\left(\Psi_n^{\mathrm{A}} - \Psi_n^{\mathrm{C}}\right)\right)\rangle}{\langle \cos\left(n\left(\Psi_n^{\mathrm{B}} - \Psi_n^{\mathrm{C}}\right)\right)\rangle}} \tag{7.20}$$

3. Alternatively, the signal in the detector is often divided in two or more ***sub events*** of equal number of particles N_{sub}. The sub events should be separated in pseudorapidity in order to suppress non-flow correlations. Often, the event plane is split randomly into two sub events, which will overestimate or underestimate the correlation, if non-flow correlations are present. The resolution of the full event plane can be obtained as follows: using that the dispersion χ is proportional to $\sqrt{N_{\mathrm{ref}}}$ (eq. (7.18)), the resolution parameter $R(\chi)$ of the full event plane can be estimated from the sub-event-plane resolution R_{sub} by

$$R(\chi) = R_{\mathrm{sub}}\left(\chi_{\mathrm{sub}}\sqrt{N_{\mathrm{ref}}/N_{\mathrm{sub}}}\right) \ , \tag{7.21}$$

where χ_{sub} is the dispersion of the sub-event plane [137, 308]. The relation between dispersion χ and resolution correction R was given in eq. (7.17). For practical purposes, the following interpolation [308] is used

$$R(\chi) = 0.626657\chi - 0.09694\chi^3 + 0.02754\chi^4 - 0.002283\chi^5 \ . \tag{7.22}$$

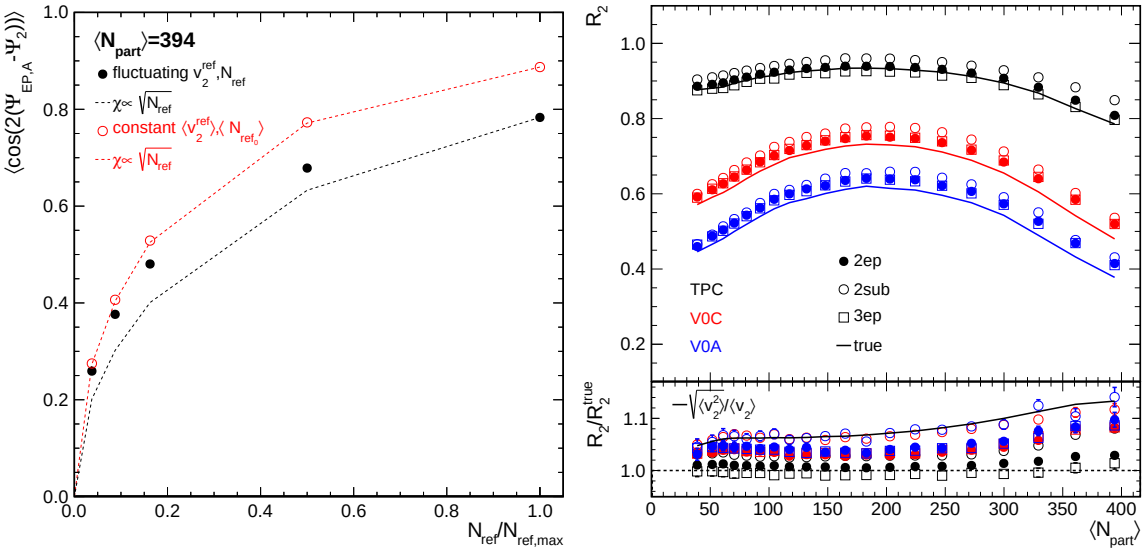

Figure 7.6: (left) Event-plane resolution as a function of the relative reference particle multiplicity $N_{\mathrm{ref}}/N_{\mathrm{ref,max}}$. (right) Estimates for the event-plane resolution as a function of $\langle N_{\mathrm{part}}\rangle$ as obtained from the correlation with a second, identical detector ('2ep'), the two other detectors ('3ep'), and random sub events ('2sub').The true resolution is shown as solid line.

The derivation and validity of the relations eqs. (7.19) and (7.20) is discussed in detail in appendix A. It is important to notice that the factorization and thus the derived resolution correction is only valid, if the correlation between the event-plane estimates Ψ_n^{EP} is only due to the flow signal. The contribution of non-flow correlations can be partially suppressed, if the event-plane detectors are sufficiently separated in pseudorapidity. However, as a quid pro quo, the estimate of the resolution correction then depends on the pseudorapidity gap $\Delta\eta$ and different values for $\Delta\eta$ might yield different values for the resolution. Recently, even a decorrelation of event planes over pseudorapidity was observed in AMPT calculations [310]. These findings might call into question, whether η gaps are an appropriate tool to reduce non-flow contributions.

It can be demonstrated that the sub-event approach is not valid, if the strength of the p_{T}-integrated reference flow $\bar{v}_n$ fluctuates event-by-event. Figure 7.6 (left) shows the true resolution R as a function of the relative reference particle multiplicity $N_{\mathrm{ref}}/N_{\mathrm{ref,max}}$. The resolution correction was calculated once for fluctuating reference flow $\bar{v}_n$ and once for constant reference flow of magnitude $\bar{v}_n = \langle \bar{v}_n \rangle$. The red and black dashed line describes the expected scaling with N_{ref} (cf. eq. (7.18)), if the reference particle multiplicity is lowered with respect to $N_{\mathrm{ref,max}}$. The scaling describes the resolution for constant $\bar{v}_n$, but overestimates the resolution in case of fluctuations. This effect just follows from the concaveness of $R(\chi)$, which implies that $\langle R(\chi) \rangle \leq R(\langle \chi \rangle)$.

Figure 7.6 (right) shows a simulation for the resolution R for three different event-plane detectors as a function of $\langle N_{\mathrm{part}} \rangle$. The reference particle multiplicities N_{ref} are chosen proportional to the number of participants $N_{\mathrm{ref}} = a_{\mathrm{EP}} N_{\mathrm{part}}$, while the parameters a_{EP} were chosen such that the true resolution R_{true} is similar to the resolution for the detectors used in the analysis described in chapter 9, namely the ALICE TPC, V0-A, and V0-C detectors. In this simulation, the only correlation is due to flow, non-flow correlations and calibration effects are explicitly neglected. The resolution is determined from a second identical detector ('2ep'), from the correlation with the other two detectors ('3ep'), and from two sub events ('2sub'). It can be seen that all three estimates differ from the true resolution R, which is shown as a solid line. In order to quantify this effect, the ratio of the estimated resolution to the true resolution R/R^{true} is shown in the lower panel. As expected from fig. 7.6 (left), the two sub-event method overestimates the resolution due to fluctuations, which can be seen when the ratio R/R^{true} is compared with the ratio $\sqrt{\langle \bar{v}_n^2 \rangle} / \langle \bar{v}_n \rangle$ (black line). Furthermore, also both other methods overestimate the resolution, but the effect decreases, if the resolution increases. The smallest deviations with respect to the true resolution are obtained for the TPC event plane, which also implies that the difference between the two-sub-event method and the three-event-planes method is most pronounced for the TPC. It can be concluded that the resolution is only estimated correctly in the perfect resolution limit ($R \to 1$), while the low resolution limit ($R \to 0$) asymptotically approaches the root mean square

$$\left\langle R^{\mathrm{2ep,3ep}} \right\rangle \underset{R^{\mathrm{true}} \to 0}{\Rightarrow} \left\langle R^{\mathrm{true}} \right\rangle \frac{\sqrt{\langle v_n^2 \rangle}}{\langle v_n \rangle} \ . \tag{7.23}$$

7.3.5 What does the event-plane method measure?

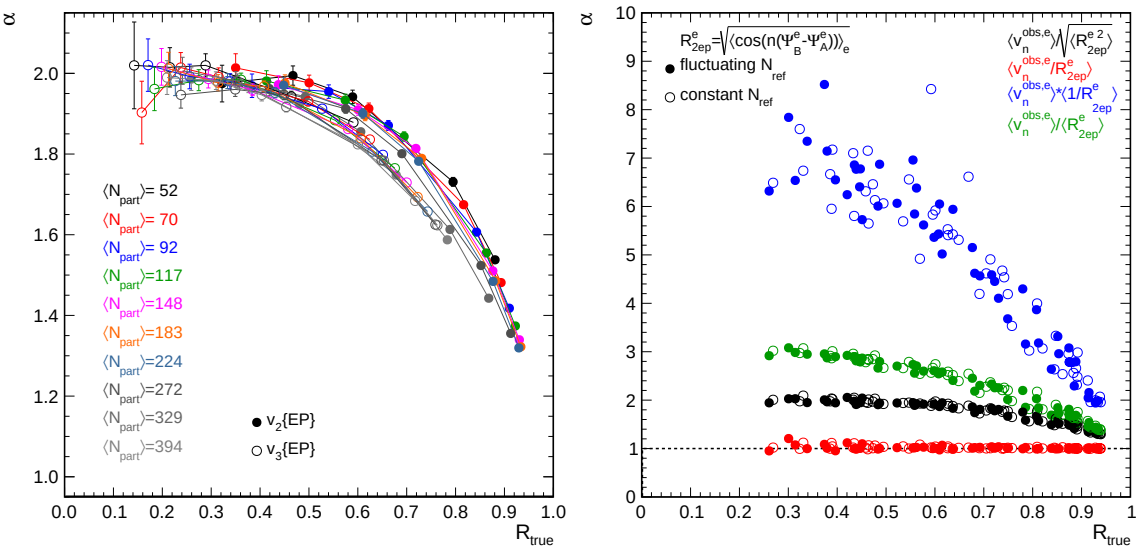

Figure 7.7: $v_n\{\mathrm{EP}\} = \langle v_n^\alpha \rangle^{1/\alpha}$ as a function of the true event-plane resolution R as obtained with the standard method for different $\langle N_{\mathrm{part}} \rangle$ (left) and as obtained from different averaging procedures (right). The event-plane resolution R was determined from the correlation with a second, identical detector ('2ep'). Details in text.

When the event-plane method was first developed, it was assumed that event-by-event fluctuations in v_n were negligible. It was explicitly stated [311] that the event-plane method measures rather the root mean square $\sqrt{\langle v_n^2 \rangle}$ than the mean value $\langle v_n \rangle$ in presence of flow fluctuations. It was further argued in [298] that the event-plane measurement is uncontrollably biased and thus yields an ambiguous measure between the root mean square and mean value

$$\langle v_n \rangle \leq v_n\{\mathrm{EP}\} \leq \sqrt{\langle v_n^2 \rangle} \ . \tag{7.24}$$

Figure 7.7 (left) shows a simulation for $v_n\{\mathrm{EP}\}$ for elliptic and triangular flow as a function of the true event-plane resolution R_{true} for different values of $\langle N_{\mathrm{ref}} \rangle$. For better comparability, $v_n\{\mathrm{EP}\}$ is expressed by $v_n\{\mathrm{EP}\} = \langle v_n^\alpha \rangle^{1/\alpha}$. Similar calculations can also be found in literature [67, 137]. It can be seen that the event-plane method measurement approaches the root mean square ($\alpha = 2$) for $R \to 0$. As the resolution increases, the measurement is continuously biased from the root mean square $\sqrt{\langle v_n^2 \rangle}$ towards the mean value $\langle v_n \rangle$ ($\alpha = 1$). The asymptotic behavior depends on $\langle N_{\mathrm{part}} \rangle$ and thus on the collision centrality. For v_3, the points are almost on a common line together with the v_2 result for central collisions. The reason might be that eccentricity fluctuations for those classes of events are almost Gaussian, while v_2 in mid-central and peripheral collisions originates mainly from the asymmetry of the nuclear overlap in the transverse plane (cf. section 7.1). In order to get a better understanding of this experimental bias and its features, the averaging procedure is studied in more detail in the following.

If fluctuations are present, the definition in eq. (7.15) is only valid for a single event. The single event average of for v_n^{e} for an event with reference flow $\bar{v}_n^{\mathrm{e}}$, $N_{\mathrm{ref}}^{\mathrm{e}}$ reference particles and $N_{\mathrm{poi}}^{\mathrm{e}}$ particles of interest can be defined as

$$v_n^{\mathrm{e}} = \frac{1}{N_{\mathrm{poi}}^{\mathrm{e}}} \sum_{i=0}^{N_{\mathrm{poi}}^{\mathrm{e}}} \frac{\cos\left(n\left(\phi_i - \Psi_n\right)\right)}{R\left(N_{\mathrm{ref}}^{\mathrm{e}}, \bar{v}_n^{\mathrm{e}}\right)} = \frac{v_n^{\mathrm{obs,e}}}{R\left(N_{\mathrm{ref}}^{\mathrm{e}}, \bar{v}_n^{\mathrm{e}}\right)} \ . \tag{7.25}$$

$R\left(N_{\mathrm{ref}}^{\mathrm{e}}, \bar{v}_n^{\mathrm{e}}\right)$ is the correction for the event-plane resolution, which depends on the reference particle multiplicity N_{ref} and the magnitude of the event reference flow $\bar{v}_n$. Averaging over N_{ev} events one obtains

$$\begin{aligned}
\left\langle v_n^{\mathrm{e}} \right\rangle &= \frac{1}{\sum_{j=0}^{N_{\mathrm{ev}}} N_{\mathrm{poi}}^{\mathrm{e}}} \sum_{j=0}^{N_{\mathrm{ev}}} \sum_{i=0}^{N_{\mathrm{poi}}^{\mathrm{e}}} \frac{\cos\left(n\left(\phi_i - \Psi_n\right)\right)}{R\left(N_{\mathrm{ref}}^{\mathrm{e}}, \bar{v}_n^{\mathrm{e}}\right)} && (7.26)\\
&= \frac{1}{\sum_{j=0}^{N_{\mathrm{ev}}} N_{\mathrm{poi}}^{\mathrm{e}}} \sum_{j=0}^{N_{\mathrm{ev}}} N_{\mathrm{poi}}^{\mathrm{e}} \frac{v_n^{\mathrm{obs,e}}}{R\left(N_{\mathrm{ref}}^{\mathrm{e}}, \bar{v}_n^{\mathrm{e}}\right)} && (7.27)\\
&= \left\langle \frac{v_n^{\mathrm{obs,e}}}{R\left(N_{\mathrm{ref}}^{\mathrm{e}}, \bar{v}_n^{\mathrm{e}}\right)} \right\rangle && (7.28)
\end{aligned}$$

It should be noted that in this definition of v_n the event average $\langle v_n^{\mathrm{e}} \rangle$ is implicitly weighted with the multiplicity $N_{\mathrm{poi}}^{\mathrm{e}}$, which is given by the centrality dependent cross-section of the particles of interest. Experimentally, the event-by-event resolution correction $R^{\mathrm{e}} = R\left(N_{\mathrm{ref}}^{\mathrm{e}}, \bar{v}_n^{\mathrm{e}}\right)$ is not accessible. Instead, the following following formula is used by many authors [52, 308, 312]

$$v_n^{\mathrm{meas}} = \frac{\left\langle v_n^{\mathrm{obs,e}} \right\rangle}{\langle R^{\mathrm{e}} \rangle} \ , \tag{7.29}$$

where $\langle R^{\mathrm{e}} \rangle$ is the resolution correction averaged over all events. Alternatively, one can also find another approximation [313]

$$v_n^{\mathrm{meas}} = \left\langle v_n^{\mathrm{obs,e}} \right\rangle \left\langle \frac{1}{R^{\mathrm{e}}} \right\rangle \ . \tag{7.30}$$

In the following, it shall be explicitly demonstrated that the two approaches eqs. (7.29) and (7.30) do generally not measure the mean value of the anisotropic flow. We do a Taylor expansion of $\frac{1}{R^{\mathrm{e}}}$ to the first order at $R^{\mathrm{e}} = \langle R^{\mathrm{e}} \rangle$ and use that $\frac{1}{R^{\mathrm{e}}}$ is a convex function ($\left(\frac{1}{R^{\mathrm{e}}}\right)'' > 0$) and strictly monotonically decreasing, which gives

$$\frac{1}{R^{\mathrm{e}}} \geq \frac{1}{\langle R^{\mathrm{e}} \rangle} - \frac{\left(R^{\mathrm{e}} - \langle R^{\mathrm{e}} \rangle\right)}{\langle R^{\mathrm{e}} \rangle^2} \ . \tag{7.31}$$

Taking the expected value, the second term vanishes ($\langle x - \langle x \rangle \rangle = 0$) and we obtain Jenssen's inequality

$$\left\langle \frac{1}{R^{\mathrm{e}}} \right\rangle \geq \frac{1}{\langle R^{\mathrm{e}} \rangle} \qquad \Rightarrow \qquad \left\langle v_n^{\mathrm{obs,e}} \right\rangle \left\langle \frac{1}{R^{\mathrm{e}}} \right\rangle \geq \frac{\left\langle v_n^{\mathrm{obs,e}} \right\rangle}{\langle R^{\mathrm{e}} \rangle} \ . \tag{7.32}$$

Similarly, we expand $v_n^{\mathrm{obs,e}}/R^{\mathrm{e}}$ to the first order. It is not obvious how $v_n^{\mathrm{obs,e}}/R^{\mathrm{e}}$ behaves as a function of $v_n^{\mathrm{obs,e}}/R^{\mathrm{e}}$. The resolution scales with the reference flow signal $\bar{v}_n$ and the multiplicity N_{ref} while the reference flow itself also changes with centrality. However, it is reasonable to assume the following asymptotic behavior:

$$v_n^{\mathrm{obs,e}}/R^{\mathrm{e}} = \begin{cases} \to 0 & \text{for} \quad R^{\mathrm{e}} \to 0 \\ \leq \bar{v}_{max} & \text{for} \quad R^{\mathrm{e}} \to 1 \end{cases} \tag{7.33}$$

Under the assumption of monotonicity and using that $\bar{v}_{max} < 1$, it is reasonable to assume that $v_n^{\mathrm{obs,e}}/R^{\mathrm{e}}$ behaves like a concave function. It follows that

$$\frac{v_n^{\mathrm{obs,e}}}{R^{\mathrm{e}}} \leq \frac{v_n^{\mathrm{obs,e}}}{\langle R^{\mathrm{e}} \rangle} - \frac{v_n^{\mathrm{obs,e}} \left(R^{\mathrm{e}} - \langle R^{\mathrm{e}} \rangle\right)}{\langle R^{\mathrm{e}} \rangle^2} \tag{7.34}$$

and evaluating the expected value gives

$$\left\langle \frac{v_n^{\mathrm{obs,e}}}{R^{\mathrm{e}}} \right\rangle \leq \frac{\left\langle v_n^{\mathrm{obs,e}} \right\rangle}{\langle R^{\mathrm{e}} \rangle} \ . \tag{7.35}$$

Finally, we obtain the following relation between eqs. (7.28) to (7.30):

$$\left\langle \frac{v_n^{\mathrm{obs,e}}}{R^{\mathrm{e}}} \right\rangle \leq \frac{\left\langle v_n^{\mathrm{obs,e}} \right\rangle}{\langle R^{\mathrm{e}} \rangle} \leq \left\langle v_n^{\mathrm{obs,e}} \right\rangle \left\langle \frac{1}{R^{\mathrm{e}}} \right\rangle \tag{7.36}$$

It can be seen that the calculation based on eq. (7.29) tends to give larger values than the mean value $\langle v_n \rangle$. In the limit of perfect resolution ($\Psi_n^{\mathrm{EP}} = \Psi_n \Rightarrow R = 1$), the outcome does not depend on the averaging procedure and $v_n\{\mathrm{EP}\}$ indeed measures the mean value

$$v_n\{\mathrm{EP}\} \underset{R=1}{=} \langle v_n \rangle \ . \tag{7.37}$$

Analytically, it is not obvious how $v_2\{\mathrm{EP}\}$ behaves for non-perfect resolution. Figure 7.7 (right) shows a simulation for $v_n\{\mathrm{EP}\}$ as determined by different averaging procedures. $v_n^{\mathrm{obs,e}}$ and $R\left(N_{\mathrm{ref}}^{\mathrm{e}}, \bar{v}_n^{\mathrm{e}}\right)$ are measured in small bins of $\bar{v}_n$ and N_{ref} and then $v_n\{\mathrm{EP}\}$ is evaluated according to the three approaches given in eqs. (7.28) to (7.30). The resolution correction is estimated from the correlation of two event planes ('2ep') as defined in eq. (7.19).
Using the exact formula eq. (7.28) (red), $v_n\{\mathrm{EP}\}$ exactly measures the mean value $\langle v_n \rangle$, while using eq. (7.29) the extracted $v_n\{\mathrm{EP}\}$ (black) approaches the root mean square ($\alpha \to 2$) as the resolution deteriorates. The third approach eq. (7.30) (blue) even overestimates the root mean square and should not be used. The green points show a modified version of eq. (7.28), where the resolution correction was averaged

$$\left\langle \sqrt{\cos\left(n\left(\Psi_n^{\mathrm{A}} - \Psi_n^{\mathrm{B}}\right)\right)} \right\rangle \approx \sqrt{\langle R_{\mathrm{true}}^2 \rangle} \tag{7.38}$$

instead of averaging the cosine expression before taking the square-root

$$\left\langle \cos\left(n\left(\Psi_n^{\mathrm{A}} - \Psi_n^{\mathrm{B}}\right)\right)\right\rangle = R_{\mathrm{true}} \tag{7.39}$$

The second approach eq. (7.39) yields exactly the true resolution R_{true}, while eq. (7.39) yields the root mean square of R_{true}, which can be seen in fig. 7.6 (right). Using the true resolution, the result approaches $\alpha = 3$. It can also be seen that multiplicity fluctuations in N_{ref} do not change the result.
Experimentally, $\bar{v}_n$ is not accessible unless the N_{ref} and $\bar{v}_n$ are large enough to be precisely determined event-by-event and thus eq. (7.29) (black) is the commonly used standard method. While the transition between mean and root mean square is not trivial to explain, the rms-like behavior for small resolutions can be understood as follows: In the low resolution limit ($R \to 0$), the numerator of eq. (7.15) is just a two-particle correlation, which measures $\langle v_n \bar{v}_n \rangle$. It was demonstrated in section 7.3.4 that the resolution correction measures the root mean square of the reference flow $\sqrt{\langle \bar{v}_n^2 \rangle}$ in the low resolution limit. Under the assumption that $v_n/\bar{v}_n = a$ is constant one obtains

$$v_n\{\mathrm{EP}\} \underset{R\to 0}{\Rightarrow} \frac{\langle v_n \bar{v}_n \rangle}{\sqrt{\langle \bar{v}_n^2 \rangle}} \underset{v_n = a\bar{v}_n}{\approx} \sqrt{\langle v_n^2 \rangle}\ . \tag{7.40}$$

A detailed discussion of the impact of non-flow contributions can be found in [137].

7.4 The scalar-product method

It was demonstrated that the event-plane method yields an ambiguous measure between the mean value and the root mean square. It is argued in [298] that the ambiguity of the event-plane method can be overcome by a simple modification of the event-plane method referred to as the ***scalar-product method*** [314]:

$$v_n\{\mathrm{SP}\} = \frac{\langle |Q_n| \cos\left(n\left(\phi - \Psi_n\right)\right)\rangle}{\bar{Q}_n} \tag{7.41}$$

The resolution correction $\bar{Q}_n$ is similar to that of the event-plane method, except without dividing by the magnitude of the measured flow vector. For two identical detectors A and B it is given by [298]

$$\bar{Q}_n = \sqrt{\left\langle \vec{Q}_{n,\mathrm{A}} \vec{Q}_{n,\mathrm{B}} \right\rangle} \tag{7.42}$$

and using a third detector C by

$$\bar{Q}_n = \sqrt{\frac{\left\langle \vec{Q}_{n,\mathrm{A}} \vec{Q}_{n,\mathrm{B}} \right\rangle \left\langle \vec{Q}_{n,\mathrm{A}} \vec{Q}_{n,\mathrm{C}} \right\rangle}{\left\langle \vec{Q}_{n,\mathrm{B}} \vec{Q}_{n,\mathrm{C}} \right\rangle}}\ . \tag{7.43}$$

The modified numerator measures $\langle N_{\mathrm{ref}} v_n \bar{v}_n \rangle$ and the denominator $\sqrt{\langle N_{\mathrm{ref}}^2 \bar{v}_n^2 \rangle}$. Neglecting fluctuations ($\sqrt{\langle N_{\mathrm{ref}}^2 \rangle} = \langle N_{\mathrm{ref}} \rangle$), the scalar-product method always yields the root mean square $\sqrt{\langle v_n^2 \rangle}$ regardless of the resolution:

$$v_n\{\mathrm{SP}\} = \frac{\langle N_{\mathrm{ref}} v_n \bar{v}_n \rangle}{\sqrt{\langle N_{\mathrm{ref}}^2 \bar{v}_n^2 \rangle}} \underset{N_{\mathrm{ref}}=const}{=} \sqrt{\langle v_n^2 \rangle} \tag{7.44}$$

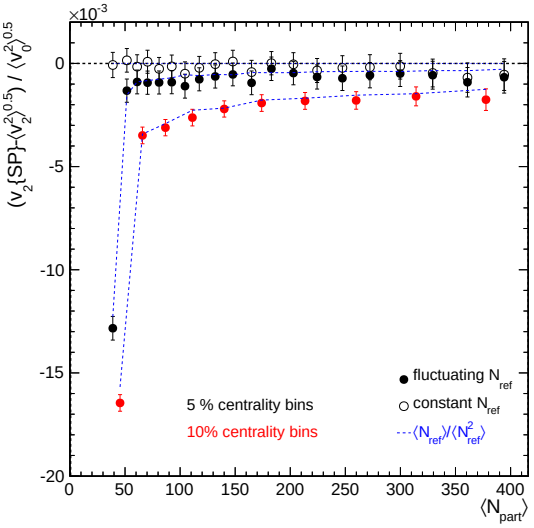

Figure 7.8: $v_n\{\mathrm{SP}\}/\sqrt{\langle v_n^2 \rangle}$ extracted in centrality bins of 5% and 10% as a function of $\langle N_{\mathrm{part}} \rangle$ with constant ($N_{\mathrm{ref}} = \mathrm{const}$) and fluctuating multiplicity ($N_{\mathrm{ref}} = \mathrm{const} \cdot N_{\mathrm{part}}$).

However, it can be shown that this statement is no longer valid, if the number of reference particles N_{ref} fluctuates. Figure 7.8 shows the ratio $v_n\{\mathrm{SP}\}/\sqrt{\langle v_n^2 \rangle}$ as a function of $\langle N_{\mathrm{part}} \rangle$. Analyses of heavy-ion collisions are usually done in finite centrality or multiplicity bins, which implies that $\langle N_{\mathrm{ref}} \rangle \neq \sqrt{\langle N_{\mathrm{ref}}^2 \rangle}$ and thus the measured $v_n\{\mathrm{SP}\}$ is expected to deviate from the root mean square. Only if fluctuations of N_{ref} within a given centrality bin (open points) are explicitly disabled, $v_n\{\mathrm{SP}\}$ exactly yields the root mean square. The simulation is done in 20 centrality bins including 5% of the inelastic cross section each with $N_{\mathrm{ref}} = \mathrm{const} \cdot N_{\mathrm{part}}$ (closed points). According to the considerations made above, the ratio $v_n\{\mathrm{SP}\}/\sqrt{\langle v_n^2 \rangle}$ can be described by

$$v_n\{\mathrm{SP}\} = \langle N_{\mathrm{ref}} \rangle / \sqrt{\langle N_{\mathrm{ref}}^2 \rangle} \sqrt{\langle v_n^2 \rangle} \,, \tag{7.45}$$

which is shown as a blue dashed line in fig. 7.8. It is obvious that relative fluctuations are more pronounced in mid-central and peripheral collisions, where the reference particle multiplicity N_{ref} is smaller. For comparison, the result is also shown for 10 centrality bins of 10% width each, which increases the width of fluctuations and decreases the measured value for $v_n\{\mathrm{SP}\}$. In central collisions, $v_n\{\mathrm{SP}\}$ is about 0.2% smaller than the root mean square and in peripheral collisions more than 1%, which are negligible corrections compared to typical systematic uncertainties.

7.5 Comparison of the cumulant, event-plane and scalar-product method

Figure 7.9 shows a simulation for the elliptic and triangular flow measured with the event-plane method $v_n\{\mathrm{EP}\}$, the scalar-product method $v_n\{\mathrm{SP}\}$ and the cumulant method $v_n\{2\}$ as a function of $\langle N_{\mathrm{part}} \rangle$. The measured anisotropies are normalized to the true anisotropy v_n. The root mean square of the true anisotropy is shown as a black line. It can be seen that the root mean square of the elliptic flow exceeds the mean value by about 6% in mid-central up

to 13% in the most central collisions for v_2. The root mean square of the triangular flow is about 13% larger than the mean value in all centrality classes for v_3. Similar results can be found in [298]. As expected from the considerations above, $v_2\{\mathrm{EP}\}$ shows a rms-like behavior, if the event-plane resolution is low, which is the case for V0-A and V0-C event plane for v_3 and in peripheral collisions also for v_2. Due to the higher resolution, the measurement with the TPC event plane is uncontrollably biased between the root mean square and the mean value. While the two-particle cumulant method exactly yields the root mean square, the scalar-product method shows small deviations in very peripheral collisions due to fluctuations in the number of reference particles N_{ref}. For more central collisions this effect can be neglected.

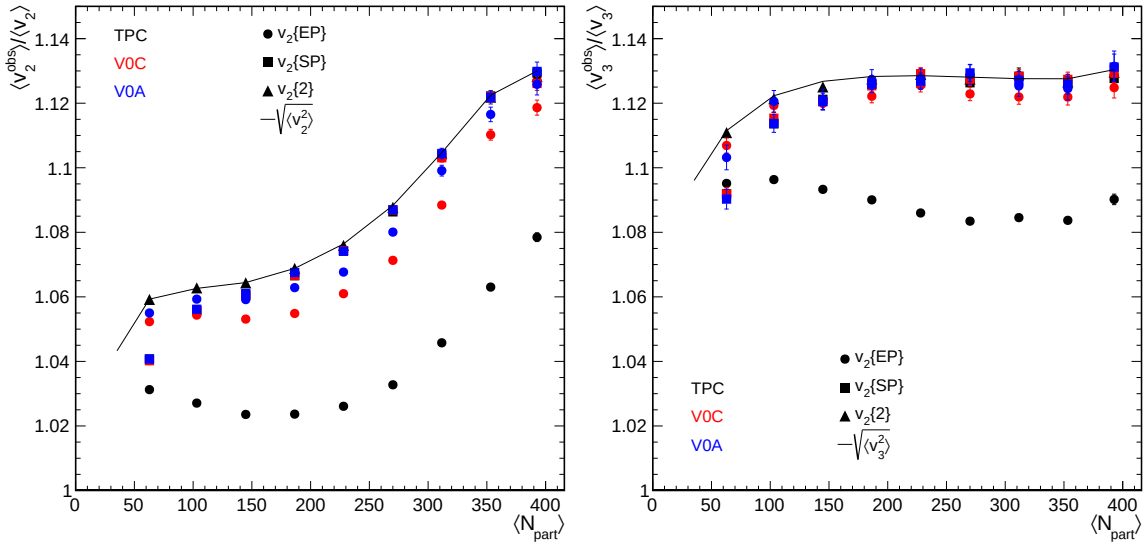

Figure 7.9: Simulation for elliptic (left) and triangular (right) flow measured with the event-plane, scalar-product, and two-particle cumulant method.

7.6 Extraction of the direct-photon anisotropic flow

7.6.1 Single event direct-photon anisotropy

The definition of experimentally observed inclusive photons includes photons from hadronic decays and a contribution of direct photons $N_{\gamma,\mathrm{inc}} = N_{\gamma,\mathrm{bg}} + N_{\gamma,\mathrm{dir}}$. The presence of azimuthal anisotropy leads to the following relation for inclusive photons for a single event

$$v_n^{\gamma,\mathrm{inc}} = \frac{1}{N_{\gamma,\mathrm{inc}}} \sum_i^{N_{\gamma,\mathrm{inc}}} \cos\left(n\left(\phi_i - \Psi_n\right)\right) \tag{7.46}$$

$$= \frac{N_{\gamma,\mathrm{bg}}}{N_{\gamma,\mathrm{inc}}} \underbrace{\frac{1}{N_{\gamma,\mathrm{bg}}} \sum_i^{N_{\gamma,\mathrm{bg}}} \cos\left(n\left(\phi_i - \Psi_n\right)\right)}_{v_n^{\gamma,\mathrm{bg}}} + \frac{N_{\gamma,\mathrm{dir}}}{N_{\gamma,\mathrm{inc}}} \underbrace{\frac{1}{N_{\gamma,\mathrm{dir}}} \sum_i^{N_{\gamma,\mathrm{dir}}} \cos\left(n\left(\phi_i - \Psi_n\right)\right)}_{v_n^{\gamma,\mathrm{dir}}} \tag{7.47}$$

$$= \frac{v_n^{\gamma,\mathrm{bg}} + (R-1)\, v_n^{\gamma,\mathrm{dir}}}{R} \tag{7.48}$$

with $R = N_{\gamma,\mathrm{inc}}/N_{\gamma,\mathrm{bg}}$. Solving for $v_n^{\gamma,\mathrm{dir}}$, we obtain

$$v_n^{\gamma,\mathrm{dir}} = \frac{R v_n^{\gamma,\mathrm{inc}} - v_n^{\gamma,\mathrm{bg}}}{R-1} \ , \tag{7.49}$$

which is the relation that can be found in literature (cf. section 4.4).

7.6.2 Event mean and root mean square of the direct-photon anisotropy

In the following, it shall be clarified, whether relation eq. (7.49) still holds, if the anisotropic flow is averaged over many events with fluctuating initial conditions. From $E[X+Y] = E[X] + E[Y]$, it directly follows that the above relation eq. (7.49) holds for the event mean value

$$\left\langle v_n^{\gamma,\mathrm{dir}} \right\rangle = \frac{R\left\langle v_n^{\gamma,\mathrm{inc}} \right\rangle - \left\langle v_n^{\gamma,\mathrm{bg}} \right\rangle}{R-1} \ . \tag{7.50}$$

However, it has been shown in section 7.5 that most experimental methods measure the root mean square rather than the mean value depending on the details of the analysis. We will now derive the corresponding relation for the root mean square value:

$$\sqrt{\left\langle v_n^{\gamma,\mathrm{dir}\ 2} \right\rangle} = \left\langle \frac{\left(R v_n^{\gamma,\mathrm{inc}} - v_n^{\gamma,\mathrm{bg}}\right)^2}{(R-1)^2} \right\rangle \tag{7.51}$$

$$= \sqrt{\frac{R^2\left\langle v_n^{\gamma,\mathrm{inc}\ 2} \right\rangle + \left\langle v_n^{\gamma,\mathrm{bg}\ 2} \right\rangle - 2R\left\langle v_n^{\gamma,\mathrm{inc}} v_n^{\gamma,\mathrm{bg}} \right\rangle}{(R-1)^2}} \tag{7.52}$$

We apply the binomial formula, which gives

$$\sqrt{\left\langle v_n^{\gamma,\mathrm{dir}\ 2} \right\rangle} = \frac{1}{(R-1)} \sqrt{\left(R\sqrt{\left\langle v_n^{\gamma,\mathrm{inc}\ 2} \right\rangle} - \sqrt{\left\langle v_n^{\gamma,\mathrm{bg}\ 2} \right\rangle} \right)^2 + 2A} \tag{7.53}$$

with

$$A = \sqrt{\left\langle v_n^{\gamma,\mathrm{inc}\ 2} \right\rangle}\sqrt{\left\langle v_n^{\gamma,\mathrm{bg}\ 2} \right\rangle} - \left\langle v_n^{\gamma,\mathrm{inc}} v_n^{\gamma,\mathrm{bg}} \right\rangle \ . \tag{7.54}$$

It can be seen that eq. (7.49) does generally not hold for the root mean square for $A \neq 0$.

7.6.3 Study of different scenarios for the direct-photon production

The mean value is experimentally only accessible in the perfect resolution limit of the event-plane method, or if the anisotropy coefficients are measured event by event. It was shown in section 7.5 that the event-plane $v_n\{\mathrm{EP}\}$ and scalar-product $v_n\{\mathrm{SP}\}$ measurements yield

$$\begin{matrix} v_n\{\mathrm{EP}\} \\ v_n\{\mathrm{SP}\} \end{matrix} = \frac{\langle v_n \bar{v}_n \rangle}{\sqrt{\langle \bar{v}_n^2 \rangle}} \begin{cases} \text{if} & R \to 0 \\ \text{if} & \sqrt{\left\langle N_{\mathrm{ref}}^2 \right\rangle} / \left\langle N_{\mathrm{ref}} \right\rangle \to 0 \end{cases} \tag{7.55}$$

in the low resolution limit and if multiplicity fluctuations are negligible. The cumulant method $v_n\{2\}$ always yields the root mean square

$$v_n\{2\} = \sqrt{\langle v_n^2 \rangle} \; . \tag{7.56}$$

It was also argued in section 7.3.5 that under the assumption of a linear relation between the reference flow $\bar{v}_n$ and the particle of interest v_n ($\bar{v}_n = x v_n$), the scalar-product and event-plane method measure the root mean square

$$\frac{\langle v_n \bar{v}_n \rangle}{\sqrt{\langle \bar{v}_n^2 \rangle}} = \frac{x \left\langle v_n^2 \right\rangle}{x \sqrt{\langle v_n^2 \rangle}} = \sqrt{\langle v_n^2 \rangle} \tag{7.57}$$

Even though the linear relation might be a good assumption for any particle produced at the same time as the hadronic bulk, it is not obvious at all, if that relation ($v_n^{\gamma,\mathrm{dir}} = x \bar{v}_n$) holds for direct photons, which are are emitted over the whole system evolution. It will be interesting to see what different methods yield under different assumptions for the direct-photon anisotropic flow

$$v_n^{\gamma,\mathrm{dir}}\{\mathrm{EP,SP,2}\} = \frac{R v_n^{\gamma,\mathrm{inc}}\{\mathrm{EP,SP,2}\} - v_n^{\gamma,\mathrm{bg}}\{\mathrm{EP,SP,2}\}}{R-1} \; . \tag{7.58}$$

From eq. (7.53) we obtain

$$v_n^{\gamma,\mathrm{dir}}\{2\} = \sqrt{v_n^{\gamma,\mathrm{dir}\ 2} - \frac{A}{R-1}} \; . \tag{7.59}$$

It can be demonstrated that the relation eq. (7.49) also holds for $\langle v_n \bar{v}_n \rangle$:

$$\left\langle v_n^{\gamma,\mathrm{inc}} \bar{v}_n \right\rangle = \frac{1}{N_{\gamma,\mathrm{inc}} N_{\mathrm{ref}}} \sum_i^{N_{\gamma,\mathrm{inc}}} \sum_j^{N_{\mathrm{ref}}} \cos\left(n\left(\phi_i - \phi_j\right)\right) \tag{7.60}$$

$$= \frac{1}{R^2} \underbrace{\frac{1}{N_{\gamma,\mathrm{bg}}^2} \sum_i^{N_{\gamma,\mathrm{bg}}} \sum_j^{N_{\gamma,\mathrm{bg}}} \cos\left(n\left(\phi_i - \phi_j\right)\right)}_{\left\langle v_n^{\gamma,\mathrm{bg}} \bar{v}_n \right\rangle}$$

$$= + \frac{R-1}{R} \underbrace{\frac{1}{N_{\gamma,\mathrm{dir}} N_{\mathrm{ref}}} \sum_i^{N_{\gamma,\mathrm{dir}}} \sum_j^{N_{\mathrm{ref}}} \cos\left(n\left(\phi_i - \phi_j\right)\right)}_{\left\langle v_n^{\gamma,\mathrm{dir}} \bar{v}_n \right\rangle} \tag{7.61}$$

$$= \frac{\left\langle v_n^{\gamma,\mathrm{bg}} \bar{v}_n \right\rangle + (R-1) \left\langle v_n^{\gamma,\mathrm{dir}} \bar{v}_n \right\rangle}{R} \tag{7.62}$$

Solving for $\left\langle v_n^{\gamma,\mathrm{dir}}\bar{v}_n\right\rangle$ and dividing by $\sqrt{\langle\bar{v}_n^2\rangle}$ we obtain

$$v_n^{\gamma,\mathrm{dir}}\{\mathrm{EP,SP}\} = \frac{\left\langle v_n^{\gamma,\mathrm{dir}}\bar{v}_n\right\rangle}{\sqrt{\langle\bar{v}_n^2\rangle}} = \frac{1}{R-1}\left(R\underbrace{\frac{\left\langle v_n^{\gamma,\mathrm{inc}}\bar{v}_n\right\rangle}{\sqrt{\langle\bar{v}_n^2\rangle}}}_{v_n^{\gamma,\mathrm{inc}}\{\mathrm{EP,SP}\}} - \underbrace{\frac{\left\langle v_n^{\gamma,\mathrm{bg}}\bar{v}_n\right\rangle}{\sqrt{\langle\bar{v}_n^2\rangle}}}_{v_n^{\gamma,\mathrm{bg}}\{\mathrm{EP,SP}\}}\right) \tag{7.63}$$

and it follows that event-plane and scalar-product method will always measure $\left\langle v_n^{\gamma,\mathrm{dir}}\bar{v}_n\right\rangle/\sqrt{\langle\bar{v}_n^2\rangle}$ regardless of any detail on the photon production. However, it is not clear how this measure is related to the root mean square and mean value of $v_n^{\gamma,\mathrm{dir}}$.

In the following, we four different scenarios for the direct photon production and the outcome using the event-plane, the scalar-product and the two-particle cumulant method are studied. In particular, for all cases upper limits are determined in order to demonstrate that a large direct-photon anisotropy cannot appear due to artifacts of the methods. In our model, we make the following assumptions:

1. The direction of the maximum direct-photon anisotropy is the same as for the reference particles. A decorrelation of the maximum flow direction would always reduce the correlation between photons and reference particles and thus reduce the measured anisotropy. Hydrodynamic calculations yield a tight correlation between the thermal photon flow angle and the hadron flow angle, which is reduced by p_T-dependent viscous corrections. The decorrelation is largest for photons produced at early times [315].

2. We assume a linear relation between the anisotropy of the particles used to calculate the event plane and the decay photons $v_n^{\gamma,\mathrm{bg}} = c_{\gamma,\mathrm{bg}}\bar{v}_n$. Since the result does not depend on the choice of the constant $c_{\gamma,\mathrm{bg}}$, we set $c_{\gamma,\mathrm{bg}} = 1$ in order to minimize statistical uncertainties.

3. The inclusive-photon anisotropy is calculated from the decay and direct-photon anisotropy according to eq. (7.48). For simplicity, it is assumed that $R^{\gamma,dir} = 1.2$, which is close to the direct-photon excess observed in 0 - 40% Pb-Pb collisions at the LHC (cf. section 10.2.1).

4. In the cumulant method, $v_n^{\gamma,\mathrm{inc}}\{2\}$ is calculated from the correlation of inclusive photons and $v_n^{\gamma,\mathrm{bg}}\{2\}$ from the correlation of decay photons.

5. The direct-photon anisotropy is evaluated using equation eq. (7.58).

7.6.3.1 Constant relation between direct-photon and reference flow

In case of a linear relation $c_{\gamma,\mathrm{inc}}v_n^{\gamma,\mathrm{inc}} = c_{\gamma,\mathrm{bg}}v_n^{\gamma,\mathrm{bg}} = c_{\gamma,\mathrm{dir}}v_n^{\gamma,\mathrm{dir}} = \bar{v}_n$ with

$$c_{\gamma,\mathrm{inc}} = (c_{\gamma,\mathrm{bg}} + (R-1)c_{\gamma,\mathrm{dir}})/R\ , \tag{7.64}$$

we can substitute all contributions in eq. (7.63) according to eq. (7.57) by the root mean square and obtain

$$\sqrt{\left\langle v_n^{\gamma,\mathrm{dir}^2}\right\rangle} = \frac{R\sqrt{\left\langle v_n^{\gamma,\mathrm{inc}^2}\right\rangle} - \sqrt{\left\langle v_n^{\gamma,\mathrm{bg}^2}\right\rangle}}{R-1}\ . \tag{7.65}$$

We can also derive this relation from eq. (7.53) by using

$$\left\langle v_n^{\gamma,\mathrm{inc}} v_n^{\gamma,\mathrm{bg}} \right\rangle = x \left\langle \left(v_n^{\gamma,\mathrm{bg}} \right)^2 \right\rangle = x^{-1} \left\langle \left(v_n^{\gamma,\mathrm{inc}} \right)^2 \right\rangle = \sqrt{\left\langle v_n^{\gamma,\mathrm{inc}\,2} \right\rangle} \sqrt{\left\langle v_n^{\gamma,\mathrm{bg}\ 2} \right\rangle} \tag{7.66}$$

with $x = c_{\gamma,\mathrm{inc}}/c_{\gamma,\mathrm{bg}}$. In this case $A = 0$ and we obtain again eq. (7.65).
Such conditions could most likely be the case, if direct photons were emitted in a similar stage compared to the hadronic bulk. In that case, relation eq. (7.49) also holds for the root mean square and the scalar-product and event-plane method deliver similar results than for hadrons:

$$v_n^{\gamma,\mathrm{dir}}\{\mathrm{EP}\} < v_n^{\gamma,\mathrm{dir}}\{\mathrm{SP}\} \leq v_n^{\gamma,\mathrm{dir}}\{2\} = \sqrt{\left\langle v_n^{\gamma,\mathrm{dir}\ 2} \right\rangle} \tag{7.67}$$
$$\text{for} \qquad c_{\gamma,\mathrm{inc}} v_n^{\gamma,\mathrm{inc}} = c_{\gamma,\mathrm{bg}} v_n^{\gamma,\mathrm{bg}} = c_{\gamma,\mathrm{dir}} v_n^{\gamma,\mathrm{dir}} = \bar{v}_n$$

The outcome of the simulation is shown in fig. 7.10 (left). Under this assumption, systematic biases of the measurement with respect to the root mean square value similar to the systematic effects for hadrons as described in section 7.5. While the cumulant method and the scalar-product method exactly measure the root mean square, the event-plane method yields a measure between root mean square and mean value. Deviations are most pronounced for the measurement with respect to the TPC event plane, for the V0-A and V0-C event plane, deviations from the root mean square are smaller than 1%.

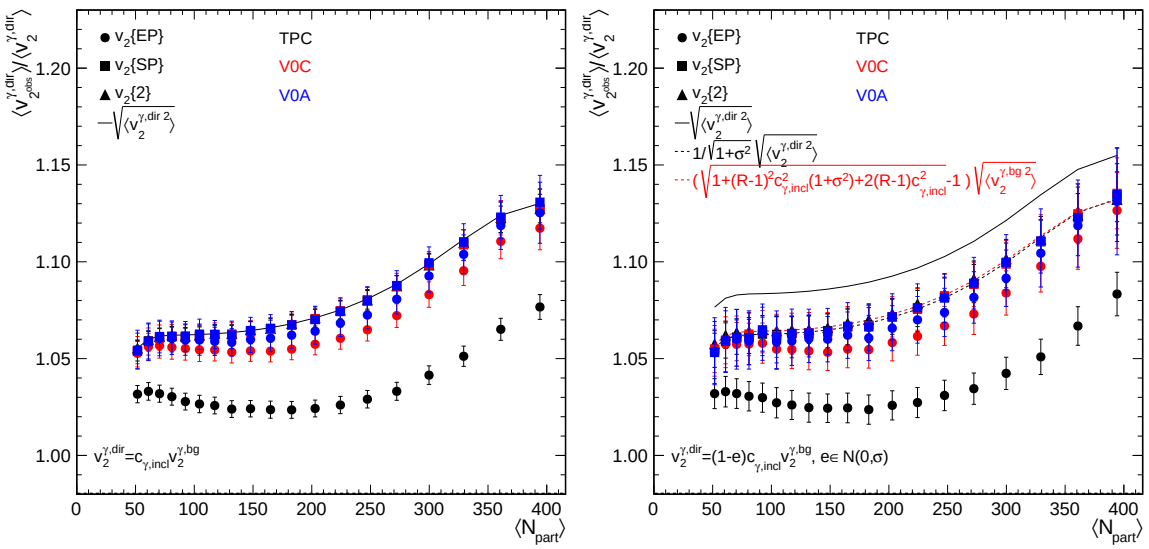

Figure 7.10: Direct-photon elliptic flow measured with the event-plane, scalar-product, and two-particle cumulant method in a Glauber Monte Carlo simulation with a constant (left) and a fluctuating (right) relation between direct-photon and event-by-event bulk anisotropic flow.

7.6.3.2 Fluctuating relation between direct-photon and reference flow

Now we consider that the direct-photon anisotropy is correlated with the bulk, but contains some independent Gaussian fluctuations $v_n^{\gamma,\mathrm{dir}} = (1-\epsilon)\, c_{\gamma,\mathrm{dir}} \bar{v}_n$ with $\langle\epsilon\rangle = 0$ and $\sqrt{\langle\epsilon^2\rangle} = \sigma_\epsilon$. This assumption could be valid, if direct photons are emitted early, when pressure gradients are still changing. If the direction of the maximum flow changes over time, direct photons and the bulk become even more decorrelated resulting into smaller values for the extract direct-photon anisotropy. It follows that

$$\left\langle v_n^{\gamma,\mathrm{dir}} \right\rangle = c_{\gamma,\mathrm{dir}} \left\langle \bar{v}_n \right\rangle \qquad (\langle\epsilon\rangle = 0) \ , \tag{7.68}$$

$$\sqrt{\left\langle v_n^{\gamma,\mathrm{dir}\ 2} \right\rangle} = \sqrt{1+\sigma_\epsilon^2} c_{\gamma,\mathrm{dir}}^{-1} \sqrt{\langle \bar{v}_n^2 \rangle} \qquad \left(\langle\epsilon^2\rangle = \sigma_\epsilon^2\right) \ , \tag{7.69}$$

and

$$\left\langle v_n^{\gamma,\mathrm{dir}} \bar{v}_n \right\rangle = \left\langle (1-\epsilon)\, c_{\gamma,\mathrm{dir}}^{-1} \bar{v}_n^2 \right\rangle = c_{\gamma,\mathrm{dir}}^{-1} \left\langle \bar{v}_n^2 \right\rangle = \frac{\left\langle v_n^{\gamma,\mathrm{dir}\ 2} \right\rangle}{c_{\gamma,\mathrm{dir}}^{-1} (1+\sigma_\epsilon^2)} \ . \tag{7.70}$$

Combining eqs. (7.69) and (7.70), we obtain

$$\frac{\left\langle v_n^{\gamma,\mathrm{dir}} \bar{v}_n \right\rangle}{\sqrt{\langle \bar{v}_n^2 \rangle}} = \frac{\sqrt{1+\sigma_\epsilon^2} c_{\gamma,\mathrm{inc}}^{-1} \left\langle v_n^{\gamma,\mathrm{dir}\ 2} \right\rangle}{c_{\gamma,\mathrm{inc}}^{-1} (1+\sigma_\epsilon^2) \sqrt{\left\langle v_n^{\gamma,\mathrm{dir}\ 2} \right\rangle}} = \frac{1}{\sqrt{1+\sigma_\epsilon^2}} \sqrt{\left\langle v_n^{\gamma,\mathrm{dir}\ 2} \right\rangle} \ . \tag{7.71}$$

It can already be seen that the event-plane and scalar product method always yield values smaller than the root mean square. In order to deduce the corresponding relations for the two-particle cumulant method, we use that

$$\sqrt{\left\langle v_n^{\gamma,\mathrm{dir}\ 2} \right\rangle} = \left(\frac{c_{\gamma,\mathrm{dir}}}{c_{\gamma,\mathrm{bg}}} \right)^2 (1+\sigma_\epsilon^2) \sqrt{\left\langle v_n^{\gamma,\mathrm{bg}\ 2} \right\rangle} \tag{7.72}$$

and

$$\left\langle v_n^{\gamma,\mathrm{dir}} v_n^{\gamma,\mathrm{bg}} \right\rangle = \frac{c_{\gamma,\mathrm{dir}}}{c_{\gamma,\mathrm{bg}}} \sqrt{\left\langle v_n^{\gamma,\mathrm{bg}\ 2} \right\rangle} \ . \tag{7.73}$$

Evaluating **??**, the cumulant methods gives for the inclusive-photon anisotropy

$$\sqrt{\left\langle v_n^{\gamma,\mathrm{inc}\ 2} \right\rangle} = \frac{1}{R} \sqrt{1 + (R-1)^2 \left(\frac{c_{\gamma,\mathrm{dir}}}{c_{\gamma,\mathrm{bg}}} \right)^2 (1+\sigma^2) + 2\,(R-1)\, \frac{c_{\gamma,\mathrm{dir}}}{c_{\gamma,\mathrm{bg}}}} \sqrt{\left\langle v_n^{\gamma,\mathrm{bg}\ 2} \right\rangle} \ . \tag{7.74}$$

We insert $1+\sigma_\epsilon^2$ in the third term and obtain the following inequality

$$\sqrt{\left\langle v_n^{\gamma,\mathrm{inc}\ 2} \right\rangle} \leq \frac{1}{R} \sqrt{\left(1 + (R-1) \left(\frac{c_{\gamma,\mathrm{dir}}}{c_{\gamma,\mathrm{bg}}} \right) \sqrt{1+\sigma_\epsilon^2} \right)^2} \sqrt{\left\langle v_n^{\gamma,\mathrm{bg}\ 2} \right\rangle} \ . \tag{7.75}$$

Inserting eq. (7.75) in eq. (7.58) we finally obtain

$$v_n^{\gamma,\mathrm{dir}}\{2\} \leq \frac{c_{\gamma,\mathrm{dir}}}{c_{\gamma,\mathrm{bg}}}\sqrt{1+\sigma_\epsilon}\sqrt{\left\langle v_n^{\gamma,\mathrm{bg}\ 2}\right\rangle} = \sqrt{\left\langle v_n^{\gamma,\mathrm{dir}\ 2}\right\rangle} \tag{7.76}$$

Finally, we obtain:

$$\begin{aligned} v_n^{\gamma,\mathrm{dir}}\{\mathrm{EP}\} < v_n^{\gamma,\mathrm{dir}}\{\mathrm{SP}\} &\leq \frac{\sqrt{\left\langle v_n^{\gamma,\mathrm{dir}\ 2}\right\rangle}}{\sqrt{1+\sigma_\epsilon^2}} \\ v_n^{\gamma,\mathrm{dir}}\{2\} &\leq \sqrt{\left\langle v_n^{\gamma,\mathrm{dir}\ 2}\right\rangle} \\ \text{for} \qquad v_n^{\gamma,\mathrm{dir}} &= (1-\epsilon)\, c\bar{v}_n\ ,\ \epsilon \in \mathcal{N}(0,\sigma_\epsilon) \end{aligned} \tag{7.77}$$

It can be immediately seen that the extracted anisotropy is always smaller than the root mean square for all three methods. The results of the simulation are shown in fig. 7.10 (right). In the simulation, we have chosen $c_{\gamma,\mathrm{dir}} = 0.5$ and $\sigma_\epsilon = 0.2$. For the scalar-product method, the extracted anisotropies are consistent with the upper limit (black dashed line) and always smaller than the upper limit for the event-plane method. For the two-particle cumulant method, the results seem to be consistent with the upper limit for the event-plane and scalar-product method, the exact outcome for the two-particle cumulant method is given by

$$v_n^{\gamma,\mathrm{dir}}\{2\} = \frac{\left(\sqrt{1+(R-1)^2\left(\frac{c_{\gamma,\mathrm{dir}}}{c_{\gamma,\mathrm{bg}}}\right)^2(1+\sigma^2)+2\,(R-1)\,\frac{c_{\gamma,\mathrm{dir}}}{c_{\gamma,\mathrm{bg}}}}-1\right)}{R-1}\sqrt{\left\langle v_n^{\gamma,\mathrm{bg}\ 2}\right\rangle}\ , \tag{7.78}$$

which is shown as a red dashed line in fig. 7.10 (right). The result is slightly above the upper limit for the event-plane and scalar-product method, which can be shown by setting $1+\sigma_\epsilon^2 = 1$ in eq. (7.74):

$$v_n^{\gamma,\mathrm{dir}}\{2\} \geq \frac{\sqrt{\left\langle v_n^{\gamma,\mathrm{dir}\ 2}\right\rangle}}{\sqrt{1+\sigma_\epsilon^2}} \tag{7.79}$$

7.6.3.3 Zero direct-photon anisotropy

It can be easily shown that all methods measure zero for a zero direct-photon anisotropy. Such conditions are expected, if direct photons are created early, for instance in hard initial scattering in next-to-leading-order pQCD processes. It immediately follows that $\langle v_n \bar{v}_n \rangle = 0$ and thus both, scalar-product and event-plane method, yield zero. Using $\left\langle v_n^{\gamma,\mathrm{dir}} v_n^{\gamma,\mathrm{bg}}\right\rangle = 0$ in **????** gives $\left\langle v_n^{\gamma,\mathrm{inc}} v_n^{\gamma,\mathrm{bg}}\right\rangle = v_n^{\gamma,\mathrm{bg}\ 2}/R$ and $\sqrt{\left\langle v_n^{\gamma,\mathrm{inc}\ 2}\right\rangle} = \sqrt{\left\langle v_n^{\gamma,\mathrm{bg}\ 2}\right\rangle}/R$, from which follows that $A = 0$ and $\sqrt{\left\langle v_n^{\gamma,\mathrm{dir}\ 2}\right\rangle} = 0$. Finally, we obtain:

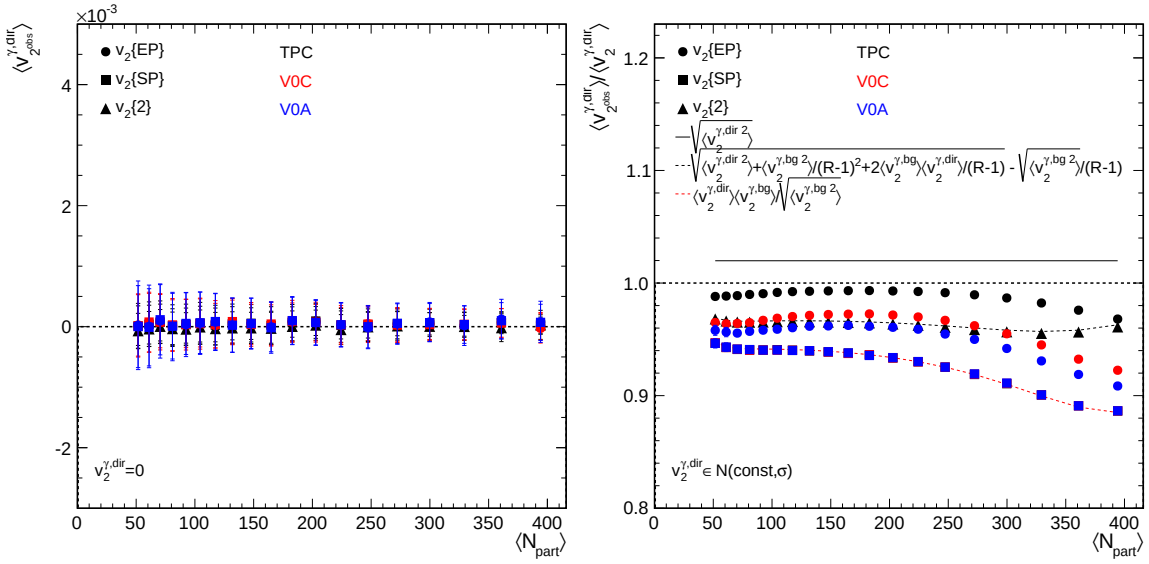

Figure 7.11: Direct-photon elliptic flow measured with the event-plane, scalar-product, and two-particle cumulant method in a Glauber Monte Carlo simulation with zero direct-photon anisotropic flow (left) and direct-photon anisotropic flow with an independent probability distribution with respect to the bulk flow (right).

$$v_n^{\gamma,\mathrm{dir}}\{\mathrm{SP}\} = v_n^{\gamma,\mathrm{dir}}\{\mathrm{EP}\} = v_n^{\gamma,\mathrm{dir}}\{\mathrm{SP}\} \leq v_n^{\gamma,\mathrm{dir}}\{2\} = 0 \quad \text{for} \quad v_n^{\gamma,\mathrm{dir}} = 0 \tag{7.80}$$

The results of the simulation (fig. 7.11 (left)) are consistent with zero within uncertainties and thus confirm the considerations made above.

7.6.3.4 Independent probability distribution of the direct-photon anisotropy

Now we consider that the direct-photon flow undergoes small independent fluctuations $v_n \in \mathcal{N}(\mathrm{const}, \sigma)$. Such an independent probability distribution might apply to photons, which are produced very early or if the mechanism that produces the direct-photon azimuthal anisotropy is not the hydrodynamic evolution. Since the probabilities are independent, it immediately follows that $\langle v_n \bar{v}_n \rangle = \langle v_n \rangle \langle \bar{v}_n \rangle$ and thus both, scalar-product and event-plane method, measure

$$\frac{\left\langle v_n^{\gamma,\mathrm{dir}} \bar{v}_n \right\rangle}{\sqrt{\langle \bar{v}_n^2 \rangle}} = \left\langle v_n^{\gamma,\mathrm{dir}} \right\rangle \frac{\langle \bar{v}_n \rangle}{\sqrt{\langle \bar{v}_n^2 \rangle}} \,, \tag{7.81}$$

which gives a a constant correction $\langle \bar{v}_n \rangle / \sqrt{\langle \bar{v}_n^2 \rangle} < 1$. Evaluating **??**, the cumulant methods yields for the inclusive photons

$$\sqrt{\left\langle v_n^{\gamma,\mathrm{inc}\ 2} \right\rangle} = \sqrt{\frac{\left\langle v_n^{\gamma,\mathrm{bg}\ 2} \right\rangle + (R-1)^2 \left\langle v_n^{\gamma,\mathrm{dir}\ 2} \right\rangle + 2\,(R-1) \left\langle v_n^{\gamma,\mathrm{dir}} \right\rangle \left\langle v_n^{\gamma,\mathrm{bg}} \right\rangle}{R^2}} \,. \tag{7.82}$$

Inserting eq. (7.82) in eq. (7.58), we obtain

$$v_n^{\gamma,\mathrm{dir}}\{2\} = \sqrt{\left\langle v_n^{\gamma,\mathrm{dir}\ 2}\right\rangle + \frac{\left\langle v_n^{\gamma,\mathrm{bg}\ 2}\right\rangle}{(R-1)^2} + \frac{2\left\langle v_n^{\gamma,\mathrm{dir}}\right\rangle\left\langle v_n^{\gamma,\mathrm{bg}}\right\rangle}{R-1}} - \frac{\sqrt{\left\langle v_n^{\gamma,\mathrm{bg}\ 2}\right\rangle}}{R-1}\ . \tag{7.83}$$

Upper limits can be estimated by replacing the mean values $\left\langle v_n^{\gamma,\mathrm{dir}}\right\rangle$ and $\left\langle v_n^{\gamma,\mathrm{bg}}\right\rangle$ with the corresponding root mean square values, which finally gives:

$$\begin{aligned} v_n^{\gamma,\mathrm{dir}}\{\mathrm{SP}\} = \left\langle v_n^{\gamma,\mathrm{dir}}\right\rangle \frac{\langle \bar{v}_n\rangle}{\sqrt{\langle \bar{v}_n^2\rangle}} \leq v_n^{\gamma,\mathrm{dir}}\{\mathrm{EP}\} \leq \left\langle v_n^{\gamma,\mathrm{dir}}\right\rangle \\ v_n^{\gamma,\mathrm{dir}}\{2\} \leq \sqrt{\left\langle v_n^{\gamma,\mathrm{dir}\ 2}\right\rangle} \\ \text{if} \qquad v_n^{\gamma,\mathrm{dir}} = 0 \end{aligned} \tag{7.84}$$

The sign of the inequality for the event-plane method follows from the fact that the event-plane method measures the mean value in the perfect resolution limit. The results of the simulation are shown in fig. 7.11 (right), together with the deduced relations. The outcome for the event-plane and scalar-product method are always smaller than the mean value $\left\langle v_n^{\gamma,\mathrm{dir}}\right\rangle$, since the mean to root mean square ratio $\langle \bar{v}_n\rangle / \sqrt{\langle \bar{v}_n^2\rangle}$ is always smaller than unity.

7.7 Summary

This chapter reviewed the most relevant methods for measuring anisotropic flow, with particular focus on the role of flow fluctuations.
It was demonstrated that the event-plane method rather measures the root mean square $\sqrt{\langle v_n^2\rangle}$ than the mean value v_n of the azimuthal anisotropy. However, the measurement is not generally uncontrollably biased as quoted by the authors of [298]. It was demonstrated that using the event planes from the V0-A or V0-C, relative deviations for the extracted $v_n\{\mathrm{EP}\}$ from the root mean square $\sqrt{\langle v_n^2\rangle}$ are expected to be less than 1%. The full TPC event plane should not be used for the measurement, since it yields values somewhere between the root mean square and mean value. Furthermore, it was shown that the experimentally measured resolution correction does not follow the expected scaling with $\sqrt{N_{\mathrm{ref}}}$ and thus the resolution correction should not be estimated from sub events.
It has been further stressed out that the analysis should be done in small centrality bins in order to reduce systematic biasses due to fluctuations. It was shown that even the scalar-product method yields slightly smaller values than the root mean square, if multiplicity fluctuations are present. The cumulant method always yields the root mean square of the azimuthal anisotropy. It was shown that using Glauber initial conditions fluctuations yield an up to 13% larger root mean square $\sqrt{\langle v_n^2\rangle}$ than the mean value $\langle v_n\rangle$ in central collisions. Since all experimental methods can only access the root mean square, fluctuations should be taken into account by any hydrodynamic calculation when compared to data. Estimates for the magnitude of corrections for different centralities were explicitly calculated.

Finally, it was shown that the three different methods yield different results for the direct-photon azimuthal anisotropy, depending on the details of the direct photon production. Theorists should calculate rather the root mean square than the mean value or even both quantities, if possible. Furthermore, it would be fruitful to run the simulation with input from hydrodynamic calculations. Four different hypotheses for the direct-photon anisotropic flow were tested and it was demonstrated that all measurements never exceed the root mean square of the direct-photon anisotropic flow. In particular, all methods measure zero, if the azimuthal anisotropy is zero, so it will be an important check that the direct-photon anisotropic flow is consistent with zero at high p_{T}, where prompt photons dominate.

8. Photon and neutral pion reconstruction via photon conversions

At energies above 1 MeV, pair production is the dominant mechanism for the interaction between photons and matter. The physics of pair production shall be briefly introduced in section 8.1. At these energies, photons can either be reconstructed via their conversion in the detector material or by calorimetry. The first method was already used by the STAR [316] and CDF [317] collaborations, while the second method is also used by the PHENIX collaboration [318]. In ALICE, the photon conversion method reconstructs photons from neutral secondary vertices (V0) of oppositely-charged dielectron tracks measured in the ITS and TPC. This method provides photon reconstruction in a broad rapidity window of $|\eta| < 0.9$ at mid rapidity with full azimuthal coverage ($\Delta\phi = 360°$). In addition, photons can be measured using the two ALICE calorimeters, EMCAL ($|\eta| < 0.7$, $\Delta\phi = 110°$) and PHOS ($|\eta| < 0.12$, $\Delta\phi = 100°$). The reconstruction of photons is described in section 8.2. Thereafter, the measurement of neutral pions via the decay $\pi^0 \to \gamma\gamma$ using conversion photons is described in section 8.3.

8.1 Electron-positron pair production by photons

Photons at energies above $2m_e$ (1.022 MeV) can be transformed into an electron-positron pair by their interaction with the Coulomb field of an atomic nucleus. Photon pair production can also take place in the field of an atomic electron, for photons with energies above $4m_e$ (2.044 MeV). Electron-positron pair production by photons was predicted by Dirac in 1928 [319, 320] and first observed in cloud-chamber experiments by Anderson in 1933 [321]. A detailed historical overview can be found in [322]. Figure 8.1 (right) shows a bubble chamber cosmic ray event. An electron and positron produce invisible bremsstrahlung, which is indicated by the blue dashed line. On the right, the Bremsstrahlung photon transfers a part of its momentum to an electron by Compton scattering. On the upper left, the Bremsstrahlung photon converts into an electron-positron pair. Due to their characteristic V-like shape, such neutral vertices are called V0s.

Figure 8.1 (left) shows the photon total cross section as a function of the photon energy in lead and the contributions of different processes: the atomic photoelectric effect $\sigma_{\text{p.e.}}$ (electron ejection, photon absorption), Rayleigh (coherent) scattering σ_{Rayleigh}, Compton (incoherent) scattering σ_{Compton}, and pair production in an electron field κ_e or nuclear field κ_{nuc} [9]. Nuclear photon pair production becomes dominant at about 2 MeV and is the only relevant mechanism for the interaction between photons and matter in ultra-relativistic hadron collisions. The pair production cross section is given by

$$\sigma = \frac{7}{9}\frac{A}{N_A X_0} \ , \tag{8.1}$$

where X_0 is the radiation length, A the atomic mass number and N_A Avogadro's number [9]. The radiation length depends on the charge number Z of the material, approximately like

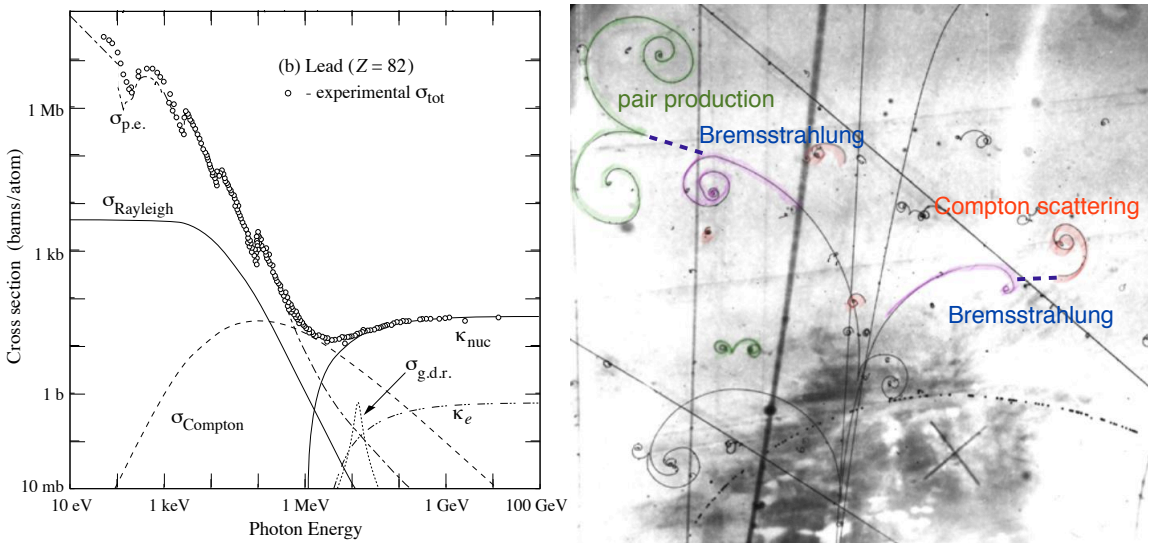

Figure 8.1: (left) Photon total cross section as a function of the photon energy in lead [9]. (right) Bubble chamber cosmic ray event with photon pair creation and Compton scattering. Figure adapted from [323].

$X_0(g/cm^2) = [180A/Z]/Z$, such that photons have a shorter mean free path in materials with a large charge number [324].

Compared with other neutral particles, photon conversions are characterized by almost parallel dilepton momenta at the secondary vertex. Neglecting the masses of the positron and electron and the recoil of the nucleus, the dilepton tracks can be considered to be parallel at the decay vertex. The most probable electron-positron opening angle θ_{p} for a photon with energy k is given by

$$\theta_{\mathrm{p}} = \frac{4m_e c^2}{k}\phi_Z(a) \ , \tag{8.2}$$

where $a = E^+/k$ is the fraction of energy of the positron daughter particle and $\phi_Z(a)$ a factor larger than unity that depends on the atomic charge Z and a [325]. An experimental method of reconstructing the photon energy from the pair opening angle was discussed in [326]. Experimental results for the opening angle can be found in literature [327, 328].

8.2 Photon reconstruction via conversions in ALICE

8.2.1 Material budget

Figure 8.2 shows the distribution of photon conversions in transverse and longitudinal plane of the ALICE detector. When reconstruction effects are neglected, the density of conversions provides a direct measure of the material budget. A large number of conversions at a given position corresponds to material with a large radiation length. The inner structure of the detector is clearly visible as regions with a large number of conversions, the corresponding detector components are labeled in fig. 8.2. Conversions result mainly from the material budget of the

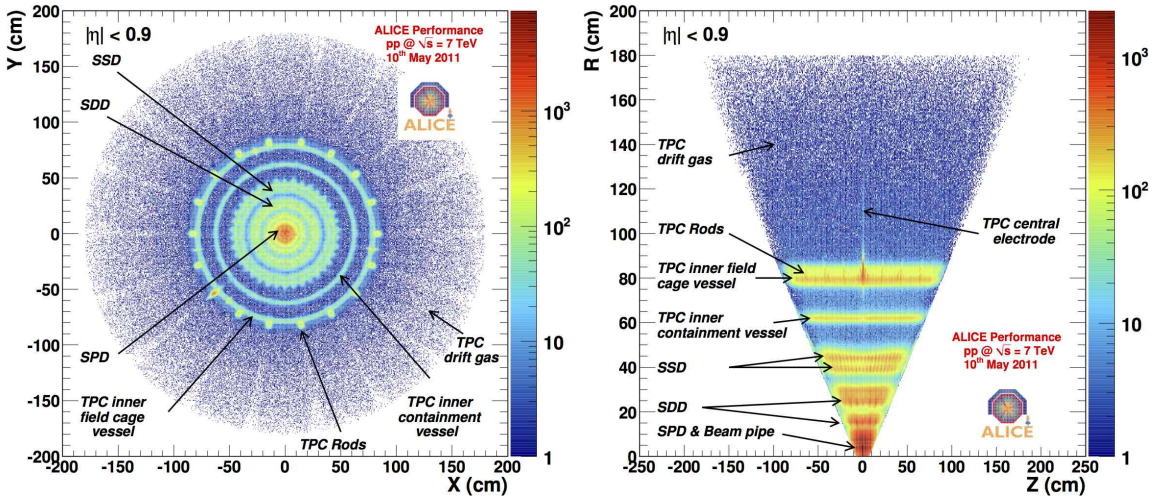

Figure 8.2: Distribution of photon conversions (left) in the transverse plane and (right) in the longitudinal plane [329, 330].

beam pipe, the three layers of the ITS, the TPC inner containment vessel, the TPC inner field cage vessel, the 18 TPC rods, and also the TPC central electrode foil. Due to a smaller reconstruction efficiency at the small gap between two adjacent TPC readout chambers, the eighteen fold segmentation of the TPC is also visible in the distribution of conversions in the TPC gas. The material budget of the detector in $|\eta| < 0.9$ up to $R = 180\,\text{cm}$ is $11.4 \pm 0.5\%$ of a radiation length corresponding to a conversion probability of about 8.5% for $p_{\text{T}} \geq 1\,\text{GeV}/c$ [329–331].

8.2.2 Topological cuts

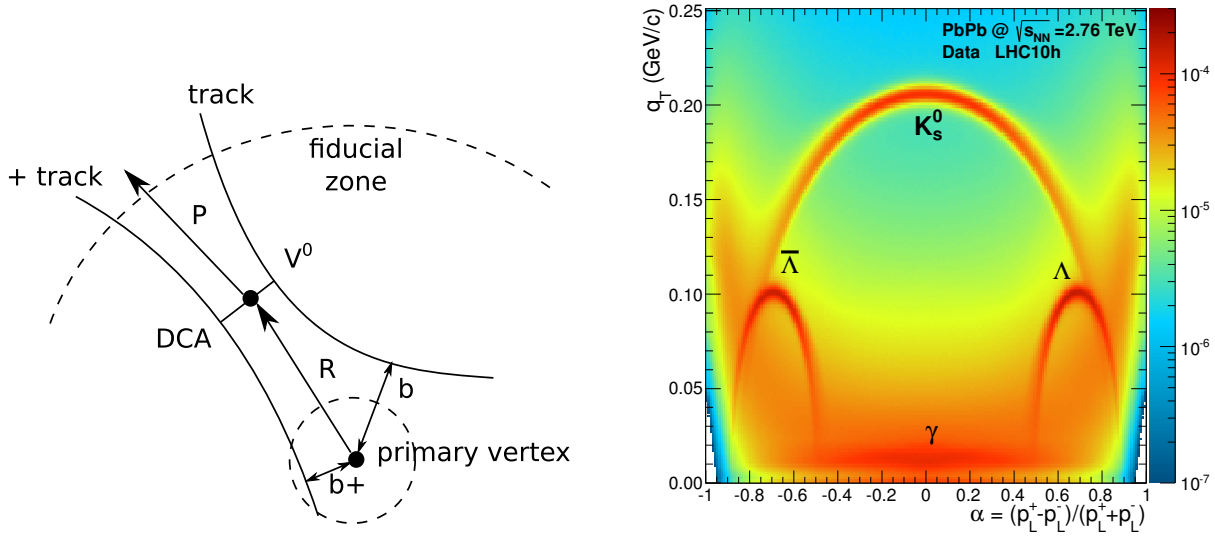

Figure 8.3: (left) Sketch of a V0 vertex [206]. (right) Armenteros-Podolanski plot for reconstructed neutral vertices in Pb-Pb collisions [332].

Photon conversions are characterized by neutral secondary vertices of two oppositely-charged tracks named named V0 vertices. Figure 8.3 (left) shows a sketch of a V0 vertex. The V0 algo-

rithm searches for two oppositely-charged tracks, which are not assigned to the primary vertex, since their reconstructed impact parameters b at the primary vertex are above a certain threshold. Their point of closest approach (dca) is displaced from the primary vertex by the radius R, and their four momenta at this point add up such that the mother particle momentum vector P points towards the primary vertex.

Figure 8.3 (right) shows an Armenteros-Podolanski plot [333] for secondary vertices (without any selection cuts). α is the energy asymmetry

$$\alpha = \frac{{p^+}_{\mathrm{L}} - {p^-}_{\mathrm{L}}}{{p^+}_{\mathrm{L}} + {p^-}_{\mathrm{L}}} \ , \tag{8.3}$$

${p^+}_{\mathrm{L}}$ and ${p^-}_{\mathrm{L}}$ are the longitudinal components of the total momentum for the positive and negative daughters respectively, relative to the direction of the V0 momentum vector, and q_{T} the transverse momentum transfer

$$q_{\mathrm{T}} = p_{\mathrm{daughter}} \sin\left(\phi_{\mathrm{mother}} - \phi_{\mathrm{daughter}}\right) \ . \tag{8.4}$$

Besides photon conversion, also the bands from the symmetric decay $K^0_{\mathrm{s}} \to \pi^+\pi^-$ and the asymmetric decays $\Lambda \to p\pi^-$ and $\bar{\Lambda} \to \bar{p}\pi^+$ are clearly visible. The photons converting to e^+ e^- with the detector material are distributed symmetrically in α and located in the low q_{T} region due to the small dilepton opening angle θ_p,

$$q_{\mathrm{T}} \underset{\theta_p \to 0}{\Rightarrow} 0 \ . \tag{8.5}$$

The width results mainly from the finite momentum resolution. For a 1 GeV photon, the most probable opening angle is about $\theta_p \approx 2$ mrad. The angular resolution of the ALICE ITS is about 1.2 - 1.7 mrad [232] for a particle with a momentum of 1 GeV/c at the primary vertex and deteriorates at lower momenta. The opening angle is smeared out by multiple scattering of the charged daughter particles. Thus, the opening angle cannot be resolved and is considered to be zero for practical purposes.

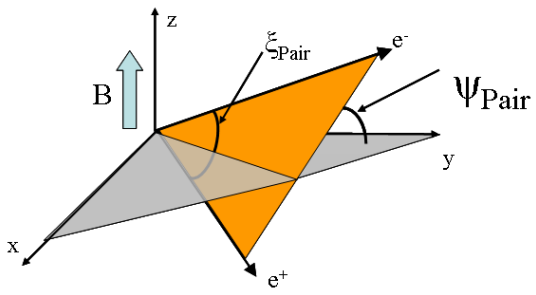

Figure 8.4: Ψ_{pair} is the angle between the plane spanned up by the dilepton tracks (yellow) and the bending plane of the magnetic field (gray) [334].

In order to ensure the reconstruction of the dilepton tracks inside the TPC, only secondary vertices with $R_{\mathrm{conv}} < 180$ cm and $Z_{\mathrm{conv}} < 240$ cm are selected. In addition, only events are selected with a reconstructed primary vertex within $|z| < 10$ cm. The contamination from $\pi^0 \to \gamma\mathrm{e}^+\mathrm{e}^-$ and $\eta \to \gamma\mathrm{e}^+\mathrm{e}^-$ is reduced by rejecting all V0s with $R_{\mathrm{conv}} < 5$ cm.

Candidate track pairs for photon conversions are reconstructed using a secondary vertex finding algorithm based on the Kalman filter [294]. A χ^2 value is calculated based on constraints on the reconstructed invariant mass and the dilepton opening angle, and candidates with a $\chi^2 < 30$ are selected. Looking at fig. 8.3 (right), most candidate pairs from Λ and K^0_{s} decays and a substantial portion of combinatorial background can be rejected by requiring that $q_{\mathrm{T}} < 0.05$.

The dilepton momenta are almost parallel at the conversion point with no preferred direction of emission in azimuthal ϕ or polar θ direction. As the particles propagate in the magnetic field, their opening angle in the transverse plane $\Delta\phi = \phi^{e^-} - \phi^{e^+}$ increases due to the curvature of the tracks, while the opening angle in polar direction $\Delta\theta = \theta^{e^-} - \theta^{e^+}$ stays constant. The situation is sketched in fig. 8.4. The angle between the plane spanned up by the dilepton momenta (some finite distance away from the secondary vertex) and the bending plane of the magnetic field is defined as

$$\Psi_{\text{pair}} = \arcsin\left(\frac{\Delta\theta}{\xi_{\text{pair}}}\right) , \tag{8.6}$$

with

$$\xi_{\text{pair}} = \arccos\left(\frac{\vec{p}_{e^-} \cdot \vec{p}_{e^+}}{|\vec{p}_{e^-}| \cdot |\vec{p}_{e^+}|}\right) \tag{8.7}$$

The standard cut is $\Psi_{\text{pair}} < 0.05$.

8.2.3 Particle identification cuts

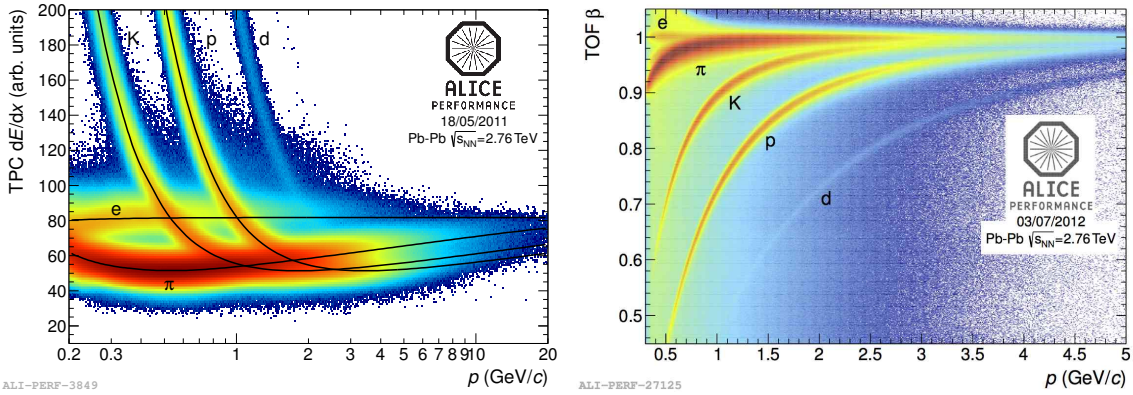

Figure 8.5: (left) $\mathrm{d}E/\mathrm{d}x$ spectrum in the TPC and (right) relative velocity β determined with TOF as a function of the momentum in Pb-Pb collisions at $\sqrt{s_{\text{NN}}} = 2.76\,\text{TeV}$.

The purity of the photon selection can be improved by particle identification applied to the daughter tracks. Figure 8.5 (left) shows the specific energy loss spectrum in the ALICE TPC and fig. 8.5 (left) the time-of-flight measurement in the ALICE TOF detector as a function of the momentum for charged particles in Pb-Pb collisions. Clearly visible are the characteristic bands for electrons, pions, kaons, protons and even deuterons. Electrons can be selected by requiring that the signal of a given track lies within a certain interval around the expected energy loss and time of flight for electrons. Deviations from the expected energy loss and time-of-flight are commonly expressed in units of the standard deviation $N_{\sigma,\text{TPC}}$ and $N_{\sigma,\text{TOF}}$, both defined in eq. (5.2) and eq. (5.2), respectively. The standard cuts for this analysis are $N^{\text{e}}_{\sigma,\text{TPC}} \in [-3, 5]$ and $N^{\text{e}}_{\sigma,\text{TOF}} \in [-5, 5]$. In addition, the pion contamination in the region, where the $\mathrm{d}E/\mathrm{d}x$ curves start to overlap, is further reduced by removing all tracks within $N^{\pi^\pm}_{\sigma,\text{TPC}} \in [-10, 3]$ with respect to the expected pion energy loss for transverse momenta above $0.4\,\text{GeV}/c$. At higher momenta, the characteristic energy loss and time-of-flight curves overlap and thus the separation power

decreases.
The separation of electrons and pions can be significantly improved with the Transition Radiation Detector (cf. chapter 6). During the first period of operation, the TRD was not fully installed (cf. fig. 6.12) and thus not used for this analysis, since it would introduce azimuthally anisotropic photon purities and efficiencies, which could introduce non-flow correlations.

8.2.4 Performance of the photon reconstruction

The performance of the photon reconstruction is characterized by the detector acceptance acc^{γ}, efficiency ϵ^{γ} and purity p^{γ}, which are defined as:

$$\mathrm{acc}^{\gamma} = \frac{N^{\gamma}{}_{\mathrm{true,findable}}}{N^{\gamma}{}_{\mathrm{true}}} \tag{8.8}$$

$$p^{\gamma} = \frac{N^{\gamma}{}_{\mathrm{true,found}}}{N^{\gamma}{}_{\mathrm{true,findable}}} \tag{8.9}$$

$$\epsilon^{\gamma} = \frac{N^{\gamma}{}_{\mathrm{true,found}}}{N^{\gamma}{}_{\mathrm{found}}} \tag{8.10}$$

Only a certain fraction of photons is findable due to the limited coverage of the detector and conversion probability inside the fiducial volume. The acceptance accounts for the fraction of photons that escape the detector volume without any detectable signal. The efficiency accounts for the fraction of photons that generate a signal inside the detector, but cannot be reconstructed due to inefficiencies in the track and V0 finding algorithm and the application of particle identification cuts. The purity is the fraction of reconstructed photons, which can be assigned to true photons. In other words, $(1 - p^{\gamma})$ is fraction of combinatorial background and contamination from Λ and K^0_{s} decays, which passes the selection cuts. Combinatorial background means falsely combined particles, which do not originate from the decay of the same mother particle.

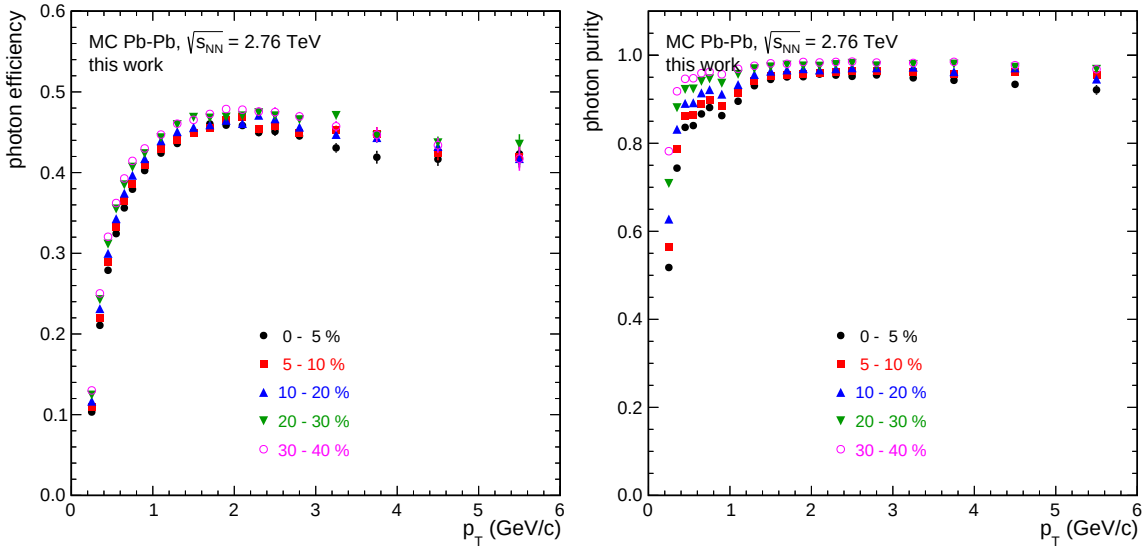

Figure 8.6: (left) Photon efficiency and (right) purity as a function of p_{T} for different centralities.

The photon purity, efficiency and acceptance can be calculated in a Monte Carlo simulation

based on HIJING [335], with the same selection cuts as for data. Details on the Monte Carlo simulation, in particular on the agreement between data and simulation, can be found in [332]. Figure 8.6 shows the photon efficiency and purity as a function of the transverse momentum for different centralities.

The photon reconstruction efficiency is about 45% at intermediate p_{T} and decreases towards lower momenta, since the track reconstruction efficiency deteriorates. Photons below about 100 MeV/c cannot be reconstructed, since tracks below 50 MeV/c curl up in the magnetic field and cannot be reconstructed. The radius of curvature is given by $R \approx p_{\mathrm{T}}/(0.3B)[mT/\mathrm{GeV}/c]$ [41], which gives a radius of about 30 cm for $p_{\mathrm{T}} = 50$ MeV/c and $B = 0.5$ T. At high p_{T}, the efficiency slightly decreases, since the separation power and thus the efficiency of the particle identification cuts decreases. The efficiency is some percent larger in mid-central compared to peripheral collisions due to the smaller detector occupancy.

The photon purity at intermediate p_{T} is between 95% for central and 99% in mid-central collisions. The purity is much worse at low p_{T} due to combinatorial background of photon candidates reconstructed at small radii R_{conv} in the first layers of the ITS, where the track densities are very large.

Both, purity and efficiency, depend strongly on the photon selection cuts. The purity can be significantly increased if photon candidates reconstructed at small radii are excluded, but at the expense of a significantly lower efficiency. In particular, the efficiency and purity are not smooth in p_{T} due to cuts, which depend on the transverse momentum itself.

8.2.5 Inclusive photon spectra in Pb-Pb collisions

Figure 8.7 shows the inclusive photon invariant yield in 0 - 40% and 40 - 80% Pb-Pb collisions, measured with the photon conversion method. At high p_{T}, where next-to-leading-order pQCD photon production dominates, the yields are expected to scale with the number of binary collisions N_{coll}. In 0 - 40% central collisions, about $\mathcal{O}(10^3)$ photons are produced per event. Taking the photon efficiency of about 45% and the conversion probability of about 8% into account, about 30 to 50 photons are reconstructed central Pb-Pb collisions. The systematic uncertainty of the spectra is dominated by the uncertainty on the material budget, which is about 4.5% [336].

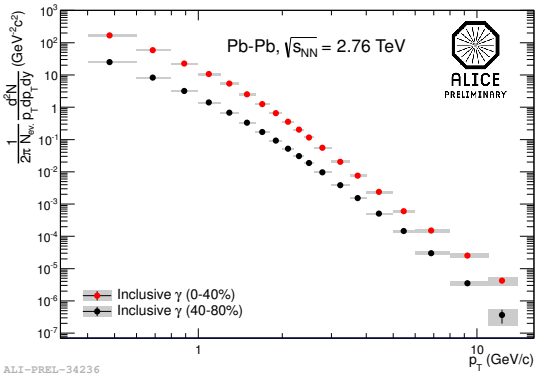

Figure 8.7: Inclusive photon invariant yield in 0 - 40% and 40 - 80% Pb-Pb collisions [201].

8.3 Neutral pion reconstruction using photon conversions

The neutral pion is the lightest strongly interacting hadron observed in nature. The neutral pion dominantly decays into two photons, which has been suggested by Lewis, Oppenheimer, and Wouthuysen as a possible origin of the soft component in the cosmic radiation [337]. It was first discovered in 1947 with photographic emulsions exposed to cosmic rays at mountain altitudes by Lattes et al. [338] and later in 1950 by Carlson et al. [339]. Its dominant electromagnetic decay

channel $\pi^0 \to \gamma\gamma$ was first detected in 1950 at the Berkeley synchrocyclotron in proton fixed target experiments by Bjorklund, Panofsky, Steinberger, et al. [340–343]. A historical review can be found in [344, 345].
In ALICE, the neutral pion decay $\pi^0 \to \gamma\gamma$ can be reconstructed from photons measured via the conversion method. The combinatorial background is estimated by the combination of photons from two uncorrelated events (mixed event technique).

8.3.1 Invariant mass spectrum

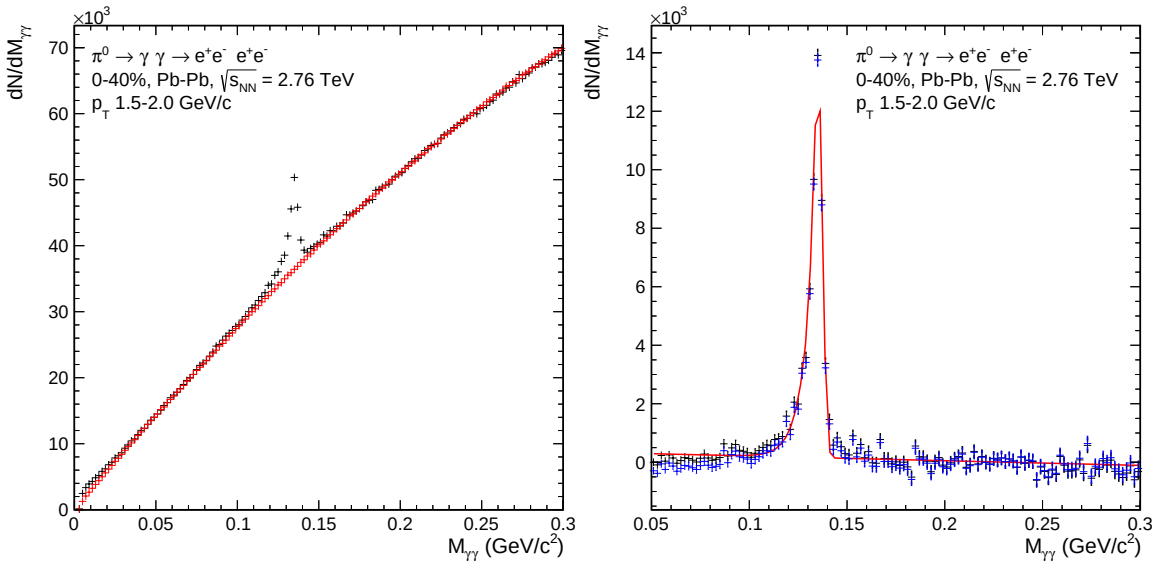

Figure 8.8: (left) Invariant mass $M_{\gamma\gamma}$ spectrum (black) and estimated background spectrum from event mixing (red). (right) pizero signal after background subtraction (black), fit of the peak (red) with first order polynomial for remaining background correction (blue).

Since the invariant mass $M_{\gamma\gamma}$ is constrained by the relative kinematical properties of the two photons, it is important to mix only events with a similar topology in terms of the event centrality, photon multiplicity, the orientation of the reaction plane [1] and the z-position of the primary vertex. For a proper normalization, each mixed-event pair gets the weight $w_{\mathrm{BG}} = (n_1 - 1)/(2n_2)$, which corrects for the fact that a mixed-event yields $n_1 n_2$ pairs instead of $n_1(n_1 - 1)/2$. Since one event can be mixed more than once, the background is finally normalized by $N_{\mathrm{same}}/N_{\mathrm{mixed}}$.

Figure 8.8 (left) shows the photon pair invariant mass spectrum in the transverse momentum range from 1.5 - 2.0 GeV/c. The black points are the distribution from same events $\mathrm{d}N_{\mathrm{SE}}/\mathrm{d}M_{\gamma\gamma}$, the red points are the background estimated from mixed events $\mathrm{d}N_{\mathrm{ME}}/\mathrm{d}M_{\gamma\gamma}$, which is normalized as described in the following. The excess of neutral pions peaks at the physical rest mass $m_\pi^0 = (134.9766 \pm 0.0006)$ MeV/c^2. The background is subtracted after a final normaliza-

[1] For any study of the azimuthal anisotropy, it is important to take the reaction plane orientation into account in order to get the most precise description of the background. Due to a technical limitation related to the number of events that can be processed at the same time, the reaction plane dependence was not taken into account here.

tion with a function $n(M_{\gamma\gamma})$:

$$\frac{\mathrm{d}N_{\pi^0}}{dM_{\gamma\gamma}} = \frac{\mathrm{d}N_{\mathrm{SE}}}{\mathrm{d}M_{\gamma\gamma}} - n(M_{\gamma\gamma})\frac{\mathrm{d}N_{\mathrm{ME}}}{\mathrm{d}M_{\gamma\gamma}} \tag{8.11}$$

In order to estimate systematic effects of the background subtraction, three different methods are applied:

1. Side band integral right of the invariant mass peak ($0.145 \leq M_{\gamma\gamma} \leq 0.3\,\mathrm{GeV}/c^2$):

$$n(M_{\gamma\gamma}) = \frac{\int \frac{\mathrm{d}N_{\mathrm{SE}}}{\mathrm{d}M_{\gamma\gamma}}\mathrm{d}M_{\gamma\gamma}}{\int \frac{\mathrm{d}N_{\mathrm{ME}}}{\mathrm{d}M_{\gamma\gamma}}\mathrm{d}M_{\gamma\gamma}} = \mathrm{const} \tag{8.12}$$

2. First order polynomial fitted in the range left ($0.145 \leq M_{\gamma\gamma} \leq 0.3\,\mathrm{GeV}/c^2$) and right ($0.05 \leq M_{\gamma\gamma} \leq 0.1\,\mathrm{GeV}/c^2$) of the invariant mass peak:

$$n(M_{\gamma\gamma}) = a + bM_{\gamma\gamma} \tag{8.13}$$

3. Exponential function plus constant fitted in the same range:

$$n(M_{\gamma\gamma}) = a(1 - \exp(bM_{\gamma\gamma})) + c \tag{8.14}$$

Figure 8.8 (right) shows the invariant mass spectra $\mathrm{d}N_{\mathrm{Signal}}/\mathrm{d}M_{\gamma\gamma}$ after background subtraction. It can be seen that the invariant mass peak is only roughly at the physical rest mass m_π^0. The physical decay width is only about 8 eV [9], so that the actual width and position of the invariant mass peak is modified by detector effects. In particular, the tail towards small invariant masses can be explained by bremsstrahlung of the converted electrons and positrons. Figure 8.9 shows the width and position of the π^0 invariant mass peak measured with the photon calorimeter PHOS and the photon conversion method ('PCM') in pp collisions at $\sqrt{s} = 7\,\mathrm{TeV}$. It can be seen that the width is smaller at low transverse momentum using the conversion method, since the momentum resolution of charged tracks reconstructed with ITS and TPC is better than the energy resolution of the PHOS calorimeter. The width growth with increasing momentum, which is a feature of the linear increase with p_T of the relative momentum resolution for reconstructed charged particle tracks (cf. fig. 5.3 (right)). The energy resolution of a calorimeter typically improves with increasing energy like $1/\sqrt{E}$, which results into a slight decrease of the π^0 width measured with PHOS. It can also be seen that the position of the peak $m_{\pi^0}(p_\mathrm{T})$ changes with momentum.

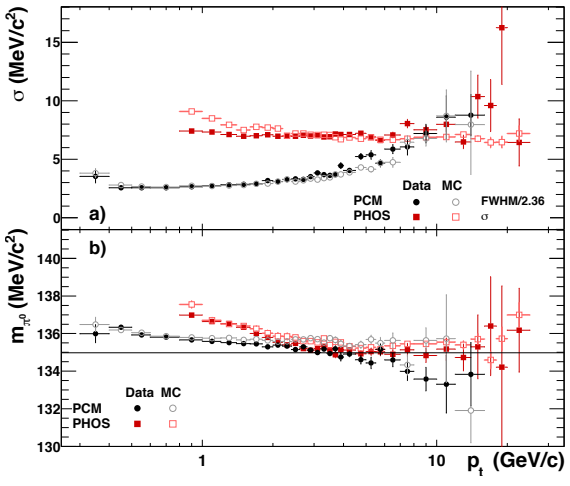

Figure 8.9: (left) Reconstructed π^0 peak width and (left) peak position as a function of p_T measured with the photon conversion method ('PCM') and by the PHOS calorimeter in pp collisions at $\sqrt{s} = 7\,\mathrm{TeV}$ [331].

Both effects, the energy dependence of the peak position and the peak width, have to be taken into account when the neutral pion yield is extracted. The invariant mass peak is fitted with the following function:

$$\frac{\mathrm{d}N_{\pi^0}}{dM_{\gamma\gamma}} = \begin{cases} a\left(G\left(M_{\gamma\gamma}\right) + \exp\left(\left(M_{\gamma\gamma} - b\right)/d\right)\left(1 - G\left(M_{\gamma\gamma}\right)\right)\right) & \text{if} \quad M_{\gamma\gamma} < b \\ aG\left(M_{\gamma\gamma}\right) & \text{else} \end{cases} \tag{8.15}$$

with

$$G(M_{\gamma\gamma}) = \exp\left(-0.5\left(\left(M_{\gamma\gamma} - b\right)/c\right)^2\right) \tag{8.16}$$

The parameter b is the peak position and determines the experimental neutral pion mass m_{π^0}, and the parameter c the corresponding width of the invariant mass peak σ. In order to correct for remaining background after background subtraction, eq. (8.15) is fitted together with a first order polynomial, which can be seen as red curve in fig. 8.8 (right). Finally, the remaining background is subtracted (blue points).

8.3.2 Yield extraction

The neutral pion yield is extracted by integrating the signal invariant mass distribution

$$N_{\pi^0} = \sum_{M_{\min}}^{M_{\max}} \frac{\mathrm{d}N_{\mathrm{Signal}}}{\mathrm{d}M_{\gamma\gamma}} \tag{8.17}$$

in the flexible range $[M_{\min}, M_{\max}]$, with $M_{\min} = m_{\pi^0}(p_{\mathrm{T}}) - 0.045\,\mathrm{GeV}/c^2$ and $M_{\max} = m_{\pi^0}(p_{\mathrm{T}}) + 0.01\,\mathrm{GeV}/c^2$. The extended integration window towards low $M_{\gamma\gamma}$ accounts for the tail resulting from bremsstrahlung of the converted electrons and positrons. The statistical error of the signal $\mathrm{d}N_{\pi^0}/\mathrm{d}M_{\gamma\gamma}$ is given by

$$s^2_{\frac{\mathrm{d}N_{\mathrm{Signal}}}{\mathrm{d}M_{\gamma\gamma}}}(M_{\gamma\gamma}) = s^2_{\frac{\mathrm{d}N_{\mathrm{SE}}}{\mathrm{d}M_{\gamma\gamma}}}(M_{\gamma\gamma}) + n(M_{\gamma\gamma})^2 s^2_{\frac{\mathrm{d}N_{\mathrm{ME}}}{\mathrm{d}M_{\gamma\gamma}}}(M_{\gamma\gamma}) + s_n^2 \left(\frac{\mathrm{d}N_{\mathrm{ME}}}{\mathrm{d}M_{\gamma\gamma}}(M_{\gamma\gamma})\right)^2 . \tag{8.18}$$

The error of the yield N_{π^0} follows from eq. (8.17):

$$s^2_{N_{\pi^0}} = \sum_{M_{\min}}^{M_{\max}} s^2_{\frac{\mathrm{d}N_{\mathrm{Signal}}}{\mathrm{d}M_{\gamma\gamma}}}(M_{\gamma\gamma}) \tag{8.19}$$

8.3.3 Performance of the neutral pion reconstruction

Neutral pions can only be identified statistically, since the signal-to-noise ratio is rather low, particularly at low momentum. Only particles with a large signal-to-noise ratio can be identified on a event-by-event basis, while the fraction of misidentified background is corrected by a purity correction determined from a Monte Carlo simulation. The reconstruction efficiency of photons is smaller than 50% (cf. fig. 8.6 (left)) and the conversion probability of about 8.5%, which results into a pion efficiency of about $(50\%)^2(8.5\%)^2 = \mathcal{O}(10^3)$ (cf. [332,336]). Per Pb-Pb collision, $\mathcal{O}(10^3)$ neutral pions are produced, which gives about one reconstructable neutral pion per central Pb-Pb collision. On the other hand, about 50 inclusive photons are detected, which

gives about $N_{\gamma,\mathrm{inc}}(N_{\gamma,\mathrm{inc}}-1)=\mathcal{O}(10^3)$ photon pair combinations per event. Even if only a small fraction of photon pairs contributes to the neutral pion invariant mass range, the signal-to-noise ratio is smaller than 0.3 at 1.5 - 2 GeV/c^2 in 20 - 40% mid-central collisions (cf. fig. 9.10 (left)) and gets even smaller at low p_{T} and in central collisions.

The neutral pion significance can be improved by a cut on the energy asymmetry

$$\alpha = \frac{E_1^{\gamma} - E_2^{\gamma}}{E_1^{\gamma} + E_2^{\gamma}} \ . \tag{8.20}$$

A large energy asymmetry means that one photon has rather small energy compared to the other photon. At large momenta, the energy asymmetry of photons from π^0 decays is almost uniformly distributed, while background pairs typically have large asymmetries. The combinatorial background increases with α, since the inclusive production cross-sections fall steeply with increasing momentum, such that photon pair combinations with large energy asymmetry are more likely than symmetric combinations. Thus, the significance of neutral pions can be increased at high p_{T} by cut on the energy asymmetry. The standard cut used in this analysis is $\alpha < 0.65$.

8.3.4 Neutral pion spectra in Pb-Pb collisions

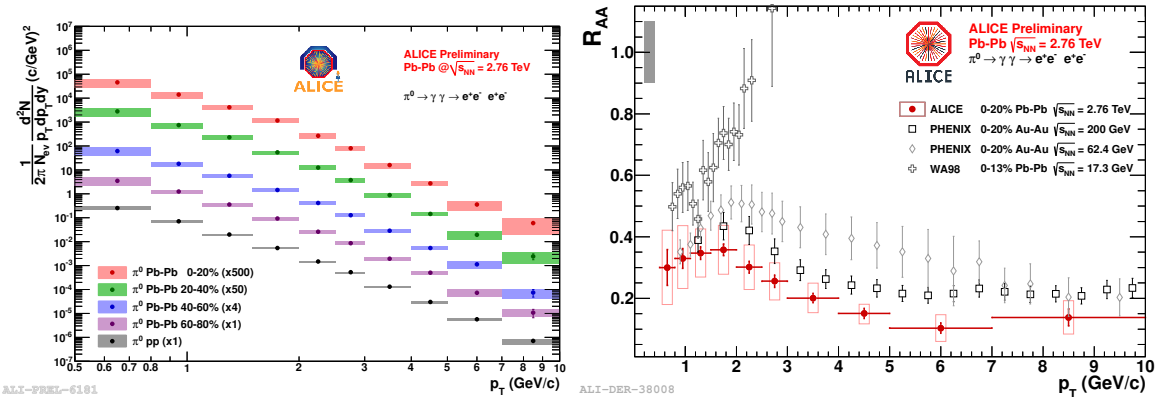

Figure 8.10: (left) π^0 invariant yield in Pb-Pb collisions at different centralities [346]. (right) Neutral pion $R_{\mathrm{AA}}^{\pi^0}$ measured in Pb-Pb collisions in comparison to data at different energies [332].

Figure 8.10 (left) shows the neutral pion invariant yield measured in different centrality bins in Pb-Pb collisions at $\sqrt{s_{\mathrm{NN}}}=2.76$ TeV. For comparison, data points for pp collisions at $\sqrt{s}=7$ TeV are shown. The data points were obtained with the photon conversion method. Similar than for photons, the systematic uncertainties are dominated by the uncertainty on the material budget (4.5%), which results into a systematic uncertainty of 9% on the neutral pion spectra. Figure 8.10 (right) shows the neutral pion $R_{\mathrm{AA}}^{\pi^0}$ as a function of the transverse momentum p_{T} in 0 - 20% central Pb-Pb collisions in comparison to data at different energies measured by the PHENIX [347, 348] and W98 [349] collaboration. While the neutral pion suppression is similar for all energies below $p_{\mathrm{T}} < 2$ GeV/c, the suppression increases with $\sqrt{s_{\mathrm{NN}}}$ for larger momenta. This observation indicates that the increased parton energy loss due to the higher initial energy density dominates over the flattening of parton p_{T} spectra with increasing $\sqrt{s_{\mathrm{NN}}}$ [332, 346].

9. Measurement of the neutral-pion and inclusive-photon anisotropic flow

The anisotropic flow of direct-photons can be accessed from the measurement of inclusive photons. In order to subtract all photons from hadron decays, also the azimuthal anisotropy of neutral pions as the dominant source of decay photons is measured. Photons and neutral pions are reconstructed from conversions in the ALICE detector material at mid rapidity. Their anisotropic flow is measured by the event-plane method, while the event plane is either determined by one of the two V0 detectors or by the TPC.
The presented analysis is based on 19.5 million minimum bias Pb-Pb collisions at $\sqrt{s_{\mathrm{NN}}} = 2.76\,\mathrm{TeV}$ recorded in 2010, which pass the ALICE physics selection cuts [74, 350]. In order to ensure a uniform performance of the photon reconstruction, about 2.5 million events were rejected with a primary vertex position along the beam axis deviating by more than 10 cm from the geometrical center of the ALICE detector [331]. The centrality is determined from the V0 multiplicity [74]. The analysis is performed with about 6.8 million 0 - 40% central events. In order to reduce the impact of the centrality dependence of cross sections and of the resolution correction as well as the impact of flow fluctuations (cf. chapter 7), v_n is measured in small bins of centrality:

$$0\text{-}5\%,\ 5\text{-}10\%,\ 10\text{-}20\%,\ 20\text{-}30\%,\ 30\text{-}40\%$$

Experimentally, it is not always feasible for certain particles, such as neutral pions, to measure in arbitrarily small centrality bins, e.g. if particles can only be statistically identified and the expected number of particles per event or the significance are rather low. For this reason, neutral pions are measured in 0 - 20%, 20 - 40% and 0 - 40% centrality. A method for the resolution correction for measurements in wide centrality bins is described in [313]. The inclusive-photon anisotropic flow in these wide centrality bins can be calculated as the weighted average of the measurements in small centrality bins,

$$v_n([c_{\mathrm{min}}, c_{\mathrm{max}}]) = \frac{\sum_{c_{\mathrm{min}}}^{c_{\mathrm{max}}} v_n^{\mathrm{c}} N_{\mathrm{poi}}^{\mathrm{c}}}{\sum_{c_{\mathrm{min}}}^{c_{\mathrm{max}}} N_{\mathrm{poi}}^{\mathrm{c}}} \ , \tag{9.1}$$

where $v_n^{\mathrm{c}} = v_n(c, p_{\mathrm{T}})$ is the corresponding azimuthal anisotropy in the centrality bin c. Since v_n is defined as a particle average, the anisotropic flow in larger centrality bins is weighted by the total number of particles of interest $N_{\mathrm{poi}}^{\mathrm{c}} = N_{\mathrm{poi}}(c, p_{\mathrm{T}})$.
The event-plane reconstruction, calibration and resolution is discussed in section 9.1. Thereafter, the extraction of the inclusive-photon and neutral-pion azimuthal anisotropy is described in sections 9.2 and 9.3.

9.1 Event-plane reconstruction

The event planes used in this work and their corresponding pseudorapidity range are summarized in table 9.1. In addition, the corresponding average and minimum pseudorapidity gap $\Delta\eta$ with respect to inclusive photons and neutral pions ($|\eta| \leq 0.8$) were estimated assuming

flat pseudorapidity distributions. Since non-flow contributions can be significantly suppressed,

event plane	η range	average $\langle\Delta\eta\rangle$	minimum $\Delta\eta$
V0-A	$-3.7 \leq \eta \leq -1.7$	2.70	0.9
V0-C	$2.8 \leq \eta \leq 5.1$	3.95	2.0
TPC	$-0.8 \leq \eta \leq 0.8$	0.55	0.0
TPC-A/C	$0.5 \leq \lvert\eta\rvert \leq 0.8$	1.05	0.5

Table 9.1: Event planes with their corresponding pseudorapidity range and the average and minimum pseudorapidity gap $\Delta\eta$ with respect to inclusive photons and neutral pions ($|\eta| \leq 0.8$).

if the event-plane detector and the particles of interest are separated in pseudorapidity, the anisotropic flow measurement with respect to the V0 event planes is chosen as the standard method. The standard procedure for the V0 measurement is to measure the anisotropic flow v_n with respect to the V0-A and the V0-C event plane individually and to calculate $v_n\{\text{V0}\}$ as the error weighted average of $v_n\{\text{V0-A}\}$ and $v_n\{\text{V0-C}\}$,

$$v_n\{\text{V0}\} = \frac{v_n\{\text{V0-A}\}/s^2_{v_n\{\text{V0-A}\}} + v_n\{\text{V0-C}\}/s^2_{v_n\{\text{V0-C}\}}}{1/s^2_{v_n\{\text{V0-A}\}} + 1/s^2_{v_n\{\text{V0-C}\}}} \,. \tag{9.2}$$

The statistical error is given by $s_{v_n\{\text{EP}\}} = s_{v_n^{\text{raw}}\{\text{EP}\}}/R$, where R is the correction for the event-plane resolution and $s_{v_n^{\text{raw}}\{\text{EP}\}}$ the experimentally observed anisotropy before the event-plane resolution correction. Since the number of particles of interest is the same for both methods, differences in the uncertainties only result from differences in the event-plane resolution R. Thus, the weighting gives more weight to the measurement with better resolution. In this standard approach, event plane and particles of interest are separated by at least one unit of pseudorapidity.
For comparisons and in order to estimate the magnitude of non-flow effects, the anisotropic flow is also measured with respect to the TPC event plane. In order to avoid autocorrelations, the dilepton tracks of the reconstructed photons are always removed from the flow vector $\vec{Q}_n$. In addition to the standard TPC event plane, we define two TPC sub-event planes ***TPC-C*** ($-0.8 \leq \eta \leq -0.5$) and ***TPC-A*** ($0.5 \leq \eta \leq 0.8$). In this approach, particles at positive pseudorapidity are correlated with the event plane at negative pseudorapidity and vice versa, which gives an average pseudorapidity gap of $\Delta\eta \geq 1$. A comparison of different event plane methods is given in section 9.2.4.

9.1.1 Event-plane calibration

The flow vector $\vec{Q}_n = (X_n, Y_n)$ and the event-plane angle Ψ_n^{EP} are calculated according to their definitions given in eqs. (7.10) and (7.14), respectively. The V0 event planes are reconstructed from the signal in the V0 cells, the TPC event planes are reconstructed from TPC tracks passing the ALICE track cut selection, which are additionally weighted with their momentum. Since the orientation the participant plane and thus the direction of maximum n-th order flow Ψ_n are isotropically distributed, also the reconstructed event plane angle Ψ_n^{EP} should be isotropically distributed. For a perfectly calibrated, full acceptance and high-granularity detector, the X_n and Y_n components of the flow vector are distributed symmetrically around zero and thus the

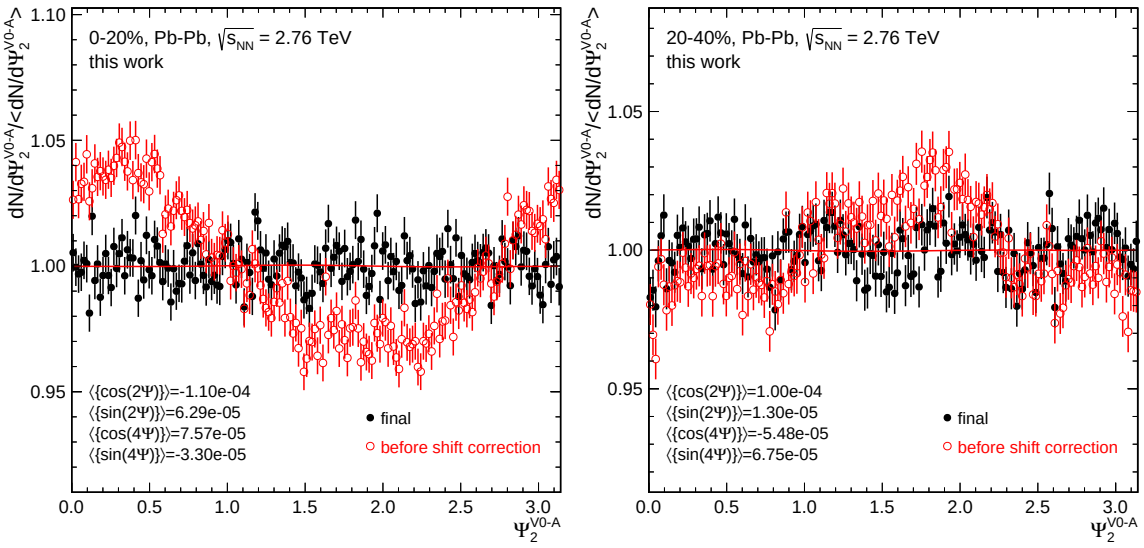

Figure 9.1: Distribution of the V0-A event plane for 0 - 20% (left) and 20 - 40% (right) central Pb-Pb collisions.

event-plane distribution is uniform. Non-uniformities arise from azimuthal non-uniformities of the detector efficiency and acceptance. The event-plane calibration is performed in three steps:

Weighting: Detector inefficiencies are corrected by weighting each track or each cell signal s_{cell} with the inverse of the observed laboratory azimuthal distribution. This procedure was first applied by [351]. The signal in each cell s_{cell} of the V0 detector is calibrated such that the laboratory azimuthal distribution is uniform. Therefore, each cell signal is weighted by $w_{\text{cell}} = \langle s \rangle \,/\, \langle s_{\text{cell}} \rangle$, where $\langle s \rangle$ is the average over all cells. Reconstruction inefficiencies in the TPC are corrected by η and p_{T} dependent weights, which are determined from the inverse laboratory azimuthal distribution of reference particles $w(\eta, p_{\text{T}}) = 1/N_{\text{ref}}(\eta, p_{\text{T}})$.

Recentering: Acceptance effects are corrected by a ***recentering*** of the flow vector

$$\vec{Q}_n = \begin{pmatrix} (X_n - \langle X_n \rangle)/\sigma_{X_n} \\ (Y_n - \langle Y_n \rangle)/\sigma_{Y_n} \end{pmatrix} , \tag{9.3}$$

where $\langle X_n \rangle$ is the mean value and σ_{X_n} is the width of the X_n-component of the flow vector.

Shift correction: After the first two calibration steps, non-uniformities of the event-plane angle distribution result from efficiency and acceptance effects, which are not fully corrected by the weighting and recentering procedure. The anisotropy of the event-plane distribution can be expressed by its n-th order harmonics $\langle \cos(n\Psi_n) \rangle$ and $\langle \sin(n\Psi_n) \rangle$. Further flattening can be achieved by an event-by-event shift correction

$$n\Delta\Psi_n = \sum_{i=1}^{i_{\max}} \frac{2}{i} \left(- \langle \sin\left(in\Psi_n\right) \rangle \cos\left(in\Psi_n\right) + \langle \cos\left(in\Psi_n\right) \rangle \sin\left(in\Psi_n\right) \right) \text{ [308, 352].} \tag{9.4}$$

For illustration, the V0-A event-plane distribution for 0 - 20% and 20 - 40% central Pb-Pb collisions is shown in fig. 9.1. The red points show the distribution before and the black points

after the shift correction. Non-uniformities are more pronounced in 0 - 20% central collisions compared to 20 - 40% mid-central collisions, since the strength of the reference flow signal $\bar{v}_n$ and thus the event-plane resolution is smaller, which gives more relative weight to detector non-uniformities. According to eq. (9.4), only first and second order non-uniformities are corrected, the remaining, periodic non-uniformity is of higher order with a magnitude of less than 1%. The effect of non-uniformities will be discussed in section 9.2.1.

9.1.2 Event-plane resolution

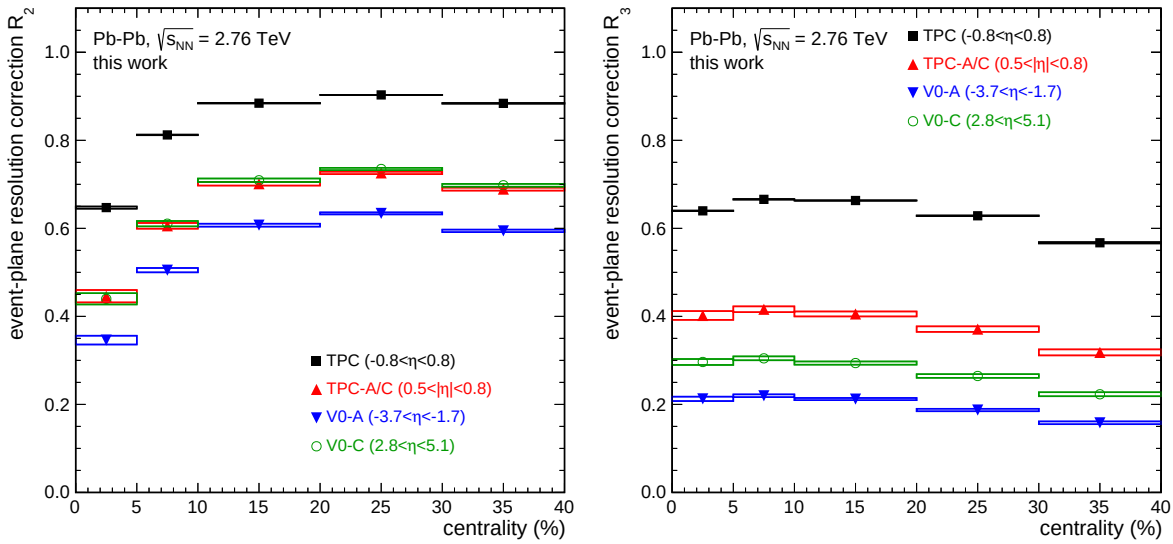

Figure 9.2: Correction factor for the event-plane resolution for n=2 (left) and n=3 (right) as a function of the centrality in 0 - 40% central Pb-Pb collisions.

Figure 9.2 shows the resolution correction factor R for different event-plane estimates as a function of the collision centrality. A large correction factor R corresponds to a higher resolution and leads to a smaller correction to the extracted v_n^{meas}. The best resolution is reached with the full TPC measurement, followed by the TPC-A/C event plane. As expected from the higher acceptance, V0-C provides a better resolution than V0-A. The V0-C resolution is similar to the resolution of the TPC-A/C event planes. Qualitatively, the observed ordering can be understood by the fact that the dispersion is proportional to $\bar{v}_n\sqrt{N_{\mathrm{ref}}}$ (cf. section 7.3), where $\bar{v}_n$ is the p_{T}-integrated reference flow and N_{ref} the number of reference particles. For $n=2$, the resolution is maximal in 20 - 30% mid-central collisions, where $\bar{v}_2$ is large compared to central collisions. Towards central collisions, the reference particle multiplicity N_{ref} increases, but the strength of the reference flow $\bar{v}_2$ decreases, such that the resolution deteriorates. It can be seen that the resolution is smaller for $n=3$ compared to $n=2$, but also the centrality dependence is weaker for $n=3$. The reason is that v_3 originates exclusively from the eccentricity ϵ_3 generated by fluctuations, while the second order eccentricity ϵ_2 is mainly caused by the asymmetry of the transverse nuclear overlap in non-central collisions. As a consequence, v_3 is much smaller than v_2, but almost constant as a function of the centrality (cf. section 3.4.1). The resolution improves slightly towards more central collisions due to the increase in the multiplicity N_{ref}.

The resolution is estimated by the three and two event-plane method defined by eqs. (7.19) and (7.20), where the event-plane resolution is either estimated from the correlation with a second identical event plane ('2ep') or from the correlation with two other event planes ('3ep'), respectively. The corresponding correlations used to determine the event-plane resolution are summarized in table 9.2[1].
Systematic uncertainties arise from the fact that non-flow contributions are only partially suppressed, if the event planes are separated in pseudorapidity, and thus the estimated event-plane resolution depends on the width of the pseudorapidity gap. The estimate for the resolution changes, if the pseudorapidity gap between the correlated event planes is varied. To give an example, slightly different resolution factors are obtained by correlating [V0-A,V0-C,TPC] compared to [V0-A,TPC-A,TPC-C]. Deviations between estimates obtained from different combinations are considered as systematic uncertainty of the event-plane resolution correction.

Event plane	3 ep	2 ep
V0-A	V0-C,TPC,TPC-A,TPC-C	-
V0-C	V0-A,TPC,TPC-A,TPC-C	-
TPC:	V0-A,V0-C	-
TPC-A	V0-A,V0-C,TPC-C	TPC-C
TPC-C	V0-A,V0-C,TPC-A	TPC-A

Table 9.2: Candidates for event-plane correlations used to determine the resolution correction.

Further systematic uncertainty might arise from the fact that v_n is defined as a particle average, but the event-plane resolution is calculated as an event average:

$$R = \left\langle \cos(n(\Psi_n^{\mathrm{EP}} - \Psi_n)) \right\rangle = \frac{\sum_{j=0}^{N_{\mathrm{ev}}} N_{\mathrm{poi}} \cos(n(\Psi_n^{\mathrm{EP}} - \Psi_n))}{\sum_{j=0}^{N_{\mathrm{ev}}} N_{\mathrm{poi}}} \tag{9.5}$$

$$\underset{N_{\mathrm{poi}} \neq \mathrm{const}}{\neq} \frac{\sum_{j=0}^{N_{\mathrm{ev}}} \cos(n(\Psi_n^{\mathrm{EP}} - \Psi_n))}{\sum_{j=0}^{N_{\mathrm{ev}}}} \tag{9.6}$$

In small bins of centrality, this effect might be negligible. In wide centrality bins, the particle and event averages will generally differ due to the centrality dependence of the resolution shown in fig. 9.2 and the cross section e.g. number of particles of interest N_{poi}. This effect could be corrected, if N_{poi} and its centrality dependence were known. However, the exact number of particles of interest is not precisely known for an individual event, e.g. if the particle can only be identified statistically or impurities and inefficiencies are large. Therefore, the event average instead of the particle average is used within small centrality bins; a dedicated correction method for wide centrality bins is described in [313]. The magnitude of the systematic bias related to this approximation is estimated by comparing the event-averaged resolution with the particle-averaged resolution, where N_{poi} is estimated by either the charged particle multiplicity,

[1] The TPC event-plane resolution is often determined from the correlation of the TPC-A and TPC-C sub-event planes or from two random sub events. The resolution is then be calculated from the sub-event plane resolution according to eq. (7.21). It was shown in section 7.3.4 that the scaling of the event-plane resolution with N_{ref} fails, if multiplicity fluctuations are present, and thus this approach is not used within this work.

the photon multiplicity or V0 multiplicity. Deviations are considered as systematic uncertainty of the event-plane resolution.

The systematic uncertainties of the event-plane resolution correction factor R – indicated by the boxes in fig. 9.2 – are propagated to the systematic uncertainty of the measured anisotropy (cf. sections 9.2.2, 9.3.2 and 10.2.2.3).

9.2 Anisotropic flow of inclusive photons

The standard analysis is based on the $\mathrm{d}N/\mathrm{d}\Delta\phi$ method described in appendix B, where particle yields are measured as a function of the azimuthal angle ϕ relative to the event plane angle Ψ_n^{EP}. The Fourier expansion is given by

$$N\left(\Delta\phi\right) = \frac{N_0}{2\pi}\left(1 + 2v_n\cos\left(n\left(\Delta\phi\right)\right)\right) \ , \tag{9.7}$$

with $\Delta\phi = \arccos\left(\left|\cos\left(\phi - \Psi_n^{\mathrm{EP}}\right)\right|\right)$. The azimuthal anisotropy is studied in six bins for the azimuthal angle with respect to the event plane $\Delta\phi$. Figure 9.3 (left) shows for illustration the distribution of reconstructed photons in the momentum range from 1.0 - 1.2 GeV/c in the six aforementioned $\Delta\phi$ bins. Even though the number of photons per event would be large enough for a direct calculation of the Fourier coefficients, the $\mathrm{d}N/\mathrm{d}\Delta\phi$ method was chosen in order to study efficiency and purity effects (cf. section 9.2.3). Using the finite bin size corrections discussed in appendix B, the evaluation of $\langle\cos\left(n\Delta\phi\right)\rangle$ from finite $\Delta\phi$ bins gives exactly the same as the direct calculation. The Fourier expansion is shown as a red line. The anisotropy is either calculated directly from $\langle\cos\left(n\Delta\phi\right)\rangle$ by evaluating eq. (B.12) or extracted by fitting the corresponding Fourier expansion to the $\mathrm{d}N/\mathrm{d}\Delta\phi$ distribution. The Fourier harmonics are independent if calculated directly, but using a fit of the Fourier distribution, the harmonics are not linear independent and significant differences may arise, if the statistical uncertainty of the points is large. Deviations are considered as systematic uncertainty.

9.2.1 Effects of non-uniform acceptance and reconstruction efficiencies

Non-uniform detector acceptance and efficiency lead to non-vanishing values for the harmonics of the laboratory azimuthal distribution of the reconstructed particles of interest, $\langle\cos(n\phi)\rangle$ and $\langle\sin(n\phi)\rangle$, and the reconstructed event plane, $\left\langle\cos(n\Psi_n^{\mathrm{EP}})\right\rangle$ and $\left\langle\sin(n\Psi_n^{\mathrm{EP}})\right\rangle$. A detailed discussion of the effects of non-uniformities on the anisotropic flow measurement can be found in [353]. Systematic bias due to non-flow correlations arising from non-uniformities of the event-plane and photon azimuthal distribution can be estimated by terms like

$$\left\langle\cos\left(n\Psi_n^{\mathrm{EP}}\right)\right\rangle\left\langle\cos\left(n\phi\right)\right\rangle \qquad \left\langle\sin\left(n\Psi_n^{\mathrm{EP}}\right)\right\rangle\left\langle\sin\left(n\phi\right)\right\rangle \tag{9.8}$$

and corresponding mixed terms

$$\left\langle\cos\left(n\Psi_n^{\mathrm{EP}}\right)\right\rangle\left\langle\sin\left(n\phi\right)\right\rangle \qquad \left\langle\sin\left(n\Psi_n^{\mathrm{EP}}\right)\right\rangle\left\langle\cos\left(n\phi\right)\right\rangle \ . \tag{9.9}$$

Figure 9.3 (right) shows the corresponding terms for reconstructed photons and the V0 event plane, which are on the order of $\mathcal{O}(10^{-6})$. Thus, even for a inclusive photon flow of 1%, relative systematic biases are on the order of $\mathcal{O}(10^{-4})$. As an additional cross-check, we extract the

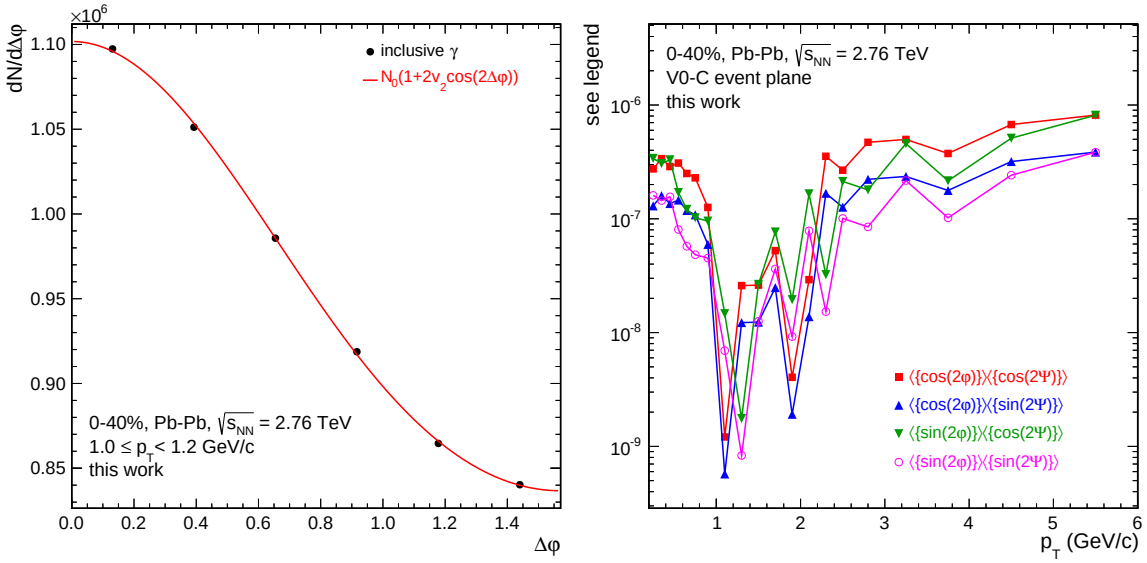

Figure 9.3: (left) Inclusive-photon raw yield in azimuthal bins with respect to the V0-C event plane. (right) Estimates for the magnitude of systematic bias due to non-flow correlations arising from non-uniformities of the event-plane and photon azimuthal distribution.

inclusive photon flow from the event-plane angle before the shift correction yielding relative deviations on the order of $\mathcal{O}(10^{-3})$, which are considered as systematic uncertainty. It can be seen in section 9.2.2 that the contribution of the afore mentioned effects of non-uniformities to the total systematic uncertainty is rather negligible.

9.2.2 Systematic uncertainties

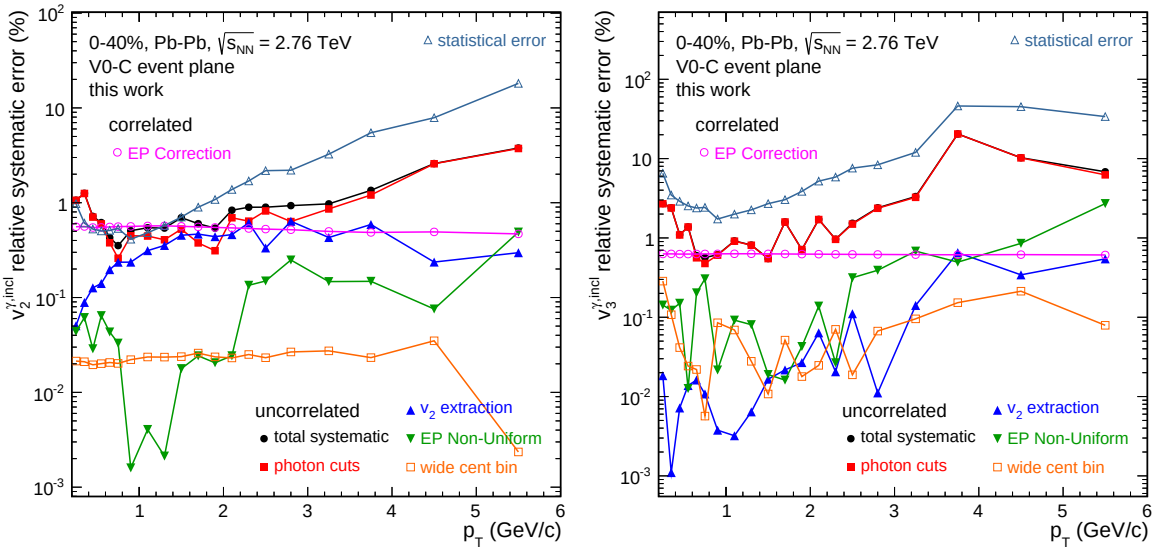

Figure 9.4: Individual contributions to the systematic uncertainties for $v_2^{\gamma,\mathrm{inc}}$ (left) and $v_3^{\gamma,\mathrm{inc}}$ (right) measured with the V0-C event plane

Within this thesis, it is assumed that systematic uncertainties are associated with Gaussian

probability density functions. Thus, systematic uncertainties are estimated by the root mean square of results obtained by different selection cuts or methods for the anisotropic flow extraction. The total systematic uncertainty is then calculated as the square root of the quadratic sum of all contributions. The relative systematic uncertainties $\sigma_{v_n^{\gamma,\mathrm{inc}}}/v_n^{\gamma,\mathrm{inc}}$ of the inclusive-photon elliptic and triangular flow are shown in fig. 9.4. It is distinguished between uncorrelated systematic uncertainties and correlated systematic uncertainties arising from the propagation of the event-plane resolution correction. For comparison, also the statistical error is shown (gray open up-pointing triangles). The individual contributions to the total systematic uncertainty (black full circles) are briefly discussed in the following:

Cut	Standard	Variation
$N^{\mathrm{e}}_{\sigma,\mathrm{TPC}}$	$[-3, 5]$	$[-5, 5]$,$[-2.5, 4]$
$N^{\mathrm{e}}_{\sigma,\mathrm{TOF}}$	$[-5, 5]$	
$N^{\pi^{\pm}}_{\sigma,\mathrm{TPC}}$ (track $p_{\mathrm{T}} \geq 0.4\,\mathrm{GeV}/c$)	$[3, -10]$	$[3.5, -10]$,$[2.5, -10]$
Max χ^2	30	20,50
Min track p_{T} [GeV/c]	0.05, 0.1, 0.075	
Max q_{T}	0.05	0.03 ,0.07
Max Ψ_{pair}	0.05	0.1, 0.035, ∞
Min R_{conv} [cm]	5	13, 20, 35, 55

Table 9.3: Standard photon cuts and their variation

(red full boxes) Systematic uncertainties arising from the yield extraction, but also from the missing efficiency and purity corrections, are estimated by a variation of the standard photon selection cuts (cf. sections 8.2.2 and 8.2.3). Standard values for the main cuts as well as their variation are summarized in table 9.3. Since the photon yields are not corrected for efficiencies and purities, a variation of the photon selection cuts introduces small changes of both quantities and deviations allow to estimate the magnitude of possible corrections. Since local track densities become smaller at larger conversion radii, a significantly higher purity can be achieved by neglecting conversions in the first layers of the ITS material. Thus, the minimum conversion radius is varied from 5 cm to 55 cm, corresponding to a removal of photons reconstructed in the ITS. The variation of all aforementioned photon selection cuts gives the dominant contribution to the total systematic uncertainty.

(blue full up-pointing triangles) $v_n^{\gamma,\mathrm{inc}}$ can be either be calculated directly or extracted by fitting the Fourier expansion to the $\mathrm{d}N/\mathrm{d}\Delta\phi$ distribution. As a cross check, the Fourier distribution is once fitted exclusively with the n-th harmonic and once including the next higher harmonic ($2n$). Deviations are most pronounced at high p_{T}, where the statistical uncertainties are large.

(orange open boxes) In wide centrality bins, v_n is calculated from the measurements in small centrality bins according to eq. (9.1). By default, each measurement is weighted by the uncorrected raw yield in a given centrality bin $N^{\mathrm{C}}_{\mathrm{poi}} = N_{\gamma,\mathrm{inc}}$. Since the efficiency and purity depend on the centrality (cf. figs. 8.6 (left) and 8.6 (right)), as a cross check, the purity and efficiency corrected yield is used for N_{poi} in eq. (9.1). As another cross check, the

inclusive-photon yield is directly extracted from the yields in the wide centrality bin using the method described in [313]. Except for the first low-p_{T} point, those effects have a rather small contribution to the total systematic uncertainty.

(green full down-pointing triangles) Uncertainties arising from the non-uniformity of the laboratory azimuthal distribution of reconstructed photons and the event plane are estimated as described in section 9.1.1. Those contributions are small, since the photon acceptance and efficiency do not have any low order periodic non-uniformities, since the TPC is an almost uniform 2π detector. Small periodic non-uniformities of the efficiency and acceptance arise from the eighteen fold segmentation of the detector read out and its supply structures, which are not relevant for lower order harmonics.

(magenta open circles) The uncertainty of the event-plane resolution correction (cf. section 9.1.2) gives a constant relative systematic uncertainty, which is correlated. In wide bins, the systematic uncertainty is estimated by

$$\sigma^{\mathrm{EP}}_{\mathrm{v_n}} = \frac{\sum_{c_{\mathrm{min}}}^{c_{\mathrm{max}}} \left(\sigma^{\mathrm{c}}_{\mathrm{EP}} v^{\mathrm{c}}_n N^{\mathrm{c}}_{\mathrm{poi}}\right)^2}{\sum_{c_{\mathrm{min}}}^{c_{\mathrm{max}}} N^{\mathrm{c}}_{\mathrm{poi}}} \,, \tag{9.10}$$

where $\sigma^{\mathrm{c}}_{\mathrm{EP}}$ is the systematic uncertainty on the event-plane resolution correction in a given centrality bin c.

Since the event-plane resolution is smaller for triangular flow than for elliptic flow, systematic and statistical uncertainties are larger for the triangular flow than for the elliptic flow. It can be generally stated that the systematic uncertainties of the inclusive-photon anisotropy $v_n^{\gamma,\mathrm{inc}}$ are much smaller than the uncertainties of the inclusive-photon spectra (cf. section 8.2.5). The reason is that v_n is a measure of the in-plane photon production relative to the out-of-plane photon production and thus any uncertainty arising from normalizations, efficiency, purity or acceptance corrections cancel out. As discussed in section 8.2.5, the systematic uncertainty of the inclusive-photon spectrum is dominated by the uncertainty on the conversion probability (4.5%), which is not relevant for the anisotropic flow analysis. Even non-uniformities in the conversion probability are expected to cancel out, since the event-plane Ψ_n^{EP} is uniformly distributed with fluctuations smaller than 1% (cf. section 9.1.1).
As indicated by their centrality dependence shown on figs. 8.6 (left) and 8.6 (right), the purity and efficiency of the photon reconstruction depend on the TPC track multiplicity, which is a measure for the detector occupancy. The azimuthal anisotropy of the bulk of particles generated in heavy-ion collisions implies that the photon purity and efficiency depend on the azimuthal angle. A variation of the photon selection cuts introduces small variations of the efficiency and purity and allows to estimate the magnitude of missing purity and efficiency corrections. The azimuthal non-uniformity of the photon purity and efficiency is not reproduced by current Monte Carlo implementations, since the magnitude of the azimuthal anisotropy was not known a priori. In the following, these effects shall be estimated with the help of a simple model.

9.2.3 Effects of azimuthal non-uniform photon purity and efficiency

It can be assumed that the multiplicity dependence of the purity and the efficiency are correctly described in current Monte Carlo productions. The TPC track multiplicity is studied in six

azimuthal bins with respect to the TPC event plane. In the following, the track multiplicity in a given $\Delta\phi$ bin is referred to as local track multiplicity. Figure 9.5 (right) shows the average local track multiplicity $\langle N_{\text{track}} \rangle$ as a function of $\Delta\phi$, which gives access to the p_{T}-integrated elliptic flow with a magnitude of about 2% in 0 - 40% central Pb-Pb collisions. Figure 9.5 (left) shows the photon reconstruction efficiency ϵ^{γ} and purity p^{γ} as a function of the local TPC track multiplicity. It can be seen that both quantities decrease with increasing multiplicity. The multiplicity dependence is parametrized by a second order polynomial function. Combining both results, it is found that the inclusive photon measurement has a higher purity p^{γ} and efficiency ϵ^{γ} out-of-plane than in-plane. A bin-by-bin correction for this effect can be obtained by

$$\text{corr}^{\gamma}\left(\Delta\phi\right) = \frac{p^{\gamma}\left(\langle N_{\text{track}} \rangle \left(\Delta\phi\right)\right)}{\epsilon^{\gamma}\left(\langle N_{\text{track}} \rangle \left(\Delta\phi\right)\right)} \,. \tag{9.11}$$

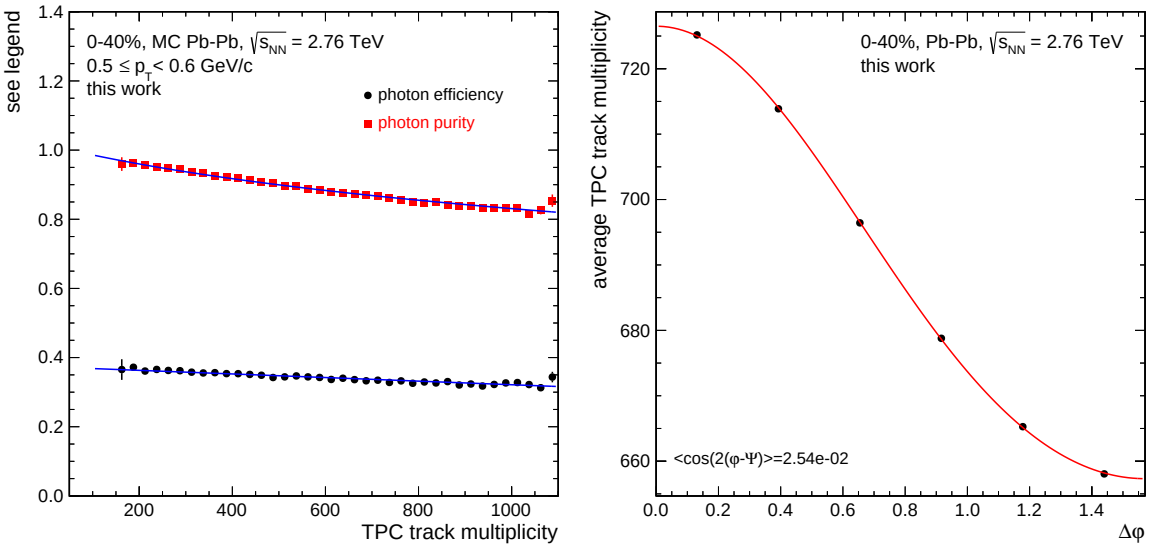

Figure 9.5: (left) Purity and efficiency as a function of the local track multiplicity for photons with 0.5 - 0.6 GeV/c transverse momentum. (right) Average local track multiplicity as a function of the azimuthal angle with respect to the event-plane angle.

The obtained correction factors $v_n^{\gamma,\text{corr}}/v_n^{\gamma,\text{meas}}$ are shown in fig. 9.6. For comparison, also the systematic uncertainty of $v_n^{\gamma,\text{inc}}$ (orange dashed open boxes) is shown. Uncertainties of the correction consider only the uncorrelated statistical uncertainties of the purity and efficiency, since the correlated part would just involve a constant bias of the yield and thus cancels out. Due to a slightly larger in-plane than out-of-plane contamination, contamination in the photon sample increases the measured anisotropy. On the other hand, the photon reconstruction efficiency is lower in-plane than out-of-plane, which decreases the measured anisotropy. Consequently, the purity correction reduces v_n (blue full down-pointing triangles), while the efficiency correction enlarges v_n (red full up-pointing triangles). It can be seen that both corrections almost cancel out, such that the full correction factor (black full points) fluctuates around unity. Within the statistical uncertainties of the correction and the systematic uncertainty of the measurement, the correction factor is consistent with unity and does not indicate any correlated systematic bias towards smaller or larger values. Only the first low-p_{T} point for $v_2^{\gamma,\text{inc}}$ might indicate a systematic deviation.

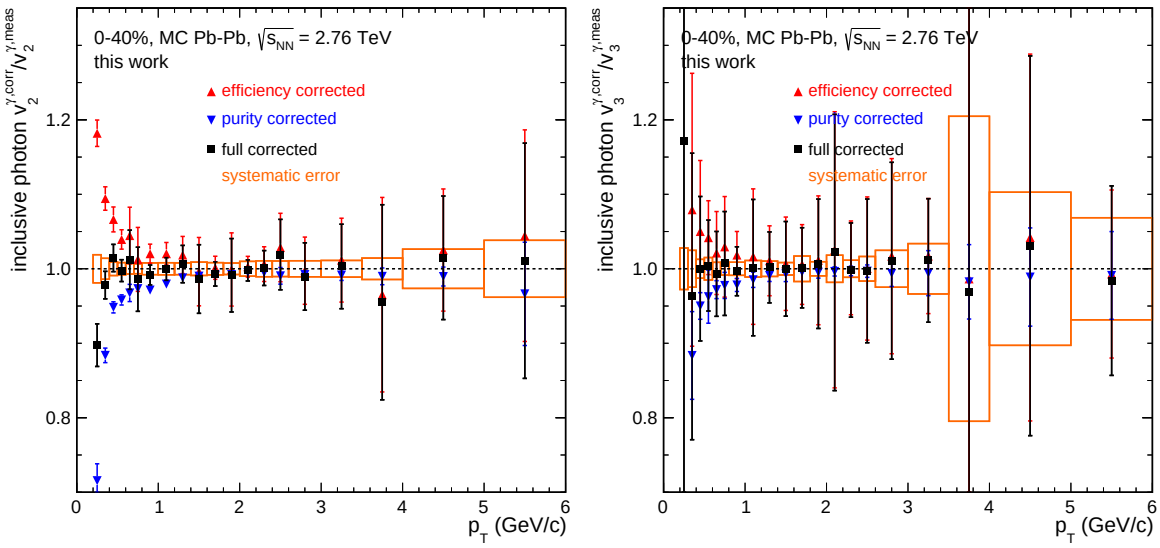

Figure 9.6: Efficiency and purity correction factors for $v_2^{\gamma,\mathrm{inc}}$ (left) and $v_3^{\gamma,\mathrm{inc}}$ (right) in comparison to the systematic uncertainty.

It can be concluded that the dominant uncorrelated systematic uncertainty related to the variation of photon selection cuts might result from an azimuthally anisotropic photon reconstruction efficiency and purity. It should be noticed that the correction factors were obtained from a simple model as a cross check. Since the application of these corrections would not change the result significantly and the corrections itself are affected by systematic uncertainties, the correction is not applied to the data.

9.2.4 Comparison of different event-plane methods

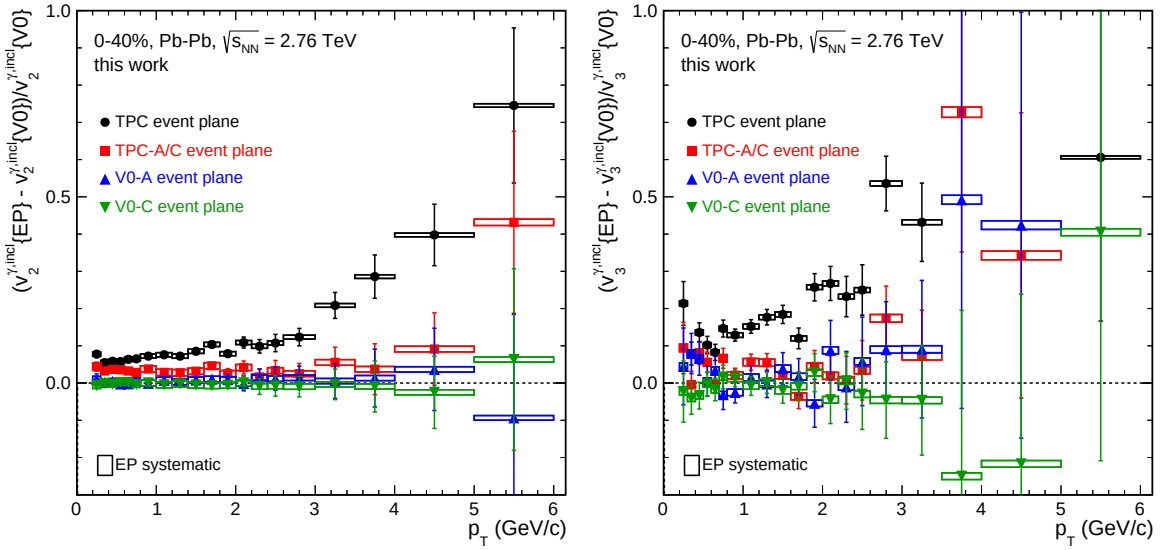

Figure 9.7: Relative deviations of $v_2^{\gamma,\mathrm{inc}}$ (left) and $v_3^{\gamma,\mathrm{inc}}$ (right) measured with the TPC, TPC-A/C, V0-A and V0-C event plane from the standard V0 measurement.

Figure 9.7 shows a comparison of the inclusive-photon elliptic and triangular flow measured with respect to different event planes. In more detail, the relative deviation from the standard event-plane method

$$\left(v_n\{\mathrm{EP}\} - v_n\{\mathrm{V0}\}\right)/v_n\{\mathrm{V0}\} \tag{9.12}$$

is shown. $v_n\{\mathrm{V0\text{-}A}\}$ and $v_n\{\mathrm{V0\text{-}C}\}$ agree within uncertainties. For triangular flow, also the TPC-A/C measurement is consistent within uncertainties, while the elliptic flow measurement indicates a constant systematic bias by about 5% towards higher values. The measurement using the full TPC event plane deviates by more than 8% for $v_2^{\gamma,\mathrm{inc}}$ and by more than 10% for $v_3^{\gamma,\mathrm{inc}}$. The deviations increase with the transverse momentum p_T.
It was shown in section 7.5 that also the systematic bias between mean value and root mean square ($\langle v_n\rangle \leq v_n\{\mathrm{EP}\} \leq \sqrt{\langle v_n^2\rangle}$) needs to be taken into account, when results obtained with event planes of different resolution are compared. The resolution of the V0-C and the TPC-A/C event plane are comparable (cf. fig. 9.2), so a comparison of both methods is expected to give unbiased access to non-flow effects of the order of 5%, which can be explained by the about four times larger average pseudorapidity gap of the V0-C measurement compared to the TPC-A/C measurement. Due to the higher resolution of the full TPC event plane, the elliptic and triangular flow extracted with the full TPC event plane is expected to be around 4% smaller compared to the V0-C event plane (cf. fig. 7.9). If this systematic bias is taken into account, deviations between the TPC and standard measurement are even larger than 10%, which indicates a strong non-flow contribution to the TPC measurement.
From the observation that the V0-A and V0-C measurement agree within uncertainties, even though the pseudorapidity gaps differ, it can be concluded that non-flow correlations are sufficiently suppressed for the standard method.

9.2.5 Centrality and momentum dependence

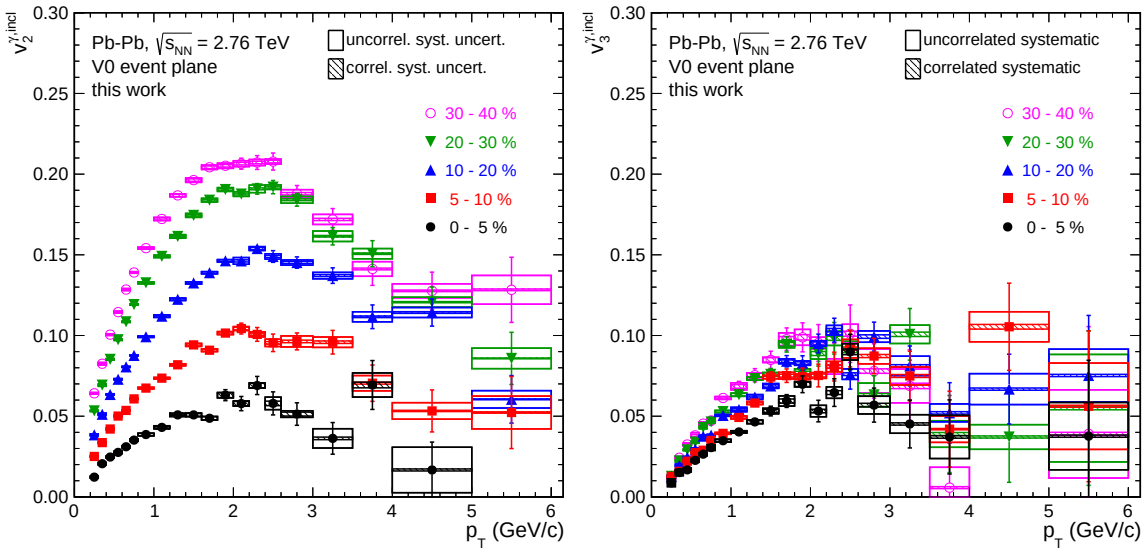

Figure 9.8: Inclusive-photon elliptic (left) and triangular (right) flow measured with the standard V0 method for different centrality ranges.

Figure 9.8 shows the inclusive-photon elliptic and triangular flow for different centrality ranges. The results show the expected increase of $v_2^{\gamma,\mathrm{inc}}$ with decreasing centrality, while the centrality dependence of $v_3^{\gamma,\mathrm{inc}}$ is rather weak. As expected from the hydrodynamical expansion, the anisotropic flow v_n increases almost linearly at low p_T, then saturates and reaches its maximum between 2 - 2.5 GeV/c transverse momentum. Hereafter, the anisotropic flow decreases but remains positive.

9.3 Anisotropic flow of neutral pions

The neutral pion raw yields are extracted as described in section 8.3. The analysis of the neutral pion anisotropy is done analogously to the inclusive photon analysis using the $\mathrm{d}N/\mathrm{d}\Delta\phi$ method. The π^0 raw yield is measured in six $\Delta\phi$ bins. Figure 9.9 shows for illustration the neutral pion raw yield as a function of $\Delta\phi$ as measured with respect to the V0-C event plane for transverse momenta of 1.5 - 2.0 GeV/c. Comparing the $\mathrm{d}N/\mathrm{d}\Delta\phi$ distribution for neutral pions with the inclusive photon $\mathrm{d}N/\mathrm{d}\Delta\phi$ distribution shown in fig. 9.3 (left), it can be seen that statistical uncertainties are much larger for neutral pions. Due to the limited statistics, the neutral pion flow is studied in 0 - 20%, 20 - 40% and 0 - 40% centrality using the event-plane resolution correction for wide centrality bins described in [313]. As an alternative to the $\mathrm{d}N/\mathrm{d}\Delta\phi$ method, the neutral pion anisotropy can be calculated from a different approach named ***invariant mass sideband method***, which is described in the following subsection.

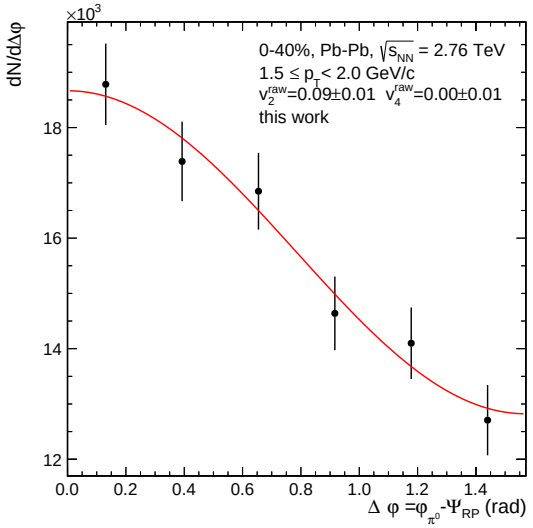

Figure 9.9: Neutral pion raw yield as a function of $\Delta\phi$ measured with the V0-C event plane.

9.3.1 The invariant mass sideband method

Another way to study the anisotropic flow of short lived particles was suggested by the authors of [354]. The anisotropic flow of all photon pairs is measured as a function of the invariant mass, $v_n^{\gamma\gamma}\,(M_{\gamma\gamma})$, which is shown in fig. 9.10 (right). The relation between $v_n^{\gamma\gamma}\,(M_{\gamma\gamma})$, the neutral pion anisotropic flow $v_n^{\pi^0}$ and the combinatorial background anisotropy v_n^{BG} is given by

$$v_n^{\gamma\gamma}\,(M_{\gamma\gamma}) = \frac{N\pi^0}{N_{\gamma\gamma}}\,(M_{\gamma\gamma})\,v_n^{\pi^0} + \frac{N_{\mathrm{BG}}}{N_{\gamma\gamma}}\,(M_{\gamma\gamma})\,v_n^{\mathrm{BG}}\,(M_{\gamma\gamma})\ , \tag{9.13}$$

where N_{π^0} is the neutral pion raw yield, N_{BG} is the combinatorial background and $N_{\gamma\gamma} = N_{\pi^0} + N_{\mathrm{BG}}$ is the number of photon pairs. The relative contribution of signal and background to the two-photon invariant mass spectrum is shown in fig. 9.10 (left). Both contributions are fitted with eq. (8.15) with a constant offset, the fits are shown as red (dashed) lines. The azimuthal anisotropy of the combinatorial background is estimated using a sideband fit within the intervals defined in section 8.3.2. The combinatorial background anisotropy v_n^{BG} is fitted

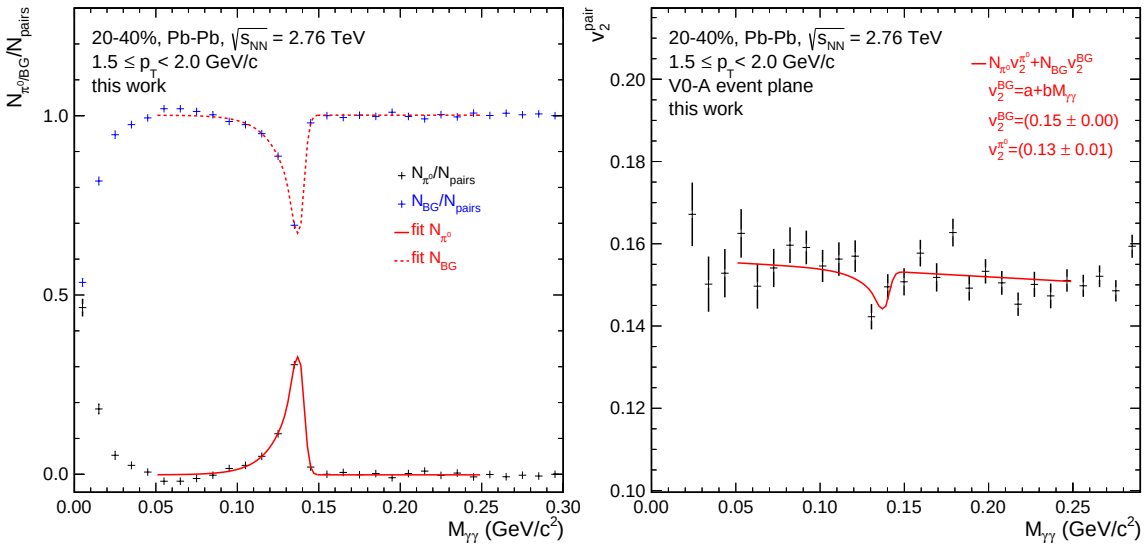

Figure 9.10: (left) Relative contribution of signal and background to the two-photon invariant mass spectrum as a function of $M_{\gamma\gamma}$ with corresponding fits. (right) $v_n^{\gamma\gamma}$ $(M_{\gamma\gamma})$ as a function of $M_{\gamma\gamma}$ with fit for $v_n^{\pi^0}$ extraction.

with a constant, a first and a second order polynomial. The method with the smallest χ^2_{red} value is chosen as default, deviations to the fit with the second best χ^2_{red} value are considered as systematic uncertainty. In fig. 9.10 (right), the shape of v_n^{BG} is best described by a second order polynomial, but also a first order polynomial would fit, while a constant would obviously fail to describe the shape. Thus, the constant fit gives the worst χ^2_{red} value and is not considered here. The situation is different at high p_{T}, where statistical uncertainties become large. There, a constant or first order polynomial can give a better description of the combinatorial background v_n shape.
Finally, $v_n^{\pi^0}$ can be calculated from $v_n^{\gamma\gamma}$ $(M_{\gamma\gamma})$ by fitting eq. (9.13) with only $v_n^{\pi^0}$ as a free parameter. The fit is shown as red line in fig. 9.10 (right).

9.3.2 Systematic uncertainties with the dN/d$\Delta\phi$ method

Figure 9.11 shows the individual contributions to the systematic uncertainties for $v_2^{\pi^0}$ and $v_3^{\pi^0}$ measured with the V0-C event plane as obtained with the dN/d$\Delta\phi$ method. For comparison, also the statistical error is shown (gray open up-pointing triangles). The following sources of systematic uncertainty are taken into account:

(red full boxes) In the case of a perfect background subtraction, the extracted azimuthal anisotropy should not depend on the choice of the integration window. In order to estimate systematic uncertainties arising from non-perfect background subtraction, the lower integration limit M_{min} is varied in $[m_{\pi^0} - 0.055, m_{\pi^0} - 0.05]$ and the upper limit M_{max} in $[m_{\pi^0} + 0.005, m_{\pi^0} + 0.025]$. The variation of the integration window yields a distribution for $v_n^{\pi^0}$. Since the integration window is only varied in the tails of the invariant mass peak, differences in the statistical uncertainties are neglected. We define $v_n^{\pi^0}$ as the mean value of the distribution and use the mean statistical error. The systematic uncertainty is estimated from the width of the $v_n^{\pi^0}$ distribution, which is the dominant contribution to the total systematic

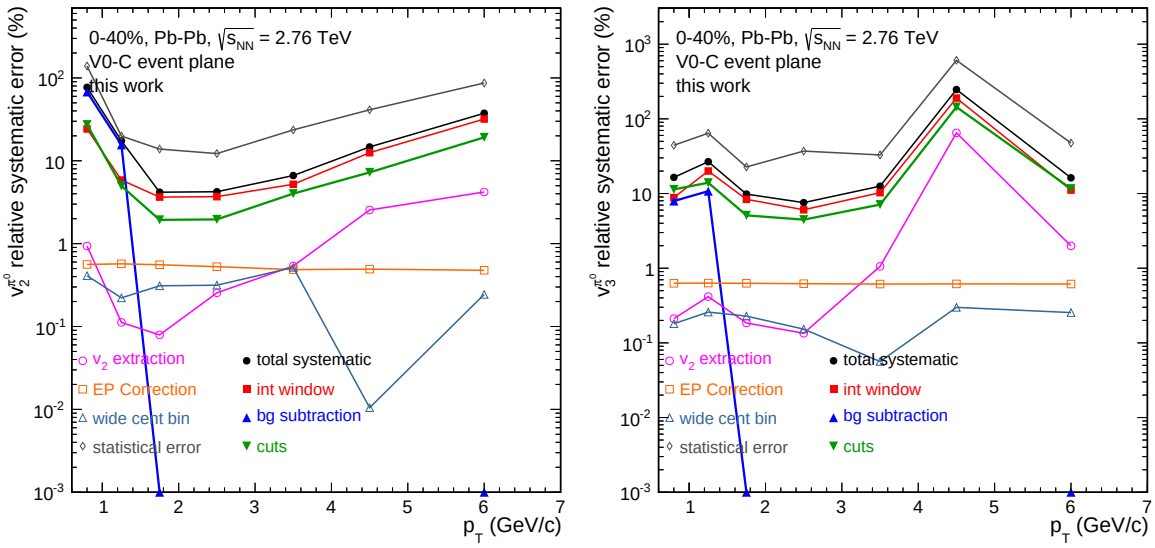

Figure 9.11: Individual contributions to the systematic uncertainties for $v_2^{\pi^0}$ (left) and $v_3^{\pi^0}$ (right) measured with the $\mathrm{d}N/\mathrm{d}\Delta\phi$ method using the V0-C event plane.

uncertainty at intermediate and high p_{T}.

(blue full up-pointing triangles) Systematic effects of the background subtraction are further studied by using the three different normalization procedures described in section 8.3.2. By default, the method with the smallest χ^2_{red} value for the fit of the signal invariant mass distributions in the six $\Delta\phi$ bins with eq. (8.15) is used. Systematic uncertainties are estimated from deviations to the method with the second best χ^2_{red} value. Systematic uncertainty arise only at low transverse momentum, where the signal-to-noise ratio is small.

(green full down-pointing triangles) A variation of the photon selection cuts (cf. table 9.3) and of the energy asymmetry cut lead to small modifications of the neutral pion signal-to-noise ratio, the efficiency and statistical uncertainties. For photons, we have found in section 9.2.3 that corrections for the non-uniformity of the efficiency and purity almost cancel out and remaining corrections are covered by the systematic uncertainty estimated from the variation of photon selection cuts. Since neutral pions can be identified by their peak in the two photon invariant mass spectrum, purity corrections can be neglected and the extracted yields are mainly affected by the efficiency. It can be seen in section 9.2.3 that the correction for the photon efficiency would enhance the inclusive-photon anisotropic flow by less than 10% at low p_{T} below 1 GeV/c, whether at higher momenta are not significant. At small momenta, the opening angle of photon pairs from neutral pion decays is rather large, such that efficiency corrections on the extracted anisotropy are expected to be small. The systematic uncertainty estimated from the photon cut variation seems to be correlated with the uncertainty estimated by the variation of the integration window, which might indicate that the photon cut variation is more sensitive to the non-perfect background subtraction than to non-uniformities in the neutral pion efficiency.

(magenta open circles) In analogy to the inclusive photon analysis, the azimuthal anisotropy is extracted directly from $\langle \cos(n\Delta\phi) \rangle$ and by fitting the Fourier distribution with and without

higher harmonics to the measured neutral pion $\mathrm{d}N/\mathrm{d}\Delta\phi$ distribution. Similar to the inclusive photon measurement, the systematic uncertainty of the v_n extraction increases with p_T, since the statistical uncertainty increases.

(orange open boxes) Analogously to the inclusive photon analysis, the uncertainties of the event-plane resolution correction are propagated. Since it gives only a small contribution to the systematic uncertainty, the correlation is neglected in the following.

(cyan open up-pointing triangles) Analogously to the inclusive photon $\mathrm{d}N/\mathrm{d}\Delta\phi$ analysis, the integration over a wide centrality window is related with a small systematic uncertainty.

Comparing the total systematic uncertainties (black) with the statistical uncertainties (light blue), it can be seen that the systematic uncertainty is about a factor of 2 - 3 smaller than the statistical uncertainty, but seems to be at least partially correlated with the statistical uncertainty. On the one hand, this behavior is expected, since the probability of residual background increases with the statistical uncertainties, on the other hand, it could mean that part of the statistical uncertainty is considered to be systematic and thus the systematic uncertainty is overestimated. However, when comparing different results it is hard to trace the correlated part of the statistical uncertainty, due to the complex extraction procedure. Therefore, the statistical significance of deviations is neglected, which might give rather conservative estimates for the systematic uncertainty.

9.3.3 Systematic uncertainties with the invariant mass sideband method

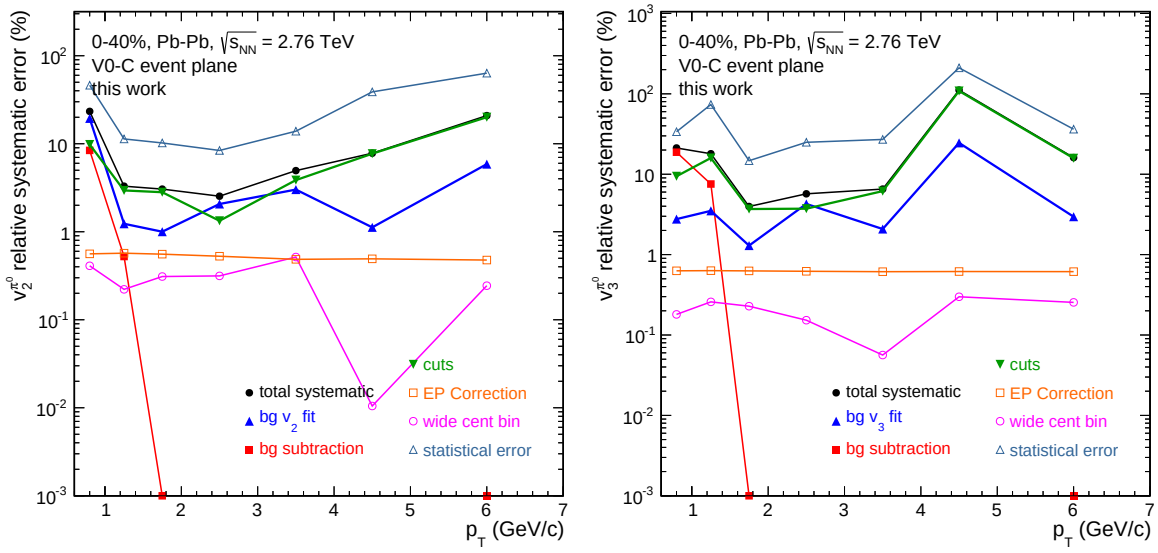

Figure 9.12: Individual contributions to the systematic uncertainties for $v_2^{\pi^0}$ (left) and $v_3^{\pi^0}$ (right) measured with sideband invariant mass method using the V0-C event plane.

Figure 9.12 shows the individual contributions to the systematic uncertainties for $v_2^{\pi^0}$ and $v_3^{\pi^0}$ for the V0-C event plane as obtained with the invariant mass sideband method. For comparison, also the statistical error is shown (gray open up-pointing triangles). The following aspects are considered:

(blue up-pointing triangles) The combinatorial background v_n^{BG} is fitted with a constant, first and second order polynomial. The best fit in terms of its χ^2_{red} value is used as default, deviations from the second best fit are considered as systematic uncertainty. Systematic uncertainty arises from a small significance at low p_{T} and large statistical uncertainties at high p_{T}.

(red full boxes) Systematic effects of the background subtraction method are studied by using three different normalization procedures, which are described in section 8.3.2. The method with the smallest χ^2_{red} value for the fit of the signal invariant mass distributions eq. (8.15) is used as default, deviations to the method with the second best χ^2_{red} value are considered as systematic uncertainty. Systematic uncertainty arises only at low transverse momentum, where significances are very low.

(green full down-pointing triangles) A variation of the photon selection cuts (cf. table 9.3) and of the energy asymmetry cut leads to changes in the neutral pion significance, efficiency and statistical uncertainties. Thus, the corresponding uncertainty is correlated with the statistical uncertainty. The systematic uncertainty might be overestimated, but due to the complex extraction procedure, it is hard to trace the statistically correlated part.

(orange open boxes) Analogously to the $\mathrm{d}N/\mathrm{d}\Delta\phi$ analysis, the uncertainties of the event-plane resolution correction are propagated, which gives a constant contribution to the relative systematic error. The correlation of this source of systematic uncertainty is neglected.

(magenta open up-pointing triangles) The integration over a wide centrality window (compare with sections 9.2.2 and 9.3.2) is related with a small systematic uncertainty.

Compared with the $\mathrm{d}N/\mathrm{d}\Delta\phi$ method, the invariant mass sideband method seems to give smaller systematic and statistical uncertainties, in particular at low p_{T}. In the $\mathrm{d}N/\mathrm{d}\Delta\phi$ method, the signal extraction is done in $\Delta\phi$ six bins, which gives an up to $\sqrt{6}$ times larger statistical uncertainty on the extracted signal invariant mass distribution compared to the sideband method. Since systematic and statistical uncertainties are at least partially correlated, the smaller statistical uncertainties also involve smaller systematic uncertainties.

9.3.4 Comparison with charged pions

Figure 9.13 shows a comparison of neutral and charged pion elliptic and triangular flow. Both measurements are obtained with the V0 event-plane method. Even though the invariant mass sideband method provides much smaller uncertainties compared to the $\mathrm{d}N/\mathrm{d}\Delta\phi$ method, the neutral pion measurement has much larger statistical and systematic uncertainties compared to the charged pion measurement. The reason is that the neutral pion reconstruction efficiency is about 1000 times smaller than the charged pion reconstruction efficiency. The neutral pion analysis via photon conversions is limited by the conversion probability of at maximum $P_{\mathrm{conv}} \approx 8.5\%$ at $p_{\mathrm{T}} \geq 2\,\mathrm{GeV}/c$ (section 8.2.4) and the photon reconstruction efficiency of about 50% (section 8.2.1), which gives $(50\%)^2\,(8.5\%)^2 = \mathcal{O}(10^{-3})$. The measurements agree within uncertainties, which is expected from isospin symmetry. Due to the significantly smaller systematic and statistical uncertainties, the cocktail simulation for the neutral pion decay photons is parametrized with the charged pion measurement.

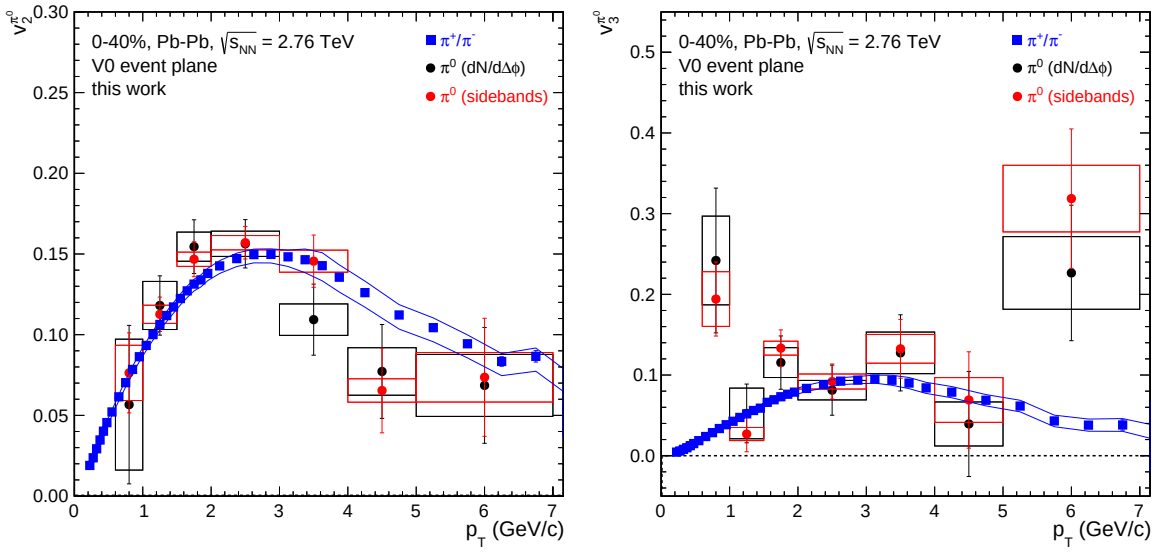

Figure 9.13: Neutral and charged pion elliptic (left) and triangular (right) flow in 0 - 40% central Pb-Pb collisions, both determined with the V0 event-plane method.

10. Extraction of the direct-photon anisotropic flow

This chapter describes the extraction of the direct-photon elliptic and triangular flow. The anisotropic flow of direct photons can be extracted from the measurement of inclusive photons by subtracting all photons from hadron decays. The details of the cocktail simulation and the calculation of the decay photon anisotropic flow are described in section 10.1. Thereafter, the extraction of the direct-photon anisotropic flow and the related uncertainties are discussed in section 10.2.

10.1 Decay-photon spectra and anisotropic flow

Meson	Mass (MeV/c^2)	Decay Mode	Γ_i/Γ (%)
π^0	134.9766 ± 0.0006	$\gamma\gamma$	(98.823 ± 0.034)
		$e^+e^-\gamma$	(1.174 ± 0.035)
η	547.853 ± 0.024	$\gamma\gamma$	(39.31 ± 0.20)
		$\pi^+\pi^-\gamma$	(4.60 ± 0.16)
		$e^+e^-\gamma$	$(6.9 \pm 0.4) \times 10^{-3}$
		$\pi^0\gamma\gamma$	$(2.7 \pm 0.5) \times 10^{-4}$
ρ	775.49 ± 0.34	$\pi^+\pi^-\gamma$	$(9.9 \pm 1.6) \times 10^{-3}$
		$\pi^0\gamma$	$(6.0 \pm 0.8) \times 10^{-4}$
		$\eta\gamma$	$(3.00 \pm 0.20) \times 10^{-4}$
ω	782.65 ± 0.12	$\pi^0\gamma$	(8.28 ± 0.28)
		$\eta\gamma$	$(4.6 \pm 0.4) \times 10^{-4}$
η'	957.78 ± 0.06	$\rho\gamma$	(29.3 ± 0.6)
		$\omega\gamma$	(2.75 ± 0.22)
		$\gamma\gamma$	(2.18 ± 0.08)
ϕ	1019.455 ± 0.020	$\eta\gamma$	(1.309 ± 0.024)
		$\pi^0\gamma$	$(1.27 \pm 0.06) \times 10^{-3}$
		$\omega\gamma$	< 5

Table 10.1: Cocktail hadrons, their electromagnetic decay modes and the corresponding relative branching ratio. Values taken from [9].

Even though the decay-photon spectrum and its anisotropic flow cannot be measured directly, it can be calculated in a cocktail simulation from the spectrum and anisotropy of those hadrons, which undergo electromagnetic decays. The cocktail simulation includes decays of neutral pions, η, η', ω, ρ and ϕ mesons. Table 10.1 summarizes the relevant decay channels and the corresponding branching ratios. The dominant fraction of decay photons comes from the neutral pion

decay. The decay-photon spectrum can be estimated in a cocktail simulation, where the decay kinematics are simulated by PYTHIA [355] and the production cross sections are parametrized by the experimentally measured hadron spectra. As described in detail in the following, the neutral pion spectra are parametrized by the measured neutral and charged pion spectra, while the spectra of other hadrons are estimated from m_{T} scaling. The parameterization of the neutral pion azimuthal anisotropy is taken from the charged pion anisotropic flow measurement, which has much smaller uncertainties than the neutral pion measurement (cf. section 9.3.4). The anisotropy of the remaining hadrons is estimated by KE_{T}-scaling. Spectra and anisotropic flow are parametrized in the same centrality bins used for the inclusive-photon anisotropic flow analysis.

10.1.1 Implementation of the cocktail simulation

The hadron spectra are generated with flat distributions for the transverse momentum $p_{\mathrm{T}} \in [0, 15\,\mathrm{GeV}/c]$, the rapidity $y \in [-1.2, 1.2]$ and the azimuthal angle $\phi \in [0, 2\pi]$. Flat spectra in transverse momentum yield almost uniform statistical uncertainties, while steeply falling spectra would lead to small uncertainties at low p_{T} and large uncertainties at high p_{T}. The spectral shape is then modulated by a weight for each particle of species h,

$$w^{\mathrm{h}}\left(p_{\mathrm{T}}, \eta, \phi\right) = \frac{\Delta p_{\mathrm{T}} \Delta y 2\pi p_{\mathrm{T}}}{N_{\mathrm{gen}}} Y^{\mathrm{h}}\left(p_{\mathrm{T}}\right) \left(1 + 2v_n^{\mathrm{h}}\left(p_{\mathrm{T}}\right) \cos\left(n\phi\right)\right) \ , \tag{10.1}$$

with $\Delta p_{\mathrm{T}} = {p_{\mathrm{T}}}^{\mathrm{max}} - {p_{\mathrm{T}}}^{\mathrm{min}}$, $\Delta y = 2|y|^{\mathrm{max}}$, where N_{gen} is the number of generated particles per event, $Y^{\mathrm{h}}\left(p_{\mathrm{T}}\right)$ is the invariant yield and $v_n^{\mathrm{h}}\left(p_{\mathrm{T}}\right)$ is the azimuthal anisotropy for the generated particle of species h. The decays of these hadrons are simulated by PYTHIA 6 [355], while each photon with mother particle h is weighted with

$$w^{\gamma,\mathrm{h}} = w^{\mathrm{h}}\left({p_{\mathrm{T}}}^{\mathrm{h}}, \eta^{\mathrm{h}}, \phi^{\mathrm{h}}\right) w_{\mathrm{BR}} \ , \tag{10.2}$$

where w_{BR} is the branching ratio for the corresponding decay.

It is important to notice that the hadrons should be simulated in a slightly larger rapidity window y^{max} compared to the experimentally measured pseudorapidity window ($|\eta| \leq 0.8$), since photons at small momenta can have large decay angles with respect to their mother particles. If the rapidity window $|y|^{\mathrm{max}}$ is chosen too narrow, photons, which are produced by hadrons outside the rapidity window, but contribute to the experimentally measured inclusive-photon spectrum in $|\eta| \leq 0.8$, might be missed by the cocktail simulation. Figure 10.1 (left) shows a calculation for the fraction of missing photons $(N_{\mathrm{tot}} - N_{|\mathrm{y}|^{\mathrm{max}}})/N_{\mathrm{tot}}$ from $\pi^0 \to \gamma\gamma$ (full symbols) and $\eta \to \gamma\gamma$ (open symbols) decays in $|\eta| \leq 0.8$ as a function of p_{T} for different values of $|y|^{\mathrm{max}}$. For $|y|^{\mathrm{max}} = 0.8$, 50% of the photons stemming from neutral pion decays in the first momentum bin and still more than 1% at higher momenta would be missed by the cocktail simulation. Due to the higher mass, even 90% of the photons from η meson decays would be missed at low p_{T}. In the first bin containing photons with momenta below $100\,\mathrm{MeV}/c$, photons cannot be reconstructed and thus this momentum range is not analyzed. For $|y|^{\mathrm{max}} = 1.2$, less than 1% of the photons from neutral pions are missed for momenta above $100\,\mathrm{MeV}/c$. The fraction of missing photons from the η meson is still above 1% for momenta below $500\,\mathrm{MeV}/c$, but it will later be shown (cf. fig. 10.2 (right)) that more than 90% of the decay photons at low

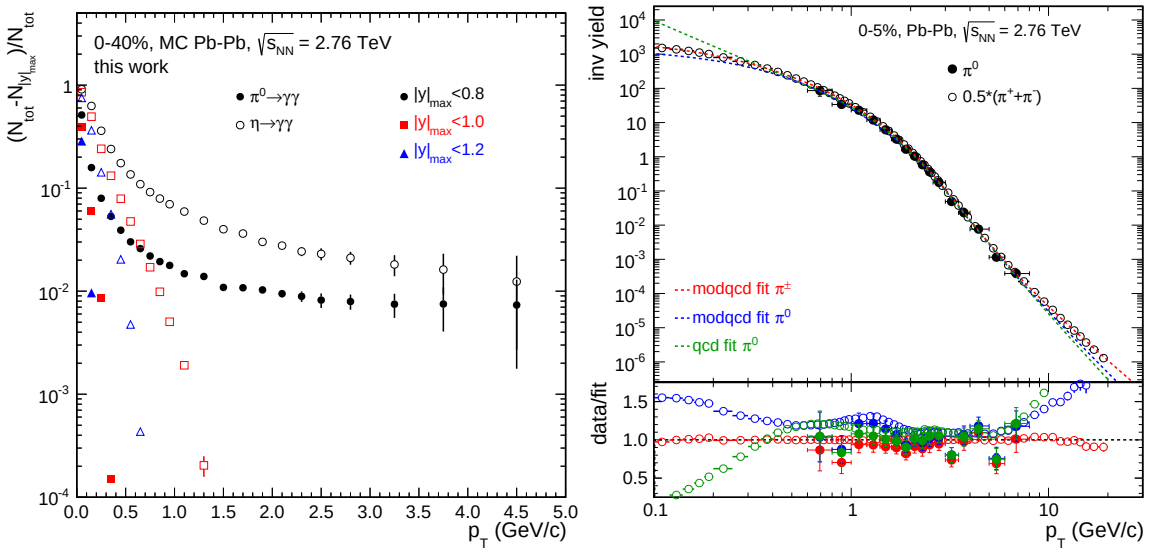

Figure 10.1: (left) Fraction of missing photons from $\pi^0 \to \gamma\gamma$ and $\eta \to \gamma\gamma$ decays in $|\eta| \leq 0.8$ as a function of p_{T} for different values of $y^{\max}$. The default value is $|y|^{\max} = 1.2$. (right) Neutral and charged pion invariant yield with different parameterizations.

p_{T} come from the decay of neutral pions, such that deviations are smaller than 1% at low p_{T}. Consequently, the rapidity window for hadrons is chosen as $|y|^{\max} = 1.2$.

10.1.2 Parametrization of the hadron production cross sections

The spectra produced in pp collisions are often described by a modified Hagedorn function [102]

$$Y^{\pi^0}_{\mathrm{Hag}}(p_{\mathrm{T}}) = a\left(\exp\left(-bp_{\mathrm{T}} - |c|\,p_{\mathrm{T}}^2\right) + \frac{p_{\mathrm{T}}}{d}\right)^{-e} , \tag{10.3}$$

or, at small transverse momenta, by a Tsallis distribution [356]

$$Y^{\pi^0}_{\mathrm{Ts}}(p_{\mathrm{T}}) = a\,(1 + bx/c)^{c} . \tag{10.4}$$

In Pb-Pb collisions, the spectra are modified by the hydrodynamical evolution at lower p_{T} and suppression due to the parton energy loss at high p_{T}. The following parameterization was found [201] to describe the measured neutral pion spectra in central Pb-Pb collisions:

$$Y^{\pi^0}_{\mathrm{qcd}}(p_{\mathrm{T}}) = a p_{\mathrm{T}}^{-\left(b + c/\left((p_{\mathrm{T}})^d + e\right)\right)} \tag{10.5}$$

Charged pions can be identified down to momenta of 0.1 GeV/c, where the signal-to-background ratio is too small to extract the neutral pion yield. Since the function $Y^{\pi^0}_{\mathrm{qcd}}$ cannot describe the charged pion spectrum at low p_{T}, a combination of this function at high p_{T} and a Tsallis distribution at low p_{T} is used to parametrize the spectra,

$$Y^{\pi^0}_{\mathrm{modqcd}}(p_{\mathrm{T}}) = F(p_{\mathrm{T}})\,Y^{\pi^0}_{\mathrm{Ts}}(p_{\mathrm{T}}) + (1 - F(p_{\mathrm{T}}))\,Y^{\pi^0}_{\mathrm{qcd}}(p_{\mathrm{T}}) , \tag{10.6}$$

where a smooth transition between the two functions is given by a Fermi function

$$F\left(p_{\mathrm{T}}\right) = \frac{1}{1+\exp\left(-\left(p_{\mathrm{T}}-s\right)/w\right)} \tag{10.7}$$

with two free parameters s and w.

Figure 10.1 (right) shows the neutral pion and charged pion invariant yield with different parameterizations. Both, the neutral and charged pion spectrum, are fitted with the parameterization eq. (10.6), which agrees reasonably well with the data over the whole momentum range. In addition, the neutral pion spectrum is also fitted with the modified Hagedorn function, which describes the neutral pion data, but shows deviations from the charged pions at low p_{T}. Differences between the parameterizations are later used to estimate the systematic uncertainty. Small deviations between the charged and neutral pion measurement can be observed, which are covered by the systematic uncertainties. The uncertainties of the neutral pion measurement are rather large (9%) due to the uncertainty on the material budget (cf. section 8.3.4).

By now, only the neutral pion spectrum is measured with a sufficient precision in Pb-Pb collisions. Thus, the neutral pion invariant yield $Y\left(p_{\mathrm{T}}\right)$ is parametrized with the measured spectrum and the spectra of the heavier mesons are estimated by m_{T} scaling (cf. section 3.3.3):

$$Y^{\mathrm{h}}\left(p_{\mathrm{T}}\right) = A_{\mathrm{h}/\pi^0} Y^{\pi^0}\left(\sqrt{p_{\mathrm{T}}^2 + m_{\mathrm{h}}^2 - m_{\pi^0}^2}\right) \tag{10.8}$$

The constants A_{h} are taken either from the particle ratios A_{h}/A_{π^0} measured in Au-Au collisions at RHIC or the corresponding ratios calculated in PYTHIA. The values used in this work are summarized in table 10.2. Figure 10.2 (left) shows the meson spectra calculated for 0 - 40% central collisions. It can be seen that the ratios become constant at large transverse momenta, where the particle masses are negligible ($p_{\mathrm{T}} \approx m_{\mathrm{T}}$ for $p_{\mathrm{T}} \to \infty$). Thus, the normalization of the m_{T}-scaled hadron spectra should be taken from the particle ratios at infinity, but for practical purposes, the particle ratios at $p_{\mathrm{T}} = 5\,\mathrm{GeV}/c$ are used for the normalization. The relative contribution of the individual meson decays to the decay-photon spectrum is shown in fig. 10.2 (right). The decay-photon spectrum is dominated by the neutral pion decay followed by the decay of the η meson, while other contributions are of the order $\mathcal{O}(10^{-2})$.

A_{h/π^0}	pp	Au-Au (MB)	Reference
η/π^0	0.497 ± 0.003	0.525 ± 0.002	RHIC [101]
ρ/π^0	1.0 ± 0.3		PYTHIA [355]
ω/π^0	0.903 ± 0.021	0.845 ± 0.145	RHIC [101]
η'/π^0	0.40 ± 0.12		PYTHIA [355]
ϕ/π^0	0.233 ± 0.021	0.348 ± 0.017	RHIC [101]

Table 10.2: Standard meson ratios in the literature for Au-Au collisions at $\sqrt{s_{\mathrm{NN}}} = 200\,\mathrm{GeV}$.

At first glance, this approach may seem inappropriate, as m_{T} scaling is expected to be explicitly broken in nucleus-nucleus collisions by the radial flow at low p_{T} (cf. section 3.3.3) and the suppression of hadron yields at high p_{T} (cf. section 3.3.5). The dominant fraction of decay photons comes from the neutral pion decay followed by the η meson. Since the neutral pion

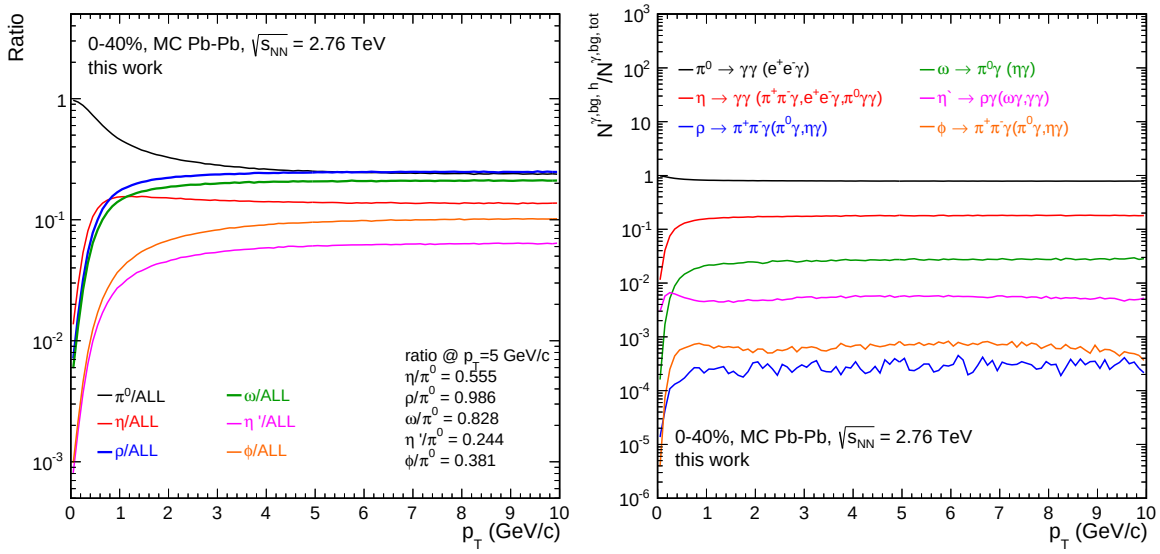

Figure 10.2: Relative abundance of mesons in the cocktail. (right) Relative contribution of the individual meson decays to the decay-photon spectrum.

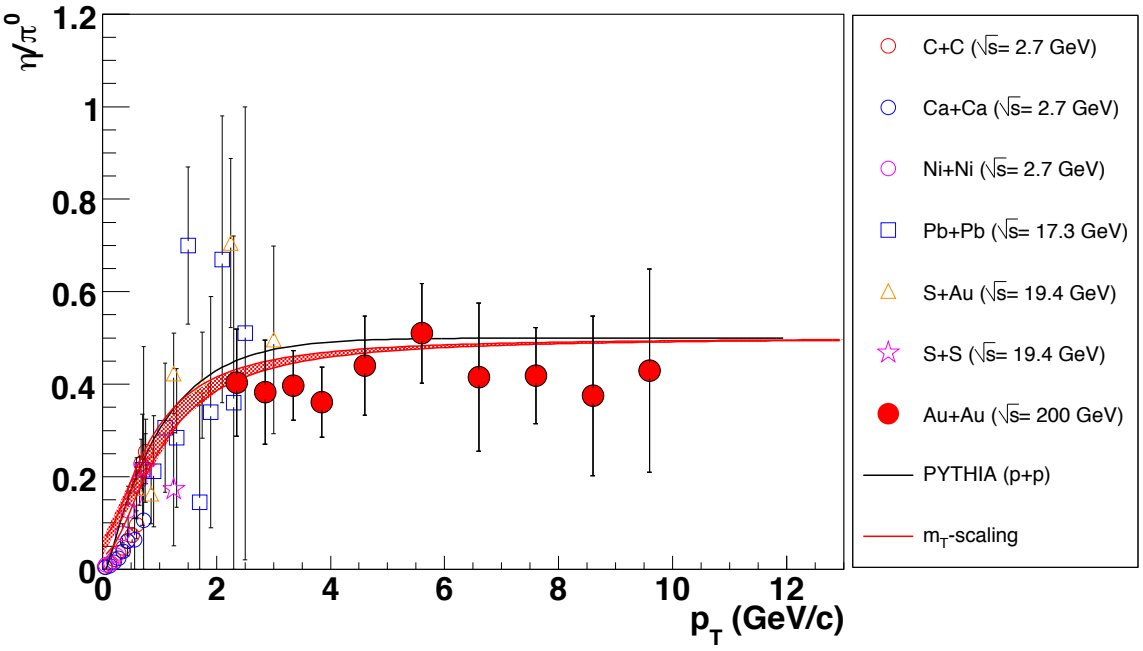

Figure 10.3: η/π^0 ratio in different A-A systems compared with the expectation from m_{T} scaling and the PYTHIA event generator [109].

invariant yield is known from measurements (section 8.3.4), the deviation of the η/π^0 ratio from m_{T} scaling will quantify the dominant systematic uncertainty of the estimated decay-photon spectrum. Figure 10.3 shows the η/π^0 ratio measured in different A-A systems compared with the expectation from m_{T} scaling and the ratio obtained with PYTHIA for pp collisions. It can be seen that m_{T} scaling still gives a good description of the data in A-A collisions except for small transverse momenta below 1 GeV/c. Measurements in pp collisions at $\sqrt{s} = 7$ TeV even indicate a deviation from m_{T} scaling in pp collisions [331, 357]. However, deviations due to the

hydrodynamical flow are expected at small transverse momenta and indications for systematic deviations can only be observed at momenta below 1 GeV/c. The spectra could also be estimated from the AMPT model [358] or the HIJING event generator [335] and it will be interesting to see comparisons. However, those generators are associated with additional systematic uncertainties and it needs to be shown that they reproduce the measured neutral pion spectrum. The main fraction of decay photons comes from neutral pion decays, which in our approach is directly calculated from the measured neutral pion spectra.
The particles ratios A_{h/π^0} shown in table 10.2 are taken from measurements at RHIC and PYTHIA. The measured ratios also indicate a centrality dependence [101]. The high-p_{T} data points in fig. 10.3 indicate that the η/π^0 ratio might be lower than the extracted value of about 0.5. In order to take possible deviations from m_{T} scaling into account, a variation of $\pm 20\%$ of the η/π^0 ratio is considered as systematic uncertainty (cf. section 10.1.6).

10.1.3 Parametrization of the hadron azimuthal anisotropy

In section 9.3.4 it can be seen that the neutral pion elliptic and triangular flow has much larger uncertainties than the charged pion anisotropic flow. The excess of direct photons in 0 - 40% is about 10 - 20% [201]. According to eq. (4.6), uncertainties in the decay-photon anisotropy $v_n^{\gamma,\mathrm{bg}}$ are scaled by $1/(R^{\gamma,dir}-1)$, which is roughly a factor of 5 - 10. If the uncertainties of the neutral pion v_n measurement were propagated to the cocktail, already a systematic uncertainty of about 10 - 20% on the neutral pion v_n would result in a non-significant direct-photon anisotropic flow.

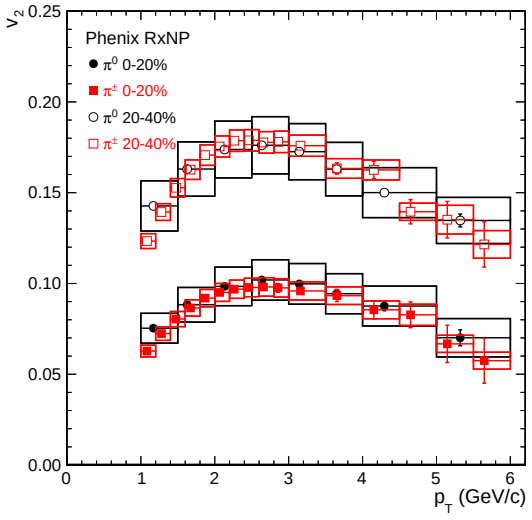

Figure 10.4: Charged and neutral pion v_2 in Au-Au collisions at $\sqrt{s_{\mathrm{NN}}} = 200\,\mathrm{GeV}$. Data points from [204, 359].

The measurement of charged pion anisotropic flow has much smaller uncertainties than the neutral pion measurement, and from the strong isospin symmetry it is expected that the neutral and charged pion production is equal. We have seen in section 9.3.4 that the measured neutral pion anisotropy is consistent within uncertainties with the charged pions. This observation is consistent with the measurements at RHIC shown in fig. 10.4, which indicate no systematic deviation between charged and neutral pions. Small deviations could arise from the fact that the strong isospin symmetry is broken electroweak and also some strong decays and in addition due to Coulomb repulsion between charged pions [360]. The impact of feed down from decays is discussed in detail in section 10.1.5 and shall be neglected for the moment. The breakdown of NCQ scaling between charged particles and their anti-particles was discussed in section 3.4.5. It can be seen in fig. 3.15 (left) that the splitting of positive and negative pions becomes negligible for collisions energies above $\sqrt{s_{\mathrm{NN}}} = 60\,\mathrm{GeV}$, so that NCQ scaling seems to be fulfilled for charged pions at LHC energies.
The azimuthal anisotropy of other hadrons in the cocktail can be estimated from the scaling

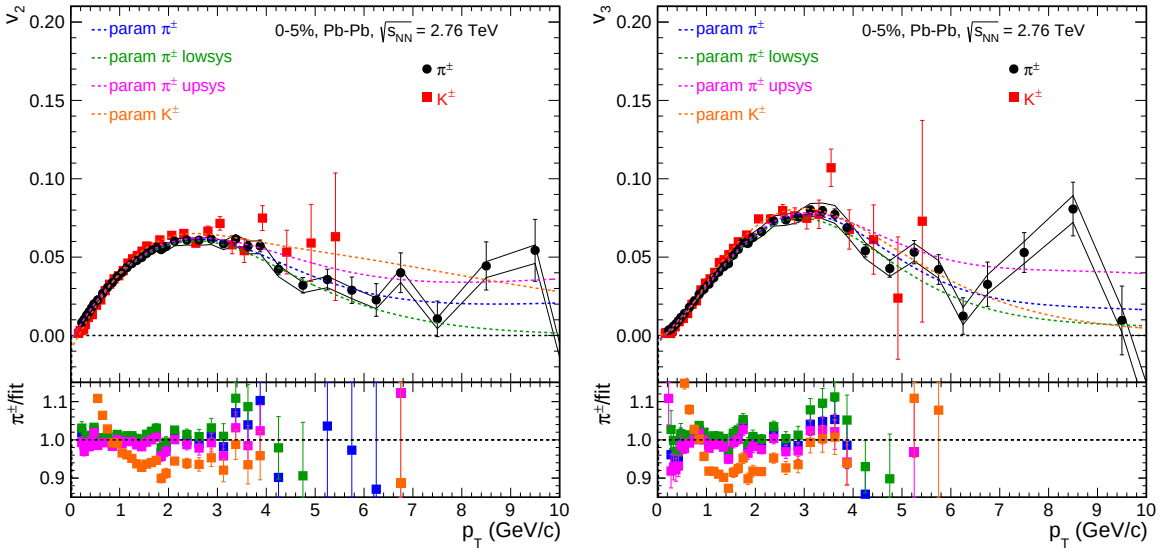

Figure 10.5: Charged pion and KE_{T}-scaled charged kaon elliptic (left) and triangular (right) flow with parameterizations. Data points taken from [152].

in transverse kinetic energy KE_{T}, which was discussed in section 3.4.4. Since only mesons are considered, the quark number ($n_{\mathrm{q}} = 2$) is neglected and $v_n^{\mathrm{h}}(p_{\mathrm{T}})$ for a meson of species h is given by

$$v_n^{\mathrm{h}}\left(p_{\mathrm{T}}^{\mathrm{h}}\right) = v_n^{\pi^{\pm}}\left(\sqrt{\left(KE_{\mathrm{T}}^{\mathrm{h}} + m_{\pi^{\pm}}\right)^2 - m_{\pi^{\pm}}^2}\right) \ . \tag{10.9}$$

This equality can be derived by using that

$$p_{\mathrm{T}}^2 = \left(KE_{\mathrm{T}} + m\right)^2 - m^2 \tag{10.10}$$

and

$$\begin{aligned} v_n^{\mathrm{h}}\left(KE_{\mathrm{T}}\right) = v_n^{\pi^{\pm}}\left(KE_{\mathrm{T}}\right) \ &\Rightarrow \ KE_{\mathrm{T}}^{\pi^{\pm}} = KE_{\mathrm{T}}^{\mathrm{h}} \\ \Rightarrow \ p_{\mathrm{T}}^{\pi^{\pm}(\mathrm{h})} &= \left(KE_{\mathrm{T}}^{\mathrm{h}} + m_{\pi^{\pm}}\right)^2 - m_{\pi^{\pm}}^2 \ , \end{aligned} \tag{10.11}$$

where $p_{\mathrm{T}}^{\pi^{\pm}(\mathrm{h})}$ is the transverse momentum of a pion with the same transverse kinetic energy as the meson of species h. Figure 10.5 shows for illustration the parameterizations for $v_2^{\pi^0}$ and $v_3^{\pi^0}$ in 0 - 5% central collisions in comparison to the charged pion v_2 and v_3, respectively. The charged pion v_n was parametrized with a third order polynomial at low p_{T} and a Landau distribution with constant offset at high p_{T}. Systematic uncertainties of the charged pion measurement are considered by two additional parameterizations, which are fitted to the points shifted by the lower and upper systematic uncertainty, respectively. Since the η meson and the kaon have similar masses,

$$m_{\eta} = 547.85\,\mathrm{MeV}/c^2 \ \approx \ m_{K^{\pm}} = 493.67\,\mathrm{MeV}/c^2 \ \ [9] \ ,$$

an additional parameterization is fitted to the charged kaon measurement. In fig. 10.5, the

charged kaon data points are already KE_{T}-scaled to the charged pion transverse momentum. This parameterization is only used for the η and heavier mesons as an alternative to the KE_{T}-scaled charged pion parameterization and deviations are used as an estimate for the systematic uncertainty arising from KE_{T}-scaling.

10.1.4 Decay-photon anisotropic flow

Figure 10.6 (left) shows the p_{T}-differential elliptic flow of the six mesons contributing to the decay-photon spectrum. As the mass of the mesons increases, the data points are shifted towards higher transverse momenta, which reproduces the mass ordering

$$v_n^{\pi^0} > v_n^{\eta} > v_n^{\rho} \approx v_n^{\omega} > v_n^{\eta'} \approx v_n^{\phi} \tag{10.12}$$

at low p_{T} (cf. section 3.4.4). Since the ρ and ω meson as well as the η' and ϕ meson have similar masses, their azimuthal anisotropy is very similar and the curves overlap in fig. 10.6 (left).

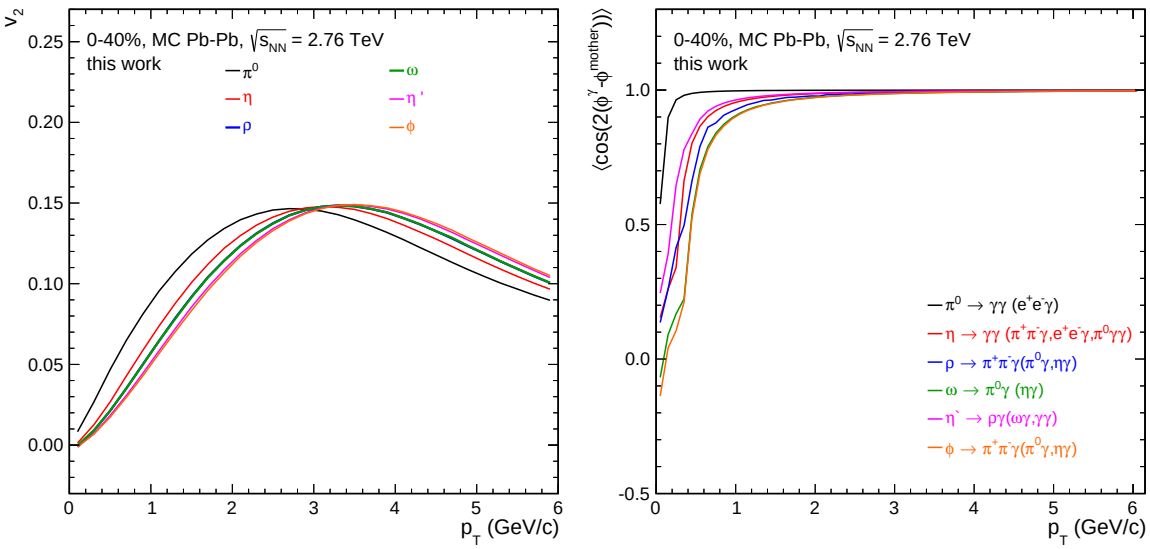

Figure 10.6: (left) Azimuthal anisotropy of cocktail mesons as a function of p_{T}. (right) Average cosine of the photon decay angle with respect to its mother hadron $\left\langle \cos\left(n\left(\phi^{\gamma} - \phi^{\mathrm{mother}}\right)\right)\right\rangle$ as a function of p_{T}.

The azimuthal anisotropy of the decay photons is determined by the anisotropy of the mother hadrons and smeared out by the decay kinematics. The azimuthal anisotropy of decay photons is given by

$$\left\langle \cos\left(n\left(\phi^{\gamma} - \Psi_n^{\mathrm{EP}}\right)\right)\right\rangle = \left\langle \cos\left(n\left(\phi^{\mathrm{mother}} - \Psi_n^{\mathrm{EP}}\right) + n\left(\phi^{\gamma} - \phi^{\mathrm{mother}}\right)\right)\right\rangle \tag{10.13}$$

$$= \underbrace{\left\langle \cos\left(n\left(\phi^{\mathrm{mother}} - \Psi_n^{\mathrm{EP}}\right)\right)\right\rangle}_{\tilde{v}_n^{\mathrm{mother}}} \left\langle \cos\left(n\left(\phi^{\gamma} - \phi^{\mathrm{mother}}\right)\right)\right\rangle , \tag{10.14}$$

where $\tilde{v}_n^{\mathrm{mother}}$ is the p_{T}-integrated azimuthal anisotropy of all mother hadrons decaying into photons at a given momentum. It directly follows that the azimuthal anisotropy of decay photons

is constrained by the maximum anisotropy of their mother hadrons. Figure 10.6 (right) shows the average second-order cosine of the photon decay decay angle ϕ^{γ} with respect to its mother hadron ϕ^{mother}, $\left\langle \cos\left(2\left(\phi^{\gamma}-\phi^{\text{mother}}\right)\right)\right\rangle$, as a function of the transverse momentum. At high p_{T}, the decay angles are typically small, which implies that the decay-photon azimuthal anisotropy is similar to the anisotropy of their mother hadrons,

$$\left\langle \left|\phi^{\gamma}-\phi^{\text{mother}}\right|\right\rangle \to 0 \;\Rightarrow\; \left\langle \cos\left(n\left(\phi^{\gamma}-\phi^{\text{mother}}\right)\right)\right\rangle \to 1 \,. \tag{10.15}$$

At small momenta, the decay angles increase implying that the azimuthal anisotropy of the mother hadrons $\tilde{v}_n^{\text{mother}}$ is smeared out by the decay kinematics and for decay angles larger than $\frac{\pi}{2n}$, the direction of the azimuthal anisotropy is even inverted

$$\left\langle \left|\phi^{\gamma}-\phi^{\text{mother}}\right|\right\rangle \to \frac{\pi}{2} \;\Rightarrow\; \left\langle \cos\left(n\left(\phi^{\gamma}-\phi^{\text{mother}}\right)\right)\right\rangle \to -1 \,. \tag{10.16}$$

Figure 10.7 shows the elliptic flow $v_2^{\gamma,\text{bg}}$ and and triangular flow $v_3^{\gamma,\text{bg}}$ for photons from individual meson decay channels. At low p_{T}, the photons stemming from neutral pion decays carry the largest azimuthal anisotropy. As a consequence of large decay angles, the decay-photon anisotropy $v_n^{\gamma,\text{bg}}$ for photons stemming from decays of mesons heavier than neutral pions decreases rapidly towards small momenta and becomes even negative. For momenta above 3 GeV/c, the anisotropic flow of photons from decays of the η mesons exceeds the anisotropy of photons from neutral pion decays.

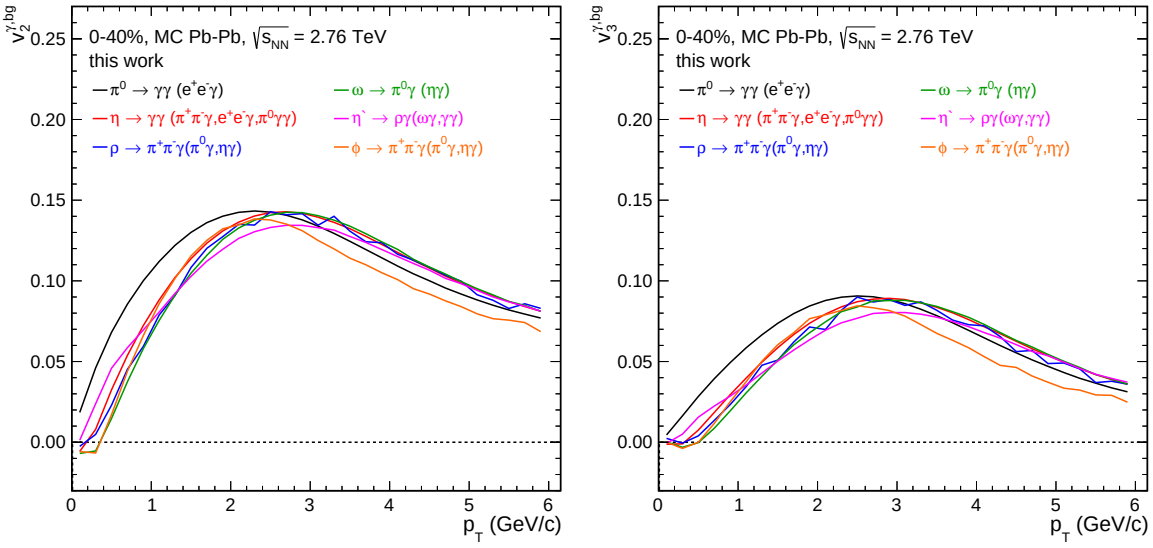

Figure 10.7: Individual components of the decay-photon elliptic (left) and triangular (right) flow from individual meson decay channels.

10.1.5 Impact of feed down

For this analysis, the neutral pion azimuthal anisotropy is parametrized with the charged pion anisotropy, since the uncertainties of the charged pion measurement are much smaller than those of the neutral pion measurement. This procedure is justified by the assumption that neutral and charged pions are expected to have the same azimuthal anisotropy due to their isospin

symmetry. However, a substantial portion of neutral and charged pions – particularly at small momenta – originates from feed down decays and is not directly produced during the hadronic freeze out. Thus, the symmetry between neutral and charged pions is broken due to isospin violation in strong decays and in weak decays:

Isospin violating scalar meson decays: Reactions such as $\eta \to \pi^0\pi^0\pi^0$ or $\eta \to \pi^+\pi^-\pi^0$ do not conserve the G-parity. According to the Sutherland theorem [361], electromagnetic processes can be neglected. It is shown in [362] that the conventional electromagnetic interaction underestimates the decay width by about three orders of magnitude. Instead, the decay mechanism is described by strong isospin violating processes based on the fact that the current masses of the u and d quark are not equal [362–364]. Charged and neutral pions have a different quark compositions,

$$|\pi^0\rangle = 1/\sqrt{2}\left(|u\bar{u}\rangle + |d\bar{d}\rangle\right) \ , \quad |\pi^+\rangle = |u\bar{d}\rangle \ , \quad |\pi^-\rangle = |d\bar{u}\rangle \ ,$$

implying that the symmetry between neutral and charged pions is broken.

Weak decays: Weak decays such as $K^0_s \to \pi\pi$ break the symmetry between charged and neutral pions:

$$\frac{\Gamma(K^0_s \to \pi^0\pi^0)}{\Gamma(K^0_s \to \pi^+\pi^-)} \underset{[9]}{=} \frac{(30.69 \pm 0.05)\%}{(69.20 \pm 0.05)\%} < \frac{1}{2} \tag{10.17}$$

If the isospin symmetry were conserved, the charged and neutral pion production would be equal and the branching ratio would be twice as large for charged pions, which is experimentally excluded. The short lived neutral kaon K^0_s has a $c\tau_{K^\pm}$ of about 2.6844 cm and thus its decay vertex can be experimentally resolved. The long living K^0_l and the charged kaons $K^\pm$ decay far away from the primary vertex ($c\tau_{K^0_l} = 15.34\,\text{m}$,$c\tau_{K^\pm} = 3.712\,\text{m}$) and are not relevant for feed down.
In the measured neutral and charged pion spectra, contributions from secondary weak decays are explicitly corrected [331, 365]. In the charged pion analysis, the contribution of weak secondary decays is excluded by strict cuts on the distance of closest approach (dca) of the tracks with respect to the primary vertex. Similarly, in the neutral pion analysis it is required that the reconstructed photons point towards the primary vertex, which removes a substantial part of feed down and further corrections are applied using Monte Carlo simulations.
However, these corrections could not be applied to the anisotropic flow measurement, since Monte Carlo simulations do not include anisotropic flow yet.

The measured neutral and charged pion azimuthal anisotropy are not corrected for weak feed down. Nevertheless, it is assumed that neutral and charged pions – either directly produced during the hadronic freeze out or by strong decays of scalar mesons – have the same azimuthal anisotropy, while deviations are expected from isospin violating strong decays. In order to estimate the effect of feed down, besides primary hadron production also the most relevant weak and strong feed down decays are included in the cocktail simulation. The most relevant processes are summarized in table 10.3.

In the standard cocktail simulation, the primary hadron production $N_{\text{h,prim}}$ is parametrized with the measured invariant yields $N_{\text{h,meas}}$ and only primary hadrons contribute to the hadron

Meson	Feed down Decay	Γ_i/Γ (%)
π^0	$\omega \to \pi^+\pi^-\pi^0$	(89.2 ± 0.7)
	$\eta \to \pi^0\pi^0\pi^0$	(32.57 ± 0.23)
	$K^0_s \to \pi^0\pi^0$	(30.68 ± 0.05)
	$\eta \to \pi^+\pi^-\pi^0$	(22.74 ± 0.28)
	$\eta' \to \pi^0\pi^0\eta$	(21.6 ± 0.8)
	$\phi \to \rho\pi + \pi^+\pi^-\pi^0$	(15.32 ± 0.32)
	$\omega \to \pi^0\gamma$	(8.28 ± 0.28)
η	$\eta' \to \pi^+\pi^-\eta$	(29.4 ± 0.9)
	$\eta' \to \pi^0\pi^0\eta$	(21.6 ± 0.8)
	$\phi \to \eta\gamma$	(1.309 ± 0.024)
ρ	$\eta' \to \rho\gamma$	(29.3 ± 0.6)
ω	$\eta' \to \omega\gamma$	(2.75 ± 0.22)

Table 10.3: Feed-down decay modes and the corresponding relative branching ratio. Values taken from [9].

spectra

$$N_{\mathrm{h,tot}} = N_{\mathrm{h,prim}} = N_{\mathrm{h,meas}} \tag{10.18}$$

In order to obtain the decay-photon spectra, only photons from electromagnetic decays need to be considered. Now, also feed down decays are considered, implying that the hadron invariant yield $N'_{\mathrm{h,tot}}$ is composed of a component of primary produced hadrons $N_{\mathrm{h,prim}}$ and a component from feed down decays $N_{\mathrm{h,FD}}$,

$$N'_{\mathrm{h,tot}} = N_{\mathrm{h,prim}} + N_{\mathrm{h,FD}} \geq N_{\mathrm{h,meas}} \ , \tag{10.19}$$

which implies that the simulated hadron spectra $N'_{\mathrm{h,tot}}$ exceed the measured spectra $N_{\mathrm{h,meas}}$. In order to reproduce the experimentally observed spectrum, the parameterizations for primary hadron spectra would need to be corrected for secondary hadron production. Since we are only interested in rough estimates for the impact on the azimuthal anisotropy, it is reasonable to assume that those corrections almost cancel out in the primary-to-feed-down ratio, which can be estimated by

$$\frac{N_{\mathrm{h,FD}}}{N_{\mathrm{h,tot}}} \approx \frac{N_{\mathrm{h,FD}}}{N'_{\mathrm{h,prim}}} = \frac{N_{\mathrm{h,FD}}}{N_{\mathrm{h,FD}} + N_{\mathrm{h,prim}}} \tag{10.20}$$

and in the corresponding ratio for the decay photons

$$\frac{N_{\gamma,\mathrm{FD}}}{N_{\gamma,\mathrm{tot}}} \approx \frac{N_{\gamma,\mathrm{FD}}}{N_{\gamma,\mathrm{FD}} + N_{\gamma,\mathrm{prim}}} \ . \tag{10.21}$$

Figure 10.8 (left) shows the fraction $N_{\gamma,\mathrm{FD}}/N_{\gamma,\mathrm{tot}}$ for photons from neutral pion and η meson decays. Contributions from other mesons are smaller than $\mathcal{O}(10^{-2})$ and can thus be neglected.

It can be seen that feed down becomes relevant at small transverse momenta below 1 GeV/c, where more than 10% of photons come from decays of secondary hadrons, with a maximum contribution of about 80% at around 0.1 GeV/c. The azimuthal anisotropy for photons from primary and secondary hadrons is shown in fig. 10.8 (right). It can be seen that the elliptic flow for photons from secondary hadrons is shifted towards lower transverse momenta compared to photons from primary hadrons. Deviations are most pronounced in p_{T} regions, where the feed-down contribution is rather small. As a consequence, the combined decay-photon anisotropy,

$$v_n^{\gamma,\mathrm{prim+FD}} = \frac{N_{\gamma,\mathrm{FD}} v_n^{\gamma,\mathrm{FD}} + N_{\gamma,\mathrm{prim}} v_n^{\gamma,\mathrm{prim}}}{N'_{\gamma,\mathrm{tot}}} \,, \tag{10.22}$$

is only slightly different from photons from primary meson decays. Deviations between $v_n^{\gamma,\mathrm{bg}}$ and $v_n^{\gamma,\mathrm{prim+FD}}$ are smaller than 0.1% above 0.8 GeV/c, such that the lines overlap in fig. 10.8 (left). The deviations increase as the transverse momentum goes to zero, such that the decay-photon anisotropy at very small momenta could be systematically biased by isospin violating feed-down. The root mean square of the standard combined decay-photon anisotropy is added as systematic uncertainty to the cocktail systematic uncertainty (section 10.1.6). Since the direct-photon excess is only extracted at momenta above 0.8 GeV/c, the effect of isospin violation in feed-down decays can be neglected for the direct-photon anisotropy, but it will be important, when the measured inclusive-photon anisotropy is compared with the decay-photon anisotropy estimated from the cocktail simulation.

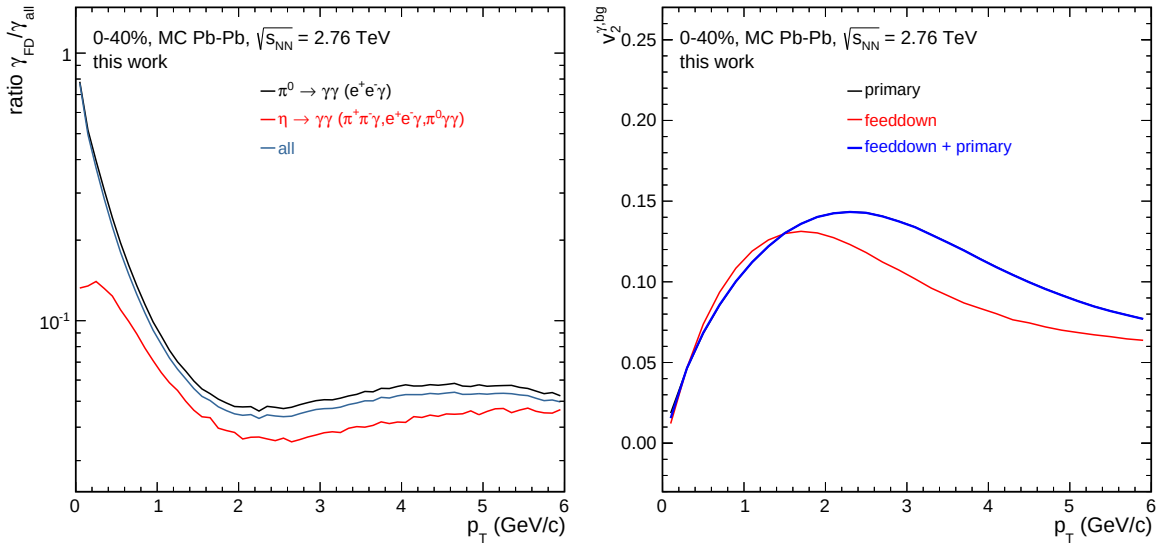

Figure 10.8: (left) Fraction of photons from secondary hadrons. (right) $v_2^{\gamma,\mathrm{bg}}$ of photons from primary and secondary hadron decays and sum.

10.1.6 Systematic uncertainty of the decay-photon anisotropic flow

The individual contributions to the systematic uncertainty are shown in fig. 10.9 and account for the following effects:

(blue up-pointing full triangles) Three different parameterizations for the neutral pion

invariant yield are used (cf. fig. 10.1 (right)) and the root mean square is considered as systematic uncertainty. Herewith, also systematic discrepancies between the charged and neutral pion spectrum are taken into account.

(green down-pointing full triangles) Possible deviations from m_{T} scaling are taken into account by varying the π^0/η ratio by $\pm 20\%$. The breakdown of NCQ-scaling was discussed in section 3.4.5. Kaons and pions agree at intermediate p_{T}, but show significant deviations at low p_{T}. Therefore, the azimuthal anisotropy of the η meson is estimated from the KE_{T} scaled charged kaon measurement. Both particles have similar mass and quark content and such a possible violation of KE_{T} scaling between pions and other hadrons is estimated. The discontinuity between 2.5 - 3.0 GeV/c appears, since the azimuthal anisotropy of photons from neutral pion and η meson decays overlap in this momentum range (cf. fig. 10.7) and thus any variation of the contribution of η mesons does not change the decay-photon anisotropy.

(red full boxes) In order to account for the systematic uncertainty of $v_n^{\pi^0}$, deviations between the three parameterizations shown in fig. 10.5 (measured charged pion v_n and shifted by the systematic error $v_n \pm \sigma_{sys}$) are considered as systematic uncertainty.

(magenta open circles) Possible deviations between charged and neutral pions may arise from strong isospin violating and weak feed-down decays. This effect is estimated by the magnitude of the feed-down correction discussed in section 10.1.5. The root mean square of the feed-down corrected and standard $v_n^{\gamma,\mathrm{bg}}$ is considered as systematic uncertainty. The discontinuity in the systematic uncertainty at about 1.7 GeV/c corresponds to the intersection point of $v_n^{\gamma,\mathrm{prim+FD}}$ and $v_n^{\gamma,\mathrm{bg}}$ shown in fig. 10.8 (right).

The total systematic uncertainty is calculated as the square root of the quadratic sum of all contributions, which yields an total relative uncertainty of about 2% for transverse momenta above 0.5 GeV/c. The dominant source of uncertainty for $v_2^{\gamma,\mathrm{bg}}$ comes from the parameterization of the spectra. Triangular flow is much smaller in mid central collisions and uncertainties are larger, such that the parameterization of $v_3^{\pi^0}$ becomes the dominant source of uncertainty for $v_3^{\gamma,\mathrm{bg}}$.

10.2 Direct-photon anisotropic flow

10.2.1 Measurement of the direct-photon excess

For practical purposes, the ratio of inclusive $N_{\gamma,\mathrm{inc}}$ and decay photons $N_{\gamma,\mathrm{bg}}$ is often evaluated as a double ratio

$$R^{\gamma,dir} = \frac{\frac{\mathrm{d}N_{\gamma,\mathrm{inc}}/\mathrm{d}y}{\mathrm{d}N_{\pi^0}/\mathrm{d}y}}{\left(\frac{\mathrm{d}N_{\gamma,\mathrm{bg}}/\mathrm{d}y}{\mathrm{d}N_{\pi^0}/\mathrm{d}y}\right)_{MC}} \approx \frac{N_{\gamma,\mathrm{inc}}}{N_{\gamma,\mathrm{bg}}} \,. \tag{10.23}$$

If the photon and neutral pion yields are measured with the same detector, they have common systematic uncertainties that partially cancel out in the double ratio. The systematic uncertainty on the material budget is 4.5%, which implies an uncertainty of 4.5% on the inclusive-photon spectrum (cf. section 8.2.5) and 9% on the neutral pion spectrum reconstructed via $\pi \to \gamma\gamma$ (cf. section 8.3.4). Since nominator and denominator are affected by the same source of uncertainty,

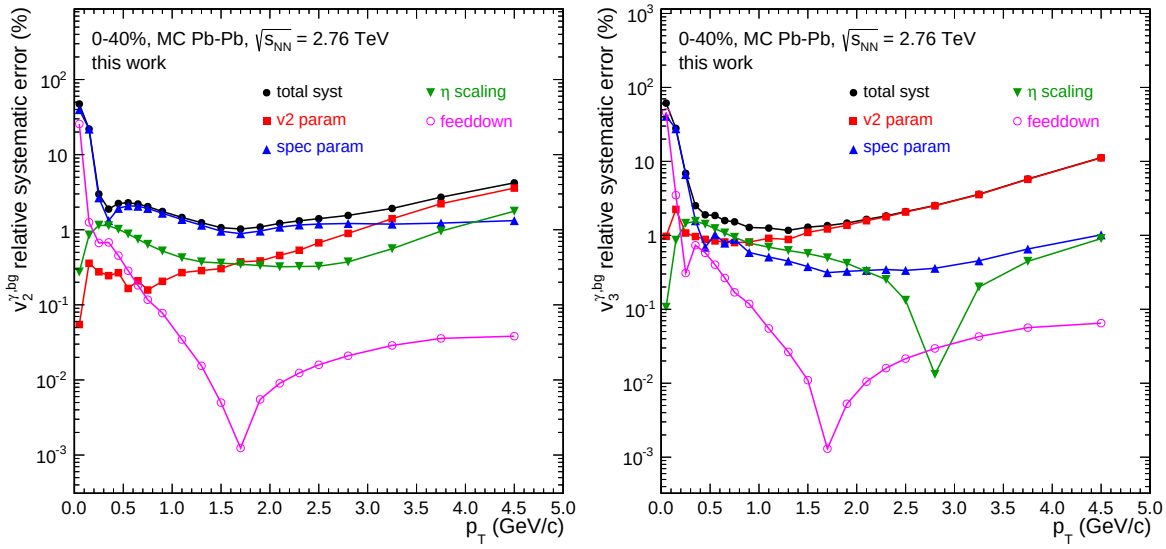

Figure 10.9: Individual components of the systematic uncertainty of $v_2^{\gamma,\mathrm{bg}}$ (left) and $v_3^{\gamma,\mathrm{bg}}$ (right).

the systematic uncertainty of the double ratio due to the material budget reduces to 4.5%.

Within this work, the direct-photon anisotropic flow is extracted using the ALICE preliminary direct-photon excess measured in 0 - 40% central collisions [201]. Since the ALICE preliminary direct-photon excess is measured in 0 - 40% central collisions, the p_{T}-differential direct-photon anisotropic flow is extracted in the same centrality range, for comparisons to PHENIX results also in 0 - 20% and 20 - 40% centrality. In order to access the centrality dependence of the direct-photon anisotropic flow with reduced statistical uncertainties, we calculate the p_{T}-integrated anisotropic flow for direct photons with transverse momenta above 1 GeV/c in small centrality bins. Thereby, it is implicitly assumed that the direct-photon excess is does not depend on the collision centrality in 0 - 40% central collisions. Measurements of the direct-photon excess in Pb-Pb collisions in smaller centrality bins are not yet published.

10.2.2 Extraction of the p_{T}-differential direct-photon flow

The direct-photon anisotropic flow is calculated as

$$v_n^{\gamma,\mathrm{dir}} = \frac{R^{\gamma,dir} v_n^{\gamma,\mathrm{inc}} - v_n^{\gamma,\mathrm{bg}}}{R^{\gamma,dir} - 1} \,, \tag{10.24}$$

where $R^{\gamma,dir}$ is the direct-photon excess, $v_n^{\gamma,\mathrm{inc}}$ is the inclusive and $v_n^{\gamma,\mathrm{bg}}$ the decay-photon anisotropic flow. The three input variables $R^{\gamma,dir}$, $v_n^{\gamma,\mathrm{inc}}$ and $v_n^{\gamma,\mathrm{bg}}$ are affected by statistical and systematic uncertainties. When propagating those uncertainties to the uncertainty of the extracted direct-photon anisotropy, we are confronted with two difficulties:

1. Gaussian propagation of uncertainty is based on a first order Taylor expansion, which can generally only be applied, if the relation between the observable and the input observables is linear or if uncertainties are sufficiently small. The formula for the anisotropy eq. (10.24) has a pole at $R^{\gamma,dir} = 1$, while the direct-photon excess $R^{\gamma,dir}$ is close to unity with large

uncertainties, implying that Gaussian error propagation cannot be applied.

2. The gradients of $v_n^{\gamma,\mathrm{dir}}$ with respect to $R^{\gamma,dir}$ depend on $v_n^{\gamma,\mathrm{inc}}$ and $v_n^{\gamma,\mathrm{bg}}$. By differentiating with respect to $R^{\gamma,dir}$,

$$\frac{\partial v_n^{\gamma,\mathrm{dir}}}{\partial R^{\gamma,dir}} = \frac{\left(R^{\gamma,dir}-1\right)v_n^{\gamma,\mathrm{inc}} - \left(R^{\gamma,dir}v_n^{\gamma,\mathrm{inc}} - v_n^{\gamma,\mathrm{bg}}\right)}{\left(R^{\gamma,dir}-1\right)^2} = \frac{v_n^{\gamma,\mathrm{bg}} - v_n^{\gamma,\mathrm{inc}}}{\left(R^{\gamma,dir}-1\right)^2}\ , \tag{10.25}$$

it can be seen that the gradients vanish, if $v_n^{\gamma,\mathrm{bg}} = v_n^{\gamma,\mathrm{inc}}$. In case that inclusive and decay-photon anisotropy are very similar, the gradient could appear to be zero due to statistical fluctuations. Similarly, the derivative also depends on $R^{\gamma,dir}$ itself, such that fluctuations in $R^{\gamma,dir}$ result in alternating gradients and thus uncertainties of $v_n^{\gamma,\mathrm{dir}}$ could be significantly underestimated or overestimated.

In order to deal with those difficulties, uncertainties are sampled within a Monte Carlo simulation and in addition a smoothing is applied.

10.2.2.1 Monte Carlo sampling

Within this work, systematic and statistical uncertainties of the direct-photon anisotropic flow are determined in a Monte Carlo simulation. The three input variables $\tilde{R^{\gamma,dir}}$, $\tilde{v}_n^{\gamma,inc}$ and $\tilde{v}_n^{\gamma,bg}$ are independently drawn from Gaussian probability distributions

$$\tilde{v}_n^{\gamma,inc} \in \mathcal{N}\left(v_n^{\gamma,\mathrm{inc}}, \sigma_{v_n^{\gamma,\mathrm{inc}}}\right) \qquad \tilde{v}_n^{\gamma,bg} \in \mathcal{N}\left(v_n^{\gamma,\mathrm{bg}}, \sigma_{v_n^{\gamma,\mathrm{bg}}}\right) \qquad \tilde{R}^{\gamma,dir} \in \mathcal{N}\left(R^{\gamma,dir}, \sigma_{R^{\gamma,dir}}\right)\ , \tag{10.26}$$

where the width of the distribution is either given by the statistical or systematic uncertainties. The probability distributions for the input variables are samples within four standard deviations of the systematic and statistical uncertainty, except for the direct-photon excess, where we use our prior knowledge that $R^{\gamma,dir} \geq 1$. In principle, we could also use the excess expected from next-to-leading-order pQCD photons ($R^{\gamma,dir} \geq R^{\gamma,dir}_{\mathrm{pQCD}}$) as lower bound, but this would introduce a model dependence. Since $R^{\gamma,dir} \to 1$ implies that $v_n^{\gamma,\mathrm{dir}} \to \pm\infty$, unphysical values $|v_n^{\gamma,\mathrm{dir}}| > 1$ are not taken into account.
The direct-photon azimuthal anisotropy $v_n^{\gamma,\mathrm{dir}}$ is evaluated according to eq. (10.24) for each set of variables ($\tilde{R}^{\gamma,dir}$,$\tilde{v}_n^{\gamma,inc}$,$\tilde{v}_n^{\gamma,bg}$) and such the probability distribution for $v_n^{\gamma,\mathrm{dir}}$ is sampled. Figure 10.10 (left) shows for illustration the probability distribution of $v_n^{\gamma,\mathrm{dir}}$ as determined by sampling the input variables within their statistical uncertainties. The black line shows the distribution for $v_n^{\gamma,\mathrm{dir}}$, if all input variables are varied at the same time. The contribution of individual input variables is estimated by setting all other parameters to their measured values and by varying only the parameter of interest. It can be seen that the variation of the direct-photon excess results into an asymmetric distribution for v_n due to the pole behavior. In order to account for the skewness of the distribution, lower and upper statistical and systematic uncertainties are determined by the 68.27% confidence interval. The median corresponds to the value $v_n^{\gamma,\mathrm{dir}}$ determined from the measured input variables.

For convenience, systematic and statistical uncertainties are often considered as normally distributed, even if they have non-Gaussian tails. In particular, the assumption of Gaussian prob-

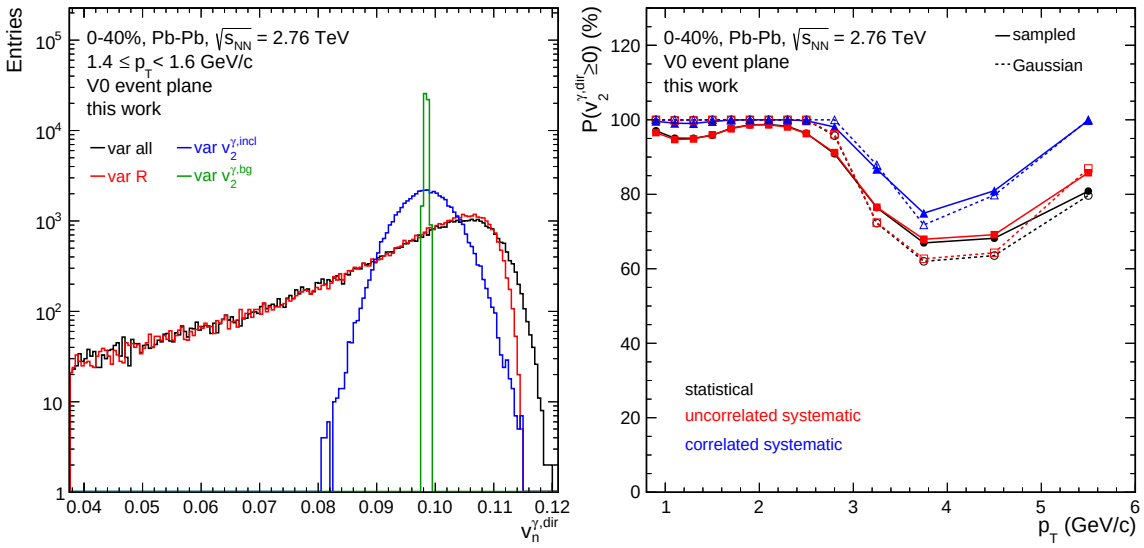

Figure 10.10: (left) Probability distribution for $v_n^{\gamma,\mathrm{dir}}$ as determined from $R^{\gamma,dir}$, $v_n^{\gamma,\mathrm{dir}}$ and $v_n^{\gamma,\mathrm{bg}}$ sampled within their statistical uncertainties. (right) Probability $P\left(v_n^{\gamma,\mathrm{dir}} \geq 0\right)$ calculated from sampled probability distributions.

ability distributions allows us to apply chi-squared tests for various hypotheses to the measured direct-photon anisotropic flow. In principle it is possible to calculate p-values for different hypotheses directly from the sampled probability distributions for $v_n^{\gamma,\mathrm{dir}}$ instead of assuming chi-squared distributions. Figure 10.10 (right) shows the probability for $v_2^{\gamma,\mathrm{dir}} \geq 0$ as calculated by integrating once the sampled probability distribution (full symbols, solid lines) and once a Gaussian probability distribution with the same 68.27% confidence interval (open symbols, dashed lines). It can be seen that the assumption of Gaussian uncertainties underestimates the tails of the distribution and thus overestimates the significance of the direct-photon elliptic flow at low p_{T}.

10.2.2.2 Smoothing

In order to reduce the impact of statistical fluctuations on the error propagation, the input variables are estimated from a parametrization instead of using the measured values. It shall be noted that the points itself are not changed, the parameterizations are only used for the calculation of the confidence intervals. Speaking in the framework of Gaussian error propagation, we evaluate the derivatives at the parametrized value and such suppress the impact of statistical point-by-point fluctuations on the error propagation procedure. The input variables are now drawn from

$$\tilde{v}_n^{\gamma,inc} \in \mathcal{N}\left(\hat{v}_n^{\gamma,inc}, \sigma_{v_n^{\gamma,\mathrm{inc}}}\right) \qquad \tilde{v}_n^{\gamma,bg} \in \mathcal{N}\left(v_n^{\gamma,\mathrm{bg}}, \sigma_{v_n^{\gamma,\mathrm{bg}}}\right) \qquad \tilde{R}^{\gamma,dir} \in \mathcal{N}\left(\hat{R}^{\gamma,dir}, \sigma_{R^{\gamma,dir}}\right) , \tag{10.27}$$

where $\hat{R}^{\gamma,dir}$ and $\hat{v}_n^{\gamma,inc}$ are the parametrized values for the direct-photon excess $R^{\gamma,dir}$ and the inclusive-photon anisotropic flow, respectively. Since the decay-photon anisotropic flow was calculated from a cocktail simulation, statistical fluctuations in $v_n^{\gamma,\mathrm{bg}}$ are sufficiently suppressed

and it is not necessary to find a parametrization.

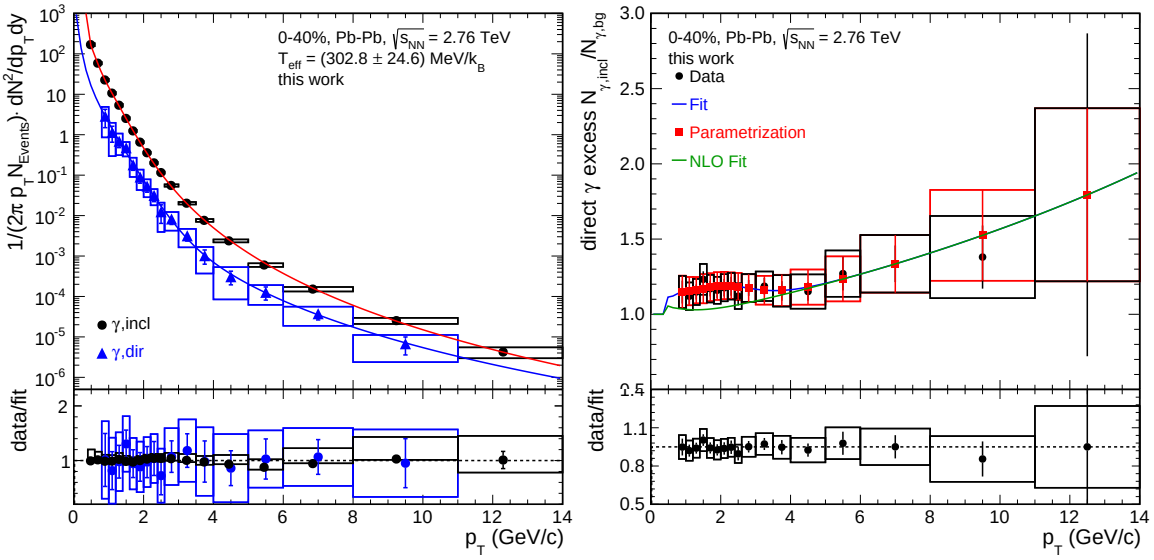

Figure 10.11: (right) Inclusive-photon and direct-photon spectra fitted with the parameterization (right) Direct-photon excess in 0 - 40% centrality plotted with the parameterization calculated from the inclusive and direct-photon spectrum (blue). The green line shows a parametrization for the excess of next-to-leading-order pQCD photons. Data points taken from [201].

The inclusive-photon spectrum can be described by eq. (10.6), while the direct-photon spectrum is fitted with the sum of an exponential function for the thermal-photon spectrum

$$Y^{\gamma,\mathrm{therm}}(p_\mathrm{T}) = A \exp\left(-\frac{p_\mathrm{T}}{T_\mathrm{eff}}\right) \tag{10.28}$$

and a Hagedorn function for the prompt-photon spectrum

$$Y^{\gamma,\mathrm{pQCD}}(p_\mathrm{T}) = a\left(1+\frac{p_\mathrm{T}}{cb}\right)^{-c} . \tag{10.29}$$

Figure 10.11 (left) shows the inclusive and direct photon spectrum fitted with the parameterizations mentioned above. The combined fit of the direct-photon spectrum yields an inverse slope parameter of $T_\mathrm{eff} = (302.8 \pm 24.6)$ MeV/k_B, which is consistent within uncertainties with the parameter quoted by the ALICE collaboration [201].
The direct-photon excess can now be parametrized by

$$R^{\gamma,dir}_\mathrm{param}(p_\mathrm{T}) = \frac{Y^{\gamma,\mathrm{inc}}(p_\mathrm{T})}{Y^{\gamma,\mathrm{inc}}(p_\mathrm{T}) - (Y^{\gamma,\mathrm{therm}}(p_\mathrm{T}) + Y^{\gamma,\mathrm{pQCD}}(p_\mathrm{T}))} . \tag{10.30}$$

Figure 10.11 (right) shows the ALICE preliminary direct-photon excess in 0 - 40% central Pb-Pb collisions. The parametrization is shown as blue curve. The green curve shows the direct-photon excess for next-to-leading-order pQCD photons, which can be calculated by subtracting the contribution of thermal photons. The red points correspond to the parametrization with systematic and statistical uncertainties scaled by $R^{\gamma,dir}_\mathrm{param}/R$.

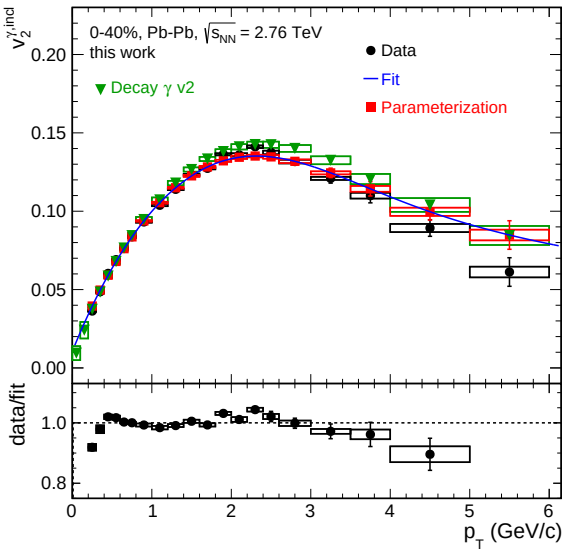

Figure 10.12: Inclusive-photon elliptic flow fitted with a parameterization and in comparison with the decay-photon elliptic flow.

Figure 10.12 shows the inclusive-photon elliptic flow fitted with the same function that was used to parametrize the neutral pion anisotropic flow in section 10.1.3. For comparison, also the decay-photon elliptic flow is shown. It can be seen that the inclusive and decay-photon elliptic flow are very similar at low-p_{T}. The measured inclusive-photon elliptic flow fluctuates around the parametrization resulting into fluctuating gradients in the error propagation. Figure 10.13 shows for illustration the relative statistical uncertainties of the p_{T}-differential direct-photon elliptic flow measurement before and after the smoothing procedure. It can be seen that the statistical uncertainties at low p_{T} evaluated at the measured input variables fluctuate by almost one order of magnitude. Evaluating the probability distributions for $v_n^{\gamma,\mathrm{dir}}$ at the parametrized values for the direct-photon excess $\hat{R}^{\gamma,dir}$ and for the inclusive-photon elliptic flow $\hat{v}_n^{\gamma,inc}$, these fluctuations are significantly reduced.

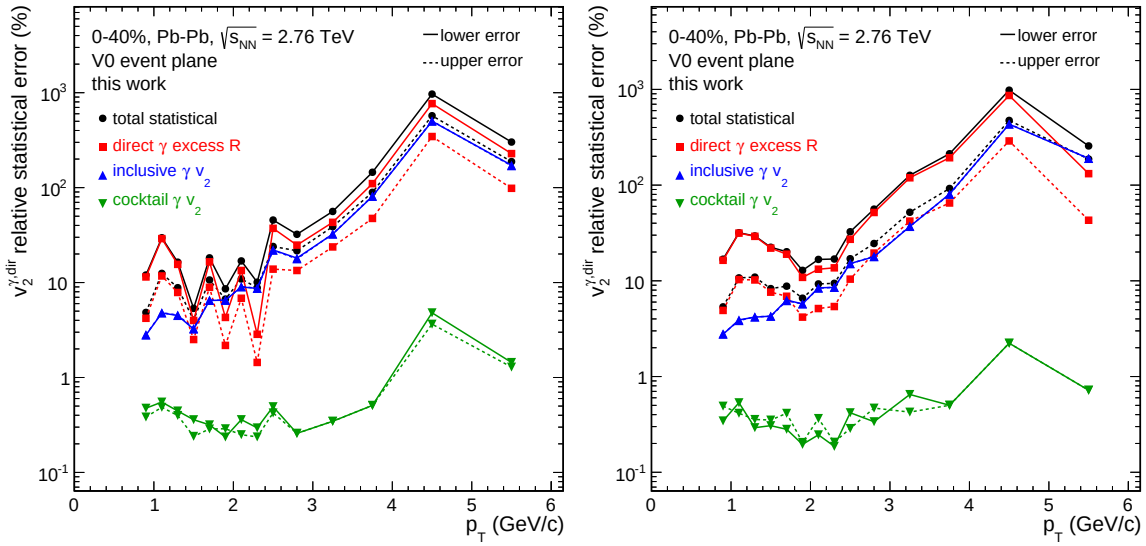

Figure 10.13: Statistical uncertainties of the p_{T}-differential direct-photon elliptic flow before (left) and after smoothing (right).

10.2.2.3 Statistical and systematic uncertainties

Within this work, the statistical and systematical uncertainties of the direct-photon anisotropic flow are given by the 68.27% confidence interval of the sampled probability distribution for $v_n^{\gamma,\mathrm{dir}}$. Due to the asymmetry of the probability distribution, lower and upper uncertainties are

treated separately. The upper (solid lines) and lower (dashed lines) statistical and systematic uncertainties are shown in fig. 10.14. While the contributions of the inclusive-photon and decay-photon anisotropy result in symmetric uncertainties, the uncertainties on the direct-photon excess $R^{\gamma,dir}$ result into asymmetric uncertainties (red). Both, statistical and systematic uncertainties are mainly dominated by the uncertainties on the direct-photon excess $R^{\gamma,dir}$, followed by the inclusive-photon anisotropic flow. Correlated systematic uncertainties arise mainly from the uncertainty on the material budget, but also from the uncertainty on the event-plane resolution correction. A substantial contribution to the upper uncorrelated systematic uncertainty also arises from the cocktail simulation, mainly from the discrepancy between the parameterizations obtained from charged and neutral pions. The statistical uncertainties and partially also the uncorrelated systematic uncertainties will be significantly decreased, when additional data from the 2011 Pb-Pb run is analyzed. Furthermore, it will be important to reevaluate the material budget in order to reduce the correlated systematic uncertainties.

10.2.3 Extraction of the p_{T}-integrated direct-photon anisotropic flow

Since the p_{T}-differential measurement is affected by large statistical uncertainties, when measured in small bins of centrality, In order to access the centrality dependence with reduced statistical uncertainties, we calculate the p_{T}-integrated direct-photon anisotropic flow $\bar{v}_n^{\gamma,dir}$ for transverse momenta $p_{\mathrm{T}}^i \geq 1\,\mathrm{GeV}/c$,

$$\bar{v}_n^{\gamma,dir} = \frac{\sum_{i=i_0}^{N_{\mathrm{bins}}^{p_{\mathrm{T}}}} N_{\gamma,\mathrm{dir}}(p_{\mathrm{T}}^i) v_n^{\gamma,\mathrm{dir}}(p_{\mathrm{T}}^i)}{\sum_{i=i_0}^{N_{\mathrm{bins}}^{p_{\mathrm{T}}}} N_{\gamma,\mathrm{dir}}(p_{\mathrm{T}}^i)} \,, \tag{10.31}$$

where $v_n^{\gamma,\mathrm{dir}}(p_{\mathrm{T}}^i)$ and $N_{\gamma,\mathrm{dir}}(p_{\mathrm{T}}^i)$ are the p_{T}-differential direct-photon anisotropic flow and yield, respectively. The direct-photon yield is given by $N_{\gamma,\mathrm{dir}} = \left(1 - 1/R^{\gamma,dir}\right) N_{\gamma,\mathrm{inc}}$. Since $v_n^{\gamma,\mathrm{dir}}$ and $N_{\gamma,\mathrm{dir}}$ have partially correlated uncertainties resulting from the measurement of the direct-photon excess, we evaluate the p_{T}-integrated direct-photon anisotropic flow directly from

$$\bar{v}_n^{\gamma,dir} = \frac{\sum_{i=i_0}^{N_{\mathrm{bins}}^{p_{\mathrm{T}}}} \left(1 - \frac{1}{R^{\gamma,dir}(p_{\mathrm{T}}^i)}\right) N_{\gamma,\mathrm{inc}}(p_{\mathrm{T}}^i) \left(\frac{R^{\gamma,dir}(p_{\mathrm{T}}^i) v_n^{\gamma,\mathrm{inc}}(p_{\mathrm{T}}^i) - v_n^{\gamma,\mathrm{bg}}(p_{\mathrm{T}}^i)}{R^{\gamma,dir}(p_{\mathrm{T}}^i) - 1}\right)}{\sum_{i=i_0}^{N_{\mathrm{bins}}^{p_{\mathrm{T}}}} \left(1 - \frac{1}{R^{\gamma,dir}(p_{\mathrm{T}}^i)}\right) N_{\gamma,\mathrm{inc}}(p_{\mathrm{T}}^i)} \tag{10.32}$$

instead of using the extracted direct-photon spectrum.

10.2.3.1 Statistical and systematic uncertainties

For the same reasons as for the p_{T}-differential measurement, the statistical and systematic uncertainties of the p_{T}-integrated direct-photon anisotropic flow are estimated from a Monte Carlo simulation and smoothed by the use of parameterizations for the error propagation. The inclusive and decay-photon anisotropy, $v_n^{\gamma,\mathrm{inc}}$ and $v_n^{\gamma,\mathrm{bg}}$, the inclusive-photon yield $N_{\gamma,\mathrm{inc}}$ and the direct-photon excess $R^{\gamma,dir}$ are independently drawn in each momentum bin p_{T}^i from Gaussian

probability distributions within four sigma of their standard deviation:

$$\tilde{v}_n^{\gamma,inc}\left(p_{\mathrm{T}}^i\right) \in \mathcal{N}\left(\hat{v}_n^{\gamma,inc}\left(p_{\mathrm{T}}^i\right), \sigma_{v_n^{\gamma,\mathrm{inc}}}\left(p_{\mathrm{T}}^i\right)\right) \tag{10.33}$$

$$\tilde{v}_n^{\gamma,bg}\left(p_{\mathrm{T}}^i\right) \in \mathcal{N}\left(v_n^{\gamma,\mathrm{bg}}\left(p_{\mathrm{T}}^i\right), \sigma_{v_n^{\gamma,\mathrm{bg}}}\left(p_{\mathrm{T}}^i\right)\right) \tag{10.34}$$

$$\tilde{R}^{\gamma,dir}\left(p_{\mathrm{T}}^i\right) \in \mathcal{N}\left(\hat{R}^{\gamma,dir}\left(p_{\mathrm{T}}^i\right), \sigma_{R^{\gamma,dir}}\left(p_{\mathrm{T}}^i\right)\right) \tag{10.35}$$

$$\tilde{N}^{\gamma,inc}\left(p_{\mathrm{T}}^i\right) \in \mathcal{N}\left(\hat{N}^{\gamma,inc}\left(p_{\mathrm{T}}^i\right), \sigma_{N_{\gamma,\mathrm{inc}}}\left(p_{\mathrm{T}}^i\right)\right) \tag{10.36}$$

The parameterizations of the inclusive-photon yield and anisotropic flow as well as for the direct-photon excess were described in section 10.2.2.2. The uncertainty on the material budget is treated as overall systematic uncertainty, which gives a correction on $R^{\gamma,dir}$ and $N_{\gamma,\mathrm{inc}}$ that does not depend on the momentum. The p_{T}-integrated direct-photon flow $\bar{v}_n^{\gamma,dir}$ is evaluated according to eq. (10.32) for each set of input variables and such the probability distribution for $\bar{v}_n^{\gamma,dir}$ is sampled.

Figure 10.15 shows the relative statistical and systematic uncertainties for the elliptic and triangular p_{T}-integrated direct-photon flow. The asymmetry between lower and upper the systematic and statistical uncertainties is smaller compared to the p_{T}-differential measurement. The statistical and systematic uncertainties are dominated by the direct-photon anisotropic flow measurement and direct-photon excess. The correlated systematic uncertainty is given by the uncertainty on the material budget and the event-plane resolution correction.

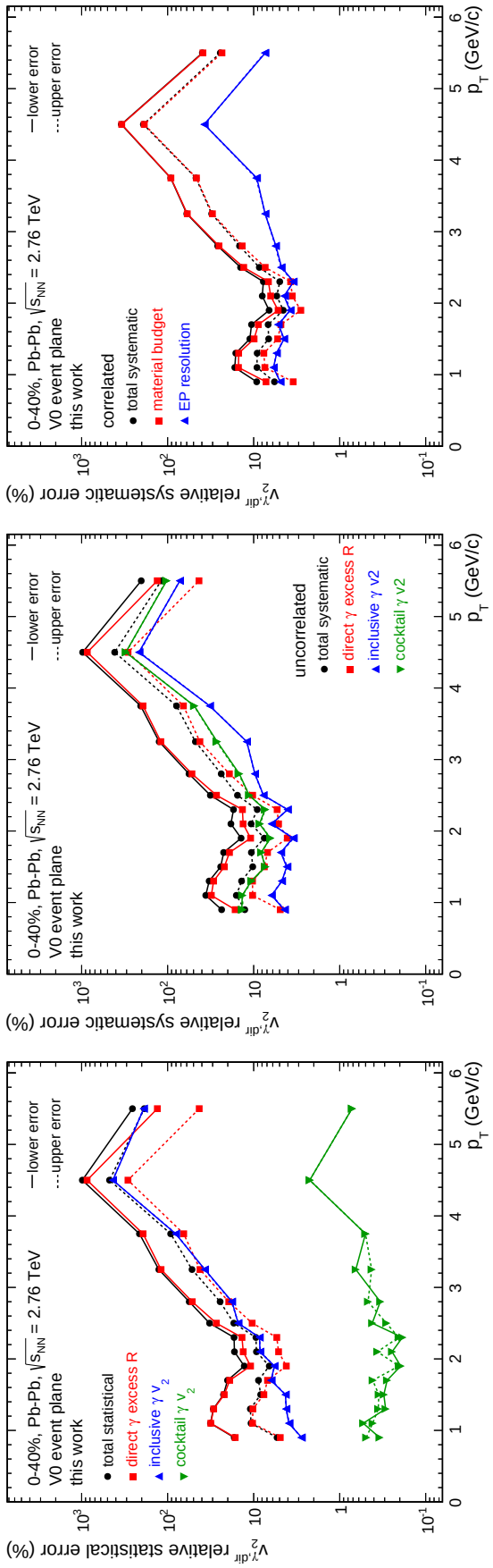

Figure 10.14: Relative statistical (left), uncorrelated systematic (mid) and correlated systematic (right) uncertainties of the direct-photon elliptic (top) and triangular (bottom) flow in 0 - 40% central Pb-Pb collisions.

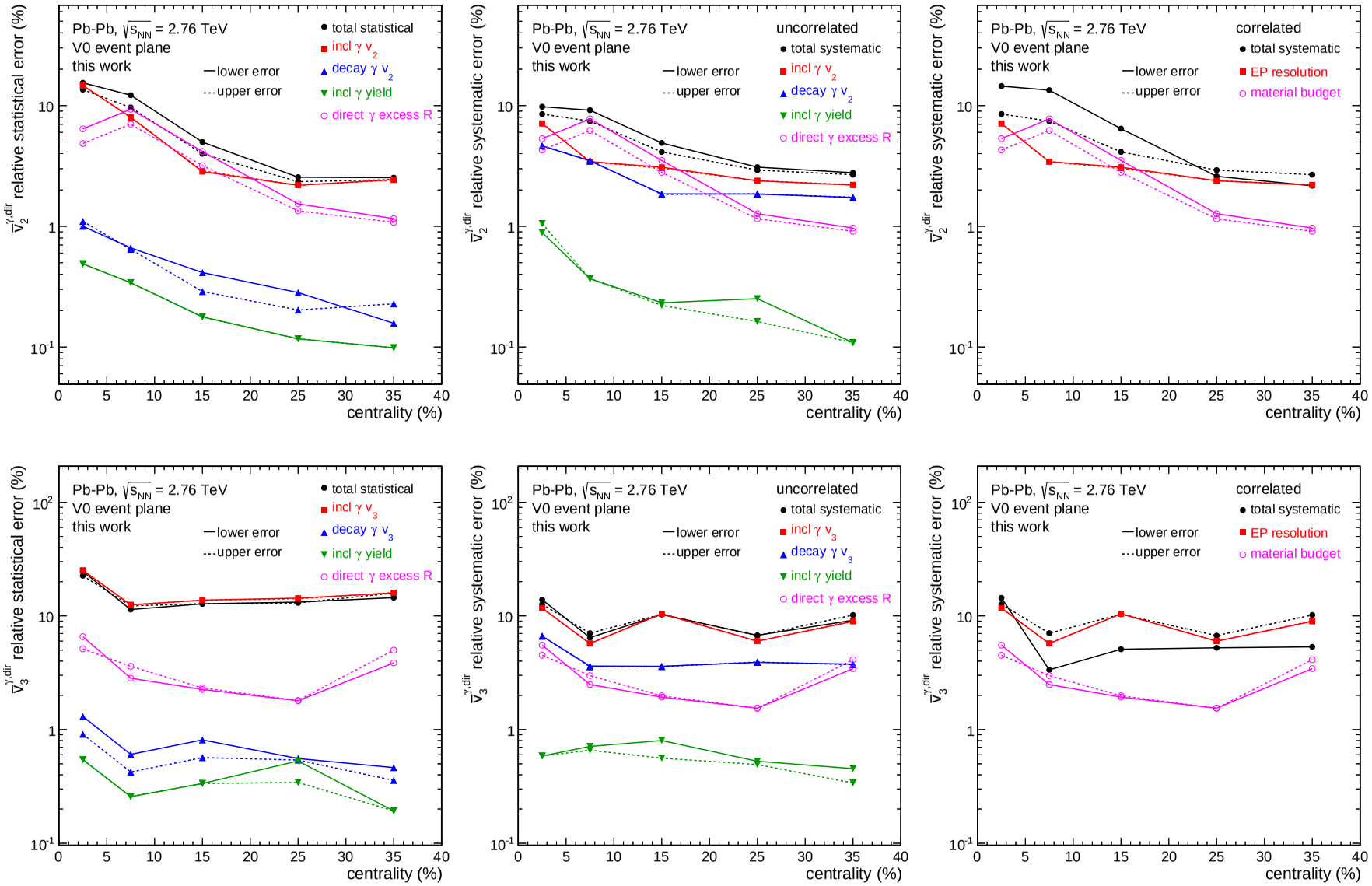

Figure 10.15: Relative statistical (left), uncorrelated systematic (mid) and correlated systematic (right) uncertainties of the p_{T}-integrated ($p_{\mathrm{T}} > 1\,\mathrm{GeV}/c$) elliptic (top) and triangular (bottom) direct-photon flow as a function of the collision centrality.

11. Final Results

In this work, photons were detected by their conversion in the ALICE detector material. The photon reconstruction is based on a Kalman filter secondary vertex reconstruction algorithm, combining oppositely-charged electron tracks reconstructed and identified in the Time Projection Chamber and the Inner Tracking System. Neutral pions were identified via their decay into two externally converted photons. The elliptic and triangular flow of inclusive photons and neutral pions was measured using the event planes from the two V0 detectors, providing a pseudorapidity gap larger than 0.9 and 2. Comparisons of inclusive photon anisotropic flow measurements using different event planes and pseudorapidity gaps indicated that non-flow effects are negligible for the V0 event-plane method.
The neutral pion anisotropic flow was found to be consistent with the anisotropy of charged pions, as expected from isospin symmetry. However, the neutral pion measurement suffers from a low significance due to the small pion reconstruction efficiency ($\mathcal{O}(10^{-3})$), and thus the statistical and systematic uncertainties are large compared to those of the charged pion measurement. The inclusive-photon azimuthal anisotropy was measured with much smaller statistical and systematic uncertainties compared to the neutral pion measurement. The spectrum and azimuthal anisotropy of decay photons was estimated in a cocktail simulation. The neutral pion spectrum was parametrized by the measured spectrum and other contributions were obtained from transverse mass scaling. The neutral pion anisotropy was parametrized by the measured charged pion anisotropy due to its significantly smaller uncertainties, while the anisotropy of other contributions was estimated from number-of-constituent-quarks scaling in transverse kinetic energy. Thereafter, the p_{T} differential elliptic and triangular direct-photon flow was extracted in 0 - 40% central Pb-Pb collisions. In order to suppress statistical fluctuations, the centrality dependence of the direct-photon anisotropy was measured by the p_{T}-integrated direct-photon flow. While the direct-photon elliptic flow was already measured in Au-Au collisions at $\sqrt{s_{\mathrm{NN}}} = 200\,\mathrm{GeV}$ by the PHENIX experiment [204] and in Pb-Pb collisions at $\sqrt{s_{\mathrm{NN}}} = 2.76\,\mathrm{TeV}$ by the ALICE experiment [366], this work presents the first measurement of the direct-photon triangular flow and the centrality dependence of elliptic and triangular flow.

The final results shall be discussed in the following. In order to study the significance of the direct-photon excess, the question of whether the inclusive-photon spectrum and anisotropy can be explained by decay photons alone is studied. The momentum and centrality dependence of the direct-photon elliptic and triangular flow are discussed in detail and compared to hydrodynamic calculations. Quantitative comparisons between data and different hypotheses are obtained from a Pearson's χ^2 test. This takes statistical and systematic uncertainties into account appropriately, distinguishing between uncorrelated (type A), correlated (type B) and overall systematic (type C) errors. The χ^2 calculation is described in detail in appendix C. The direct-photon elliptic flow measurement is compared with measurements by the PHENIX collaboration. After a critical assessment of the analysis, the implications of this measurement on the production time of direct photons and for our understanding of the time evolution of heavy-ion collisions are discussed.

11.1 Significance of the direct-photon excess

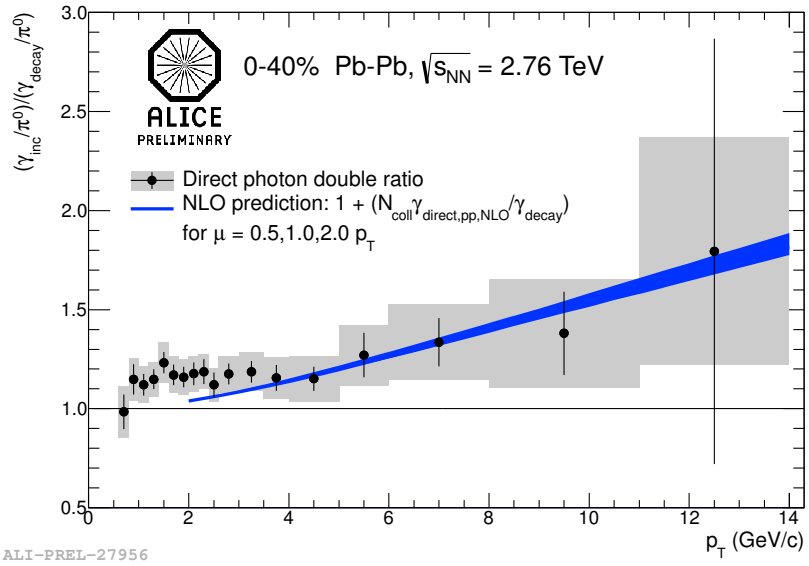

Figure 11.1: Direct-photon excess in 0 - 40% central Pb-Pb collisions at $\sqrt{s_{\rm NN}} = 2.76\,\text{TeV}$ in comparison to a binary scaled NLO prediction [201].

Figure 11.1 shows the ALICE preliminary direct-photon excess in 0 - 40% central Pb-Pb collisions [201]. The direct-photon excess $R^{\gamma,dir} = N_{\gamma,\rm inc}/N_{\gamma,\rm bg}$ was determined using the double ratio approach discussed in section 10.2.1. At first glance, the measurement indicates a significant excess of direct photons above unity. We test the hypothesis H0: $R^{\gamma,dir} = 1$, i.e. that the spectrum of inclusive photons can be explained by the spectrum of decay photons alone. The uncertainty on the material budget is considered as a type C overall systematic uncertainty with the remaining uncertainty being considered as uncorrelated type A uncertainty. Since different production processes are expected to contribute at low and high $p_{\rm T}$, the χ^2 test is evaluated once for the full $p_{\rm T}$ range and once separately for photons above and below $3\,\text{GeV}/c$. The results are summarized in table 11.1. The H0: $R^{\gamma,dir} = 1$ hypothesis cannot be rejected at the 5% significance level, neither in the low-$p_{\rm T}$ nor in the high-$p_{\rm T}$ range. Due to the large overall systematic uncertainty on the material budget, all points of the measured direct-photon excess can be shifted towards smaller values. Consequently, the apparent excess could be explained by a systematic bias in the material budget and the derived conversion probability.

			p-value (χ^2/dof)	
H0	centrality	full $p_{\rm T}$	$p_{\rm T} < 3\,\text{GeV}/c$	$p_{\rm T} \geq 3\,\text{GeV}/c$
$R^{\gamma,dir} = 1$	0 - 40%	0.085 (25.5/17)	0.071 (17.2/10)	0.230 (9.3/7)

Table 11.1: χ^2 test for H0: $R^{\gamma,dir} = 1$ in 0 - 40% central Pb-Pb collisions

The measured direct-photon excess is compared to the excess expected from exclusive next-to-

leading-order pQCD photon production,

$$R_{\mathrm{pQCD}} = 1 + N_{\mathrm{coll}} \frac{N_{\gamma,\mathrm{pQCD,pp}}}{N_{\gamma,\mathrm{bg}}} \ , \tag{11.1}$$

where $N_{\gamma,\mathrm{pQCD,pp}}$ is a next-to-leading-order pQCD prediction by W. Vogelsang [201]. R_{pQCD} is shown as a blue line in fig. 11.1. The calculation stops below 2 GeV/c, since perturbative QCD cannot be applied at small momenta. Theoretical next-to-leading-order pQCD calculations are affected by systematic uncertainties. The truncation of the perturbative series at next-to-leading order leads to an artificial dependence on the unphysical renormalization scale μ and the initial- and final-state factorization scales [367]. The systematic uncertainty of the next-to-leading-order pQCD calculation σ_μ is estimated from the difference between calculations for $\mu = 0.5 p_{\mathrm{T}}$, $\mu = p_{\mathrm{T}}$ and $\mu = 2 p_{\mathrm{T}}$. The data are reasonably well described by the pQCD prediction at momenta above 3 GeV/c, where prompt photon production dominates over thermal photon production. At small transverse momenta, the data points are numerically above the pQCD prediction, which is usually attributed to the production of thermal photons. Since the H0 hypothesis H0: $R^{\gamma,dir} = 1$ could not be rejected, it is obvious that any pQCD prediction R_{pQCD} with $1 < R_{\mathrm{pQCD}} < R^{\gamma,dir}$ cannot be rejected from the data either, which has two implications: First, the uncertainties of the data are too large to test any details of the next-to-leading-order pQCD photon production. Second, the hypothesis that pQCD photons alone could describe the low-p_{T} photon excess cannot be rejected from the data alone. This calls into question, whether the apparent thermal-photon excess might be explained by a systematic bias in the estimated material budget and photon conversion probability. The implications for the direct-photon anisotropy will be discussed in section 11.6.

11.2 Comparison between $v_n^{\gamma,\mathrm{bg}}$ and $v_n^{\gamma,\mathrm{inc}}$

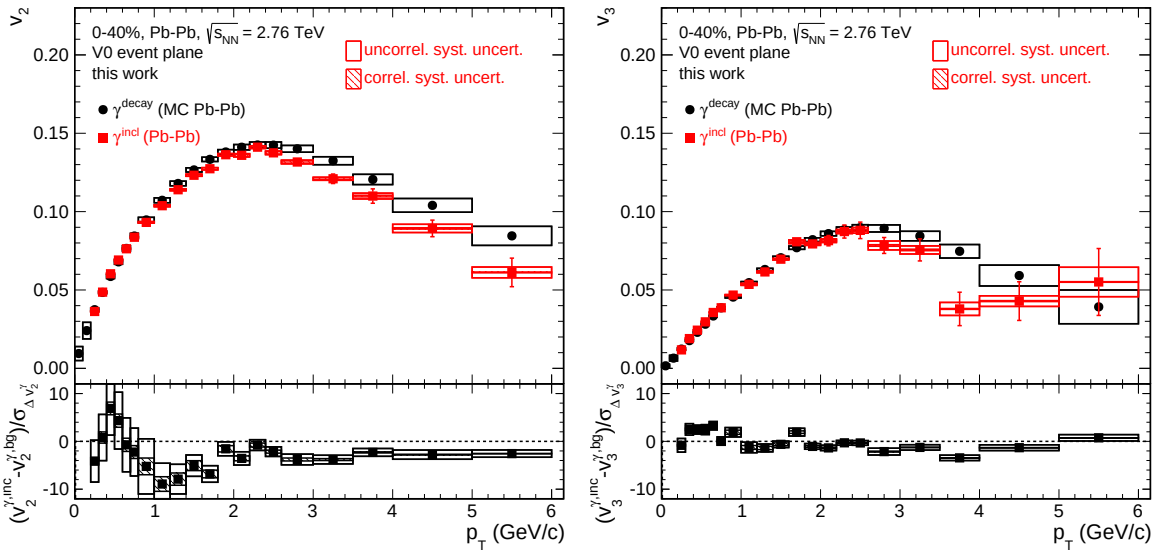

Figure 11.2: Comparison of inclusive and decay photon elliptic (left) and triangular (right) flow in 0 - 40% central Pb-Pb collisions at $\sqrt{s_{\mathrm{NN}}} = 2.76$ TeV. The lower panel shows the difference in units of the statistical error $\sigma_{\Delta v_n}$.

v_n	centrality	p-value (χ^2/dof) full p_T	$p_T < 3$ GeV/c	$p_T \geq 3$ GeV/c
v_2	0 - 5%	0.002 (43.1/20)	0.002 (36.6/16)	0.166 (6.5/4)
	5 - 10%	<0.001 (110.7/20)	<0.001 (105.3/16)	0.211 (5.8/4)
	10 - 20%	<0.001 (113.5/20)	<0.001 (105.6/16)	0.077 (8.4/4)
	20 - 30%	<0.001 (69.4/20)	<0.001 (55.9/16)	0.010 (13.3/4)
	30 - 40%	<0.001 (189.2/20)	<0.001 (165.0/16)	<0.001 (22.7/4)
	0 - 40%	<0.001 (139.9/20)	<0.001 (112.9/16)	<0.001 (27.9/4)
	0 - 20%	<0.001 (102.7/20)	<0.001 (94.8/16)	0.070 (8.7/4)
	20 - 40%	<0.001 (170.2/20)	<0.001 (136.3/16)	<0.001 (34.8/4)
v_3	0 - 5%	0.446 (20.2/20)	0.609 (13.9/16)	0.189 (6.1/4)
	5 - 10%	0.437 (20.3/20)	0.477 (15.7/16)	0.323 (4.7/4)
	10 - 20%	0.068 (30.1/20)	0.042 (27.0/16)	0.557 (3.0/4)
	20 - 30%	0.040 (32.3/20)	0.035 (27.6/16)	0.344 (4.5/4)
	30 - 40%	0.297 (22.8/20)	0.495 (15.4/16)	0.182 (6.2/4)
	0 - 40%	<0.001 (50.8/20)	0.002 (36.5/16)	0.008 (13.7/4)
	0 - 20%	0.351 (21.8/20)	0.513 (15.2/16)	0.158 (6.6/4)
	20 - 40%	0.005 (40.3/20)	0.017 (30.2/16)	0.048 (9.6/4)

Table 11.2: χ^2 test for H0: $v_n^{\gamma,\mathrm{inc}} = v_n^{\gamma,\mathrm{bg}}$ in different centrality bins.

Figure 11.2 shows a comparison of the measured inclusive-photon elliptic and triangular flow and the corresponding calculated decay-photon anisotropic flow in 0 - 40% central Pb-Pb collisions at $\sqrt{s_{\mathrm{NN}}} = 2.76$ TeV. The lower panel shows the relative difference normalized to the statistical error of the difference,

$$\frac{v_n^{\gamma,\mathrm{inc}} - v_n^{\gamma,\mathrm{bg}}}{\sigma_{\Delta v_n^{\gamma}}} \qquad \text{with} \qquad \sigma_{\Delta v_n^{\gamma}} = \sqrt{\sigma^2_{v_n^{\gamma,\mathrm{inc}}} + \sigma^2_{v_n^{\gamma,\mathrm{bg}}}} \,. \tag{11.2}$$

At larger momenta, $v_n^{\gamma,\mathrm{inc}}$ tends to be smaller than $v_n^{\gamma,\mathrm{bg}}$, which can be explained by a contribution of direct photons with a smaller $v_n^{\gamma,\mathrm{dir}}$ than the decay photons. Such a behavior is expected from the dominance of next-to-leading-order pQCD photons, which are mostly emitted before the equilibration of the quark-gluon plasma and thus have zero azimuthal anisotropy. At low p_T, the similarity of the anisotropy of inclusive and decay photons indicates that direct-photon anisotropic flow might be similar in magnitude compared to the inclusive-photon flow.
The results of a χ^2 test for the hypothesis H0: $v_n^{\gamma,\mathrm{inc}} = v_n^{\gamma,\mathrm{bg}}$ are summarized in table 11.2. The systematic uncertainties of the decay-photon anisotropy were considered as a type A uncorrelated uncertainties. The uncertainty of the inclusive photon measurement resulting from the event-plane resolution correction is considered as a type B correlated uncertainty and the remaining uncertainty as a type A uncorrelated uncertainty.
For elliptic flow, the H0 hypothesis must be rejected at the 5% significance level for the full p_T range and at low p_T. At high p_T, the H0 hypothesis cannot be rejected for 0 - 20% central collisions and in smaller bins of centrality below 20% centrality. For triangular flow, the H0 can only be rejected in 0 - 40% and 20 - 40% centrality at the 5% significance level. It should

be noted that the systematic and statistical uncertainties are much larger for the triangular flow than for the elliptic flow due to the reduced event-plane resolution. The smallest statistical uncertainties are obtained in the 0 - 40% centrality bin, where the H0 hypothesis must be rejected for elliptic and triangular flow. Systematic differences between the measurements in small and large centrality bins arise from the different centrality dependence of the cross section for inclusive and decay photons. The fact that the centrality dependence of inclusive and decay photon production is not exactly known is taken into account in the systematic uncertainties of the measurement and cocktail simulation. Consequently, it can be concluded that the inclusive-photon anisotropy cannot be explained by the presence of decay photons alone. This is an important cross check, since from the measurement of the direct-photon excess alone this hypothesis could not be rejected.

11.3 Centrality dependence of the p_{T}-integrated direct-photon anisotropic flow

Figure 11.3 shows the centrality dependence of the p_{T}-integrated ($p_{\mathrm{T}} \geq 1\,\mathrm{GeV}/c$) direct-photon elliptic and triangular flow in comparison to the p_{T}-integrated anisotropic flow of charged hadrons. Since the direct-photon anisotropy is calculated from the measurement of the direct-photon excess in 0 - 40% centrality, it is implicitly assumed that the direct-photon excess does not significantly change with the collision centrality. Direct photons exhibit a similar p_{T}-integrated flow pattern to pions, namely a weak centrality dependence of the triangular flow, a similar magnitude of triangular and elliptic flow in the 0 - 5% most central collisions, and an increase of elliptic flow from central towards mid-central collisions. At first glance, the direct-photon elliptic flow seems to be slightly smaller than the charged pion flow, while the triangular direct-photon flow seems to be consistent with the charged pion triangular flow. A χ^2 test (table 11.3) for the hypothesis H0: $\bar{v}_n^{\gamma,dir} = \bar{v}_n^{\pi^{\pm}}$ yields a p-value of about 20% for triangular flow, such that the hypothesis of consistency cannot be rejected. For elliptic flow, the hypothesis can be rejected at the 5% significance level with a p-value smaller than 0.1%. For both harmonics, the hypothesis H0: $\bar{v}_n^{\gamma,dir} = 0$ can be rejected with p-values smaller than 0.1%.

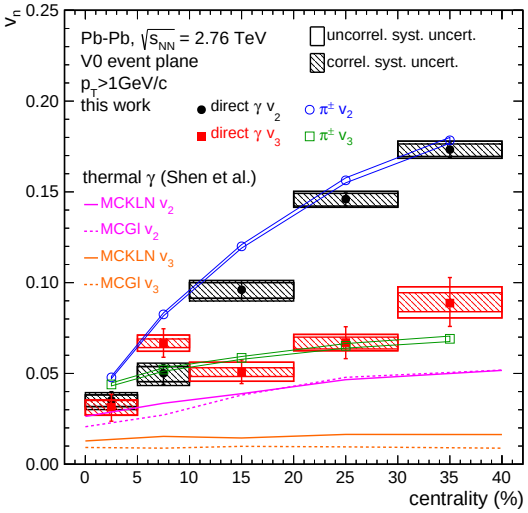

Figure 11.3: Centrality dependence of the p_{T}-integrated ($p_{\mathrm{T}} \geq 1\,\mathrm{GeV}/c$) direct-photon elliptic and triangular flow in comparison with charged pions and with hydrodynamic calculations for thermal photons.

Figure 11.3 also shows hydrodynamic calculations by Shen et al [368] for the p_{T}-integrated thermal-photon elliptic and triangular flow. In chapter 7, it was shown that the event-plane method used in this work rather measures the root mean square of the direct-photon anisotropy than the event mean and thus the data are compared to the root mean square of the thermal-photon anisotropy. The initial conditions were determined from a Monte Carlo Glauber

(MCGl) and a MCKLN calculation with a viscosity-over-entropy-density ratio of $\eta/s = 0.08$ and $\eta/s = 0.2$, respectively. The viscosity over entropy ratios were adjusted such that the resulting hadron elliptic flow describes the experimentally observed final state hadron elliptic flow [369, 370]. The contribution of next-to-leading-order pQCD photons can be neglected for the p_{T}-integrated flow, since the low p_{T} part of the spectrum is dominated by thermal photons. The inclusion of pQCD photons could only decrease the azimuthal anisotropy. The calculation for elliptic flow yields a similar centrality dependence and describes the elliptic flow in the most central collisions, but clearly underestimates the data by about a factor of 3 as the centrality increases. The magnitude of triangular flow is clearly underestimated by the calculation. These observations are confirmed by a χ^2 test for the hypothesis H0: $\bar{v}_n^{\gamma,dir} = \bar{v}_n^{\gamma,therm}$, which gives p-values smaller than 0.1%.

From these observations it is very likely that the majority of direct photons are emitted from a similar stage of the medium evolution as charged particles. It has been argued by Basar et al. [205] that the large direct-photon elliptic flow could be generated through a non-perturbative pre-equilibrium mechanism involving the huge initial magnetic fields generated by the spectator nucleons. Since the direction of triangular flow is uncorrelated with the direction of elliptic flow, this mechanism would not produce any direct-photon triangular flow, which must be rejected based on the measurement. The hadron-like direct-photon triangular flow suggests that triangular and elliptic flow are generated by the same mechanism and that pre-equilibrium processes play a rather minor role in low-p_{T} direct-photon production.

	p-value (χ^2/dof)	
H0	$\bar{v}_2^{\gamma,dir}$	$\bar{v}_3^{\gamma,dir}$
$\bar{v}_n^{\gamma,dir} = v_n^{\pi^\pm}$	< 0.001 (28.8/5)	0.186 (7.5/5)
$\bar{v}_n^{\gamma,dir} = 0$	< 0.001 (1354.6/5)	< 0.001 (169.6/5)
$\bar{v}_n^{\gamma,dir} = \bar{v}_n^{\gamma,therm}$ (MCKLN)	< 0.001 (571.6/5)	< 0.001 (93.4/5)
$\bar{v}_n^{\gamma,dir} = \bar{v}_n^{\gamma,therm}$ (MCGl)	< 0.001 (580.7/5)	< 0.001 (120.4/5)

Table 11.3: χ^2 tests for the p_{T}-integrated direct-photon anisotropic flow.

11.4 Transverse momentum dependence of direct-photon anisotropic flow

Figure 11.4 shows the p_{T}-differential direct-photon elliptic and triangular flow in 0 - 40% central Pb-Pb collisions. We test the hypothesis H0: $v_n^{\gamma,\mathrm{dir}} = 0$ for the measurements in 0 - 40% as well as in 0 - 20% and 20 - 40%. The resulting p-values are summarized in table 11.4. At low p_{T}, the H0 hypothesis can always be rejected at the 5% significance level. At high p_{T}, the H0 hypothesis cannot be rejected.

Hydrodynamic calculations for the thermal-photon anisotropic flow are also shown in fig. 11.4. It was discussed in section 3.2.4 that the azimuthal anisotropy vanishes as the momentum

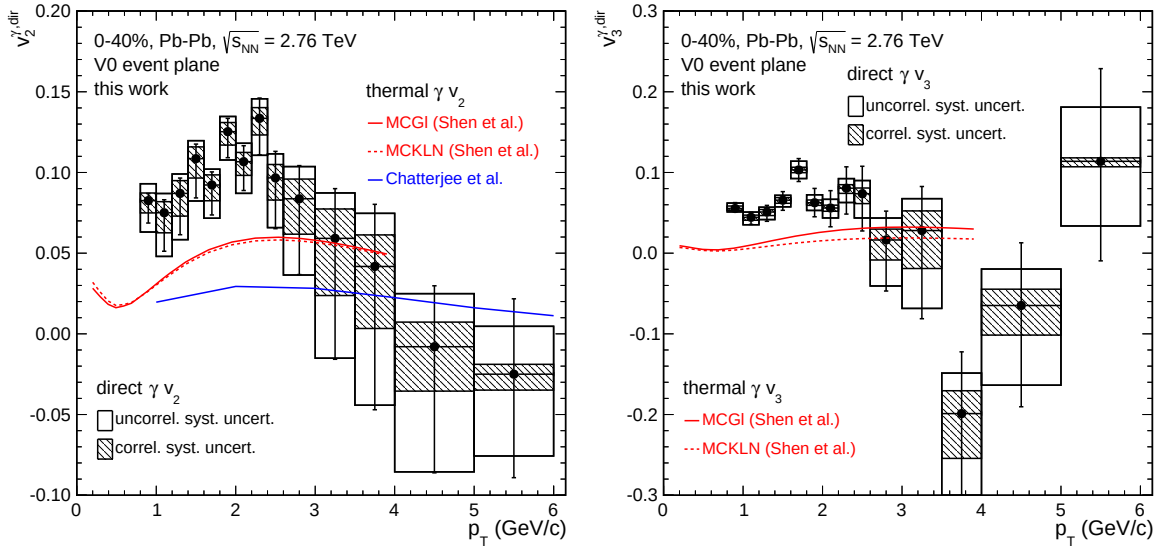

Figure 11.4: Direct-photon p_{T}-differential elliptic (left) and triangular (right) flow in 0 - 40% central Pb-Pb collisions.

		p-value (χ^2/dof)		
v_n	centrality	full p_{T}	$p_{\mathrm{T}} < 3\,\mathrm{GeV}/c$	$p_{\mathrm{T}} \geq 3\,\mathrm{GeV}/c$
v_2	0 - 40%	< 0.001 (101.0/14)	< 0.001 (99.8/10)	0.964 (0.6/4)
	0 - 20%	< 0.001 (73.0/14)	< 0.001 (71.5/10)	0.852 (1.4/4)
	20 - 40%	< 0.001 (97.3/14)	< 0.001 (96.0/10)	0.984 (0.4/4)
v_3	0 - 40%	0.027 (23.0/12)	0.030 (17.0/8)	0.388 (4.1/4)
	0 - 20%	0.075 (19.6/12)	0.044 (15.9/8)	0.673 (2.3/4)
	20 - 40%	0.026 (23.2/12)	0.048 (15.7/8)	0.149 (6.8/4)

Table 11.4: χ^2 test for H0: $v_n^{\gamma,\mathrm{dir}} = 0$ in different centrality bins.

goes to zero. It can be seen in fig. 11.4 that the thermal photon elliptic and triangular flow approaches non-zero values at small momenta, which is a feature that distinguishes massless from massive particles. For massive particles, the pole in the Bose distribution at zero momentum is regulated by their rest mass implying that for massive particles v_n vanishes like p_{T}^n for $p_{\mathrm{T}} \to 0$ [94, 95]. The situation is different for massless particles, which can have a non-zero azimuthal anisotropy at zero transverse momentum [371]. The calculation for the direct-photon elliptic flow by Chatterjee et al. [372] is based on Monte Carlo Glauber initial conditions and the photon flow is measured with respect to the participant plane, where the anisotropy is larger than in the reaction plane direction. While the calculation by Shen et al. starts at $\tau_0 = 0.6\,\mathrm{fm}/c$, the calculation by Chatterjee at al. already starts at $\tau_0 = 0.14\,\mathrm{fm}/c$ yielding about 25% more photons from the hot quark-gluon plasma phase. Those photons carry almost zero anisotropic flow, which results in a much smaller direct-photon anisotropy. Furthermore, the calculation by Chatterjee et al. shows the mean value of the thermal photon flow and not the root mean square like the calculation by Shen et al., which has only minor implications with regard to the large numerical difference.

Since thermal photon production is dominant at small momenta, when testing the hypothesis H0: $v_n^{\gamma,\mathrm{dir}} = v_n^{\gamma,\mathrm{therm}}$ for $p_\mathrm{T} < 3\,\mathrm{GeV}/c$ one finds that none of the calculations can describe the data (table 11.5). Similar calculations can be found in literature [373–375], but all of them underestimate the experimentally observed direct-photon azimuthal anisotropy.

v_n	H0	p-value (χ^2/dof)
$v_2^{\gamma,\mathrm{dir}}$	MCGl, Shen et al.	0.006 (24.6/10)
	MCKLN, Shen et al.	0.004 (25.9/10)
	MCGl, Chatterjee et al.	<0.001 (48.2/9)
$v_3^{\gamma,\mathrm{dir}}$	MCGl, Shen et al.	<0.001 (83.9/10)
	MCKLN, Shen et al.	<0.001 (101.7/10)

Table 11.5: χ^2 test for H0: $v_n^{\gamma,\mathrm{dir}} = v_n^{\gamma,\mathrm{therm}}$ for $p_\mathrm{T} < 3\,\mathrm{GeV}/c$ for different hydrodynamic calculations.

We can interpret the result as follows. At high p_T, the direct-photon anisotropic flow is consistent with zero, which is expected from the dominance of next-to-leading-order pQCD photons. At low p_T, the elliptic and triangular flow are significantly larger than zero and larger than expected from hydrodynamic calculations. It was shown in phenomenological models [376, 377] that the large direct-photon elliptic flow and spectra can be described by increasing the fraction of photons from the hadron gas. It could be concluded that direct photons are produced in a later phase of the system evolution than assumed. It is argued by Biro et al. [193] that the fireball initially consists mainly of gluons, which do not radiate electromagnetic radiation. The implications of the measurement for the direct-photon production time will be discussed further in section 11.7.

11.5 Comparison with PHENIX results

Figure 11.5 shows the direct-photon elliptic flow $v_2^{\gamma,\mathrm{dir}}$ in 0 - 20% and 20 - 40% central Pb-Pb collisions in comparison to PHENIX results in Au-Au collisions at $\sqrt{s_\mathrm{NN}} = 200\,\mathrm{GeV}$ in the same centrality classes. It can be seen that the data points in Pb-Pb collisions are numerically lower compared to Au-Au collisions, but the data points are still consistent within their large uncertainties.

Figure 11.6 (left) shows the inclusive-photon elliptic flow measured in Pb-Pb collisions in comparison to the corresponding PHENIX measurement. Comparing the PHENIX results with the measurement in Pb-Pb collisions, both data sets numerically agree at all momenta in 0 - 20% central collisions and at transverse momenta above $3\,\mathrm{GeV}/c$ in 20 - 40% mid-central collisions, while the low-p_T inclusive-photon flow at the LHC tends to be larger than the inclusive-photon flow at RHIC. At the LHC, the lifetime of the fireball is about 15% longer (cf. section 3.1.4), which allows to develop larger flow anisotropies at LHC compared to RHIC energies.

In PHENIX, inclusive photons are measured at mid rapidity ($|\eta| \leq 0.35$) by the PHENIX electromagnetic calorimeter. Photons were identified by a shower shape cut and a veto on charged particles. The event plane was determined either by the Beam-Beam-Counters (BBC) or the reaction plane detector (RXN), providing a maximum resolution in mid-central collisions of 0.4

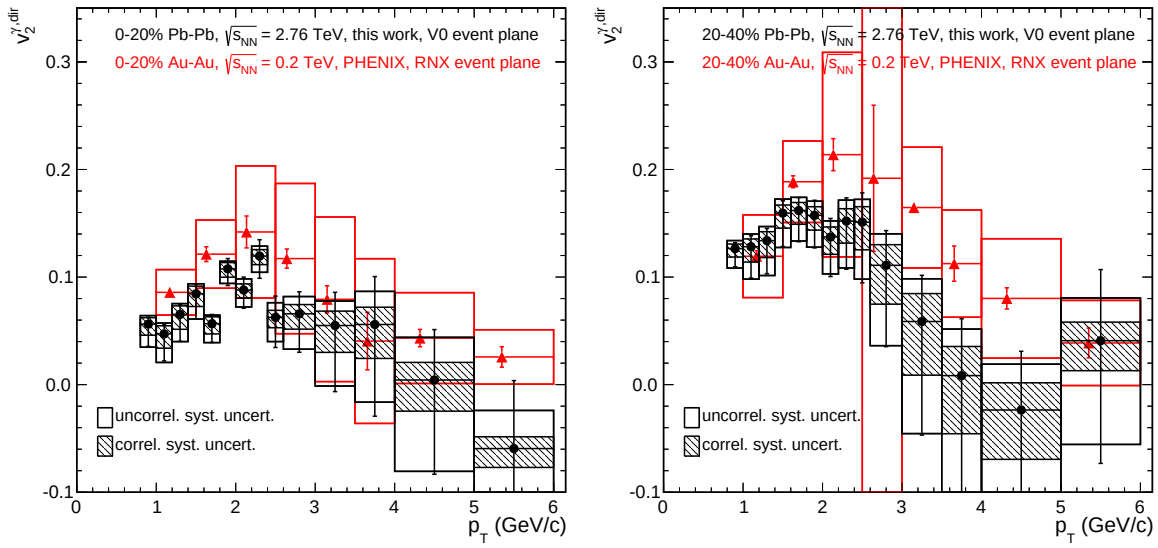

Figure 11.5: Direct-photon elliptic flow $v_2^{\gamma,\mathrm{dir}}$ in 0 - 20% and 20 - 40% central Pb-Pb collisions in comparison to PHENIX results in Au-Au collisions.

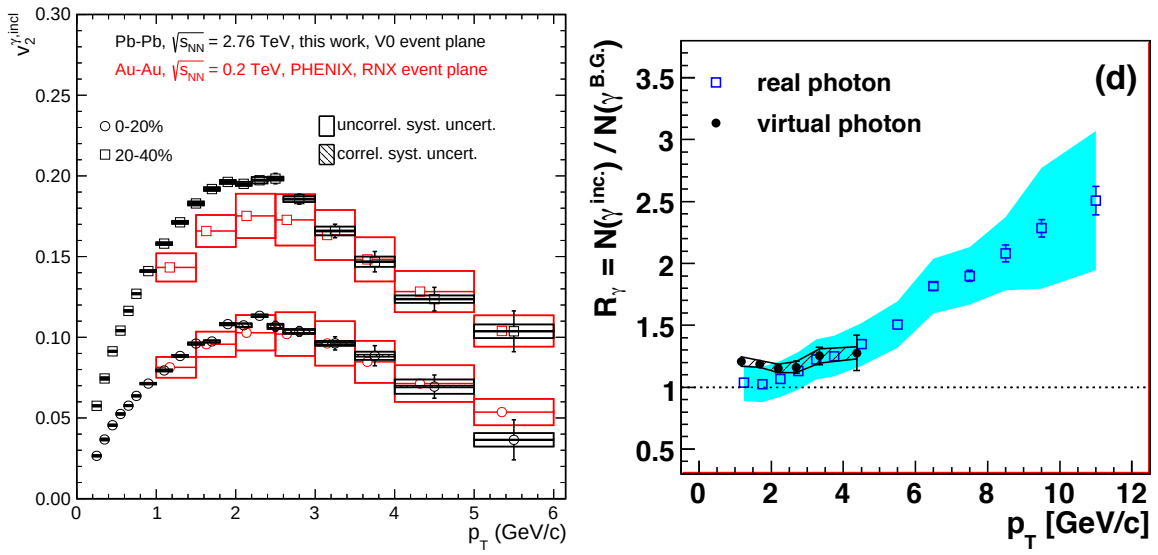

Figure 11.6: (left) Inclusive-photon elliptic flow in Pb-Pb collisions comparison the measurement in Au-Au collisions by the PHENIX collaboration (RXN). (right) Direct-photon excess in minimum bias Au-Au collisions at $\sqrt{s_{\mathrm{NN}}} = 200\,\mathrm{GeV}$ measured from real (calorimetry) and virtual (dilepton spectrum) photons [204].

and 0.7, respectively. Consequently, the RXN measurement provides a similar resolution compared to the ALICE V0 detectors (cf. section 9.1.2). In figs. 11.5 and 11.6 (left), only the result obtained with the RXN detector is shown. The inclusive-photon elliptic flow has an absolute systematic uncertainty of about 2% resulting from remaining contamination in the inclusive photon sample [204]. The uncertainties on the inclusive photon measurement using the ALICE detector are on the order of 2% (relative) at low p_{T} corresponding to an absolute error of about 0.4% for $v_n^{\gamma,\mathrm{inc}} = 0.2$, which is about 5 times smaller at low p_{T} than the systematic uncertainty of the PHENIX measurement. This is an interesting difference between the two measurements,

because the uncertainties of the direct-photon elliptic flow at low p_{T} are rather comparable. In this work, the main source of systematic uncertainty is the direct-photon excess, while in the PHENIX measurement, the main source of uncertainty comes from the inclusive-photon elliptic flow measurement. Figure 11.6 (right) shows the direct-photon excess measured with the PHENIX electromagnetic calorimeter in comparison to the excess extracted from the dilepton spectra. Since the calorimeter measurement has large uncertainties at low p_{T}, the PHENIX collaboration used the dilepton direct-photon excess instead of the calorimeter measurement for transverse momenta below $4\,\mathrm{GeV}/c$. This approach is based on the assumption that the direct-photon excess is the same for real and virtual photons at small masses and results in much smaller uncertainties. Comparing the data for virtual and real photons, the low-p_{T} data points for real photons are numerically smaller than for virtual photons. Recently, Linnyk et al. [378] claimed that the direct-photon excess is indeed smaller for real than for virtual photons and that the apparently large direct-photon elliptic flow is just an artifact caused the methodical inconsistency of the PHENIX measurement. However, more precise PHENIX preliminary results obtained from external conversions indicate no significant deviations between real and virtual photons [379, 380]. In the analysis presented in this work, the same (real photon) method was used for the extraction of the direct-photon excess and the anisotropic flow, such that the large elliptic and triangular flow cannot be explained by a hypothetical deviation between virtual and real photons. Furthermore, since both results were obtained with complementary different photon detection techniques (conversions vs. calorimetry), the qualitative consistency suggests that detector effects alone cannot explain the unexpectedly large direct-photon $v_2^{\gamma,\mathrm{dir}}$.

11.6 Critical assessment

Within this work, it is implicitly assumed that the direct-photon excess does not significantly depend on the centrality in 0 - 40% central collisions. However, a significant centrality dependence would only affect the measurement in smaller centrality bins. For the measurement in 0 - 40% centrality, the anisotropic flow was first measured or calculated in small bins of centrality and then averaged taking the centrality dependence of the inclusive or decay photon production into account, respectively. Future measurements of the centrality dependence of the direct-photon excess will clarify how this assumption affects the measurement of the centrality dependence of the direct-photon anisotropic flow.

As demonstrated in section 11.1, the ALICE preliminary direct-photon excess in 0 - 40% Pb-Pb collisions is affected by a large overall systematic uncertainty on the material budget and thus the low-p_{T} direct-photon excess could be described by a binary scaled next-to-leading-order pQCD calculation by W. Vogelsang without any contribution from thermal photons. In addition, it was shown in section 11.2 that the inclusive and decay-photon anisotropies are very similar. Consequently, it could be argued that low-p_{T} direct photons are exclusively produced in next-to-leading-order pQCD processes and thermal photon production is rather negligible. In order to cross check the robustness of the thermal photon interpretation, we assume that the true direct-photon excess is given by the excess of pQCD photons alone. We use the fit of the direct-photon spectrum at high p_{T}, extrapolate it towards smaller momenta and subtract the thermal-photon part from the direct-photon spectrum. The parametrization of the direct-photon excess without thermal photons shown in fig. 10.11 (right) is then used to extract the direct-photon elliptic and triangular flow. The result is shown in fig. 11.7. Since prompt photons

are produced isotropically, the extracted direct-photon anisotropy is tested for H0: $\bar{v}_n^{\gamma,dir} = 0$. While the H0 hypothesis cannot be rejected for triangular flow, it can be rejected at the 5% significance level for elliptic flow, which suggests that the observed inclusive-photon anisotropy cannot be explained consistently by decay photons and pQCD photons alone. Nevertheless, this cross-check demonstrates again that the direct-photon anisotropic flow measurement and the thermal photon interpretation are very sensitive to systematic bias in the direct-photon excess.

	p-value (χ^2/dof)	
H0	$\bar{v}_2^{\gamma,dir}$	$\bar{v}_3^{\gamma,dir}$
$\bar{v}_n^{\gamma,dir} = 0$ ($R^{\gamma,dir} = R^{\gamma,dir}_{\mathrm{pQCD}}$)	< 0.001 (22.7/5)	0.409 (5.1/5)

Table 11.6: χ^2 test for the p_{T}-integrated direct-photon anisotropic flow extracted with the direct-photon excess expected from next-to-leading-order pQCD photon production alone.

Similarly, it could be argued that the low-p_{T} direct-photon excess and the large direct-photon anisotropic flow could be explained by the fact that a substantial contribution of decay photons is missing in the cocktail simulation for the decay-photon spectrum and azimuthal anisotropy. If the true anisotropy of decay photons were larger than assumed, the extracted direct-photon anisotropy would essentially be smaller. However, it was demonstrated in section 10.1.4 that photons stemming from the decay of neutral pions have the largest anisotropy at low p_{T}. Consequently, even unexpectedly large deviations from m_{T} scaling of the η meson and other mesons included in the cocktail simulation could not increase the decay-photon anisotropy. Thus, it could only be speculated that additional photons are produced by the decay of experimentally yet undiscovered particles. Due to mass ordering at low p_{T}, only photons from a meson lighter than the neutral pion could have a larger anisotropy at low momentum compared to decay photons stemming from neutral pions. A meson lighter than the neutral pion is not part of the Standard Model. It should be mentioned that the possible discovery of a 38 MeV/c^2 boson decaying into two photons by the Dubna accelerator in August 2012 is under discussion [381–384]. However, as long as the discovery is not confirmed by an independent measurement and its properties, such as its interaction with other elementary particles and in particular its anisotropic flow are not measured, the impact of such a hypothetical particle is only subject to pure speculation. The contribution of decay photons was subtracted according to the best of our current knowledge and systematic uncertainties related to the measurements and the assumptions made were propagated to the final result. Thus, it will be important to reevaluate the material budget in order to reduce the

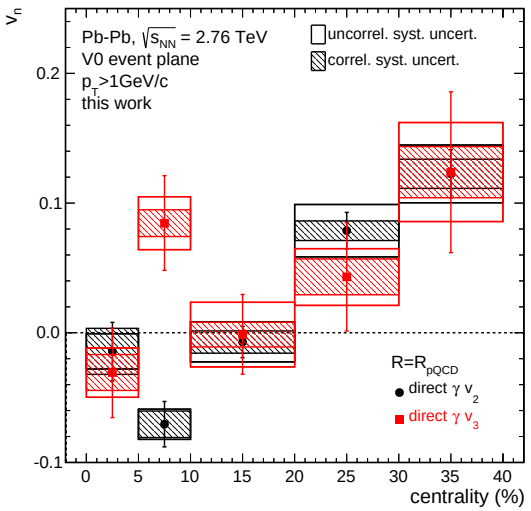

Figure 11.7: Centrality dependence of the p_{T}-integrated ($p_{\mathrm{T}} \geq 1$ GeV/c) direct-photon elliptic and triangular flow assuming exclusive next-to-leading-order pQCD photon production ($R^{\gamma,dir} = R^{\gamma,dir}_{\mathrm{pQCD}}$).

correlated systematic uncertainties on the direct-photon measurement.

Furthermore, it should be mentioned that there are several issues related to the χ^2 tests applied in this chapter. The multiple comparison problem arises from the non-zero probability of rejecting a true hypothesis, and states that for a large number of comparisons the probability of rejecting at least one true hypothesis approaches one. Furthermore, the approximation to the χ^2 distribution breaks down if expected frequencies are too low or of there is only one degree of freedom. In particular, it is assumed that the statistical and systematic uncertainties follow normal distributions. It was shown in section 10.2.2.1 that the assumption of a Gaussian probability distribution for the uncertainties of the direct-photon anisotropic flow slightly underestimates the probability for large deviations. However, it was demonstrated that a substantial fraction of the systematic uncertainties is correlated, and thus a χ^2 test provides a quantitative comparison between data and theory.

Finally, it was discussed in chapter 7, whether the measurement of the direct-photon anisotropic flow could be biased due to flow fluctuations. First, it was demonstrated that the event-plane method rather measures the root mean square of the direct-photon anisotropy than the event mean value. Second, by studying different scenarios for the direct-photon production within a simple model for the experimental extraction procedure, it was shown that fluctuations could only bias the measured direct-photon anisotropy towards values smaller than the root mean square of the true direct-photon anisotropic flow. From these observations, it is very unlikely that the present large direct-photon anisotropy arises from artifacts of the direct-photon anisotropic flow extraction procedure.

11.7 Conclusions

The idea of accessing the temperature of the quark-gluon plasma by measuring lepton pair and real photon production cross sections was first pointed out in 1981 by [385].
The low-p_{T} direct-photon spectrum is an accumulation of contributions from several production mechanisms acting over the whole evolution of the fireball. When extracting the inverse slope parameter T_{eff}, it was assumed that next-to-leading-order pQCD photons can be neglected at low p_{T}, and T_{eff} was directly extracted from the direct-photon spectrum in the transverse momentum range 0.8 - 2.2 GeV/c [201]. It was shown by Klasen et al. [367], based on next-to-leading-order pQCD calculations using JETPHOX [386] that the contribution of prompt photons in the p_{T} region 0.8 - 2.2 GeV/c is less than 10 - 20% and that the inverse slope parameter is robust against subtraction of prompt photons and a variation of the fit window.
Recent hydrodynamic calculations include a substantial portion of photons emitted in the hot quark-gluon plasma phase, where flow has not yet developed. For a dominant production in the early phase of the collision, the blue shift due to radial flow can be neglected and the inverse slope parameter T_{eff} can be interpreted as an effective temperature of the source integrated over the whole system evolution. As discussed in section 3.1.2, it is expected – using that $T^4 \propto \epsilon$ and considering that the initial energy density at the LHC is about three times larger than at RHIC – that the initial temperature at the LHC is about 30% larger than at RHIC. When the inverse slope parameters are compared directly, the result that T_{eff} is about 37% larger at the LHC than at RHIC might indicate that the inverse slope parameter is closely related to the initial

temperature. Thus T_{eff} could be interpreted as an effective temperature of the medium. The fact that $T_{\mathrm{eff}} > T_{\mathrm{c}}$ would imply a dominant thermal-photon production from the quark-gluon plasma phase and thus the low-p_{T} direct-photon spectrum would give access to the temperature in early phases of the collision. Estimates for the initial temperature can be obtained by comparing calculations to the low-p_{T} direct-photon spectrum with current estimates ranging from 300 - 600 MeV/k_{B} [200] at RHIC and 500 - 600 MeV/k_{B} at the LHC [34, 35].

Measurements of the anisotropic flow at RHIC and the LHC exhibit an unexpectedly large elliptic flow, which cannot be explained within the picture of early direct photon production. Novel approaches describing the large elliptic flow through a non-perturbative pre-equilibrium mechanism involving the spectator magnetic fields [205] or through intensive radiation of magnetic bremsstrahlung resulting from the interaction of escaping quarks with the collective confining colour field [387] cannot explain the significant direct-photon triangular flow measured within this work. Since triangular flow is purely driven by fluctuations in the initial energy density profile, its direction Ψ_3 is randomly oriented with respect to the reaction plane and magnetic field [147, 388], which was experimentally demonstrated in [140] by showing that the triangular flow vanishes if measured with respect to the second-order event plane (cf. section 3.4.1). The similarity of the elliptic and triangular direct-photon flow with the corresponding charged pion anisotropy suggests that direct photons might be produced in a much later stage of the system evolution. It is argued by Biro et al. [193] that the fireball initially consists mainly of gluons, which do not radiate electromagnetically, and thus quark-antiquark creation is delayed by several fm/c. While standard hydrodynamic calculations [176, 203, 368, 372, 389, 390] underestimate the azimuthal anisotropy, phenomenological models with a larger contribution of photons from the hadron gas are able to describe spectra and anisotropic flow consistently [376, 377]. Consequently, the production of thermal photons from the hot initial phase could be substantially lower than assumed. This picture is also supported by earlier measurements of the photon HBT radii at SPS (cf. section 4.5), which are consistent with the radii for hadrons.

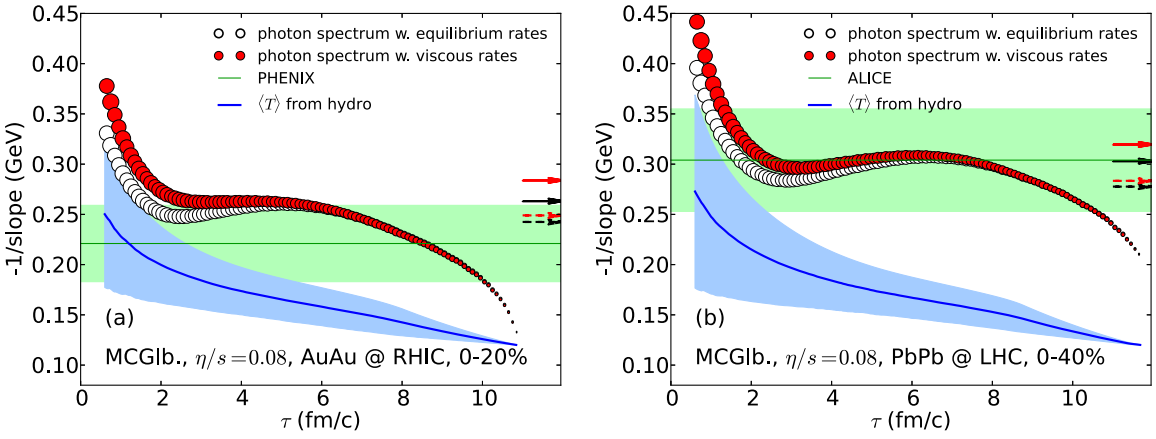

Figure 11.8: Inverse slope parameter T_{eff} as a function of the emission time from hydrodynamic calculations in Au-Au collisions at $\sqrt{s_{\mathrm{NN}}} = 200$ GeV (left) and in Pb-Pb collisions at $\sqrt{s_{\mathrm{NN}}} =$ 2.76 TeV (right) [315]. The average true cell temperature is shown as a blue line in each case. The experimentally measured effective temperature T_{eff} and its uncertainties are shown as green band.

It was already realized in 1986 by Kajantie et al. [391] that the strong collective flow generated during the expansion of the fireball will affect the photon and dilepton transverse momentum spectra. If the photons are emitted from fluid cells at relativistic velocities, the apparent temperature T_{eff} is significantly enlarged compared to the true temperature T by the blue shift,

$$T_{\mathrm{eff}} = T\sqrt{(1+\beta)/(1-\beta)}\ , \tag{11.3}$$

where β is the radial flow velocity (cf. section 3.2.3). Figure 11.8 shows the effective temperatures T_{eff} as a function of time, for photons emitted with equilibrium rates (open) and with viscously corrected rates (closed) from cells at a given temperature T within the hydrodynamic evolving viscous medium. It can be seen that viscous corrections are most pronounced at early times and become negligible at later times. The green bands indicate the effective temperature measured by ALICE [201] and PHENIX [200]. As the system cools the effective temperature begins to deviate upwards from the true temperature due to the onset of radial flow. Due to the strengthening of the radial flow, the effective temperature even begins to increase for $\tau \geq 3\,\mathrm{fm}/c$, while the true temperature decreases. At the chemical freeze-out temperature, the radial flow saturates and the effective temperature drops due to the cooling of the system. The results suggest that $T_{\mathrm{eff}} > T_{\mathrm{c}}$ alone does not necessarily prove that direct photons are dominantly produced in the early hot phase.
The solid red (equilibrium rates) and black (viscously corrected) arrows denote the inverse slopes of the final space-time integrated hydrodynamic photon spectra, which are above the limits for the measured effective temperature for PHENIX, but in agreement with $T_{\mathrm{eff}}^{\mathrm{LHC}}$. In order to account for a possible later onset of the direct photon production due to a purely gluonic early phase [193], only photons from cells with temperatures above $220\,\mathrm{MeV}/k_{\mathrm{B}}$ at times $\tau > 2\,\mathrm{fm}$ are considered in the phase space integration removing about 30% of the total photon yield. The resulting effective temperatures (dashed arrows) are in better agreement with the Au-Au data compared to the full integration, and agree reasonably well with the Pb-Pb data.

It can be concluded that the large effective temperatures observed at RHIC and the LHC reflect mostly the blue shift due to the strong radial flow and do not prove the emission of electromagnetic radiation from the quark-gluon plasma. It will be interesting to see calculations for the direct-photon anisotropic flow with enlarged hadron-gas thermal-photon production ratios, for example by a suppression of early-phase thermal photon production due to gluon dominance.

Appendix

A Event-plane resolution correction

The event-plane method measures the correlation between particles of interest and the event-plane estimate Ψ_n^{EP}:

$$\left\langle \cos\left(n\left(\phi - \Psi_n^{\mathrm{EP}}\right)\right)\right\rangle = \left\langle \cos\left(n\left((\phi - \Psi_n) - \left(\Psi_n^{\mathrm{EP}} - \Psi_n\right)\right)\right)\right\rangle \tag{A.1}$$

We use the following trigonometric identity

$$\cos\left(a \pm b\right) = \cos\left(a\right)\cos\left(b\right) \mp \sin\left(a\right)\sin\left(b\right) \tag{A.2}$$

with $a = \phi - \Psi_n$ and $b = \Psi_n^{\mathrm{EP}} - \Psi_n$ and assume that deviations between the event-plane estimate Ψ_n^{EP} and the true reference angle Ψ_n are just given by uncorrelated random fluctuations δ:

$$\Psi_n^{\mathrm{EP}} = \Psi_n + \delta \qquad \langle\delta\rangle = 0 \tag{A.3}$$

Under this assumption, the expressions inside the brackets factorize, since $\langle XY\rangle = \langle X\rangle\,\langle Y\rangle$ for uncorrelated random variables X and Y. The sin terms vanish due to the reflection symmetry

$$\sin\left(x\right) = -\sin\left(-x\right) \quad \Rightarrow \quad \langle\sin\left(x\right)\rangle = 0\ , \tag{A.4}$$

if x is symmetrically distributed around zero. We obtain:

$$\left\langle \cos\left(n\left(\phi - \Psi_n^{\mathrm{EP}}\right)\right)\right\rangle = \underbrace{\left\langle \cos\left(n\left(\phi - \Psi_n\right)\right)\right\rangle}_{v_n} \underbrace{\left\langle \cos\left(n\left(\Psi_n^{\mathrm{EP}} - \Psi_n\right)\right)\right\rangle}_{R} \tag{A.5}$$

The first factor is just the n-th order harmonic v_n defined in eq. (3.29), such that the event-plane method estimate of the n-th order anisotropic flow is given by

$$v_n\{\mathrm{EP}\} = \frac{\left\langle \cos\left(n\left(\phi - \Psi_n^{\mathrm{EP}}\right)\right)\right\rangle}{R} \tag{A.6}$$

with the resolution correction factor $R = \left\langle \cos\left(n\left(\Psi_n^{\mathrm{EP}} - \Psi_n\right)\right)\right\rangle$.
The resolution correction can be estimated from the correlation between the event-plane angle and the event-plane angle determined from a detector with identical dispersion. We assume that the only correlation between the event planes A and B is only due to flow. More formally:

$$\begin{aligned} \Psi_n^{\mathrm{A}} &= \Psi_n + \delta_{\mathrm{A}} \qquad & \Psi_n^{\mathrm{B}} &= \Psi_n + \delta_{\mathrm{B}} \\ \langle\delta_{\mathrm{A,b}}\rangle &= 0 \qquad & \mathrm{Corr}\ (\delta_{\mathrm{A}}, \delta_{\mathrm{B}}) &= 0 \end{aligned} \tag{A.7}$$

Here, δ_A and δ_A are uncorrelated random variables (white noise) and the variance is just given by the dispersion χ of the event-plane method. Using the trigonometric identity eq. (A.2) with $a = n\left(\Psi_n^\mathrm{A} - \Psi_n\right)$ and $b = n\left(\Psi_n^\mathrm{B} - \Psi_n\right)$ and averaging over all events one obtains:

$$\begin{aligned}\left\langle \cos\left(n\left(\Psi_n^\mathrm{A} - \Psi_n^\mathrm{B}\right)\right)\right\rangle = &\quad \left\langle \cos\left(n\left(\Psi_n^\mathrm{A} - \Psi_n\right)\right)\cos\left(n\left(\Psi_n^\mathrm{B} - \Psi_n\right)\right)\right\rangle \\ &+ \left\langle \sin\left(n\left(\Psi_n^\mathrm{A} - \Psi_n\right)\right)\sin\left(n\left(\Psi_n^\mathrm{A} - \Psi_n\right)\right)\right\rangle\end{aligned} \tag{A.8}$$

Under the assumptions made above, the expressions inside the brackets factorize and the sin terms vanish due to the reflection symmetry:

$$\left\langle \cos\left(n\left(\Psi_n^\mathrm{A} - \Psi_n^\mathrm{B}\right)\right)\right\rangle = \left\langle \cos\left(n\left(\Psi_n^\mathrm{A} - \Psi_n\right)\right)\right\rangle \left\langle \cos\left(n\left(\Psi_n^\mathrm{B} - \Psi_n\right)\right)\right\rangle \tag{A.9}$$

We will first consider the case that method A and B have similar dispersion. For this case the correction factor from two event planes with similar dispersion is just given by:

$$\left\langle \cos\left(n\left(\Psi_n^\mathrm{A} - \Psi_n\right)\right)\right\rangle = \sqrt{\left\langle \cos\left(n\left(\Psi_n^\mathrm{A} - \Psi_n^\mathrm{B}\right)\right)\right\rangle} \tag{A.10}$$

If detector A and B have different dispersion, the resolution correction for event plane A can be estimated from the correlation with a third event plane C. We obtain the following relations:

$$\left\langle \cos\left(n\left(\Psi_n^\mathrm{A} - \Psi_n\right)\right)\right\rangle = \frac{\left\langle \cos\left(n\left(\Psi_n^\mathrm{A} - \Psi_n^\mathrm{B}\right)\right)\right\rangle}{\left\langle \cos\left(n\left(\Psi_n^\mathrm{B} - \Psi_n\right)\right)\right\rangle} \tag{A.11}$$

$$\left\langle \cos\left(n\left(\Psi_n^\mathrm{B} - \Psi_n\right)\right)\right\rangle = \frac{\left\langle \cos\left(n\left(\Psi_n^\mathrm{B} - \Psi_n^\mathrm{C}\right)\right)\right\rangle}{\left\langle \cos\left(n\left(\Psi_n^\mathrm{C} - \Psi_n\right)\right)\right\rangle} \tag{A.12}$$

$$\left\langle \cos\left(n\left(\Psi_n^\mathrm{C} - \Psi_n\right)\right)\right\rangle = \frac{\left\langle \cos\left(n\left(\Psi_n^\mathrm{C} - \Psi_n^\mathrm{A}\right)\right)\right\rangle}{\left\langle \cos\left(n\left(\Psi_n^\mathrm{A} - \Psi_n\right)\right)\right\rangle} \tag{A.13}$$

Inserting eq. (A.13) into eq. (A.12) and then eq. (A.12) into eq. (A.11) yields:

$$\left\langle \cos\left(n\left(\Psi_n^\mathrm{A} - \Psi_n\right)\right)\right\rangle = \frac{\left\langle \cos\left(n\left(\Psi_n^\mathrm{A} - \Psi_n^\mathrm{B}\right)\right)\right\rangle \left\langle \cos\left(n\left(\Psi_n^\mathrm{A} - \Psi_n^\mathrm{C}\right)\right)\right\rangle}{\left\langle \cos\left(n\left(\Psi_n^\mathrm{B} - \Psi_n^\mathrm{C}\right)\right)\right\rangle \left\langle \cos\left(n\left(\Psi_n^\mathrm{A} - \Psi_n\right)\right)\right\rangle} \tag{A.14}$$

Finally, we obtain the formula for the resolution correction factor from 3 event planes:

$$\left\langle \cos\left(n\left(\Psi_n^\mathrm{A} - \Psi_n\right)\right)\right\rangle = \sqrt{\frac{\left\langle \cos\left(n\left(\Psi_n^\mathrm{A} - \Psi_n^\mathrm{B}\right)\right)\right\rangle \left\langle \cos\left(n\left(\Psi_n^\mathrm{A} - \Psi_n^\mathrm{C}\right)\right)\right\rangle}{\left\langle \cos\left(n\left(\Psi_n^\mathrm{B} - \Psi_n^\mathrm{C}\right)\right)\right\rangle}} \tag{A.15}$$

B The dN/d$\Delta\phi$ method

B.1 Extraction of the Fourier harmonics

The azimuthal distribution dN/dϕ of particles produced in an individual heavy-ion collision can be expressed as a Fourier series,

$$\frac{\mathrm{d}N}{\mathrm{d}\phi} = \frac{N_0}{2\pi}\left(1 + 2\sum_{n\geq 1} v_n \cos\left(n\left(\phi - \Psi_n\right)\right)\right) , \tag{B.1}$$

where N_0 is the average particle yield, v_n is the magnitude and Ψ_n is the corresponding angle of the maximum n-th order anisotropy. Experimentally, certain particles can only be statistically identified inhibiting a direct event-by-event evaluation of the Fourier coefficient v_n. Instead, the particle yields $N(\Delta\phi) = \mathrm{d}N/\mathrm{d}\Delta\phi_n$ are measured as a function of $\Delta\phi_n = \phi - \Psi_n$ and averaged over many events. Ψ_n is estimated by the event-plane angle Ψ_n^{EP}. The finite resolution of the event plane involves corrections that were discussed in appendix A and shall be neglected in the following. Equation (B.1) becomes:

$$N(\Delta\phi_n) = \frac{N_0}{2\pi}\left(1 + 2\sum_{m\geq 1} v_m \cos\left(m\Delta\phi_n + m\left(\Psi_n - \Psi_m\right)\right)\right) \tag{B.2}$$

We use the trigonometric identity eq. (A.2), which gives

$$\begin{aligned}\cos\left(m\Delta\phi_n + m\left(\Psi_n - \Psi_m\right)\right) = \quad & \cos\left(m\Delta\phi_n\right)\cos\left(n\left(\Psi_n - \Psi_m\right)\right) \\ & - \ \sin\left(m\Delta\phi_n\right)\sin\left(n\left(\Psi_n - \Psi_m\right)\right) \ ,\end{aligned} \tag{B.3}$$

When averaging eq. (B.2)over many events, we which defines the coefficients

$$v'_m = \langle\cos\left(m\Delta\phi_n\right)\rangle\,\langle\cos\left(n\left(\Psi_n - \Psi_m\right)\right)\rangle \tag{B.4}$$

$$s'_m = \langle\sin\left(m\Delta\phi_n\right)\rangle\,\langle\sin\left(n\left(\Psi_n - \Psi_m\right)\right)\rangle \ . \tag{B.5}$$

The measure $\Psi_n - \Psi_m$ is somewhat ambiguous, since Ψ_n is defined in $[0, 2\pi/n]$ and Ψ_m in $[0, 2\pi/m]$. The brackets denote an average over particles which are defined in the full azimuthal range. Thus, the orientation of Ψ_n and Ψ_m depend on the particle angle ϕ:

$$\Psi_n \to \Psi_n + j_n\frac{2\pi}{n} \qquad j_n = \lfloor\frac{\phi}{2\pi}n\rfloor \tag{B.6}$$

Assuming that ϕ is uniform distributed, we sum over all possible combinations of j_n and j_m:

$$\begin{aligned}&\frac{1}{mn}\sum_{j_m=0}^{m}\sum_{j_n=0}^{n}\cos\left(m\left(\Psi_n - \Psi_m\right) + m\left(j_m\frac{2\pi}{m} + j_n\frac{2\pi}{n}\right)\right) \\ &\quad = \frac{1}{mn}\sum_{j_m=0}^{m}\sum_{j_n=0}^{n}\cos\left(m\left(\Psi_n - \Psi_m\right) + j_n\frac{m}{n}2\pi\right) \qquad \text{(B.7)} \\ &\quad = \begin{cases}\cos\left(m\left(\Psi_n - \Psi_m\right)\right) & \text{if} \quad m = nk, k\in\mathbb{N} \\ 0 & \text{else}\end{cases} \qquad \text{(B.8)}\end{aligned}$$

The sum vanishes for $m \neq nk$, since we obtain something like a 2π integral over cos and sin, which is zero. The sin terms vanish also for $m = nk$, because of the mirror symmetry. Finally, we we obtain:

$$v'_m = \begin{cases} v_m & \text{if } n = m \\ v_m\,\langle\cos\left(m\left(\Psi_n - \Psi_m\right)\right)\rangle & \text{if} \quad m = nk, k\in\mathbb{N} \\ 0 & \text{else}\end{cases} \tag{B.9}$$

Here, $\langle\cos\left(m\left(\Psi_n - \Psi_m\right)\right)\rangle$ is the measure for the correlation of the n-th and m-th order event

plane. We can see that it is possible to measure higher order harmonics $m > n$ using the nth order event plane Ψ_n, if the higher order event plane Ψ_m is sufficiently correlated with Ψ_n. For example it is possible to measure $v_4\{\Psi_2\}$ from the $\mathrm{d}N/\mathrm{d}\Delta\phi$ distribution with respect to the Ψ_2^{EP} event plane. On the other hand, $N(\Delta\phi_n)$ is insensitive to harmonics with $m \neq kn$, in particular $v_3\{\Psi_2\} = 0$. Finally, we can write eq. (B.2) as:

$$N(\Delta\phi) = \frac{N_0}{2\pi}\left(1 + 2v_n\cos\left(n\left(\phi - \Psi_n\right)\right) + 2\sum_{m\geq 2} v'_m \cos\left(m\left(\phi - \Psi_n\right)\right)\right) \tag{B.10}$$

Now we can measure the yield $N(\Delta\phi)$ as a function of $\Delta\phi$ integrated over many events and obtain v_n from

$$v_n = \frac{\int_0^{\Delta\phi_{\max}} N(\Delta\phi)\cos(n\Delta\phi)\,\mathrm{d}\Delta\phi}{\int_0^{\Delta\phi_{\max}} N(\Delta\phi)\,\mathrm{d}\Delta\phi} \quad \text{with} \quad \Delta\phi_{\max} = \frac{\pi}{n}\,. \tag{B.11}$$

B.2 Finite bin size correction

For practical purposes, azimuthal distributions can only be measured in bins of finite width. For n_{b} finite bins, the integral becomes as sum:

$$v_n^{\mathrm{meas}} = \frac{\sum_{i=0}^{n_{\mathrm{b}}} N\left(\Delta\phi_i^{\mathrm{b}}\right)\cos\left(n\bar{\Delta\phi}_i^{\mathrm{b}}\right)}{\sum_{i=0}^{n_{\mathrm{b}}} N\left(\Delta\phi_i^{\mathrm{b}}\right)} \tag{B.12}$$

with

$$N\left(\Delta\phi_i^{\mathrm{b}}\right) = \int_{\Delta\phi_i^{\mathrm{b}}}^{\Delta\phi_{i+1}^{\mathrm{b}}} N(\Delta\phi)\,\mathrm{d}\Delta\phi \tag{B.13}$$

where $\Delta\phi_i^{\mathrm{b}} = i\frac{\Delta\phi_{\max}}{n_{\mathrm{b}}}$ and $\bar{\Delta\phi}_i^{\mathrm{b}} = 0.5\left(\Delta\phi_i^{\mathrm{b}} + \Delta\phi_{i+1}^{\mathrm{b}}\right)$. The nominator in eq. (B.12) is just the number of particles of interest N_{poi} and thus equal to the nominator in the unbinned case. We use that $N(\Delta\phi) = N_0\left(1 + 2v_n\cos(n\Delta\phi)\right)$ with $N_0 = N_{\mathrm{poi}}/\Delta\phi_{\max}$ and obtain:

$$\begin{aligned} v_n^{\mathrm{meas}} &= \frac{1}{\Delta\phi_{\max}}\sum_{i=0}^{n_{\mathrm{b}}}\left(\int_{\Delta\phi_i^{\mathrm{b}}}^{\Delta\phi_{i+1}^{\mathrm{b}}}\left(1 + 2v_n\cos(n\Delta\phi)\right)\mathrm{d}\Delta\phi\right)\cos\left(n\bar{\Delta\phi}_i^{\mathrm{b}}\right) \\ &= \underbrace{\frac{1}{n_{\mathrm{b}}}\sum_{i=0}^{n_{\mathrm{b}}}\cos\left(n\bar{\Delta\phi}_i^{\mathrm{b}}\right)}_{=0} + v_n\underbrace{\frac{1}{\Delta\phi_{\max}}\sum_{i=0}^{n_{\mathrm{b}}}\cos\left(n\bar{\Delta\phi}_i^{\mathrm{b}}\right)\int_{\Delta\phi_i^{\mathrm{b}}}^{\Delta\phi_{i+1}^{\mathrm{b}}} 2\cos(n\Delta\phi)\,\mathrm{d}\Delta\phi}_{c} \end{aligned} \tag{B.14}$$

The first term vanishes due to the symmetry of the cosine. The finite bin size correction $v_n = v_n^{\mathrm{meas}}/c$ can be evaluated analytically:

$$c = \frac{\sum_{i=0}^{n_{\mathrm{b}}}\cos\left(n\bar{\Delta\phi}_i^{\mathrm{b}}\right)\frac{2}{n}\left(\sin\left(n\Delta\phi_{i+1}^{\mathrm{b}}\right) - \sin\left(n\Delta\phi^{\mathrm{b}}\right)\right)}{\Delta\phi_{\max}} \tag{B.15}$$

For $n_{\mathrm{b}} = 6$, the correction factor is about 99%. A similar correction might be necessary for a detector with finite azimuthal granularity [392].

C Hypothesis testing including systematic uncertainties

C.1 Three types of systematic uncertainties

A detailed description for fits including systematic errors can be found in [393]. We assume that the measurement y is biased due to experimental effects. It can be distinguished between three types of systematic uncertainties:

(A) Uncorrelated random systematic errors, which vary independently from point-to-point:

$$\Delta y_i = \epsilon_{\mathrm{a,i}} \qquad \langle \epsilon_i \rangle = 0,\ \langle \epsilon_{\mathrm{a,i}} \epsilon_{\mathrm{a,j}} \rangle = \delta_{ij} \sigma^2_{\mathrm{a,i}} \tag{C.1}$$

(B) Correlated systematic uncertainties, where all points move by the same fraction ϵ_{b} of their type B uncertainty:

$$\Delta y_i = \epsilon_{\mathrm{b}} \sigma_{\mathrm{b,i}} \tag{C.2}$$

(C) Overall systematic errors (typically normalization), by which all points move by the same fraction:

$$\Delta y_i / y_i = \epsilon_{\mathrm{c}} \sigma_{\mathrm{c}} \tag{C.3}$$

The uncorrelated random systematic uncertainties $\sigma_{\mathrm{a,i}}$ can be separated out and are quadratically added to the statistical uncertainty,

$$\sigma_i = \sqrt{\sigma^2_{\mathrm{stat,i}} + \sigma^2_{\mathrm{a,i}}}\ . \tag{C.4}$$

C.2 Hypothesis testing

Pearson's χ^2 test [394] is a statistical test in order to determine, whether the measured data is consistent with a particular theoretical expectation. Assuming that all errors have a Gaussian probability density distribution, the χ^2 value with respect to the hypothesized values y_i^{H0} (i.e. $y_i^{\mathrm{H0}} = 0$) can be defined as

$$\chi^2 = \sum_{i=1}^{n} \frac{\left((y_i + \epsilon_{\mathrm{b}} \sigma_{\mathrm{b,i}} + y_i \epsilon_{\mathrm{c}} \sigma_{\mathrm{c}}) - y_i^{\mathrm{H0}} \right)^2}{\sigma_i^2} + \epsilon_{\mathrm{b}}^2 + \epsilon_{\mathrm{c}}^2\ . \tag{C.5}$$

The parameters ϵ_{b} and ϵ_{c} can be estimated by minimizing χ^2, e.g. using MINUIT. The contributions ϵ_{b}^2 and ϵ_{c}^2 are penalty terms taking into account that the systematic uncertainties are normal distributed, which implies that the most probable value is zero. Since the shift parameters ϵ_{b} and ϵ_{c} are extracted from the data, the number of degrees of freedom is given by the number of data points, since $n + m_\epsilon - m_\epsilon = n$.
If the data set is compared to another data set or a theory calculation with systematic uncertainties, we can modify eq. (C.5) to

$$\begin{aligned} \chi^2 \ = \ & \sum_{i=1}^{n} \frac{\left((y_{0,i} + \epsilon_{0,\mathrm{b}} \sigma_{0,\mathrm{b}} + y_{0,i} \epsilon_{0,\mathrm{c}} \sigma_{0,\mathrm{c}}) - (y_{1,i} + \epsilon_{1,\mathrm{b}} \sigma_{1,\mathrm{b}} + y_{1,i} \epsilon_{1,\mathrm{c}} \sigma_{1,\mathrm{c}}) \right)^2}{\sigma_i^2} \\ & + \ \epsilon_{0,\mathrm{b}}^2 + \epsilon_{1,\mathrm{b}}^2 + \epsilon_{0,\mathrm{c}}^2 + \epsilon_{1,\mathrm{c}}^2 \end{aligned} \tag{C.6}$$

with

$$\sigma_i = \sqrt{\sigma^2_{0,\mathrm{stat,i}} + \sigma^2_{0,\mathrm{a,i}} + \sigma^2_{1,\mathrm{stat,i}} + \sigma^2_{1,\mathrm{a,i}}} \,. \tag{C.7}$$

For a given χ^2 value with *dof* degrees of freedom, the p-value for a right sided test of the H0 hypothesis is given by

$$p(\chi^2, dof) = 1 - \mathrm{CDF}\big(\chi^2, dof\big) \;, \tag{C.8}$$

where

$$\mathrm{CDF}\big(\chi^2, dof\big) = \frac{1}{\Gamma\left(\frac{dof}{2}\right)}\, \gamma\left(\frac{dof}{2},\, \frac{\chi^2}{2}\right) \tag{C.9}$$

is the cumulated χ^2 distribution function. A p-value of 5% means that only 5% of repeated independent measurements with the same uncertainties will result into larger χ^2 values, if the H0 hypothesis is true. If the p-value is smaller than 5%, the H0 hypothesis is usually rejected at the **5% *significance level***. Thus, the p-value corresponds to the probability of falsely rejecting a true H0 hypothesis.

C.3 Rescaling of uncertainties

If the systematic uncertainties are dominantly multiplicative, for example if y_i is a yield determined from a raw yield $y_{0,i}$ using corrections of the form $y_i = y_{0,i} \times C_1 \times \cdots C_n$, where C_i are corrections for efficiencies, purities, acceptance or normalizations, the systematic errors propagate like

$$\sigma_i^2/y_i^2 = \sigma^2_{0,i}/y_{0,i} + \sigma^2_{C_1}/C_1^2 + \cdots \sigma^2_{C_n}/C_n^2 \;, \tag{C.10}$$

which implies that the total systematic uncertainty σ_i scales with y_i. Since the relative error is preserved under shifts, such errors have to be rescaled as

$$\tilde{\sigma}_i = \sigma_{\mathrm{i}} \frac{y_i + \epsilon_{\mathrm{b}}\sigma_{\mathrm{b}} + y_i\epsilon_{\mathrm{c}}\sigma_{\mathrm{c}}}{y_i} \;, \tag{C.11}$$

where $\tilde{\sigma}_i$ is the uncorrelated random error σ_i scaled by the multiplicative shift in y_i.

C.4 χ^2 tests within this work

C.4.1 Significance of the direct-photon excess

The uncertainty on the material budget $\sigma_{\mathrm{mat}} = 4.5\%$ is considered as correlated type C overall systematic uncertainty and separated from the total systematic uncertainty $\sigma_{\mathrm{sys,tot}}$. The remaining uncertainty,

$$\sigma^2_{\mathrm{sys,a},i} = \sqrt{\sigma^2_{\mathrm{sys,tot},i} - R^2\big(p^i_{\mathrm{T}}\big)\, \sigma^2_{\mathrm{mat}}} \;, \tag{C.12}$$

is considered as type A uncorrelated systematic uncertainty. The χ^2 value for the hypothesis H0: $R=1$ is then defined by

$$\chi^2 = \sum_{i=1}^{N_{\text{bins}}^{p_{\text{T}}}} \frac{\left(R\left(p_{\text{T}}^i\right) + \epsilon_{\text{c}} R\left(p_{\text{T}}^i\right) \sigma_{\text{mat}} - 1\right)^2}{\tilde{\sigma}_i^2} + \epsilon_{\text{c}}^2 \ , \tag{C.13}$$

with

$$\tilde{\sigma}_i = \sqrt{\sigma_{\text{stat},i}^2 + \sigma_{\text{sys,a},i}^2}\,(1+\epsilon_{\text{c}}) \ . \tag{C.14}$$

The uncorrelated uncertainty is rescaled for the shift in the direct-photon excess R, since such a shift due to a lower or higher conversion probability also implies that statistical and systematic uncertainties are overestimated or underestimated by the same fraction.

C.4.2 Consistency of inclusive and decay photon anisotropy

The systematic uncertainty on the inclusive photon anisotropy related to the event-plane resolution correction $\sigma_{\text{EP}}^{\gamma,inc}$ is treated as type B uncertainty, the remaining uncertainty $\sigma_{\text{sys}}^{\gamma,\text{inc}}$ as type A uncorrelated uncertainty. Due to the decay kinematics, the corresponding correlated part of the uncertainty of the decay photon anisotropy is complicated to trace and thus the total systematic uncertainty is considered as type A uncorrelated uncertainty. The χ^2 value for the hypothesis H0: $v_n^{\gamma,\text{inc}} = v_n^{\gamma,\text{bg}}$ is then given by

$$\chi^2 = \sum_{i=0}^{N_{\text{bins}}^{p_{\text{T}}}} \frac{\left(v_n^{\gamma,\text{inc}}\left(p_{\text{T}}^i\right) + \epsilon_{\text{b}}\sigma_{\text{EP},i}^{\gamma,inc} - v_n^{\gamma,\text{bg}}\left(p_{\text{T}}^i\right)\right)^2}{\tilde{\sigma}_i^2} \ , \tag{C.15}$$

with

$$\tilde{\sigma}_i^2 = \left(\frac{v_n^{\gamma,\text{inc}}\left(p_{\text{T}}^i\right) + \epsilon_{\text{b}}\sigma_{\text{EP},i}^{\gamma,inc}}{v_n^{\gamma,\text{inc}}\left(p_{\text{T}}^i\right)}\right)^2 \left(\sigma_{\text{stat},i}^{\gamma,\text{inc}\ 2} + \sigma_{\text{sys},i}^{\gamma,\text{inc}\ 2}\right) + \sigma_{\text{stat},i}^{\gamma,\text{bg}\ 2} + \sigma_{\text{sys},i}^{\gamma,\text{bg}\ 2} \ . \tag{C.16}$$

The uncorrelated uncertainty is rescaled for the shift in the inclusive-photon anisotropic flow related to the uncertainty on the event-plane resolution correction.

C.4.3 p_{T}-integrated direct-photon anisotropic flow

It is distinguished between correlated and uncorrelated systematic uncertainty. Correlated uncertainty arises from the uncertainty of the event-plane resolution correction and the uncertainty on the material budget, which is propagated from the direct-photon excess and inclusive photon spectrum to the p_{T}-integrated direct-photon anisotropy $\bar{v}_n^{\gamma,dir}$. We define the χ^2 value for the hypothesis H0: $\bar{v}_n^{\gamma,dir} = 0$ by

$$\chi^2 = \sum_{i=0}^{N_{\text{bins}}^{\text{cent}}} \frac{\left(\bar{v}_{n,i}^{\gamma,dir} + \epsilon_{\text{b}}\sigma_{sys,b}\right)^2}{\sigma_{\text{stat},i}^{\gamma,\text{dir}\ 2} + \sigma_{\text{sys,a},i}^{\gamma,\text{dir}\ 2}} + \epsilon_{\text{b}}^2 \tag{C.17}$$

where $\sigma_{\text{sys,b}}^{\gamma,\text{dir}}$ is the correlated and $\sigma_{\text{sys,a}}^{\gamma,\text{dir}}$ is the uncorrelated systematic uncertainty of the p_{T}-integrated direct-photon anisotropic flow in centrality bin i.

It should be noted that the random part of the uncertainties is not rescaled for the shift in $\bar{v}_{n,i}^{\gamma,dir}$, since the systematic uncertainties coming from different components are not multiplicative as for the direct-photon excess. In particular, the fact that $\bar{v}_{n,i}^{\gamma,dir}$ could be shifted to zero, if the correlated uncertainties are large enough, does not imply that the random part of the uncertainty vanishes.

In order to compared the direct-photon anisotropy with that of charged pions, we define the χ^2 value for the hypothesis H0: $\bar{v}_n^{\gamma,dir} = \bar{v}_n^{\pi^\pm}$ by

$$\chi^2 = \sum_{i=0}^{N_{\text{bins}}^{\text{cent}}} \frac{\left(\bar{v}_{n,i}^{\gamma,dir} + \epsilon_{\text{b}}\sigma_{sys,b} - \bar{v}_{n,i}^{\pi^\pm}\right)^2}{\sigma_{\text{stat},i}^{\gamma,\text{dir }2} + \sigma_{\text{sys,a},i}^{\gamma,\text{dir }2} + \sigma_{\text{stat},i}^{\pi^\pm\,2} + \sigma_{\text{sys},i}^{\pi^\pm\,2}} + \epsilon_{\text{b}}^2 \ . \tag{C.18}$$

The p_{T}-integrated charged pion flow is calculated as

$$\bar{v}_n^{\pi^\pm} = \frac{\sum_{i=0}^{N_{\text{bins}}^{p_{\text{T}}}} N_{\pi^\pm}\left(p_{\text{T}}^i\right) v_n^{\pi^\pm}\left(p_{\text{T}}^i\right)}{\sum_{i=0}^{N_{\text{bins}}^{p_{\text{T}}}} N_{\pi^\pm}\left(p_{\text{T}}^i\right)} \ , \tag{C.19}$$

where $N_{\pi^\pm}$ is estimated from $N_{\text{pion}}\left(p_{\text{T}}\right) = 1/\sigma_{\pi^\pm}^2$. The systematic uncertainty of the p_{T}-integrated pion flow $\sigma_{\text{sys}}^{\pi^\pm}$ is considered as uncorrelated type A uncertainty.

Similarly, we compare the direct-photon anisotropy with hydrodynamic calculations for thermal photons $\bar{v}_n^{\gamma,therm}$ and define the χ^2 value for the hypothesis H0: $\bar{v}_n^{\gamma,dir} = \bar{v}_n^{\gamma,therm}$ by

$$\chi^2 = \sum_{i=0}^{N_{\text{bins}}^{\text{cent}}} \frac{\left(\bar{v}_{n,i}^{\gamma,dir} + \epsilon_{\text{b}}\sigma_{sys,b} - \bar{v}_n^{\gamma,therm}\right)^2}{\sigma_{\text{stat},i}^{\gamma,\text{dir }2} + \sigma_{\text{sys,a},i}^{\gamma,\text{dir }2}} + \epsilon_{\text{b}}^2 \ . \tag{C.20}$$

C.4.4 p_{T}-differential direct-photon anisotropic flow

We define the χ^2 value for the hypothesis H0: $v_n^{\gamma,\text{dir}}(p_{\text{T}}) = 0$ as

$$\chi^2 = \sum_{i=0}^{N_{\text{bins}}^{p_{\text{T}}}} \frac{\left(v_n^{\gamma,\text{dir}}\left(p_{\text{T}}^i\right) + v_n^{\gamma,\text{dir}}\left(p_{\text{T}}^i\right)\epsilon_{\text{b}}\sigma_{\text{sys,b}}\right)^2}{\sigma_{\text{stat},i}^{\gamma,\text{dir }2} + \sigma_{\text{sys,a},i}^{\gamma,\text{dir }2}} + \epsilon_{\text{b}}^2 \ , \tag{C.21}$$

where $\sigma_{\text{sys,b}}$ is the correlated and $\sigma_{\text{sys,a}}$ is the uncorrelated uncertainty of the direct-photon anisotropic flow measurement.

Similarly, the χ^2 value for the hypothesis H0: $v_n^{\gamma,\text{dir}}(p_{\text{T}}) = v_n^{\gamma,\text{therm}}(p_{\text{T}})$ is given by

$$\chi^2 = \sum_{i=0}^{N_{\text{bins}}^{p_{\text{T}}}} \frac{\left(v_n^{\gamma,\text{dir}}\left(p_{\text{T}}^i\right) + v_n^{\gamma,\text{dir}}\left(p_{\text{T}}^i\right)\epsilon_{\text{b}}\sigma_{\text{sys,b}} - v_n^{\gamma,\text{therm}}\left(p_{\text{T}}^i\right)\right)^2}{\sigma_{\text{stat},i}^{\gamma,\text{dir }2} + \sigma_{\text{sys,a},i}^{\gamma,\text{dir }2}} + \epsilon_{\text{b}}^2 \ , \tag{C.22}$$

Bibliography

[1] D. Hume, *Treatise of Human Nature*. 1739.

[2] P. Anderson, "More Is Different: Broken symmetry and the nature of the hierarchical structure of science.," *Science*, vol. 177, pp. 393–396, 1972.

[3] G. Aad *et al.*, "Observation of a new particle in the search for the Standard Model Higgs boson with the ATLAS detector at the LHC," *Phys.Lett.*, vol. B716, pp. 1–29, 2012, arXiv:1207.7214.

[4] S. Chatrchyan *et al.*, "Observation of a new boson at a mass of 125 GeV with the CMS experiment at the LHC," *Phys.Lett.*, vol. B716, pp. 30–61, 2012, arXiv:1207.7235.

[5] P. Ade *et al.*, "Planck 2013 results. I. Overview of products and scientific results," 2013, arXiv:1303.5062.

[6] D. Fixsen, "The Temperature of the Cosmic Microwave Background," *Astrophys.J.*, vol. 707, pp. 916–920, 2009, arXiv:0911.1955.

[7] D. Spergel *et al.*, "First year Wilkinson Microwave Anisotropy Probe (WMAP) observations: Determination of cosmological parameters," *Astrophys.J.Suppl.*, vol. 148, pp. 175–194, 2003, arXiv:astro-ph/0302209.

[8] G. Hinshaw, D. Larson, E. Komatsu, D. Spergel, C. Bennett, *et al.*, "Nine-Year Wilkinson Microwave Anisotropy Probe (WMAP) Observations: Cosmological Parameter Results," 2012, arXiv:1212.5226.

[9] J. Beringer *et al.*, "Review of Particle Physics (RPP)," *Phys.Rev.*, vol. D86, p. 010001, 2012.

[10] C.-Y. Wong, *Introduction to High-Energy Heavy-Ion Collisions*. World Scientific Publishing Co Pte Ltd, 1994.

[11] S. Bethke, "World Summary of α_s (2012)," *Nuclear Physics B Proceedings Supplements*, vol. 234, pp. 229–234, 2012, arXiv:1210.0325.

[12] D. J. Gross and F. Wilczek, "Ultraviolet Behavior of Non-Abelian Gauge Theories," *Phys.Rev.Lett.*, vol. 30, pp. 1343–1346, Jun 1973.

[13] H. D. Politzer, "Reliable Perturbative Results for Strong Interactions?," *Phys.Rev.Lett.*, vol. 30, pp. 1346–1349, Jun 1973.

[14] A. Nakamura and S. Sakai, "Viscosities of hot gluon: A Lattice QCD study," *Nucl.Phys.*, vol. A774, pp. 775–778, 2006, arXiv:hep-lat/0510039.

[15] O. Philipsen, "Status of the QCD Phase Diagram from Lattice Calculations," *Acta Phys.Polon.Supp.*, vol. 5, pp. 825–835, 2012, arXiv:1111.5370.

[16] F. Karsch, "Lattice QCD at high temperature and density," *Lect.Notes Phys.*, vol. 583, pp. 209–249, 2002, arXiv:hep-lat/0106019.

[17] Z. Fodor and S. Katz, "Lattice QCD at finite T and mu and the critical point of QCD," *Nucl.Phys.Proc.Suppl.*, vol. 106, pp. 441–443, 2002, arXiv:hep-lat/0110102.

[18] R. Hagedorn, "Statistical thermodynamics of strong interactions at high-energies," *Nuovo Cim.Suppl.*, vol. 3, pp. 147–186, 1965.

[19] J. Cleymans and D. Worku, "The Hagedorn temperature Revisited," *Mod.Phys.Lett.*, vol. A26, pp. 1197–1209, 2011, arXiv:1103.1463.

[20] J. C. Collins and M. J. Perry, "Superdense Matter: Neutrons or Asymptotically Free Quarks?," *Phys.Rev.Lett.*, vol. 34, pp. 1353–1356, May 1975.

[21] N. Cabibbo and G. Parisi, "Exponential Hadronic Spectrum and Quark Liberation," *Phys.Lett.*, vol. B59, pp. 67–69, 1975.

[22] E. Shuryak, "Quark-gluon plasma and hadronic production of leptons, photons and psions," *Phys.Lett. B*, vol. 78, no. 1, pp. 150 – 153, 1978.

[23] M. G. Alford, A. Schmitt, K. Rajagopal, and T. Schäfer, "Color superconductivity in dense quark matter," *Rev.Mod.Phys.*, vol. 80, pp. 1455–1515, 2008, arXiv:0709.4635.

[24] S. Reddy, "Novel phases at high density and their roles in the structure and evolution of neutron stars," *Acta Phys.Polon.*, vol. B33, pp. 4101–4140, 2002, arXiv:nucl-th/0211045.

[25] I. Bearden *et al.*, "Nuclear stopping in Au+Au collisions at $\sqrt{s_{\mathrm{NN}}} = 200\,\mathrm{GeV}$," *Phys.Rev.Lett.*, vol. 93, p. 102301, 2004, arXiv:nucl-ex/0312023.

[26] A. Schmah, "Highlights of the Beam Energy Scan from STAR," *Eur.Phys.J.*, vol. 10, pp. 1238–1241, 2012, arXiv:1202.2389.

[27] B. Friman, C. Hohne, J. Knoll, S. Leupold, J. Randrup, *et al.*, "The CBM physics book: Compressed baryonic matter in laboratory experiments," *Lect.Notes Phys.*, vol. 814, pp. 1–980, 2011.

[28] F. Karsch, E. Laermann, and A. Peikert, "The Pressure in two flavor, (2+1)-flavor and three flavor QCD," *Phys.Lett.*, vol. B478, pp. 447–455, 2000, arXiv:hep-lat/0002003.

[29] P. Stankus, "Direct photon production in relativistic heavy-ion collisions," *Ann.Rev.Nucl.Part.Sci.*, vol. 55, pp. 517–554, 2005.

[30] P. Braun-Munzinger, K. Redlich, and J. Stachel, "Particle production in heavy-ion collisions," in *Quark Gluon Plasma 3* (R. C. Hwa and X.-N. Wang, eds.), World Scientific Publishing, 2003, arXiv:nucl-th/0304013.

[31] Y. Aoki, S. Borsanyi, S. Durr, Z. Fodor, S. D. Katz, *et al.*, "The QCD transition temperature: results with physical masses in the continuum limit II.," *JHEP*, vol. 0906, p. 088, 2009, arXiv:0903.4155.

[32] M. Cheng *et al.*, "The Transition temperature in QCD," *Phys.Rev.*, vol. D74, p. 054507, 2006, arXiv:hep-lat/0608013.

[33] A. Bazavov, T. Bhattacharya, M. Cheng, C. DeTar, H. Ding, *et al.*, "The chiral and deconfinement aspects of the QCD transition," *Phys.Rev.*, vol. D85, p. 054503, 2012, arXiv:1111.1710.

[34] J. K. Nayak and B. Sinha, "Electromagnetic signals from Au-Au collisions at RHIC energy, $\sqrt{s_{\mathrm{NN}}} = 200\,\mathrm{GeV}$ and Pb-Pb collisions at LHC energy, $\sqrt{s_{\mathrm{NN}}} = 2.76\,\mathrm{TeV}$," *Phys.Lett.*, vol. B719, pp. 110–115, 2013, arXiv:1210.3993.

[35] S. Mitra, P. Mohanty, S. Ghosh, S. Sarkar, and J.-e. Alam, "Characterizing quark gluon plasma by thermal photons and lepton pairs," 2013, arXiv:1303.0675.

[36] U. W. Heinz, "Early collective expansion: Relativistic hydrodynamics and the transport properties of QCD matter," in *Relativistic Heavy Ion Physics* (R. Stock, ed.), Landolt-Boernstein New Series, 2010, arXiv:0901.4355.

[37] UrQMD web page `http://urqmd.org`, 2013.

[38] R. Stock, "Relativistic Nucleus-Nucleus Collisions and the QCD Matter Phase Diagram," 2008, arXiv:0807.1610.

[39] S. Bass, M. Belkacem, M. Bleicher, M. Brandstetter, L. Bravina, *et al.*, "Microscopic models for ultrarelativistic heavy ion collisions," *Prog.Part.Nucl.Phys.*, vol. 41, pp. 255–369, 1998, arXiv:nucl-th/9803035.

[40] M. Bleicher, E. Zabrodin, C. Spieles, S. Bass, C. Ernst, *et al.*, "Relativistic hadron hadron collisions in the ultrarelativistic quantum molecular dynamics model," *J.Phys.*, vol. G25, pp. 1859–1896, 1999, arXiv:hep-ph/9909407.

[41] B. Povh, *Particles and Nuclei*. Springer Verlag, 2006. ISBN 0-387-59439-6.

[42] P. Braun-Munzinger and J. Stachel, "Charmonium from Statistical Hadronization of Heavy Quarks: A Probe for Deconfinement in the Quark-Gluon Plasma," in *Relativistic Heavy Ion Physics* (R. Stock, ed.), Landoldt review volume, 2009, arXiv:0901.2500.

[43] K. Geiger, "Thermalization in ultrarelativistic nuclear collisions. 1. Parton kinetics and quark gluon plasma formation," *Phys.Rev.*, vol. D46, pp. 4965–4985, 1992.

[44] J. Blaizot and A. H. Mueller, "The Early Stage of Ultrarelativistic Heavy Ion Collisions," *Nucl.Phys.*, vol. B289, p. 847, 1987.

[45] W. Broniowski, M. Chojnacki, W. Florkowski, and A. Kisiel, "Uniform Description of Soft Observables in Heavy-Ion Collisions at $\sqrt{s_{\mathrm{NN}}} = 200\,\mathrm{GeV}$," *Phys.Rev.Lett.*, vol. 101, p. 022301, 2008, arXiv:0801.4361.

[46] F. Retiere and M. A. Lisa, "Observable implications of geometrical and dynamical aspects of freeze out in heavy ion collisions," *Phys.Rev.*, vol. C70, p. 044907, 2004, arXiv:nucl-th/0312024.

[47] S. Chapman and J. R. Nix, "Realistic expanding source model for invariant one particle multiplicity distributions and two particle correlations in relativistic heavy ion collisions," *Phys.Rev.*, vol. C54, pp. 866–881, 1996, arXiv:nucl-th/9603007.

[48] C. Alt *et al.*, "Bose-Einstein correlations of pi-pi- pairs in central Pb+Pb collisions at A-20, A-30, A-40, A-80, and A-158 GeV," *Phys.Rev.*, vol. C77, p. 064908, 2008, arXiv:0709.4507.

[49] J. Adams *et al.*, "Pion interferometry in Au+Au collisions at $\sqrt{s_{\rm NN}} = 200\,\text{GeV}$," *Phys.Rev.*, vol. C71, p. 044906, 2005, arXiv:nucl-ex/0411036.

[50] K. Aamodt *et al.*, "Two-pion Bose-Einstein correlations in central Pb-Pb collisions at $\sqrt{s_{\rm NN}} = 2.76\,\text{TeV}$," *Phys.Lett.*, vol. B696, pp. 328–337, 2011, arXiv:1012.4035.

[51] B. Abelev *et al.*, "Pion, Kaon, and Proton Production in Central Pb-Pb Collisions at $\sqrt{s_{\rm NN}} = 2.76\,\text{TeV}$," *Phys.Rev.Lett.*, vol. 109, p. 252301, 2012, arXiv:1208.1974.

[52] R. Snellings, "Elliptic Flow: A Brief Review," *New J.Phys.*, vol. 13, p. 055008, 2011, arXiv:1102.3010.

[53] M. L. Miller, K. Reygers, S. J. Sanders, and P. Steinberg, "Glauber modeling in high energy nuclear collisions," *Ann.Rev.Nucl.Part.Sci.*, vol. 57, pp. 205–243, 2007, arXiv:nucl-ex/0701025.

[54] S. Chatrchyan *et al.*, "Measurement of the elliptic anisotropy of charged particles produced in Pb-Pb collisions at $\sqrt{s_{\rm NN}} = 2.76\,\text{TeV}$," *Phys.Rev.*, vol. C87, p. 014902, 2013, arXiv:1204.1409.

[55] A. Stasto, K. J. Golec-Biernat, and J. Kwiecinski, "Geometric scaling for the total gamma* p cross-section in the low x region," *Phys.Rev.Lett.*, vol. 86, pp. 596–599, 2001, arXiv:hep-ph/0007192.

[56] R. Venugopalan, "From many body wee parton dynamics to perfect fluid: a standard model for heavy-ion collisions," *PoS*, vol. ICHEP2010, p. 567, 2010, arXiv:1012.4699.

[57] C. Gale, S. Jeon, and B. Schenke, "Hydrodynamic Modeling of heavy-ion Collisions," *Int. J. of Mod. Phys. A, Vol. 28,*, vol. 1340011, 2013, arXiv:1301.5893.

[58] B. Schenke, P. Tribedy, and R. Venugopalan, "Fluctuating Glasma initial conditions and flow in heavy-ion collisions," *Phys.Rev.Lett.*, vol. 108, p. 252301, 2012, arXiv:1202.6646.

[59] F. Karsch, E. Laermann, and A. Peikert, "Quark mass and flavor dependence of the QCD phase transition," *Nucl.Phys.*, vol. B605, pp. 579–599, 2001, arXiv:hep-lat/0012023.

[60] J. Bjorken, "Highly Relativistic Nucleus-Nucleus Collisions: The Central Rapidity Region," *Phys.Rev.*, vol. D27, pp. 140–151, 1983.

[61] K. Eskola, K. Kajantie, P. Ruuskanen, and K. Tuominen, "Scaling of transverse energies and multiplicities with atomic number and energy in ultrarelativistic nuclear collisions," *Nucl.Phys.*, vol. B570, pp. 379–389, 2000, arXiv:hep-ph/9909456.

[62] A. Toia, "Bulk Properties of Pb-Pb collisions at $\sqrt{s_{\rm NN}} = 2.76\,\text{TeV}$ measured by ALICE," *J.Phys.*, vol. G38, p. 124007, 2011, arXiv:1107.1973.

[63] S. Adler *et al.*, "Systematic studies of the centrality and $\sqrt{s_{\rm NN}} = 2.76\,\text{TeV}$ dependence of the $\mathrm{d}E_{\rm T}/\mathrm{d}\eta$ and $\mathrm{d}N_{\rm ch}/\mathrm{d}\eta$ in heavy-ion collisions at mid-rapidity," *Phys.Rev.*, vol. C71, p. 034908, 2005, arXiv:nucl-ex/0409015.

[64] S. Manly *et al.*, "System size, energy and pseudorapidity dependence of directed and elliptic flow at RHIC," *Nucl.Phys.*, vol. A774, pp. 523–526, 2006, arXiv:nucl-ex/0510031.

[65] M. Miller and R. Snellings, "Eccentricity fluctuations and its possible effect on elliptic flow measurements," 2003, arXiv:nucl-ex/0312008.

[66] B. Alver *et al.*, "System size, energy, pseudorapidity, and centrality dependence of elliptic flow," *Phys.Rev.Lett.*, vol. 98, p. 242302, 2007, arXiv:nucl-ex/0610037.

[67] B. Alver, B. Back, M. Baker, M. Ballintijn, D. Barton, *et al.*, "Importance of correlations and fluctuations on the initial source eccentricity in high-energy nucleus-nucleus collisions," *Phys.Rev.*, vol. C77, p. 014906, 2008, arXiv:0711.3724.

[68] F. G. Gardim, F. Grassi, M. Luzum, and J.-Y. Ollitrault, "Mapping the hydrodynamic response to the initial geometry in heavy-ion collisions," *Phys.Rev.*, vol. C85, p. 024908, 2012, arXiv:1111.6538.

[69] B. Alver and G. Roland, "Collision geometry fluctuations and triangular flow in heavy-ion collisions," *Phys.Rev.*, vol. C81, p. 054905, 2010, arXiv:1003.0194.

[70] P. F. Kolb and U. W. Heinz, "Hydrodynamic description of ultrarelativistic heavy-ion collisions," in *Quark Gluon Plasma*, pp. 634–714, Hwa, R.C., 2003, arXiv:nucl-th/0305084.

[71] J.-Y. Ollitrault, "Impact parameter dependence of transverse momentum in nucleus-nucleus collisions," *Phys.Lett.*, vol. B273, pp. 32–36, 1991.

[72] T. Hirano, U. W. Heinz, D. Kharzeev, R. Lacey, and Y. Nara, "Hadronic dissipative effects on elliptic flow in ultrarelativistic heavy-ion collisions," *Phys.Lett.*, vol. B636, pp. 299–304, 2006, arXiv:nucl-th/0511046.

[73] C. Nonaka and S. A. Bass, "Space-time evolution of bulk QCD matter," *Phys.Rev.*, vol. C75, p. 014902, 2007, arXiv:nucl-th/0607018.

[74] K. Aamodt *et al.*, "Centrality dependence of the charged-particle multiplicity density at mid-rapidity in Pb-Pb collisions at $\sqrt{s_{\rm NN}} = 2.76\,\text{TeV}$," *Phys.Rev.Lett.*, vol. 106, p. 032301, 2011, arXiv:1012.1657.

[75] B. Schenke, P. Tribedy, and R. Venugopalan, "Event-by-event gluon multiplicity, energy density, and eccentricities in ultrarelativistic heavy-ion collisions," *Phys.Rev.*, vol. C86, p. 034908, 2012, arXiv:1206.6805.

[76] J. E. Elias, W. Busza, C. Halliwell, D. Luckey, P. Swartz, L. Votta, and C. Young, "Experimental study of multiparticle production in hadron-nucleus interactions at high energy," *Phys. Rev. D*, vol. 22, pp. 13–35, Jul 1980.

[77] B. Abelev *et al.*, "Centrality determination of Pb-Pb collisions at $\sqrt{s_{\rm NN}} = 2.76\,\text{TeV}$ with ALICE," 2013, arXiv:1301.4361.

[78] S. Eremin and S. Voloshin, "Nucleon participants or quark participants?," *Phys.Rev.*, vol. C67, p. 064905, 2003, arXiv:nucl-th/0302071.

[79] R. Hanbury Brown and R. Twiss, "A New type of interferometer for use in radio astronomy," *Phil.Mag.*, vol. 45, pp. 663–682, 1954.

[80] R. Hanbury Brown and R. Twiss, "A Test of a new type of stellar interferometer on Sirius," *Nature*, vol. 178, pp. 1046–1048, 1956.

[81] G. Goldhaber, S. Goldhaber, W.-Y. Lee, and A. Pais, "Influence of Bose-Einstein statistics on the anti-proton proton annihilation process," *Phys.Rev.*, vol. 120, pp. 300–312, 1960.

[82] U. A. Wiedemann and U. W. Heinz, "Particle interferometry for relativistic heavy-ion collisions," *Phys.Rept.*, vol. 319, pp. 145–230, 1999, arXiv:nucl-th/9901094.

[83] S. Akkelin and Y. Sinyukov, "The HBT interferometry of expanding sources," *Phys.Lett.*, vol. B356, pp. 525–530, 1995.

[84] G. Bertsch, M. Gong, and M. Tohyama, "Pion Interferometry in Ultrarelativistic heavy-ion collisions," *Phys.Rev.*, vol. C37, pp. 1896–1900, 1988.

[85] S. Pratt, "Pion Interferometry of Quark-Gluon Plasma," *Phys.Rev.*, vol. D33, pp. 1314–1327, 1986.

[86] S. Pratt, "Pion Interferometry for Exploding Sources," *Phys.Rev.Lett.*, vol. 53, pp. 1219–1221, 1984.

[87] M. A. Lisa, S. Pratt, R. Soltz, and U. Wiedemann, "Femtoscopy in relativistic heavy-ion collisions," *Ann.Rev.Nucl.Part.Sci.*, vol. 55, pp. 357–402, 2005, arXiv:nucl-ex/0505014.

[88] J.-Y. Ollitrault, "Relativistic hydrodynamics for heavy-ion collisions," *Eur.Phys.J.*, vol. 29, pp. 275–302, 2008, arXiv:0708.2433.

[89] P. Huovinen and P. Ruuskanen, "Hydrodynamic Models for heavy-ion collisions," *Ann.Rev.Nucl.Part.Sci.*, vol. 56, pp. 163–206, 2006, arXiv:nucl-th/0605008.

[90] F. Cooper and G. Frye, "Comment on the Single Particle Distribution in the Hydrodynamic and Statistical Thermodynamic Models of Multiparticle Production," *Phys.Rev.*, vol. D10, p. 186, 1974.

[91] E. Schnedermann, J. Sollfrank, and U. W. Heinz, "Thermal phenomenology of hadrons from 200-A/GeV S+S collisions," *Phys.Rev.*, vol. C48, pp. 2462–2475, 1993, arXiv:nucl-th/9307020.

[92] M. Abramowitz and I. Stegun, *Handbook of Mathematical Functions.* New York: Dover, fifth ed., 1964.

[93] B. H. Alver, C. Gombeaud, M. Luzum, and J.-Y. Ollitrault, "Triangular flow in hydrodynamics and transport theory," *Phys.Rev.*, vol. C82, p. 034913, 2010, arXiv:1007.5469.

[94] P. M. Dinh, N. Borghini, and J.-Y. Ollitrault, "Effects of HBT correlations on flow measurements," *Phys.Lett.*, vol. B477, pp. 51–58, 2000, arXiv:nucl-th/9912013.

[95] P. Danielewicz, "Effects of compression and collective expansion on particle emission from central heavy ion reactions," *Phys.Rev.*, vol. C51, pp. 716–750, 1995, arXiv:nucl-th/9408018.

[96] B. Abelev *et al.*, "Systematic Measurements of Identified Particle Spectra in pp, d+Au and Au+Au Collisions from STAR," *Phys.Rev.*, vol. C79, p. 034909, 2009, arXiv:0808.2041.

[97] R. Akers *et al.*, "Measurement of the production rates of charged hadrons in e+ e- annihilation at the Z0," *Z.Phys.*, vol. C63, pp. 181–196, 1994.

[98] A. Andronic, P. Braun-Munzinger, K. Redlich, and J. Stachel, "The statistical model in Pb-Pb collisions at the LHC," 2012, arXiv:1210.7724.

[99] R. Hagedorn, "Multiplicities, p_{T} distributions and the expected hadron $\rightarrow$ quark-gluon phase transition," *Riv.Nuovo Cim.*, vol. 6N10, pp. 1–50, 1984.

[100] R. Blankenbecler and S. J. Brodsky, "Unified Description of Inclusive and Exclusive Reactions at All Momentum Transfers," *Phys.Rev.*, vol. D10, p. 2973, 1974.

[101] P. Khandai, P. Shukla, and V. Singh, "Meson spectra and m_{T} scaling in pp, d+Au, and Au+Au collisions at $\sqrt{s} = 200\,\mathrm{GeV}$," *Phys.Rev.*, vol. C84, p. 054904, 2011, arXiv:1110.3929.

[102] A. Adare *et al.*, "Detailed measurement of the e^+e^- pair continuum in pp and Au+Au collisions at $\sqrt{s} = 200\,\mathrm{GeV}$ and implications for direct photon production," *Phys.Rev.*, vol. C81, p. 034911, 2010, arXiv:0912.0244.

[103] M. Bourquin and J.-M. Gaillard, "A Simple Phenomenological Description of Hadron Production," *Nucl.Phys.*, vol. B114, p. 334, 1976.

[104] J. Bartke *et al.*, "Simplicity of Transverse Spectra Analysis in Terms of Transverse Energy," *Nucl.Phys.*, vol. B120, p. 14, 1977.

[105] K. Guettler *et al.*, "Inclusive Production of Low Momentum Charged Pions, Kaons, and Protons at $x = 0$ at the CERN Intersecting Storage Rings," *Nucl.Phys.*, vol. B116, p. 77, 1976.

[106] R. Albrecht *et al.*, "Production of eta mesons in $\sqrt{s} = 200\,\mathrm{GeV}$ S-S and S-Au reactions," *Phys.Lett.*, vol. B361, pp. 14–20, 1995, arXiv:hep-ex/9507009.

[107] B. Andersson, G. Gustafson, G. Ingelman, and T. Sjostrand, "Parton Fragmentation and String Dynamics," *Phys.Rept.*, vol. 97, pp. 31–145, 1983.

[108] B. Andersson, "The Lund model," *Camb.Monogr.Part.Phys.Nucl.Phys.Cosmol.*, vol. 7, pp. 1–471, 1997.

[109] S. Adler *et al.*, "High transverse momentum η meson production in pp, d+Au and Au+Au collisions at $\sqrt{s} = 200\,\mathrm{GeV}$," *Phys.Rev.*, vol. C75, p. 024909, 2007, arXiv:nucl-ex/0611006.

[110] B. Abelev *et al.*, "Transverse Momentum Distribution and Nuclear Modification Factor of Charged Particles in p-Pb Collisions at $\sqrt{s_{\mathrm{NN}}} = 5.02\,\mathrm{TeV}$," 2012, arXiv:1210.4520.

[111] K. Reygers, "Private Communication." Physikalisches Institut, University of Heidelberg, 2013.

[112] B. Abelev *et al.*, "Measurement of the inclusive differential jet cross section in pp collisions at $\sqrt{s} = 7\,\mathrm{TeV}$," 2013, arXiv:1301.3475.

[113] M. Cacciari, G. P. Salam, and G. Soyez, "The Anti-k_{T} jet clustering algorithm," *JHEP*, vol. 0804, p. 063, 2008, arXiv:0802.1189.

[114] B. Abelev *et al.*, "Identified baryon and meson distributions at large transverse momenta from Au+Au collisions at $\sqrt{s_{\mathrm{NN}}} = 200\,\mathrm{GeV}$," *Phys.Rev.Lett.*, vol. 97, p. 152301, 2006, arXiv:nucl-ex/0606003.

[115] B. Abelev *et al.*, "Suppression of high transverse momentum D mesons in central Pb-Pb collisions at $\sqrt{s_{\mathrm{NN}}} = 2.76\,\mathrm{TeV}$," *JHEP*, vol. 1209, p. 112, 2012, arXiv:1203.2160.

[116] T. Renk, "Constraining the Physics of Jet Quenching," *Phys.Rev.*, vol. C85, p. 044903, 2012, arXiv:1112.2503.

[117] Y. L. Dokshitzer and D. Kharzeev, "Heavy quark colorimetry of QCD matter," *Phys.Lett.*, vol. B519, pp. 199–206, 2001, arXiv:hep-ph/0106202.

[118] A. Adare *et al.*, "Energy Loss and Flow of Heavy Quarks in Au+Au Collisions at $\sqrt{s} = 200\,\mathrm{GeV}$," *Phys.Rev.Lett.*, vol. 98, p. 172301, 2007, arXiv:nucl-ex/0611018.

[119] B. Abelev *et al.*, "Erratum: Transverse momentum and centrality dependence of high-p_{T} non-photonic electron suppression in Au+Au collisions at $\sqrt{s_{\mathrm{NN}}} = 200\,\mathrm{GeV}$," *Phys.Rev.Lett.*, vol. 98, p. 192301, 2007, arXiv:nucl-ex/0607012.

[120] D. Stocco, "Measurement of heavy-flavour decay muon production at forward rapidity in pp and Pb-Pb collisions at $\sqrt{s} = 7\,\mathrm{TeV}$ with the ALICE experiment," 2012, arXiv:1208.6171.

[121] S. Chatrchyan *et al.*, "Suppression of non-prompt J/ψ, prompt J/ψ, and $Y(1S)$ in Pb-Pb collisions at $\sqrt{s_{\mathrm{NN}}} = 2.76\,\mathrm{TeV}$," *JHEP*, vol. 1205, p. 063, 2012, arXiv:1201.5069.

[122] J. Otwinowski, "High-p_{T} processes measured with ALICE at the LHC," 2013, arXiv:1301.5285.

[123] A. Adare *et al.*, "Azimuthal anisotropy of neutral pion production in Au+Au collisions at $\sqrt{s_{\mathrm{NN}}} = 200\,\mathrm{GeV}$: Path-length dependence of jet quenching and the role of initial geometry," *Phys.Rev.Lett.*, vol. 105, p. 142301, 2010, arXiv:1006.3740.

[124] B. Betz, M. Gyulassy, and G. Torrieri, "Sensitivity of Azimuthal Jet Tomography to Early Time Energy-Loss at RHIC and LHC," *J.Phys.*, vol. G38, p. 124153, 2011, arXiv:1106.4564.

[125] J. Jia and R. Wei, "Dissecting the role of initial collision geometry for jet quenching observables in relativistic heavy-ion collisions," *Phys.Rev.*, vol. C82, p. 024902, 2010, arXiv:1005.0645.

[126] W. Horowitz and M. Gyulassy, "The Surprising Transparency of the sQGP at LHC," *Nucl.Phys.*, vol. A872, pp. 265–285, 2011, arXiv:1104.4958.

[127] N. Armesto, "Nuclear shadowing," *J.Phys.*, vol. G32, pp. 367–394, 2006, arXiv:hep-ph/0604108.

[128] Y. Mehtar-Tani and G. Wolschin, "Baryon stopping and saturation physics in relativistic collisions," *Phys.Rev.*, vol. C80, p. 054905, 2009, arXiv:0907.5444.

[129] J. Cronin, H. J. Frisch, M. Shochet, J. Boymond, R. Mermod, *et al.*, "Production of Hadrons with Large Transverse Momentum at 200-GeV, 300-GeV, and 400-GeV," *Phys.Rev.*, vol. D11, p. 3105, 1975.

[130] A. Accardi, "Cronin effect in proton nucleus collisions: A Survey of theoretical models," in *Yellow report on Hard Probes in Heavy Ion Collisions at the LHC*, CERN, 2002, arXiv:hep-ph/0212148.

[131] S. Adler *et al.*, "Absence of suppression in particle production at large transverse momentum in $\sqrt{s_{\rm NN}} = 200\,\text{GeV}$ d+Au collisions," *Phys.Rev.Lett.*, vol. 91, p. 072303, 2003, arXiv:nucl-ex/0306021.

[132] J. Adams *et al.*, "Evidence from d+Au measurements for final state suppression of high $p_{\rm T}$ hadrons in Au+Au collisions at RHIC," *Phys.Rev.Lett.*, vol. 91, p. 072304, 2003, arXiv:nucl-ex/0306024.

[133] W. Reisdorf and H. Ritter, "Collective flow in heavy-ion collisions," *Ann.Rev.Nucl.Part.Sci.*, vol. 47, pp. 663–709, 1997.

[134] S. A. Voloshin, A. M. Poskanzer, and R. Snellings, "Collective phenomena in non-central nuclear collisions," 2008, arXiv:0809.2949.

[135] A. Bilandzic, N. van der Kolk, J.-Y. Ollitrault, and R. Snellings, "Event-plane flow analysis without non-flow effects," *Phys.Rev.*, vol. C83, p. 014909, 2011, arXiv:0801.3915.

[136] A. Bilandzic, R. Snellings, and S. Voloshin, "Flow analysis with cumulants: Direct calculations," *Phys.Rev.*, vol. C83, p. 044913, 2011, arXiv:1010.0233.

[137] J.-Y. Ollitrault, A. M. Poskanzer, and S. A. Voloshin, "Effect of flow fluctuations and nonflow on elliptic flow methods," *Phys.Rev.*, vol. C80, p. 014904, 2009, arXiv:0904.2315.

[138] J. Adams *et al.*, "Azimuthal anisotropy at RHIC: The First and fourth harmonics," *Phys.Rev.Lett.*, vol. 92, p. 062301, 2004, arXiv:nucl-ex/0310029.

[139] I. Selyuzhenkov, "Charged particle directed flow in Pb-Pb collisions at $\sqrt{s_{\rm NN}} = 2.76\,\text{TeV}$ measured with ALICE at the LHC," *J.Phys.*, vol. G38, p. 124167, 2011, arXiv:1106.5425.

[140] A. Adare *et al.*, "Measurements of Higher-Order Flow Harmonics in Au+Au Collisions at $\sqrt{s_{\rm NN}} = 200\,\text{GeV}$," *Phys.Rev.Lett.*, vol. 107, p. 252301, 2011, arXiv:1105.3928.

[141] K. Aamodt *et al.*, "Higher harmonic anisotropic flow measurements of charged particles in Pb-Pb collisions at $\sqrt{s_{\rm NN}} = 2.76\,\text{TeV}$," *Phys.Rev.Lett.*, vol. 107, p. 032301, 2011, arXiv:1105.3865.

[142] H.-J. Drescher and Y. Nara, "Eccentricity fluctuations from the color glass condensate at RHIC and LHC," *Phys.Rev.*, vol. C76, p. 041903, 2007, arXiv:0707.0249.

[143] G. Aad *et al.*, "Measurement of the distributions of event-by-event flow harmonics in Pb-Pb collisions at $\sqrt{s_{\rm NN}} = 2.76\,\text{TeV}$," 2012, arXiv:1305.2942.

[144] J. Dunlop, M. Lisa, and P. Sorensen, "Constituent quark scaling violation due to baryon number transport," *Phys.Rev.*, vol. C84, p. 044914, 2011, arXiv:1107.3078.

[145] M. Krzewicki, "Elliptic and triangular flow of identified particles at ALICE," *J.Phys.*, vol. G38, p. 124047, 2011, arXiv:1107.0080.

[146] B. Schenke, S. Jeon, and C. Gale, "Elliptic and triangular flow in event-by-event (3+1)D viscous hydrodynamics," *Phys.Rev.Lett.*, vol. 106, p. 042301, 2011, arXiv:1009.3244.

[147] Z. Qiu and U. W. Heinz, "Event-by-event shape and flow fluctuations of relativistic heavy-ion collision fireballs," *Phys.Rev.*, vol. C84, p. 024911, 2011, arXiv:1104.0650.

[148] J. Jia and C. Zhang, "Quark number scaling of v(2) in transverse kinetic energy and it's implications for coalescence models," *Phys.Rev.*, vol. C75, p. 031901, 2007, arXiv:hep-ph/0608187.

[149] A. Adare *et al.*, "Scaling properties of azimuthal anisotropy in Au+Au and Cu-Cu collisions at $\sqrt{s_{\rm NN}} = 200\,\text{GeV}$," *Phys.Rev.Lett.*, vol. 98, p. 162301, 2007, arXiv:nucl-ex/0608033.

[150] Y. Gu, "PHENIX Measurements of Higher-order Flow Harmonics for Identified Charged Hadrons in Au+Au collisions at $\sqrt{s_{\rm NN}} = 39$ - $200\,\text{GeV}$," 2012, arXiv:1211.4009.

[151] S. Shi, "Event anisotropy v_2 in Au+Au collisions at $\sqrt{s_{\rm NN}} = 7.7$ - $62.4\,\text{GeV}$ with STAR," *Nucl.Phys.A904-905*, vol. 2013, pp. 895c–898c, 2013, arXiv:1210.4607.

[152] F. Noferini, "Anisotropic flow of identified particles in Pb-Pb collisions at $\sqrt{s_{\rm NN}} = 2.76\,\text{TeV}$ measured with ALICE at the LHC," 2012, arXiv:1212.1292.

[153] Y. Burnier, D. E. Kharzeev, J. Liao, and H.-U. Yee, "Chiral magnetic wave at finite baryon density and the electric quadrupole moment of quark-gluon plasma in heavy-ion collisions," *Phys.Rev.Lett.*, vol. 107, p. 052303, 2011, arXiv:1103.1307.

[154] A. Schmah, "Event anisotropy v_2 of identified hadrons and light nuclei in Au+Au collisions at $\sqrt{s_{\rm NN}} = 7.7, 11.5$ and $39\,\text{GeV}$ with STAR," *J.Phys.*, vol. G38, p. 124049, 2011.

[155] K. Werner, "Lambda-to-Kaon Ratio Enhancement in heavy-ion collisions at several TeV," *Phys.Rev.Lett.*, vol. 109, p. 102301, 2012, arXiv:1204.1394.

[156] K. Werner, I. Karpenko, M. Bleicher, T. Pierog, and S. Porteboeuf-Houssais, "Jets, Bulk Matter, and their Interaction in heavy-ion collisions at several TeV," *Phys.Rev.*, vol. C85, p. 064907, 2012, arXiv:1203.5704.

[157] B. Schenke, S. Jeon, and C. Gale, "Anisotropic flow in $\sqrt{s_{\rm NN}} = 2.76\,\text{TeV}$ Pb+Pb collisions at the LHC," *Phys.Lett.*, vol. B702, pp. 59–63, 2011, arXiv:1102.0575.

[158] U. W. Heinz and R. Snellings, "Collective flow and viscosity in relativistic heavy-ion collisions," 2013, arXiv:1301.2826.

[159] C. Gombeaud and J.-Y. Ollitrault, "Elliptic flow in transport theory and hydrodynamics," *Phys.Rev.*, vol. C77, p. 054904, 2008, arXiv:nucl-th/0702075.

[160] T. Schäfer and D. Teaney, "Nearly Perfect Fluidity: From Cold Atomic Gases to Hot Quark Gluon Plasmas," *Rept.Prog.Phys.*, vol. 72, p. 126001, 2009, arXiv:0904.3107.

[161] L. P. Csernai, J. Kapusta, and L. D. McLerran, "On the Strongly-Interacting Low-Viscosity Matter Created in Relativistic Nuclear Collisions," *Phys.Rev.Lett.*, vol. 97, p. 152303, 2006, arXiv:nucl-th/0604032.

[162] H. B. Meyer, "A Calculation of the shear viscosity in SU(3) gluodynamics," *Phys.Rev.*, vol. D76, p. 101701, 2007, arXiv:0704.1801.

[163] P. Kovtun, D. Son, and A. Starinets, "Viscosity in strongly interacting quantum field theories from black hole physics," *Phys.Rev.Lett.*, vol. 94, p. 111601, 2005, arXiv:hep-th/0405231.

[164] M. Luzum and J.-Y. Ollitrault, "Extracting the shear viscosity of the quark-gluon plasma from flow in ultra-central heavy-ion collisions," *Nucl.Phys.A*, 2012, arXiv:1210.6010.

[165] G. Aad *et al.*, "Measurement of the azimuthal anisotropy for charged particle production in $\sqrt{s_{\mathrm{NN}}} = 2.76\,\mathrm{TeV}$ lead-lead collisions with the ATLAS detector," *Phys.Rev.*, vol. C86, p. 014907, 2012, arXiv:1203.3087.

[166] U. Heinz, C. Shen, and H.-C. Song, "The viscosity of quark-gluon plasma at RHIC and the LHC," *AIP Conf.Proc.*, vol. 1441, pp. 766–770, 2012, arXiv:1108.5323.

[167] J. Adams *et al.*, "Azimuthal anisotropy and correlations at large transverse momenta in pp and Au+Au collisions at $\sqrt{s} = 200\,\mathrm{GeV}$," *Phys.Rev.Lett.*, vol. 93, p. 252301, 2004, arXiv:nucl-ex/0407007.

[168] M. H. Thoma, "Applications of high temperature field theory to heavy-ion collisions," 1995, arXiv:hep-ph/9503400.

[169] M. Thoma, "Damping rate of a hard photon in a relativistic plasma," *Phys.Rev.*, vol. D51, pp. 862–865, 1995, arXiv:hep-ph/9405309.

[170] A. Collaboration, "Upgrade of the Inner Tracking System: Conceptual Design Report," tech. rep., CERN, 2012. CERN-LHCC-2012-013.

[171] F. Arleo, P. Aurenche, F. W. Bopp, I. Dadic, G. David, *et al.*, "Hard probes in heavy-ion collisions at the LHC: Photon physics in heavy-ion collisions at the LHC," 2004, arXiv:hep-ph/0311131.

[172] S. Turbide, R. Rapp, and C. Gale, "Hadronic production of thermal photons," *Phys.Rev.*, vol. C69, p. 014903, 2004, arXiv:hep-ph/0308085.

[173] F.-M. Liu and K. Werner, "A Systematic study on direct photon production from central heavy-ion collisions," *J.Phys.*, vol. G36, p. 035101, 2009, arXiv:0712.3619.

[174] S. Turbide, C. Gale, E. Frodermann, and U. Heinz, "Electromagnetic radiation from nuclear collisions at RHIC energies," *Phys.Rev.*, vol. C77, p. 024909, 2008, arXiv:0712.0732.

[175] C. Gale, "Photon Production in Hot and Dense Strongly Interacting Matter," *Landolt Börnstein*, vol. 23, p. 445, 2010, arXiv:0904.2184.

[176] R. Chatterjee, E. S. Frodermann, U. W. Heinz, and D. K. Srivastava, "Elliptic flow of thermal photons in relativistic nuclear collisions," *Phys.Rev.Lett.*, vol. 96, p. 202302, 2006, arXiv:nucl-th/0511079.

[177] T. Pietrycki and A. Szczurek, "Direct photon production in pp and p-$\bar{p}$ collisions at high energies," *Int.J.Mod.Phys.*, vol. A22, pp. 541–545, 2007, arXiv:hep-ph/0608190.

[178] N. M. Kroll and W. Wada, "Internal pair production associated with the emission of high-energy gamma rays," *Phys.Rev.*, vol. 98, pp. 1355–1359, 1955.

[179] L. Bhattacharya and P. Roy, "Jet-photons from an anisotropic *Quark-Gluon-Plasma*," *J.Phys.*, vol. G37, p. 105010, 2010, arXiv:1001.1054.

[180] S. Afanasiev *et al.*, "Measurement of Direct Photons in Au+Au Collisions at $\sqrt{s_{\mathrm{NN}}} = 200\,\mathrm{GeV}$," *Phys.Rev.Lett.*, vol. 109, p. 152302, 2012, arXiv:1205.5759.

[181] F. Arleo, "Hard pion and prompt photon at RHIC, from single to double inclusive production," *JHEP*, vol. 0609, p. 015, 2006, arXiv:hep-ph/0601075.

[182] F. Arleo, K. J. Eskola, H. Paukkunen, and C. A. Salgado, "Inclusive prompt photon production in nuclear collisions at RHIC and LHC," *JHEP*, vol. 1104, p. 055, 2011, arXiv:1103.1471.

[183] I. Vitev and B.-W. Zhang, "A Systematic study of direct photon production in heavy ion collisions," *Phys.Lett.*, vol. B669, pp. 337–344, 2008, arXiv:0804.3805.

[184] V. Baier and V. Katkov, "Variation of radiation length due to LPM effect," *Phys.Lett.*, vol. A327, pp. 202–209, 2004, arXiv:hep-ph/0403132.

[185] G. Aad *et al.*, "Measurement of Z boson Production in Pb-Pb Collisions a$\sqrt{s_{\mathrm{NN}}} = 2.76\,\mathrm{TeV}$ with the ATLAS Detector," *Phys.Rev.Lett.*, vol. 110, p. 022301, 2013, arXiv:1210.6486.

[186] S. Chatrchyan *et al.*, "Study of W boson production in Pb-Pb and pp collisions at $\sqrt{s_{\mathrm{NN}}} = 2.76\,\mathrm{TeV}$," *Phys.Lett.*, vol. B715, pp. 66–87, 2012, arXiv:1205.6334.

[187] A. Adare *et al.*, "High p_{T} direct photon and π^0 triggered azimuthal jet correlations and measurement of k_{T} for isolated direct photons in pp collisions at $\sqrt{s} = 200\,\mathrm{GeV}$," *Phys.Rev.*, vol. D82, p. 072001, 2010, arXiv:1006.1347.

[188] N. Arbor, "Isolated photon-hadron correlations in proton-proton collisions at $\sqrt{s} = 7\,\mathrm{TeV}$ with the ALICE experiment," 2012, arXiv:1211.6620.

[189] S. Chatrchyan *et al.*, "Measurement of isolated photon production in pp and Pb-Pb collisions at $\sqrt{s_{\mathrm{NN}}} = 2.76\,\mathrm{TeV}$," *Phys.Lett.*, vol. B710, pp. 256–277, 2012, arXiv:1201.3093.

[190] "Measurement of high-p_{T} isolated prompt photons in lead-lead collisions at $\sqrt{s_{\mathrm{NN}}} = 2.76\,\mathrm{TeV}$ with the ATLAS detector at the LHC," Tech. Rep. ATLAS-CONF-2012-051, CERN, Geneva, May 2012.

[191] E. Feinberg, "Direct Production of Photons and Dileptons in Thermodynamical Models of Multiple Hadron Production," *Nuovo Cim.*, vol. A34, p. 391, 1976.

[192] L. Gribov, E. Levin, and M. Ryskin, "Semihard Processes in QCD," *Phys.Rept.*, vol. 100, pp. 1–150, 1983.

[193] T. Biro, E. van Doorn, B. Muller, M. Thoma, and X. Wang, "Parton equilibration in relativistic heavy ion collisions," *Phys.Rev.*, vol. C48, pp. 1275–1284, 1993, arXiv:nucl-th/9303004.

[194] G. Brown and M. Rho, "Scaling effective Lagrangians in a dense medium," *Phys.Rev.Lett.*, vol. 66, pp. 2720–2723, 1991.

[195] G.-Q. Li, C. Ko, and G. Brown, "Enhancement of low mass dileptons in heavy-ion collisions," *Phys.Rev.Lett.*, vol. 75, pp. 4007–4010, 1995, arXiv:nucl-th/9504025.

[196] F. Geurts, "Dielectron Measurements in STAR," *EPJ Web Conf.*, vol. 36, p. 00010, 2012, arXiv:1208.3437.

[197] F. Arleo, D. G. d'Enterria, and D. Peressounko, "Direct photon spectra in Pb-Pb at $\sqrt{s_{\mathrm{NN}}} = 5.5\,\mathrm{TeV}$: hydrodynamics + pQCD predictions," *J.Phys.G*, 2007, arXiv:0707.2357.

[198] S. Adler *et al.*, "Centrality dependence of direct photon production in $\sqrt{s_{\mathrm{NN}}} = 200\,\mathrm{GeV}$ Au+Au collisions," *Phys.Rev.Lett.*, vol. 94, p. 232301, 2005, arXiv:nucl-ex/0503003.

[199] S. Adler *et al.*, "Measurement of direct photon production in pp collisions at $\sqrt{s} = 200\,\mathrm{GeV}$," *Phys.Rev.Lett.*, vol. 98, p. 012002, 2007, arXiv:hep-ex/0609031.

[200] A. Adare *et al.*, "Enhanced production of direct photons in Au+Au collisions at $\sqrt{s_{\mathrm{NN}}} = 200\,\mathrm{GeV}$ and implications for the initial temperature," *Phys.Rev.Lett.*, vol. 104, p. 132301, 2010, arXiv:0804.4168.

[201] M. Wilde, "Measurement of Direct Photons in pp and Pb-Pb Collisions with ALICE," *Nucl.Phys.A*, 2012, arXiv:1210.5958.

[202] G.-Y. Qin, J. Ruppert, C. Gale, S. Jeon, and G. D. Moore, "Jet energy loss, photon production, and photon-hadron correlations at RHIC," *Phys.Rev.*, vol. C80, p. 054909, 2009, arXiv:0906.3280.

[203] H. Holopainen, S. Rasanen, and K. J. Eskola, "Elliptic flow of thermal photons in heavy-ion collisions at Relativistic Heavy Ion Collider and Large Hadron Collider," *Phys.Rev.*, vol. C84, p. 064903, 2011, arXiv:1104.5371.

[204] A. Adare *et al.*, "Observation of direct-photon collective flow in $\sqrt{s_{\mathrm{NN}}} = 200\,\mathrm{GeV}$ Au+Au collisions," *Phys.Rev.Lett.*, vol. 109, p. 122302, 2012, arXiv:1105.4126.

[205] G. Basar, D. Kharzeev, D. Kharzeev, and V. Skokov, "Conformal anomaly as a source of soft photons in heavy ion collisions," *Phys.Rev.Lett.*, vol. 109, p. 202303, 2012, arXiv:1206.1334.

[206] G. Alessandro *et al.*, "ALICE: Physics performance report, volume II," *J.Phys.*, vol. G32, pp. 1295–2040, 2006.

[207] M. Aggarwal *et al.*, "Interferometry of direct photons in central $Pb^{208} + Pb^{208}$ collisions at 158-A-GeV," *Phys.Rev.Lett.*, vol. 93, p. 022301, 2004, arXiv:nucl-ex/0310022.

[208] D. Das, G. Lin, S. Chattopadhyay, A. Chikanian, E. Finch, *et al.*, "Preliminary results on direct photon-photon HBT measurements in $\sqrt{s_{\mathrm{NN}}} = 62.4\,\mathrm{GeV}$ and 200 GeV Au+Au collisions at RHIC," *Nukleonika*, vol. 51, pp. 55–58, 2006, arXiv:nucl-ex/0511055.

[209] D. Peressounko, "Hanbury Brown-Twiss interferometry of direct photons in heavy-ion collisions," *Phys.Rev.*, vol. C67, p. 014905, 2003.

[210] M. Aggarwal *et al.*, "Observation of direct photons in central 158-A-GeV $Pb^{208} + Pb^{208}$ collisions," *Phys.Rev.Lett.*, vol. 85, pp. 3595–3599, 2000, arXiv:nucl-ex/0006008.

[211] L. Evans and P. Bryant, "LHC Machine," *JINST*, vol. 3, p. S08001, 2008.

[212] CERN, "LHC, the guide." CERN Communication Group, February 2009.

[213] CERN Press Office, "CERN releases analysis of LHC incident," October 2008.

[214] CERN Press Office, "Incident in LHC sector 3-4," September 2008.

[215] CERN Press Office, "Final LHC magnet goes underground," April 2009.

[216] CERN Press Office, "First three-year LHC running period reaches a conclusion," February 2013.

[217] "CERN Document Server." `http://cdsweb.cern.ch`.

[218] R. Geller, *Electron Cyclotron Resonance Ion Sources and ECR Plasmas*. Inst of Physics Pub, 1996.

[219] G. Anelli *et al.*, "The TOTEM experiment at the CERN Large Hadron Collider," *JINST*, vol. 3, p. S08007, 2008.

[220] O. Adriani *et al.*, "The LHCf detector at the CERN Large Hadron Collider," *JINST*, vol. 3, p. S08006, 2008.

[221] G. Aad *et al.*, "The ATLAS Experiment at the CERN Large Hadron Collider," *JINST*, vol. 3, p. S08003, 2008.

[222] S. Chatrchyan *et al.*, "The CMS experiment at the CERN LHC," *JINST*, vol. 3, p. S08004, 2008.

[223] S. Lowette and o. b. o. t. ATLAS, "Supersymmetry Searches with ATLAS and CMS," 2012, arXiv:1205.4053.

[224] V. A. Mitsou, "Highlights from SUSY searches with ATLAS," 2012, arXiv:1210.1679.

[225] J. Alves, A. Augusto *et al.*, "The LHCb Detector at the LHC," *JINST*, vol. 3, p. S08005, 2008.

[226] R. Aaij *et al.*, "First observation of CP violation in the decays of B_s^0 mesons," *Phys.Rev.Lett.*, vol. 110, p. 221601, 2013, arXiv:1304.6173.

[227] K. Aamodt *et al.*, "The ALICE experiment at the CERN LHC," *JINST*, vol. 3, p. S08002, 2008.

[228] O. Buning, P. Collier, P. Lebrun, S. Myers, R. Ostojic, *et al.*, "LHC Design Report. 2. The LHC infrastructure and general services," 2004.

[229] "LHC Programme Coordination web page." `http://lpc.web.cern.ch/lpc/`, 2013.

[230] B. Abelev *et al.*, "Measurement of the Cross Section for Electromagnetic Dissociation with Neutron Emission in Pb-Pb Collisions at $\sqrt{s_{\rm NN}} = 2.76$ TeV," *Phys.Rev.Lett.*, vol. 109, p. 252302, 2012, arXiv:1203.2436.

[231] A. Collaboration, "ALICE Physics Performance Report, Volume I," *J.Phys.*, vol. G, no. 30, p. 1517, 2004.

[232] G. Dellacasa *et al.*, "ALICE technical design report of the inner tracking system (ITS)," 1999.

[233] G. Dellacasa *et al.*, *ALICE time projection chamber: Technical Design Report*. Technical Design Report ALICE, Geneva: CERN, 2000.

[234] A. Kalweit, "Particle Identification in the ALICE Experiment," *J.Phys.*, vol. G38, p. 124073, 2011, arXiv:1107.1514.

[235] J. Alme, Y. Andres, H. Appelshauser, S. Bablok, N. Bialas, *et al.*, "The ALICE TPC, a large 3-dimensional tracking device with fast readout for ultra-high multiplicity events," *Nucl.Instrum.Meth.*, vol. A622, pp. 316–367, 2010, arXiv:1001.1950.

[236] P. Cortese, *ALICE transition-radiation detector: Technical Design Report*. Technical Design Report ALICE, Geneva: CERN, 2001.

[237] *ALICE Time-Of-Flight system (TOF): Technical Design Report*. Technical Design Report ALICE, Geneva: CERN, 2000.

[238] *Forward Detectors: FMD, T0, V0 Technical Design Report*. No. 2004-09-15 in Technical Design Report ALICE, Geneva: CERN, 2004.

[239] B. Abelev *et al.*, "Performance of the ALICE Experiment at CERN LHC," *in preparation*, 2013.

[240] K. Aamodt *et al.*, "Alignment of the ALICE Inner Tracking System with cosmic-ray tracks," *JINST*, vol. 5, p. P03003, 2010, arXiv:1001.0502.

[241] A. Salvucci, "Measurement of muon momentum resolution of the ATLAS detector," vol. 28, p. 12039, June 2012, arXiv:1201.4704.

[242] T. Matsui and H. Satz, "J/ψ suppression by quark-gluon plasma formation," *Phys.Lett.*, vol. B, pp. 416–422, October 1986.

[243] P. Petreczky, C. Miao, and A. Mocsy, "Quarkonium spectral functions with complex potential," *Nucl.Phys.*, vol. A855, pp. 125–132, 2011, arXiv:1012.4433.

[244] J. Stachel and P. Braun-Munzinger, "The quest for the quark-gluon plasma," *Nature*, vol. Vol, pp. 302–309, July 2007.

[245] N. Collaboration, "A new measurement of J/ψ suppression in Pb-Pb collisions at 158 GeV per nucleon," *Eur.Phys.Lett.J.*, vol. C, no. 39, pp. 335–345, 2004.

[246] A. Adare *et al.*, "J/ψ Production vs Centrality, Transverse Momentum, and Rapidity in Au+Au Collisions at $\sqrt{s_{\mathrm{NN}}} = 200\,\mathrm{GeV}$," *Phys.Rev.Lett.*, vol. 98, p. 232301, 2007, arXiv:nucl-ex/0611020.

[247] P. Braun-Munzinger and J. Stachel, "On charm production near the phase boundary," *Nucl.Phys.*, vol. A690, pp. 119–126, 2001, arXiv:nucl-th/0012064.

[248] P. Braun-Munzinger, "Quarkonium production in ultra-relativistic nuclear collisions: suppression vs. enhancement," *J.Phys.*, vol. 34, pp. 471–478, 2007.

[249] J. Stachel and P. Braun-Munzinger, "Evidence for charmonium generation at the phase boundary in ultra-relativistic nuclear collisions," *Phys.Lett.*, vol. B, no. 652, pp. 259–261, 2007.

[250] L. Massacrier, "J/ψ elliptic flow measurement in Pb-Pb collisions at $\sqrt{s_{\mathrm{NN}}} = 2.76\,\mathrm{TeV}$ TeV at forward rapidity with the ALICE experiment," 2012, arXiv:1208.5401.

[251] J. Klein, "Triggering with the ALICE TRD," *Nucl.Instrum.Meth.*, vol. A706, pp. 23–28, 2013, arXiv:1112.5110.

[252] P. Fusco, C. Favuzzi, N. Giglietto, M. Mazziotta, A. Rainò, and P. Spinelli, "TRDs for the Third Millenium Proceedings of the 4th Workshop on Advanced Transition Radiation Detectors for Accelerators and Space Applications Bari, Italy September 14-16, 2011," *Nucl.Instrum.Meth.*, vol. A, pp. 1–94, April 2013.

[253] A. Andronic and J. Wessels, "Transition Radiation Detectors," *Nucl.Instrum.Meth.*, vol. A666, pp. 130–147, 2012, arXiv:1111.4188.

[254] "ATLAS inner detector: Technical design report. Vol. 1," 1997.

[255] E. Abat *et al.*, "The ATLAS TRT barrel detector," *JINST*, vol. 3, p. P02014, 2008.

[256] T. Siedenburg, "The AMS TRD: A gas detector designed for operation in space," *Nucl.Phys.Proc.Suppl.*, vol. 150, pp. 30–33, 2006.

[257] P. von Doetinchem, S. Fopp, W. Karpinski, T. Kirn, K. Luebelsmeyer, *et al.*, "Performance of the AMS-02 Transition Radiation Detector," *Nucl.Instrum.Meth.*, vol. A558, pp. 526–535, 2006, arXiv:astro-ph/0608641.

[258] M. Fasel, *Single-electron analysis and opencharm cross section in proton-proton collisions at* $\sqrt{s} = 7\,\mathrm{TeV}$. PhD thesis, University of Darmstadt, 2012.

[259] I. F. V.L. Ginzburg, "Radiation of a Uniformly Moving Electron due to its Transition from one Medium to Another," *Zh. Eksp. Theor. Phys.*, vol. 16, pp. 15 – 28, 1946.

[260] J. J. P. Goldsmith, "Optical Transition Radiation from Protons Entering Metal Surfaces," *Phil. Mag.*, vol. 4, pp. 836 – 844, 1959.

[261] G. Garibian, L. Gevorgian, and C. Yang, "The calculation of X-ray transition radiation generated in regular- and irregular-layered media," *Nucl.Instrum.Meth.*, vol. 125, no. 1, pp. 133 – 137, 1975.

[262] M. L. Cherry, D. Muller, and T. A. Prince, "The Efficient Identification of Relativistic Particles by Transition Radiation," *Nucl.Instrum.Meth.*, vol. 115, p. 141, 1974.

[263] X.-G. Lu, "Energy Loss Signals in the ALICE TRD," *Nucl.Instrum.Meth.*, vol. A706, pp. 16–19, 2013, arXiv:1204.1218.

[264] A. Andronic *et al.*, "Transition radiation spectra of electrons from 1-GeV/c to 10-GeV/c in regular and irregular radiators," *Nucl.Instrum.Meth.*, vol. A558, pp. 516–525, 2006, arXiv:physics/0511229.

[265] C. Grupen, *Particle Detectors*. Cambridge University Press, 1996. ISBN 0-521-55216-8.

[266] A. Andronic *et al.*, "Energy loss of pions and electrons of 1-GeV/c to 6-GeV/c in drift chambers operated with Xe, CO(2)(15Nucl.Instrum.Meth., vol. A519, pp. 508–517, 2004, arXiv:physics/0310122.

[267] R. Appuhn, K. Heinloth, E. Lange, R. Oedingen, and A. Schlösser, "Transition radiation detectors for electron identification beyond 1 GeV/c," *Nucl.Instrum.Meth.*, vol. A, no. 263, pp. 309 – 318, 1988.

[268] ALICE Collaboration web page. `http://aliceinfo.cern.ch`.

[269] C. Adler *et al.*, "Position reconstruction in drift chambers operated with Xe, CO2 (15%)," *Nucl.Instrum.Meth.*, vol. A, no. 540, pp. 140–157, 2005.

[270] A. Andronic, "Electron identification performance with ALICE TRD prototypes," *Nucl.Instrum.Meth.*, vol. A, no. 522, pp. 40–44, 2004.

[271] O. Busch, "Position Resolution with prototypes of ALICE Transition Radiation Detector," diploma thesis, University of Darmstadt, 2002.

[272] D. Lohner, "Tracking Resolution of the ALICE Transition Radiation Detector," diploma thesis, University of Heidelberg, 2010.

[273] M. Ivanov, I. Belikov, P. Hristov, and K. Safarik, "Track reconstruction in high density environment," *Nucl.Instrum.Meth.*, vol. A566, pp. 70–74, 2006.

[274] M. Fasel, "Hadronenproduktion in Proton-Proton Kollisionen," master thesis, University of Darmstadt, 2008.

[275] R. Bailhache, *Calibration of the ALICE Transition Radiation Detector and a study of Z0 and heavy quark production in pp collisions at the LHC*. PhD thesis, University of Darmstadt, 2009.

[276] J. Stiller, "Gain Calibration of the ALICE TRD using the Decay of 83mKr and Alignment of the ALICE TRD," diploma thesis, University of Heidelberg, 2011.

[277] S. Huber, *Ausrichtung des ALICE Übergangsstrahlungsdetektors sowie Zweiteilchenintensitäetsinterferometrie identischer Pionen aus pp Kollisionen bei LHC Energien von 900 GeV und 7 TeV*. Phd thesis, TU Darmstadt, 2011.

[278] L. Landau, "On the energy loss of fast particles by ionization," *J.Phys.(USSR)*, vol. 8, pp. 201–205, 1944.

[279] T. Ludlam, E. Platner, V. Polychronakos, M. Deutschmann, W. Struczinski, *et al.*, "Particle Identification by Electron Cluster Detection of Transition Radiation Photons," *Nucl.Instrum.Meth.*, vol. 180, p. 413, 1981.

[280] E. O'Brien, M. Bennett, V. Chernyatin, C. Chi, A. Chikanian, *et al.*, "A Transition radiation detector which features accurate tracking and dE / dx particle identification," *"IEEE Trans.Nucl.Sci.*, vol. 40, pp. 153–157, 1993.

[281] G. Dellacasa and P. Braun-Munzinger, "ALICE: a transition radiation detector for electron identification within the ALICE central detector - an addendum to the Technical Proposal," Tech. Rep. CERN-LHCC-99-013. LHCC-P-3-Add-2, CERN, Geneva, May 1999.

[282] P. M. Lee, *Bayesian Statistics: An Introduction*. 1118332571, Wiley, 4 ed., 2012.

[283] R. Bailhache and C. Lippmann, "New test beam results with prototypes of the ALICE TRD," *Nucl.Instrum.Meth.*, vol. A563, pp. 310–313, 2006.

[284] J. L. Bentley, "Multidimensional Binary Search Trees Used for Associative Searching," *Communications of the ACM*, vol. 18, pp. 509–517, 9 1975.

[285] A. Wilk, "Analysis of the electron / pion separation capability with real size ALICE TRD prototypes using a neural network algorithm," *Nucl.Instrum.Meth.*, vol. A563, pp. 314–316, 2006.

[286] A. Wilk, *Particle Identification Using Artificial Neural Networks with the ALICE Transition Radiation Detector*. Phd thesis, University of Münster, 2010.

[287] L. Feldkamp, *in preparation*. PhD thesis, University of Münster, 2014.

[288] G. Cowan, *Statistical Data Analysis*. Oxfort University Press, 1998.

[289] M. Paterno, "Calculating efficiencies and their uncertainties," 2004.

[290] G. Cowan, "Error analysis for efficiency." RHUL Physics, July 2008.

[291] R. web page. `http://root.cern.ch`.

[292] ALICE Collaboration, "Figure Repository." `http://aliceinfo.cern.ch/Figure/`.

[293] D. Baumeier, "V0 Decays: Documentation of the C++ Program AliESDv0KineCuts.cxx," bachelor thesis, University of Münster, 2011.

[294] S. Gorbunov and I. Kisel, "Reconstruction of decay particles based on the Kalman filter." CBMSOFT-note-2007-003, GSI, Darmstadt, 2007.

[295] A. Bercuci, "Private Communication." Gesellschaft für Schwerionenforschung mbH, 2010.

[296] X.-G. Lu, *in preparation.* PhD thesis, University of Heidelberg, 2013.

[297] Y. Pachmayer, "Physics with the ALICE Transition Radiation Detector," *Nucl.Instrum.Meth.*, vol. A706, pp. 6–11, 2013, arXiv:1112.2098.

[298] M. Luzum and J.-Y. Ollitrault, "The event-plane method is obsolete," 2012, arXiv:1209.2323.

[299] E. Levin and L. Frankfurt, "The Quark hypothesis and relations between cross-sections at high-energies," *JETP Lett.*, vol. 2, pp. 65–70, 1965.

[300] H. Lipkin and F. Scheck, "Quark model for forward scattering amplitudes," *Phys.Rev.Lett.*, vol. 16, pp. 71–75, 1966.

[301] J. Kokkedee and L. Van Hove, "Quark model and high-energy scattering," *Nuovo Cim.*, vol. 42, pp. 711–716, 1966.

[302] S. A. Voloshin, A. M. Poskanzer, A. Tang, and G. Wang, "Elliptic flow in the Gaussian model of eccentricity fluctuations," *Phys.Lett.*, vol. B659, pp. 537–541, 2008, arXiv:0708.0800.

[303] W. Broniowski, P. Bozek, and M. Rybczynski, "Fluctuating initial conditions in heavy-ion collisions from the Glauber approach," *Phys.Rev.*, vol. C76, p. 054905, 2007, arXiv:0706.4266.

[304] N. Borghini, P. M. Dinh, and J.-Y. Ollitrault, "A New method for measuring azimuthal distributions in nucleus-nucleus collisions," *Phys.Rev.*, vol. C63, p. 054906, 2001, arXiv:nucl-th/0007063.

[305] N. Borghini, P. M. Dinh, and J.-Y. Ollitrault, "Flow analysis from multiparticle azimuthal correlations," *Phys.Rev.*, vol. C64, p. 054901, 2001, arXiv:nucl-th/0105040.

[306] N. Borghini, P. M. Dinh, and J.-Y. Ollitrault, "Flow analysis from cumulants: A Practical guide," 2001, arXiv:nucl-ex/0110016.

[307] S. Voloshin and Y. Zhang, "Flow study in relativistic nuclear collisions by Fourier expansion of Azimuthal particle distributions," *Z.Phys.*, vol. C70, pp. 665–672, 1996, arXiv:hep-ph/9407282.

[308] A. M. Poskanzer and S. Voloshin, "Methods for analyzing anisotropic flow in relativistic nuclear collisions," *Phys.Rev.*, vol. C58, pp. 1671–1678, 1998, arXiv:nucl-ex/9805001.

[309] M. Luzum, "Flow fluctuations and long-range correlations: elliptic flow and beyond," *J.Phys.*, vol. G38, p. 124026, 2011, arXiv:1107.0592.

[310] K. Xiao, F. Liu, and F. Wang, "Event-plane decorrelation over pseudo-rapidity and its effect on azimuthal anisotropy measurement in relativistic heavy-ion collisions," *Phys.Rev.*, vol. C87, p. 011901, 2013, arXiv:1208.1195.

[311] R. S. Bhalerao and J.-Y. Ollitrault, "Eccentricity fluctuations and elliptic flow at RHIC," *Phys.Lett.*, vol. B641, pp. 260–264, 2006, arXiv:nucl-th/0607009.

[312] J.-Y. Ollitrault, "On the measurement of azimuthal anisotropies in nucleus-nucleus collisions," 1997, arXiv:nucl-ex/9711003.

[313] H. Masui and A. Schmah, "Event plane resolution correction for azimuthal anisotropy in wide centrality bins," 2012, arXiv:1212.3650.

[314] C. Adler *et al.*, "Elliptic flow from two and four particle correlations in Au+Au collisions at $\sqrt{s_{\mathrm{NN}}} = 130\,\mathrm{GeV}$," *Phys.Rev.*, vol. C66, p. 034904, 2002, arXiv:nucl-ex/0206001.

[315] C. Shen, U. W. Heinz, J.-F. Paquet, and C. Gale, "Thermal photons as a quark-gluon plasma thermometer revisited," 2013, arXiv:1308.2440.

[316] J. Adams *et al.*, "Photon and neutral pion production in Au+Au collisions at $\sqrt{s_{\mathrm{NN}}} = 130\,\mathrm{GeV}$," *Phys.Rev.*, vol. C70, p. 044902, 2004, arXiv:nucl-ex/0401008.

[317] D. Acosta *et al.*, "Direct photon cross section with conversions at CDF," *Phys.Rev.*, vol. D70, p. 074008, 2004, arXiv:hep-ex/0404022.

[318] S. Adler *et al.*, "Mid-rapidity direct-photon production in $p^{+}p$ collisions at $\sqrt{s} = 200\,\mathrm{GeV}$," *Phys.Rev.*, vol. D71, p. 071102, 2005, arXiv:hep-ex/0502006.

[319] P. Dirac, "The quantum theory of the electron," *Proc. R. Soc. (London)*, vol. A, no. 117, pp. 610–624, 1928.

[320] P. Dirac, "The quantum theory of the electron. Part II," *Proc. R. Soc. (London)*, vol. A, no. 118, pp. 351–361, 1928.

[321] C. Anderson, "Energies of cosmic-ray particles," *Phys. Rev.*, vol. 43, no. 491–494, 1933.

[322] J. Hubbell, "Electron–positron pair production by photons: A historical overview," *Radiation Physics and Chemistry*, vol. 75, no. 6, pp. 614 – 623, 2006.

[323] CERN Teachers Web `teachers.web.cern.ch`, 2013.

[324] D. Green, *The Physics of Particle Detectors*. Cambridge Monographs on Particle Physics, Nuclear Physics and Cosmology, Cambridge University Press, 2005.

[325] A. Borsellino, "Momentum Transfer and Angle of Divergence of Pairs Produced by Photons," *Phys.Rev.*, vol. 89, pp. 1023–1025, 1953.

[326] H. Olsen, "Opening Angles of Electron-Positron Pairs," *Phys.Rev.*, vol. 131, pp. 406–415, 1963.

[327] K. Hintermann, "Angle of Divergence of Pairs Produced by Photons," *Phys. Rev.*, vol. 93, pp. 898–899, Feb 1954.

[328] M. El-Nadi, A. Hussein, Z. Abou-Moussa, E. Shaat, H. Salama, *et al.*, "External electron pair production in high-energy collisions," *Nuovo Cim.*, vol. A109, pp. 1517–1528, 1996.

[329] F. Bock, "ALICE Capabilities for Studying Photon Physics with the Conversion Method at LHC Energies." Bachelor's thesis.

[330] K. Koch, "π^0 and η measurement with photon conversions in ALICE in proton-proton collisions at $\sqrt{s} = 7\,\text{TeV}$," *Nucl.Phys.*, vol. A855, pp. 281–284, 2011, arXiv:1103.2217.

[331] B. Abelev *et al.*, "Neutral pion and η meson production in proton-proton collisions at $\sqrt{s} = 0.9\,\text{TeV}$ and $\sqrt{s} = 7\,\text{TeV}$," *Phys.Lett.*, vol. B717, pp. 162–172, 2012, arXiv:1205.5724.

[332] F. Bock, "Neutral Pion and Eta Meson Production in pp and Pb-Pb Collisions at the LHC with the ALICE Detector," Master's thesis, University of Heidelberg, 2012.

[333] J. Podolanski and R. Armenteros, "Analysis of v-events," *Phil. Mag.*, vol. 7, 1954.

[334] T. Dahms, "Measurement of photons via conversion pairs with the PHENIX experiment at RHIC," Master's thesis, Stony Brook University, May 2005.

[335] X.-N. Wang and M. Gyulassy, "HIJING: A Monte Carlo model for multiple jet production in p p, p A and A A collisions," *Phys.Rev.*, vol. D44, pp. 3501–3516, 1991.

[336] M. Wilde, *Measurement of Direct Photons in pp Collisions at the LHC with ALICE at* $\sqrt{s} = 7\,\text{TeV}$ *and Pb-Pb Collisions at* $\sqrt{s_{\text{NN}}} = 2.76\,\text{TeV}$ *via Conversions.* Phd thesis in preparation, University of Münster, 2013.

[337] H. Lewis, J. Oppenheimer, and S. Wouthuysen, "The Multiple Production of Mesons," *Phys.Rev.*, vol. 73, pp. 127–140, 1948.

[338] C. Lattes, H. Muirhead, G. Occhialini, and C. Powell, "Processes involving charged Mesons," *Nature*, vol. 159, pp. 694–697, 1947.

[339] A. Carlson, J. Hooper, and D. King, "Nuclear Transmutations Produced by Cosmic-Ray Particles of Great Energy. - Part V. The Neutral Meson," *Phil. Mag.*, vol. 41, p. 701, 1950.

[340] R. Bjorklund, W. Crandall, B. Moyer, and H. York, "High Energy Photons from Proton-Nucleon Collisions," *Phys.Rev.*, vol. 77, pp. 213–218, 1950.

[341] W. K. Panofsky, L. Aamodt, J. Hadley, and R. Phillips, "The Gamma-Ray Spectrum resulting from Capture of negative Pi-Mesons in Hydrogen," *Phys.Rev.*, vol. 80, p. 94, 1950.

[342] W. K. Panofsky, R. L. Aamodt, and J. Hadley, "The Gamma-Ray Spectrum Resulting from Capture of Negative pi-Mesons in Hydrogen and Deuterium," *Phys.Rev.*, vol. 81, pp. 565–574, 1951.

[343] J. Steinberger, W. Panofsky, and J. Steller, "Evidence for the Production of Neutral Mesons by Photons," *Phys.Rev.*, vol. 78, pp. 802–805, 1950.

[344] A. Bernstein and B. R. Holstein, "Neutral Pion Lifetime Measurements and the QCD Chiral Anomaly," *Reviews of Modern Physics, 85,*, vol. 49, 2013, arXiv:1112.4809.

[345] R. Miskimen, "Neutral pion decay," *Ann.Rev.Nucl.Part.Sci.*, vol. 61, pp. 1–21, 2011.

[346] R. Rusanov, "Measurement of neutral-pion suppression in Pb-Pb collisions at $\sqrt{s_{\text{NN}}} = 2.76\,\text{TeV}$ with ALICE at the CERN LHC," Master's thesis, University of Heidelberg, 2011.

[347] A. Adare *et al.*, "Suppression pattern of neutral pions at high transverse momentum in Au+Au collisions at $\sqrt{s_{\rm NN}} = 200\,\text{GeV}$ and constraints on medium transport coefficients," *Phys.Rev.Lett.*, vol. 101, p. 232301, 2008, arXiv:0801.4020.

[348] A. Adare *et al.*, "Evolution of π^0 suppression in Au+Au collisions from $\sqrt{s_{\rm NN}} =$ 39 to 200 GeV," *Phys.Rev.Lett.*, vol. 109, p. 152301, 2012, arXiv:1204.1526.

[349] M. Aggarwal *et al.*, "Suppression of High-p(T) Neutral Pions in Central Pb+Pb Collisions at $\sqrt{s_{\rm NN}} = 17.3\,\text{GeV}$," *Phys.Rev.Lett.*, vol. 100, p. 242301, 2008, arXiv:0708.2630.

[350] K. Aamodt *et al.*, "Charged-particle multiplicity measurement in proton-proton collisions at $\sqrt{s} = 7\,\text{TeV}$ with ALICE at LHC," *Eur.Phys.J.*, vol. C68, pp. 345–354, 2010, arXiv:1004.3514.

[351] C. Alt *et al.*, "Directed and elliptic flow of charged pions and protons in Pb + Pb collisions at 40-A-GeV and 158-A-GeV," *Phys.Rev.*, vol. C68, p. 034903, 2003, arXiv:nucl-ex/0303001.

[352] J. Barrette *et al.*, "Proton and pion production relative to the reaction plane in Au+Au collisions at AGS energies," *Phys.Rev.*, vol. C56, pp. 3254–3264, 1997, arXiv:nucl-ex/9707002.

[353] I. Selyuzhenkov and S. Voloshin, "Effects of non-uniform acceptance in anisotropic flow measurement," *Phys.Rev.*, vol. C77, p. 034904, 2008, arXiv:0707.4672.

[354] N. Borghini and J. Ollitrault, "Azimuthally sensitive correlations in nucleus-nucleus collisions," *Phys.Rev.*, vol. C70, p. 064905, 2004, arXiv:nucl-th/0407041.

[355] T. Sjostrand, S. Mrenna, and P. Z. Skands, "PYTHIA 6.4 Physics and Manual," *JHEP*, vol. 0605, p. 026, 2006, arXiv:hep-ph/0603175.

[356] C. Tsallis, "Possible Generalization of Boltzmann-Gibbs Statistics," *J.Statist.Phys.*, vol. 52, pp. 479–487, 1988.

[357] K. Reygers, "Production of Neutral Pions and Eta-mesons in pp Collisions Measured with ALICE," *J.Phys.*, vol. G38, p. 124076, 2011, arXiv:1106.5932.

[358] Z.-W. Lin, C. M. Ko, B.-A. Li, B. Zhang, and S. Pal, "A Multi-phase transport model for relativistic heavy ion collisions," *Phys.Rev.*, vol. C72, p. 064901, 2005, arXiv:nucl-th/0411110.

[359] A. Adare *et al.*, "Deviation from quark-number scaling of the anisotropy parameter v_2 of pions, kaons, and protons in Au+Au collisions at $\sqrt{s_{\rm NN}} = 200\,\text{GeV}$," *Phys.Rev.*, vol. C85, p. 064914, 2012, arXiv:1203.2644.

[360] S. Kumar, S. Kumar, and R. K. Puri, "Elliptical flow and isospin effects in heavy-ion collisions at intermediate energies," *Phys.Rev.*, vol. C81, p. 014611, 2010, arXiv:1004.0895.

[361] D. Sutherland, "Current algebra and the decay $\eta \to 3\pi$," *Phys.Lett.*, vol. 23, p. 384, 1966.

[362] P. Dittner, P. H. Dondi, and S. Eliezer, "Chiral-Symmetry Breaking and the Electromagnetic Interaction in the $\eta \to 3\pi$ Decay," *Phys. Rev. D*, vol. 8, pp. 2253–2261, Oct 1973.

[363] F. Binon *et al.*, "The isospin violating decay $\eta' \to 3\pi^0$," *Phys.Lett.*, vol. B140, p. 264, 1984.

[364] A. Likhoded, A. Luchinsky, and V. Samoylenko, "Scalar Mesons in $\eta' \to 3\pi^0, \pi^0\pi^+\pi^-$ Decays," *Phys.Atom.Nucl.*, vol. 73, pp. 1789–1797, 2010, arXiv:1002.1535.

[365] M. Ivanov, "Identified charged hadron production measured with ALICE at the LHC," *Nucl.Phys.*, vol. A904-905, pp. 162c–169c, 2013.

[366] D. Lohner, "Measurement of Direct-Photon Elliptic Flow in Pb-Pb Collisions at $\sqrt{s_{\mathrm{NN}}} = 2.76\,\mathrm{TeV}$," 2012, arXiv:1212.3995.

[367] M. Klasen, C. Klein-Boesing, F. Koenig, and J. Wessels, "How robust is a thermal photon interpretation of the ALICE low-p_{T} data?," 2013, arXiv:1307.7034.

[368] C. Shen, U. W. Heinz, J.-F. Paquet, I. Kozlov, and C. Gale, "Anisotropic flow of thermal photons as a quark-gluon plasma viscometer," 2013, arXiv:1308.2111.

[369] C. Shen, U. Heinz, P. Huovinen, and H. Song, "Radial and elliptic flow in Pb+Pb collisions at the Large Hadron Collider from viscous hydrodynamic," *Phys.Rev.*, vol. C84, p. 044903, 2011, arXiv:1105.3226.

[370] Z. Qiu, C. Shen, and U. Heinz, "Hydrodynamic elliptic and triangular flow in Pb-Pb collisions at $\sqrt{s_{\mathrm{NN}}} = 2.76\,\mathrm{TeV}$," *Phys.Lett.*, vol. B707, pp. 151–155, 2012, arXiv:1110.3033.

[371] U. W. Heinz and S. Wong, "Elliptic flow from a transversally thermalized fireball," *Phys.Rev.*, vol. C66, p. 014907, 2002, arXiv:hep-ph/0205058.

[372] R. Chatterjee, H. Holopainen, I. Helenius, T. Renk, and K. J. Eskola, "Elliptic flow of thermal photons from event-by-event hydrodynamic model," 2013, arXiv:1305.6443.

[373] R. Rapp, "Dilepton Production in Heavy-Ion Collisions," 2013, arXiv:1306.6394.

[374] A. Chaudhuri, "Direct photon production and interferometry in $\sqrt{s_{\mathrm{NN}}} = 200\,\mathrm{GeV}$ Au+Au and in $\sqrt{s_{\mathrm{NN}}} = 2.76\,\mathrm{TeV}$ Pb-Pb collisions," 2013, arXiv:1305.6121.

[375] F.-M. Liu, "Study the early stage of heavy ion collisions with direct photons," 2012, arXiv:1212.6587.

[376] H. van Hees, C. Gale, and R. Rapp, "Thermal Photons and Collective Flow at the Relativistic heavy-ion Collider," *Phys.Rev.*, vol. C84, p. 054906, 2011, arXiv:1108.2131.

[377] T. Denz, "Simple Phenomenological Models for Anisotropic Direct Photon Production in Heavy-Ion Collisions." Bachelor's thesis, 2013.

[378] O. Linnyk, V. Konchakovski, W. Cassing, and E. Bratkovskaya, "Photon elliptic flow in relativistic heavy-ion collisions: hadronic versus partonic sources," 2013, arXiv:1304.7030.

[379] R. Petti, "Direct photons in Au+Au collisions measured with the PHENIX detector at RHIC," *J.Phys.Conf.Ser.*, vol. 316, p. 012026, 2011, arXiv:1107.5379.

[380] I. Tserruya, "Photons and low-mass dileptons: results from PHENIX," *Nucl.Phys.*, vol. A904-905, pp. 225c–232c, 2013, arXiv:1211.6002.

[381] K. Abraamyan, A. Anisimov, M. Baznat, K. Gudima, M. Nazarenko, *et al.*, "Observation of the E(38)-boson," 2012, arXiv:1208.3829.

[382] E. van Beveren and G. Rupp, "Reply to Comment on 'Material evidence of a 38 MeV boson'," 2012, arXiv:1204.3287.

[383] E. van Beveren and G. Rupp, "Material evidence of a 38 MeV boson," 2012, arXiv:1202.1739.

[384] E. van Beveren and G. Rupp, "First indications of the existence of a 38 MeV light scalar boson," 2011, arXiv:1102.1863.

[385] K. Kajantie and H. Miettinen, "Temperature Measurement of Quark-Gluon Plasma Formed in High-Energy Nucleus-Nucleus Collisions," *Z.Phys.*, vol. C9, p. 341, 1981.

[386] P. Aurenche, M. Fontannaz, J.-P. Guillet, E. Pilon, and M. Werlen, "A New critical study of photon production in hadronic collisions," *Phys.Rev.*, vol. D73, p. 094007, 2006, arXiv:hep-ph/0602133.

[387] V. Goloviznin, A. Snigirev, and G. Zinovjev, "Towards azimuthal anisotropy of direct photons," 2012, arXiv:1209.2380.

[388] G.-Y. Qin, H. Petersen, S. A. Bass, and B. Muller, "Translation of collision geometry fluctuations into momentum anisotropies in relativistic heavy-ion collisions," *Phys.Rev.*, vol. C82, p. 064903, 2010, arXiv:1009.1847.

[389] U. W. Heinz, R. Chatterjee, E. S. Frodermann, C. Gale, and D. K. Srivastava, "Elliptic flow of thermal photons and dileptons," *Nucl.Phys.*, vol. A783, pp. 379–386, 2007, arXiv:nucl-th/0610014.

[390] M. Dion, J.-F. Paquet, B. Schenke, C. Young, S. Jeon, *et al.*, "Viscous photons in relativistic heavy ion collisions," *Phys.Rev.*, vol. C84, p. 064901, 2011, arXiv:1109.4405.

[391] K. Kajantie, M. Kataja, L. D. McLerran, and P. Ruuskanen, "Transverse Flow Effects in Dilepton Emission," *Phys.Rev.*, vol. D34, p. 811, 1986.

[392] R. Raniwala, S. Raniwala, and Y. P. Viyogi, "Effect of finite granularity of detectors on anisotropy coefficients," *Eur.Phys.J.*, vol. C48, pp. 677–682, 2006, arXiv:nucl-ex/0502023.

[393] J. Rak and M. J. Tannenbaum, *High p_{T} physics in the heavy ion era*. Cambridge monographs on particle physics, nuclear physics and cosmology, Cambridge: Cambridge Univ. Press, 2013.

[394] K. Pearson, "X. On the criterion that a given system of deviations from the probable in the case of a correlated system of variables is such that it can be reasonably supposed to have arisen from random sampling," *Philosophical Magazine Series 5*, vol. 50, no. 302, pp. 157–175, 1900.

Acknowlegdements

I owe my deepest gratitude to my supervisor Klaus Reygers for engaging my enthusiasm for this research on direct photons and whose encouragement, patience and support enabled me to accomplish this thesis. I am also heartily thankful to my co-advisors Johanna Stachel and Carlo Ewerz for their helpful advice and support over the last three years.

I would like to thank everyone in the ALICE group at the Physikalisches Institut for creating a great working environment and many interesting discussions over the last years. I would like to express my gratitude to Anton Andronic, Yvonne Pachmayer, Markus Fasel and Linus Feldkamp for the kind collaboration during my work on the electron identification method using the ALICE Transition Radiation Detector. I also appreciate many discussions with Jochen Klein and Johannes Stiller on different topics. I am particularly grateful to Martin Wilde for a very interesting and fruitful collaboration on the direct-photon measurement. In this context, I would also like to thank the members of the Photon Conversion Group for the collaboration. I wish to thank Peter Jacobs for his hospitality during my guest visit at the Berkeley Lawrence National Laboratory. I am heartily thankful to Leo Greiner for making me patiently familiar with the STAR HFT upgrade. I am especially indebted with Arthur Poskanzer and Alexander Schmah for many interesting and fruitful discussions about anisotropic flow measurements. In this context, I would also like to thank Jean-Yves Ollitrault from Saclay for introducing me to the details of hydrodynamics.
For proof reading and fruitful discussions concerning this thesis, I wish to thank Anton Andronic, Jochen Klein, Antonin Maire, Yvonne Pachmayer, Kai Schweda, Johannes Stiller and Jeremy Wilkinson.
Lastly, I wish to express my gratitude to my family and friends for supporting me in many ways during the completion of this thesis.

For financial support over the last three years I am grateful to the DFG International Research Training Group 'Application and Development of Intelligent Detectors' and the Helmholtz-Graduate School for Hadron and Ion Research.